

國立交通大學

機械工程學系 碩士論文

使用波茲曼模型方程式模擬自由分子流到近連續流的正方



形空穴流場

**Simulation of Square Driven Cavity Flows from
Free-Molecular to Near-Continuum Regime Using Model
Boltzmann Equation**

研究生：盧勁全

指導教授：吳宗信 博士

中華民國九十六年七月

使用波茲曼模型方程式模擬自由分子流到近連續流的正方形空穴流場

Simulation of Square Driven Cavity Flows from Free-Molecular to
Near-Continuum Regime Using Model Boltzmann Equation

研究生：盧勁全

Student: Chin-Chuan Hung

指導教授：吳宗信 博士

Advisor: Dr. Jong-Shinn Wu

國立交通大學

機械工程學系

碩士論文

A Thesis

Submitted to Institute of Mechanical Engineering

College of Engineering

National Chiao Tung University

in partial Fulfillment of the Requirements

for the Degree of

Master of Science

in

Mechanical Engineering

July 2007

Hsinchu, Taiwan

中華民國九十六年七月

國立交通大學

論文口試委員會審定書

本校 機械工程 學系碩士班 盧勁全 君

所提論文(中文) 使用波茲曼模型方程式模擬自由分子流到近連續流的正方形空穴流場
(英文) Simulation of Square Driven Cavity Flows from Free-Molecular to Near-Continuum Regime Using Model Boltzmann Equation

合於碩士資格水準、業經本委員會評審認可。

口試委員：黃俊誠 _____

郭添全 _____

陳明志 _____

指導教授：吳彥信 _____

系主任：周以群 教授

中華民國 96 年 7 月 26 日

致謝

誠蒙指導教授吳宗信老師的指導與督促，使得本文得以順利完成。在研究及做學問方面，經老師的提攜與指點，讓我能順利的踏入研究的領域並且不斷地茁壯。此外老師對於台灣本土精神及文化上的努力更是令我印象深刻。同時也感謝口試委員黃俊誠老師、郭添全博士、陳明志老師在口試過程中所提供的珍貴意見，使得本文得以更加完善。另外特別感謝黃俊誠老師長期發展關於此篇論文中所用到的程式之辛勞，且不吝於付出時間與心力來教導我於研究中所遭遇的問題，以及祭哥、凱文在研究上的啟發教導與協助，在此一併致謝。

需要感謝的人實在太多了，邵雲龍、曾坤璋、許國賢、陳育進、梁偉豪、陳百彥等已畢業的學長，還有 APPL 實驗室的成員，李允民、周欣芸、李富利、洪捷榮、許哲維、鄭凱文、胡孟樺、邱沅明、江明鴻學長姊們指導受益良多，洪維呈、謝昇汎、林宗漢、陳又寧、王柏勝、林武伸、邱文山、黃昌彥同學，與你們共同努力挑燈夜戰的每一天是我日後最甘苦與美好的回憶，正勤、士傑、志良、玫琪、丞志、政霖、育宗等學弟妹們協助，還有來自紐西蘭的學者 Hadley M. Cave 外語能力的訓練，使我兩年中過的非常充實且溫馨。

特別感謝爸爸、媽媽、兩位弟弟，在生活與精神上的支持，令我得以專心研究並且無憂無慮。最後謝謝老婆思穎的關懷與體諒，給我無比的鼓勵，順利完成本文。僅將這份成果獻給你們。歡樂的時光總是過的特別的快，又到時間講辦辦。畢業之後同學們各奔東西，盼望大家都能闖出美好的將來。

盧勁全 謹誌

九六年七月于風城

使用波茲曼模型方程式模擬自由分子流到近連續流的正方形空穴流場

學生: 盧勁全

指導教授: 吳宗信 博士

國立交通大學機械工程學系

摘要

上板瞬間抽動的空穴流場在計算流體力學上是一個很基準的問題，因為它具有簡單的幾何結構並且在其角落上有差異性很大的奇異點。在流場模擬上，時常使用它來驗證不同的數值方法。然而，過去的學習都著重在連續流場上的研究。關於稀薄流場與近連續流流場的研究則是相當的稀少。因此本文的動機是模擬空穴流場在稀薄區域上的應用。

本文內容是利用建構在有限差分法(finite-difference scheme),速度空間上應用分立座標法(discrete ordinate method)的波茲曼模型方程式(MBE)來模擬二維的上板瞬間啟動之四方形穴流從自由分子流到近連續流的流場。本文中使用BGK model與Shakov model兩種模型來近似碰撞積分項。為了驗證波茲曼模型方程式(MBE)的正確性，我們比較直接蒙地卡羅模擬法(DSMC)與波茲曼模型方程式(MBE)在模擬穴流 $Kn=0.0033$ 與 $Ma=2.0$ 的結果。本文中空穴流場的模擬範圍包含了 $Kn=10\sim 0.0033$ 與 $Ma=0.5\sim 2$ 的流場。

在模擬的結果中顯示，相同的Mach number隨著氣體的稀薄化，速度滑動現

象與溫度跳動現象會更加明顯。在各種的Mach number下 ($M=0.5, 0.9, 1.1, 2$), 隨著Kn的變小, 渦流中心會朝著右上方移動, 但是當 $M=0.5, Kn=0.0033$ 與 $M=2, Kn=0.0033$ 時渦流中心會改變成朝左下方移動。此外當Kn小於0.01時, 在主要渦流的兩側角落都會產生出次渦流。當Kn大於0.01時, 除了 $M=2, Kn=10$ 這個情況下會在右下角產生一個次渦流以外, 其他的情況則不會產生次渦流。



Simulation of Square Driven Cavity Flows from Free-Molecular to Near-Continuum Regime Using Model Boltzmann Equation

Student: C. C. Lu

Advisor: Dr. J. S. Wu

Department of Mechanical Engineering
National Chiao-Tung University

Abstract

The driven cavity flow is one of the benchmark problems often used in computational fluid dynamics due to its simple geometry but highly singular points at the corners. It is often used to verify different numerical methods for fluid-flow simulation. However, past studies in this regard focused on flows in the continuum regime. Very few researches have been done systematically in the rarefied or near-continuum regime. Several applications require consideration of rarefaction, which motivates the present thesis to focus on simulation of driven cavity flows in this region.

This thesis reports the simulation of a two-dimensional top driven square cavity flows from free-molecular to near-continuum regime using a model Boltzmann equation (MBE) solver. The MBE was discretized using finite-difference scheme and discrete ordinate method for the configuration and velocity space, respectively. The collision integral was approximated by either the BGK or Shakov model. The MBE solver was first verified by comparing the results to those obtained using direct

simulation Monte Carlo method for a driven cavity flow at $Kn=0.0033$ and $Ma=2.0$.

Simulation conditions include Knudsen number and speed of the top driven plate in the range of $Kn=10-0.0033$ and $Ma=0.5-2$, respectively.

Results show that the velocity slips and temperature jumps increase at the solid walls with increasing rarefaction at the same Mach number. The vortex center move toward left and down as Knudsen number ($Kn=10, 1, 0.1, 0.01$) decreasing for $M=0.5, 0.9, 1.1, \text{ and } 2$, when $Kn=0.0033$ is opposite. But the vortex center move toward the opposite way for $M=0.5, Kn=0.0033$ and $M=2, Kn=0.0033$. For $Kn=0.01, \text{ and } 0.0033$, under the main vortex secondary eddies have been created at the two bottom corners. Only in this special example for $M=2, Kn=10$, unnder the main vortex secondary eddie have been created at the right bottom corners.

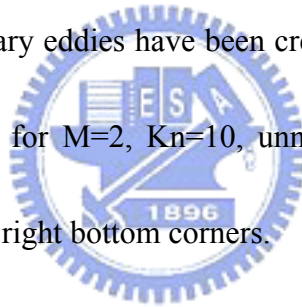


Table of Contents

Abstract	IV
Table of Contents	VI
List of Tables	VIII
List of Figures	IX
Nomenclature	XVI
Chapter 1. Introduction	1
1.1 Motivation and Background	1
1.2 Literature Reviews in Driven Cavity Flows	4
1.3 Specific Objectives of the Thesis	6
Chapter 2. Numerical Method	7
2.1 Boltzmann equation	7
2.2 Model Boltzmann equation	9
2.2.1 BGK model	10
2.2.2 Ellipsoidal model	12
2.2.3 Shakov model	13
2.3 Discrete Ordinate Method	15
2.4 Finite-difference Discretization of the Two-Dimensional MBE	15
2.5 Numerical Algorithm in solving the MBE	24
Chapter 3. Preliminary Results and Discussion	32
3.1 Comparison of MBE Results with DSMC Numerical Method	32
The computed results using MBE are found to compare well with those using the DSMC(direct simulation Monte Carlo) in the Near-continuum regime flows	32
3.2 Driven Cavity Flows	33
3.2.1 Problem Description and Test Conditions	33
3.2.2 Grid Convergence Tests	33
3.2.3 Effects of Knudsen Number	34
3.2.3.1 General Simulation Results	34
3.2.3.1.1 Subsonic Moving Plate (M=0.5, 0.9)	34
3.2.3.1.2 Supersonic Moving Plate (M=1.1, 2)	36
3.2.3.2 Property Distributions Across Cavity Centroid	38
3.2.3.3 Property Distributions Near Solid Walls	38
3.2.3.4 Recirculation Center Position	39
3.2.4 Effect of Mach Number of the Driven Plate	41
3.2.4.1 General Simulation Results	41

3.2.4.1.1 Free Molecular Regime ($Kn=10$).....	41
3.2.4.1.2 Transitional Regime ($Kn=1, 0.1, 0.01$)	42
3.2.4.1.3 Near-continuum Regime ($Kn=0.0033$)	44
3.2.4.2 Property Distributions Across Cavity Centroid	46
3.2.4.3 Property Distributions Near Solid Walls.....	46
3.2.4.4 Recirculation Center Position	47
Chapter 4. Conclusions and Recommendation of Future Work.....	49
4.1 Conclusion	49
4.2 Recommendation of Future Work.....	50
References.....	51



List of Tables

Table. I	All the Simulation cases.....	53
Table. II	Mesh information	54
Table. III	Simulation condition.....	55
Table. IV	Location of the center of the top vortex for various values of Ma and Kn.....	56



List of Figures

Fig. 1.1	Flow Regime and solution method.....	57
Fig. 2.1	The Knudsen number limits on the mathematical models.	57
Fig. 3.1	The 2D square (L/H=1) driven cavity flow with moving top plate 58	
Fig. 3.2	Grid. 1 is grid mesh of 101 by 101 and smallest grid size is 5×10^{-3}	59
Fig. 3.3	Grid. 2 is grid mesh of 101 by 101 and smallest grid size is 1×10^{-3}	60
Fig. 3.4	Grid. 3 is grid mesh of 201 by 201 and smallest grid size is 5×10^{-3}	61
Fig. 3.5	Grid. 4 is grid mesh of 101 by 101 and smallest grid size is 1×10^{-2}	62
Fig. 3.6	The residual functions for different grids (a) Grid. 1, (b) Grid. 2, (c) Grid. 3, (d)Grid. 4.....	63
Fig. 3.7	Contours of number Density for M=0.5, (a) Kn=10; (b) Kn=1; (c) Kn=0.1; (d) Kn=0.01; (e) Kn=0.0033.....	64
Fig. 3.8	Contours of Temperature for M=0.5, (a) Kn=10; (b) Kn=1; (c) Kn=0.1; (d) Kn=0.01; (e) Kn=0.0033.....	65
Fig. 3.9	Contours of Mach number for M=0.5, (a) Kn=10; (b) Kn=1; (c) Kn=0.1; (d) Kn=0.01; (e) Kn=0.0033.....	66
Fig. 3.10	Contours of U-velocity for M=0.5, (a) Kn=10; (b) Kn=1; (c) Kn=0.1; (d) Kn=0.01; (e) Kn=0.0033.....	67
Fig. 3.11	Contours of V-velocity for M=0.5, (a) Kn=10; (b) Kn=1; (c) Kn=0.1; (d) Kn=0.01; (e) Kn=0.0033.....	68
Fig. 3.12	Contours of number Density for M=0.9, (a) Kn=10; (b) Kn=1; (c) Kn=0.1; (d) Kn=0.01; (e) Kn=0.0033.....	69
Fig. 3.13	Contours of Temperature for M=0.9, (a) Kn=10; (b) Kn=1; (c) Kn=0.1; (d) Kn=0.01; (e) Kn=0.0033.....	70
Fig. 3.14	Contours of Mach number for M=0.9, (a) Kn=10; (b) Kn=1; (c) Kn=0.1; (d) Kn=0.01; (e) Kn=0.0033.....	71
Fig. 3.15	Contours of U-velocity for M=0.9, (a) Kn=10; (b) Kn=1; (c) Kn=0.1; (d) Kn=0.01; (e) Kn=0.0033.....	72
Fig. 3.16	Contours of V-velocity for M=0.9, (a) Kn=10; (b) Kn=1; (c)	

Kn=0.1; (d) Kn=0.01; (e) Kn=0.0033	73
Fig. 3.17 Contours of number Density for M=1.1, (a) Kn=10; (b) Kn=1; (c) Kn=0.1; (d) Kn=0.01; (e) Kn=0.0033	74
Fig. 3.18 Contours of Temperature for M=1.1, (a) Kn=10; (b) Kn=1; (c) Kn=0.1; (d) Kn=0.01; (e) Kn=0.0033	75
Fig. 3.19 Contours of Mach number for M=1.1, (a) Kn=10; (b) Kn=1; (c) Kn=0.1; (d) Kn=0.01; (e) Kn=0.0033	76
Fig. 3.20 Contours of U-velocity for M=1.1, (a) Kn=10; (b) Kn=1; (c) Kn=0.1; (d) Kn=0.01; (e) Kn=0.0033	77
Fig. 3.21 Contours of V-velocity for M=1.1, (a) Kn=10; (b) Kn=1; (c) Kn=0.1; (d) Kn=0.01; (e) Kn=0.0033	78
Fig. 3.22 Contours of number Density for M=2.0, (a) Kn=10; (b) Kn=1; (c) Kn=0.1; (d) Kn=0.01; (e) Kn=0.0033	79
Fig. 3.23 Contours of Temperature for M=2.0, (a) Kn=10; (b) Kn=1; (c) Kn=0.1; (d) Kn=0.01; (e) Kn=0.0033	80
Fig. 3.24 Contours of Mach number for M=2.0, (a) Kn=10; (b) Kn=1; (c) Kn=0.1; (d) Kn=0.01; (e) Kn=0.0033	81
Fig. 3.25 Contours of U-velocity for M=2.0, (a) Kn=10; (b) Kn=1; (c) Kn=0.1; (d) Kn=0.01; (e) Kn=0.0033	82
Fig. 3.26 Contours of V-velocity for M=2.0, (a) Kn=10; (b) Kn=1; (c) Kn=0.1; (d) Kn=0.01; (e) Kn=0.0033	83
Fig. 3.27 Profile of the number Density on a vertical plane x=0.5 for (a) M=0.5; (b) M=0.9; (c) M=1.1; (d) M=2	84
Fig. 3.28 Profile of the Temperature on a vertical plane x=0.5 for (a) M=0.5; (b) M=0.9; (c) M=1.1; (d) M=2	85
Fig. 3.29 Profile of the U-velocity on a vertical plane x=0.5 for (a) M=0.5; (b) M=0.9; (c) M=1.1; (d) M=2	86
Fig. 3.30 Profile of the V-velocity on a vertical plane x=0.5 for (a) M=0.5; (b) M=0.9; (c) M=1.1; (d) M=2	87
Fig. 3.31 Profile of the number Density on a horizontal plane y=-0.5 for (a) M=0.5; (b) M=0.9; (c) M=1.1; (d) M=2	88
Fig. 3.32 Profile of the Temperature on a horizontal plane y=-0.5 for (a) M=0.5; (b) M=0.9; (c) M=1.1; (d) M=2	89
Fig. 3.33 Profile of the U-velocity on a horizontal plane y=-0.5 for (a) M=0.5; (b) M=0.9; (c) M=1.1; (d) M=2	90
Fig. 3.34 Profile of the V-velocity on a horizontal plane y=-0.5 for (a) M=0.5; (b) M=0.9; (c) M=1.1; (d) M=2	91
Fig. 3.35 Profile of the number Density on a vertical plane x=0 for (a)	

M=0.5; (b) M=0.9; (c) M=1.1; (d) M=2	92
Fig. 3.36 Profile of the Temperature on a vertical plane $x=0$ for (a) M=0.5; (b) M=0.9; (c) M=1.1; (d) M=2	93
Fig. 3.37 Profile of the U-velocity on a vertical plane $x=0$ for (a) M=0.5; (b) M=0.9; (c) M=1.1; (d) M=2	94
Fig. 3.38 Profile of the V-velocity on a vertical plane $x=0$ for (a) M=0.5; (b) M=0.9; (c) M=1.1; (d) M=2	95
Fig. 3.39 Profile of the number Density on a vertical plane $x=1$ for (a) M=0.5; (b) M=0.9; (c) M=1.1; (d) M=2	96
Fig. 3.40 Profile of the Temperature on a vertical plane $x=1$ for (a) M=0.5; (b) M=0.9; (c) M=1.1; (d) M=2	97
Fig. 3.41 Profile of the U-velocity on a vertical plane $x=1$ for (a) M=0.5; (b) M=0.9; (c) M=1.1; (d) M=2	98
Fig. 3.42 Profile of the V-velocity on a vertical plane $x=1$ for (a) M=0.5; (b) M=0.9; (c) M=1.1; (d) M=2	99
Fig. 3.43 Profile of the number Density on a horizontal plane $y=-1$ for (a) M=0.5; (b) M=0.9; (c) M=1.1; (d) M=2	100
Fig. 3.44 Profile of the Temperature on a horizontal plane $y=-1$ for (a) M=0.5; (b) M=0.9; (c) M=1.1; (d) M=2	101
Fig. 3.45 Profile of the U-velocity on a horizontal plane $y=-1$ for (a) M=0.5; (b) M=0.9; (c) M=1.1; (d) M=2	102
Fig. 3.46 Profile of the V-velocity on a horizontal plane $y=-1$ for (a) M=0.5; (b) M=0.9; (c) M=1.1; (d) M=2	103
Fig. 3.47 Profile of the number Density on a horizontal plane $y=0$ for (a) M=0.5; (b) M=0.9; (c) M=1.1; (d) M=2	104
Fig. 3.48 Profile of the Temperature on a horizontal plane $y=0$ for (a) M=0.5; (b) M=0.9; (c) M=1.1; (d) M=2	105
Fig. 3.49 Profile of the U-velocity on a horizontal plane $y=0$ for (a) M=0.5; (b) M=0.9; (c) M=1.1; (d) M=2	106
Fig. 3.50 Profile of the V-velocity on a horizontal plane $y=0$ for (a) M=0.5; (b) M=0.9; (c) M=1.1; (d) M=2	107
Fig. 3.51 Velocity streamlines for M=0.5, and (a) Kn=10; (b) Kn=1; (c) Kn=0.1; (d) Kn=0.01; (e) Kn=0.0033.....	108
Fig. 3.52 Velocity streamlines for M=0.9, and (a) Kn=10; (b) Kn=1; (c) Kn=0.1; (d) Kn=0.01; (e) Kn=0.0033.....	109
Fig. 3.53 Velocity streamlines for M=1.1, and (a) Kn=10; (b) Kn=1; (c) Kn=0.1; (d) Kn=0.01; (e) Kn=0.0033.....	110
Fig. 3.54 Velocity streamlines for M=2, and (a) Kn=10; (b) Kn=1; (c)	

Kn=0.1; (d) Kn=0.01; (e) Kn=0.0033	111
Fig. 3.55 Location of the center for x/L of the top vortex for various values of Mach number and Knudsen number.	112
Fig. 3.56 Location of the center for y/L of the top vortex for various values of Mach number and Knudsen number.	113
Fig. 3.57 Contours of number Density for $Kn=10$, (a) $M=0.5$; (b) $M=0.9$; (c) $M=1.1$; (d) $M=2.0$	114
Fig. 3.58 Contours of Temperature for $Kn=10$, (a) $M=0.5$; (b) $M=0.9$; (c) $M=1.1$; (d) $M=2.0$	115
Fig. 3.59 Contours of Mach number for $Kn=10$, (a) $M=0.5$; (b) $M=0.9$; (c) $M=1.1$; (d) $M=2.0$	116
Fig. 3.60 Contours of U-velocity for $Kn=10$, (a) $M=0.5$; (b) $M=0.9$; (c) $M=1.1$; (d) $M=2.0$	117
Fig. 3.61 Contours of V-velocity for $Kn=10$, (a) $M=0.5$; (b) $M=0.9$; (c) $M=1.1$; (d) $M=2.0$	118
Fig. 3.62 Contours of number Density for $Kn=1$, (a) $M=0.5$; (b) $M=0.9$; (c) $M=1.1$; (d) $M=2.0$	119
Fig. 3.63 Contours of Temperature for $Kn=1$, (a) $M=0.5$; (b) $M=0.9$; (c) $M=1.1$; (d) $M=2.0$	120
Fig. 3.64 Contours of Mach number for $Kn=1$, (a) $M=0.5$; (b) $M=0.9$; (c) $M=1.1$; (d) $M=2.0$	121
Fig. 3.65 Contours of U-velocity for $Kn=1$, (a) $M=0.5$; (b) $M=0.9$; (c) $M=1.1$; (d) $M=2.0$	122
Fig. 3.66 Contours of V-velocity for $Kn=1$, (a) $M=0.5$; (b) $M=0.9$; (c) $M=1.1$; (d) $M=2.0$	123
Fig. 3.67 Contours of number Density for $Kn=0.1$, (a) $M=0.5$; (b) $M=0.9$; (c) $M=1.1$; (d) $M=2.0$	124
Fig. 3.68 Contours of Temperature for $Kn=0.1$, (a) $M=0.5$; (b) $M=0.9$; (c) $M=1.1$; (d) $M=2.0$	125
Fig. 3.69 Contours of Mach number for $Kn=0.1$, (a) $M=0.5$; (b) $M=0.9$; (c) $M=1.1$; (d) $M=2.0$	126
Fig. 3.70 Contours of U-velocity for $Kn=0.1$, (a) $M=0.5$; (b) $M=0.9$; (c) $M=1.1$; (d) $M=2.0$	127
Fig. 3.71 Contours of V-velocity for $Kn=0.1$, (a) $M=0.5$; (b) $M=0.9$; (c) $M=1.1$; (d) $M=2.0$	128
Fig. 3.72 Contours of number Density for $Kn=0.01$, (a) $M=0.5$; (b) $M=0.9$; (c) $M=1.1$; (d) $M=2.0$	129
Fig. 3.73 Contours of Temperature for $Kn=0.01$, (a) $M=0.5$; (b) $M=0.9$; (c)	

M=1.1; (d) M=2.0	130
Fig. 3.74 Contours of Mach number for $Kn=0.01$, (a) $M=0.5$; (b) $M=0.9$; (c) $M=1.1$; (d) $M=2.0$	131
Fig. 3.75 Contours of U-velocity for $Kn=0.01$, (a) $M=0.5$; (b) $M=0.9$; (c) $M=1.1$; (d) $M=2.0$	132
Fig. 3.76 Contours of V-velocity for $Kn=0.01$, (a) $M=0.5$; (b) $M=0.9$; (c) $M=1.1$; (d) $M=2.0$	133
Fig. 3.77 Contours of number Density for $Kn=0.0033$, (a) $M=0.5$; (b) $M=0.9$; (c) $M=1.1$; (d) $M=2.0$	134
Fig. 3.78 Contours of Temperature for $Kn=0.0033$, (a) $M=0.5$; (b) $M=0.9$; (c) $M=1.1$; (d) $M=2.0$	135
Fig. 3.79 Contours of Mach number for $Kn=0.0033$, (a) $M=0.5$; (b) $M=0.9$; (c) $M=1.1$; (d) $M=2.0$	136
Fig. 3.80 Contours of U-velocity for $Kn=0.0033$, (a) $M=0.5$; (b) $M=0.9$; (c) $M=1.1$; (d) $M=2.0$	137
Fig. 3.81 Contours of V-velocity for $Kn=0.0033$, (a) $M=0.5$; (b) $M=0.9$; (c) $M=1.1$; (d) $M=2.0$	138
Fig. 3.82 Profile of the number Density on a vertical plane $x=0.5$ for (a) $Kn=10$; (b) $Kn=1$; (c) $Kn=0.1$; (d) $Kn=0.01$; (e) $Kn=0.0033$	139
Fig. 3.83 Profile of the Temperature on a vertical plane $x=0.5$ for (a) $Kn=10$; (b) $Kn=1$; (c) $Kn=0.1$; (d) $Kn=0.01$; (e) $Kn=0.0033$	140
Fig. 3.84 Profile of the U-velocity on a vertical plane $x=0.5$ for (a) $Kn=10$; (b) $Kn=1$; (c) $Kn=0.1$; (d) $Kn=0.01$; (e) $Kn=0.0033$	141
Fig. 3.85 Profile of the V-velocity on a vertical plane $x=0.5$ for (a) $Kn=10$; (b) $Kn=1$; (c) $Kn=0.1$; (d) $Kn=0.01$; (e) $Kn=0.0033$	142
Fig. 3.86 Profile of the number Density on a horizontal plane $y=-0.5$ for (a) $Kn=10$; (b) $Kn=1$; (c) $Kn=0.1$; (d) $Kn=0.01$; (e) $Kn=0.0033$	143
Fig. 3.87 Profile of the Temperature on a horizontal plane $y=-0.5$ for (a) $Kn=10$; (b) $Kn=1$; (c) $Kn=0.1$; (d) $Kn=0.01$; (e) $Kn=0.0033$	144
Fig. 3.88 Profile of the U-velocity on a horizontal plane $y=-0.5$ for (a) $Kn=10$; (b) $Kn=1$; (c) $Kn=0.1$; (d) $Kn=0.01$; (e) $Kn=0.0033$	145
Fig. 3.89 Profile of the V-velocity on a horizontal plane $y=-0.5$ for (a) $Kn=10$; (b) $Kn=1$; (c) $Kn=0.1$; (d) $Kn=0.01$; (e) $Kn=0.0033$	146
Fig. 3.90 Profile of the number Density on a vertical plane $x=0$ for (a) $Kn=10$; (b) $Kn=1$; (c) $Kn=0.1$; (d) $Kn=0.01$; (e) $Kn=0.0033$	147
Fig. 3.91 Profile of the Temperature on a vertical plane $x=0$ for (a) $Kn=10$; (b) $Kn=1$; (c) $Kn=0.1$; (d) $Kn=0.01$; (e) $Kn=0.0033$	148
Fig. 3.92 Profile of the U-velocity on a vertical plane $x=0$ for (a) $Kn=10$;	

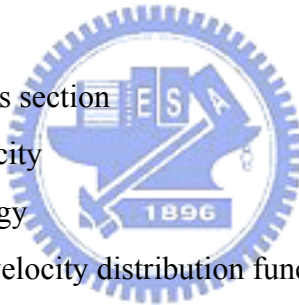
	(b) $Kn=1$; (c) $Kn=0.1$; (d) $Kn=0.01$; (e) $Kn=0.0033$	149
Fig. 3.93	Profile of the V-velocity on a vertical plane $x=0$ for (a) $Kn=10$; (b) $Kn=1$; (c) $Kn=0.1$; (d) $Kn=0.01$; (e) $Kn=0.0033$	150
Fig. 3.94	Profile of the number Density on a vertical plane $x=1$ for (a) $Kn=10$; (b) $Kn=1$; (c) $Kn=0.1$; (d) $Kn=0.01$; (e) $Kn=0.0033$	151
Fig. 3.95	Profile of the Temperature on a vertical plane $x=1$ for (a) $Kn=10$; (b) $Kn=1$; (c) $Kn=0.1$; (d) $Kn=0.01$; (e) $Kn=0.0033$	152
Fig. 3.96	Profile of the U-velocity on a vertical plane $x=1$ for (a) $Kn=10$; (b) $Kn=1$; (c) $Kn=0.1$; (d) $Kn=0.01$; (e) $Kn=0.0033$	153
Fig. 3.97	Profile of the V-velocity on a vertical plane $x=1$ for (a) $Kn=10$; (b) $Kn=1$; (c) $Kn=0.1$; (d) $Kn=0.01$; (e) $Kn=0.0033$	154
Fig. 3.98	Profile of the number Density on a horizontal plane $y=-1$ for (a) $Kn=10$; (b) $Kn=1$; (c) $Kn=0.1$; (d) $Kn=0.01$; (e) $Kn=0.0033$	155
Fig. 3.99	Profile of the Temperature on a horizontal plane $y=-1$ for (a) $Kn=10$; (b) $Kn=1$; (c) $Kn=0.1$; (d) $Kn=0.01$; (e) $Kn=0.0033$	156
Fig. 3.100	Profile of the U-velocity on a horizontal plane $y=-1$ for (a) $Kn=10$; (b) $Kn=1$; (c) $Kn=0.1$; (d) $Kn=0.01$; (e) $Kn=0.0033$	157
Fig. 3.101	Profile of the V-velocity on a horizontal plane $y=-1$ for (a) $Kn=10$; (b) $Kn=1$; (c) $Kn=0.1$; (d) $Kn=0.01$; (e) $Kn=0.0033$	158
Fig. 3.102	Profile of the number Density on a horizontal plane $y=0$ for (a) $Kn=10$; (b) $Kn=1$; (c) $Kn=0.1$; (d) $Kn=0.01$; (e) $Kn=0.0033$	159
Fig. 3.103	Profile of the Temperature on a horizontal plane $y=0$ for (a) $Kn=10$; (b) $Kn=1$; (c) $Kn=0.1$; (d) $Kn=0.01$; (e) $Kn=0.0033$	160
Fig. 3.104	Profile of the U-velocity on a horizontal plane $y=0$ for (a) $Kn=10$; (b) $Kn=1$; (c) $Kn=0.1$; (d) $Kn=0.01$; (e) $Kn=0.0033$	161
Fig. 3.105	Profile of the V-velocity on a horizontal plane $y=0$ for (a) $Kn=10$; (b) $Kn=1$; (c) $Kn=0.1$; (d) $Kn=0.01$; (e) $Kn=0.0033$	162
Fig. 3.106	Velocity streamlines for $Kn=10$, and (a) $M=0.5$; (b) $M=0.9$; (c) $M=1.1$; (d) $M=2.0$	163
Fig. 3.107	Velocity streamlines for $Kn=1$, and (a) $M=0.5$; (b) $M=0.9$; (c) $M=1.1$; (d) $M=2.0$	164
Fig. 3.108	Velocity streamlines for $Kn=0.1$, and (a) $M=0.5$; (b) $M=0.9$; (c) $M=1.1$; (d) $M=2.0$	165
Fig. 3.109	Velocity streamlines for $Kn=0.01$, and (a) $M=0.5$; (b) $M=0.9$; (c) $M=1.1$; (d) $M=2.0$	166
Fig. 3.110	Velocity streamlines for $Kn=0.0033$, and (a) $M=0.5$; (b) $M=0.9$; (c) $M=1.1$; (d) $M=2.0$	167
Fig. 3.111	Location of the center for x/L of the top vortex for various	

values of Mach number and Knudsen number.	168
Fig. 3.112 Location of the center for y/L of the top vortex for various values of Mach number and Knudsen number.	169
Fig. 3.113 Properties of $M=0.9$, $Kn=0.0033$ using UNIC for (a) number density, (b) temperature, (c) Mach number, (d) u-velocity, (e) v-velocity, (f) velocity streamlines.	170
Fig. 3.114 Properties of $M=2$, $Kn=0.0033$ using DSMC for (a) number density, (b) temperature, (c) Mach number, (d) u-velocity, (e) v-velocity, (f) velocity streamlines.	171



Nomenclature

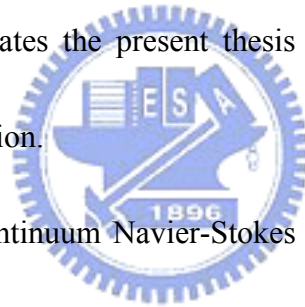
λ	:	mean free path	
ρ	:	density	
δ	:	Kronecker delta	
$\bar{\delta}$:	the Dirac delta function	
σ	:	the differential cross section	
μ	:	coefficient of viscosity	
χ	:	deflection angle	
ν	:	collision rate	
ξ	:	transformed \hat{x} coordinate	
η	:	transformed \hat{y} coordinate	
τ	:	viscous stress, relaxation time	
Ω	:	space domain	
Δt	:	time-step	
σ_T	:	the total cross section	
c	:	random velocity	
e	:	specific energy	
f	:	normalized velocity distribution function in velocity space	
f^M	:	Maxwellian velocity distribution	
g, h, j, k	:	reduced distribution function	
k	:	the Boltzmann constant	
Kn	:	Knudsen number	
L	:	characteristic length;	
m	:	molecule mass	
M	:	mach number	
n	:	number density	
P_r	:	Prandtl number	
R	:	gas constant	
Re	:	Reynolds number	
u	:	mean velocity	



Chapter 1. Introduction

1.1 Motivation and Background

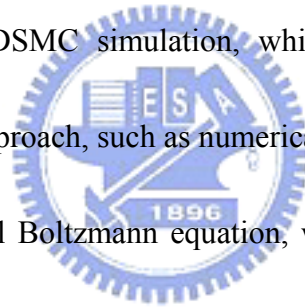
The driven cavity flow is one of the benchmark problems often used in computational fluid dynamics due to its simple geometry but highly singular points at the corners. It is often used to verify different numerical methods for fluid-flow simulation. However, past studies in this regard focused on flows in the continuum regime. Very few researches have been done systematically in the rarefied or near-continuum regime. Several applications require consideration of rarefaction on the flow fields, which motivates the present thesis to focus on the simulations of driven cavity flows in this region.



It is well known that continuum Navier-Stokes equations fails in treating these non-equilibrium effects in the transitional regime and beyond, as shown in Fig. 1.1. Even Navier-Stokes equation was often used with slip boundary conditions at walls for slightly rarefied flows, it is still uncertain how accurate they are and how far into the rarefied regime they can be applied. Thus, the Boltzmann equation based on the kinetic theory of gases needs to be used in these regimes. Due to the complexity of the nonlinear integral-differential nature of the equation, analytical solutions of the Boltzmann equation are rarely seen, hence numerical solutions is necessary.

For the simulation of gas flows in rarefied or transitional regimes, there mainly

exist two classes of methods. The first one is a probabilistic approach, such as the direct simulation Monte Carlo method (DSMC) [Bird's book, 1994], which has been proved mathematically that it solves Boltzmann equation as the number simulated particles becomes large [Wagner, 1992; Nanbu, 1986]. It is the most commonly used numerical method for solving the Boltzmann equation. DSMC was found to be very efficient and accurate in high-speed gas flows.. However, high statistical uncertainties arise for low-speed gas flows, near-continuum flows, and unsteady flow, to name a few. To obtain acceptable solution with low noise, tremendous computing power is required for the DSMC simulation, which is unpractical. The second approach is a deterministic approach, such as numerically solving Boltzmann equation. This class includes the model Boltzmann equation, which is the main theme of the present thesis or the direct Boltzmann equation solver, which is still in its infant stage and beyond the scope of the present thesis.

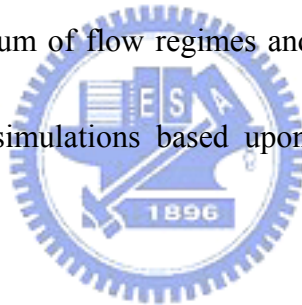


The difficulties encountered in the solution of the Boltzmann equation are largely associated with the nonlinear integral nature of the collision term. To circumvent this difficulty, statistical or relaxation models were often proposed as substitutions. The kinetic model equation proposed by Krook et al. (BGK) [1954] and Welander [1954] provides a more tractable way to solve comparatively complex rarefied gas problems routinely. Several model equations for the nonlinear Boltzmann equation

have been proposed such as the ellipsoidal model by Holway [1963], by Cercignani and Tironi [1967] and high order generalization of the BGK model by Shakhov [1968]. A hierarchy kinetic model equation similar to that of Shakhov was also proposed by Abe and Oguchi [1976]. Among the main features of these high order generalizations of BGK model are that they give the correct Prandtl number and it is generally believed that they should give a solution much closer to the solution with the Boltzmann equation than the BGK model does. All these model equations bear a resemblance to the original Boltzmann equation concerning the various order of moments. Thus, instead of solving the full Boltzmann equation one solves the kinetic model equation and hopes to produce a more economic and efficient way of computing rarefied gasdynamic flows. Recent numerical studies of rarefied gas flow problems based on the BGK type model Boltzmann equations can be found in Sugimoto and Sone [1992] and Prendergast and Xu [1993]. We consider an accurate numerical method for solving the kinetic model Boltzmann equation. The approach taken here is to apply the discrete ordinate method Huang and Giddens [1967]; Shizgal [1981] to the distribution function to replace its continuous dependency on the velocity space by a set of distribution functions which are continuous function in physical space and time but point function in velocity space. The resulting set of partial differential equations are of hyperbolic type and can be cast into hyperbolic



conservation laws from with nonlinear source terms. Once this is done, modern upwind high resolution shock capturing methods can be applied to solve them. Here, we extend our previous high-order nonoscillatory method [Yang, 1991; Yang and Hsu, 1992] for hyperbolic conservation laws to include the nonlinear source term. [Yang and Huang, 1995] was to present a high resolution numerical method for the computation of rarefied gas flow over obstacles of arbitrary shapes covering the full spectrum of flow regimes using kinetic model Boltzmann equation. They method provided an efficient tool for accurate simulations of steady and unsteady rarefied gas flows covering the full spectrum of flow regimes and can contribute to the database by providing the results of simulations based upon the kinetic model Boltzmann equations.



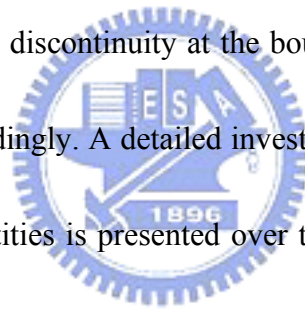
1.2 Literature Reviews in Driven Cavity Flows

Ghia [1982] used Navier-Stokes equations to simulate the driven cavity flow with high Reynolds number. Solutions are obtained for configurations with Reynolds number as high as 10000 and meshes consisting of as many as 257×257 point. Detailed accurate results have been presented for this problem and the results agree well with published fine-grid solutions but are about four times as efficient.

Erturk *et al.* [2005] used Navier-Stokes equations to simulate the 2-D steady incompressible driven cavity flow. Solution are obtained for configurations with

Reynolds number $\leq 21,000$ and using a fine uniform grid mesh of 601×601 cells. A new quaternary vortex at the bottom left corner and a new tertiary vortex at the top corner of the cavity are observed in the flow field as the Reynolds number increases.

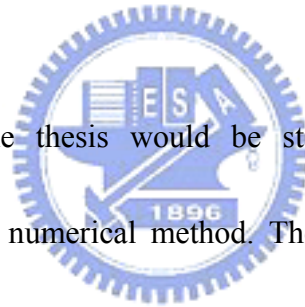
Naris and Valougeorgis [2005] used the two-dimensional linearized Bhatnagar-Gross-Krook (BGK) kinetic equation with Maxwell diffuse-specular boundary conditions to simulate the flow of a rarefied gas in a rectangular enclosure due to the motion of the upper wall is solved over the whole range of the Knudsen number. The integro-differential equations are solved numerically implementing the discrete velocity method. The discontinuity at the boundaries between stationary and moving walls is treated accordingly. A detailed investigation of the rarefaction effects on the flow pattern and quantities is presented over the whole range of the Knudsen number and various aspect (height/width) ratios. As the depth of the cavity is increased, these eddies grow and merge into additional vortices under the top one. As Knudsen number decreased, the center of the top vortex is move slightly toward the moving wall.



1.3 Specific Objectives of the Thesis

Based on previous reviews, the current objectives of the thesis are summarized as follows:

1. To benchmark the solution obtained by the previously developed 2D MBE solver with that obtained by the DMSC method;
2. To utilize the above validated 2D MBE solver to study the driven cavity flows in detail with Mach number and Knudsen number in the range of 0.5-2 and 10⁻⁵-0.0033, respectively.
3. To discuss the results considering the effects of rarefaction and compressibility.



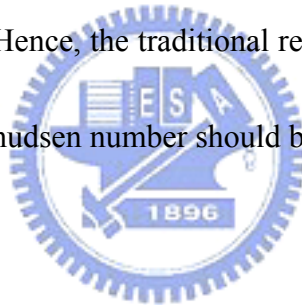
The organization of the thesis would be stated as follows. First is this introduction, and next is the numerical method. Then simulation results of Model Boltzmann equation are presented. Finally, conclusion and recommendation of future work are presented.

Chapter 2. Numerical Method

The degree of rarefaction of a gas is generally expressed through the Knudsen number (Kn) which is the ratio of the mean free path λ to the characteristic dimension L ; i.e.

$$(Kn) = \lambda / L \quad (2.1)$$

Traditionally, flows are divided into four regimes as follows: $Kn < 0.01$ (continuum), $0.01 < Kn < 0.1$ (slip flow), $0.1 < Kn < 3$ (transitional flow) and $Kn > 3$ (free molecular flow). As the Kn increases, the rarefaction becomes important and even dominates the flow behavior. Hence, the traditional requirement for the Navier-Stokes equations to be valid is that Knudsen number should be less than 0.1. (Figure 2.1)



2.1 Boltzmann equation

The Boltzmann equation is one of the most important transport equations in non-equilibrium statistical mechanics, which deals with systems far from thermodynamics equilibrium. There are some assumptions made in the derivation of the Boltzmann equation which defines limits of applicability. They are summarized as follows:

1. Molecular chaos is assumed which is valid when the intermolecular forces are short range. It allows the representation of the two particles distribution function as a product of the two single particle distribution functions.

2. Distribution functions do not change before particle collision. This implies that the encounter is of short time duration in comparison to the mean free collision time.
3. All collisions are binary collisions.
4. Particles are uninfluenced by intermolecular potentials external to an interaction.

According to these assumptions, the Boltzmann equation is derived and shown as

Eq. (2.1)

$$\frac{\partial(nf)}{\partial t} + u_i \frac{\partial(nf)}{\partial x_i} + F_i \frac{\partial(nf)}{\partial u_i} = \frac{\partial f}{\partial x_i} \Big|_c = \int_{-\infty}^{\infty} \int_0^{4\pi} n^2 (f' f'_1 - f f_1) g \sigma d\Omega dU \quad (2.1)$$

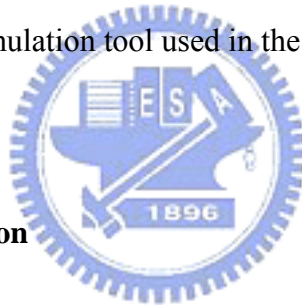
Meaning of particle phase-space distribution function f is the number of particles with center of mass located within a small volume d^3r near the point r , and velocity within a range d^3u , at time t . F_i is an external force per unit mass and t is the time and u_i is the molecular velocity. σ is the differential cross section and $d\Omega$ is an element of solid angle. The prime denotes the post-collision quantities and the subscript 1 denotes the collision partner. Meaning of each term in Eq. (2.1) is described in the following;

1. The first term on the left hand side of the equation represents the time variation of the distribution function of the particles (unsteady term).
2. The second term gives the spatial variation of the distribution function (flux

term).

3. The third term describes the effect of a force on the particles (force term).
4. The term at right hand side of the equation is called the collision integral (collision term). It is the source of most of the difficulties in obtaining solutions of the Boltzmann equation.

In general, it is very hard to solve the Boltzmann equation directly using numerical method because the difficulties of correctly modeling the integral collision term. Instead, the DSMC method was used to simulated problems involving rarefied gas dynamics, which is the simulation tool used in the current thesis.



2.2 Model Boltzmann equation

Because of the complex nonlinear structure of the collision integral, the Boltzmann equation is very difficult to solve and to analyze, which is a nonlinear integral-differential equation. Since the Boltzmann equation is difficult to handle, and its numerical solution is time expensive, some alternative, simpler expressions have been proposed to replace the Boltzmann collision term. These are known as collision models, and any Boltzmann-like equation where the Boltzmann collision integral is replaced by a collision model is called a model equation or a kinetic model.

2.2.1 BGK model

The most widely known collision model is usually called the Bhatnagar, Gross and Krook (BGK) model. We approximate the collision term in the Boltzmann equation become:

$$\left[\frac{\partial f}{\partial t}\right]_{\text{coll.}} = \nu(f^M - f) \quad (2.2)$$

Where f^M is the Maxwellian distribution function, and ν is the proportion coefficient of the BGK equation, which is also named as the collision frequency. The power law temperature dependence of the coefficient of viscosity can be obtained [.]

from the Chapman–Enskog theory, which is appropriate for the inverse power law intermolecular force model and the VHS (Variable Hard Sphere) molecular model,

$$\mu = \mu_{\text{ref}} \left(\frac{T}{T_{\text{ref}}}\right)^{\chi} \quad (2.3)$$

Where χ is the temperature exponent of the coefficient of viscosity that can also be denoted as $\chi = \frac{\zeta + 3}{2(\zeta - 1)}$ for the Chapman–Enskog gas of inverse power law, ζ is the inverse power coefficient related to the power force and the distance between centers of molecules,

$$\lambda = \frac{16}{5} \frac{\mu}{mn\sqrt{2\pi RT}} \quad (2.4)$$

Where m is the molecular mass, R is the gas constant, λ is the mean free path.

The nominal collision frequency (inverse relaxation time) can be taken in the form

$$\nu = \frac{nkT}{\mu} \quad (2.5)$$

Where n is the number density, k is Boltzmann's constant ($k = R \cdot m$), and μ is the coefficient of the viscosity.

The BGK collision model equation [1] was proposed by replacing the collision integral term of the Boltzmann equation with simple collision model:

$$\frac{\partial f}{\partial t} + \bar{v} \cdot \frac{\partial f}{\partial \bar{r}} + \bar{a} \cdot \frac{\partial f}{\partial \bar{v}} = \nu (f^M - f) \quad (2.6)$$

where $f(\bar{r}, \bar{v}, t)$ is the velocity distribution function which depends on space, \bar{r} , molecular velocity, \bar{v} , and time, t ; ν is the collision frequency and f^M is the local

Maxwellian equilibrium distribution function given by

$$f^M(\bar{r}, \bar{v}, t) = \frac{n(\bar{r}, t)}{(2\pi RT(\bar{r}, t))^{3/2}} \exp\left[-\frac{(\bar{v} - u(\bar{r}, t))^2}{2RT(\bar{r}, t)}\right] \quad (2.7)$$

The idea behind this replacement is that a large amount of detail of the two-body interaction (which is contained in the collision term) is not likely to influence significantly the values of many experimentally measured quantities. That is, unless very refined experiments are devised, it is expected that the fine structure of the collision operator can be replaced by a blurred image, based upon a simpler operator which retains only the qualitative and average properties of the true collision operator.

The numerical method uses the BGK equation as the starting point for the computation, the molecular velocity distribution function is chosen as the dependent variable, the single velocity distribution function equation can be transformed into the

hyperbolic conservation equations to be numerically solved with the finite difference method in computational fluid dynamics by the aid of the discrete velocity ordinate method in gas kinetic theory, and then the macroscopic flow variables at each point in the physical space can be evaluated from the moments of the distribution function over the velocity space.

2.2.2 Ellipsoidal model

Although that, the most widely known collision model is usually called the BGK model. But the BGK model gives the value $P_r = 1$ for the Prandtl number, a value which is not in agreement with both the true Boltzmann equation and the experimental data for a monatomic gas (which agree in giving $P_r \approx 2/3$). Therefore, Holway (1966) and Cercignani (1967) had created a new model about model Boltzmann equation is called ellipsoidal statistical (ES) model equation.

P_r is the Prandtl number with $P_r = \frac{c_p \mu}{k}$, C_p is the specific heat at constant pressure, μ is the coefficient of the viscosity, k is the heat conduction coefficient.

In order to have a correct value for the Prandtl number, the Maxwellian distribution function f^M in the BGK equation can be replaced by Three-dimensional Anisotropic Gaussian Distribution in the Ellipsoidal model.

$$\frac{\partial f}{\partial t} + \bar{v} \cdot \frac{\partial f}{\partial \bar{r}} + \bar{a} \cdot \frac{\partial f}{\partial \bar{v}} = \nu (f^E - f) \quad (2.8)$$

$$f^E(\vec{v}, \vec{r}, t) = \rho \pi^{-\frac{3}{2}} (\det A)^{\frac{1}{2}} \exp \left[- \sum_{i,j=1}^3 A_{ij} c_i c_j \right] \quad (2.9a)$$

$$A = \|A_{ij}\| = \left\| \left(\frac{2RT}{P_r} \right) \delta_{ij} - \frac{2(1-P_r)P_{ij}}{(\rho P_r)} \right\|^{-1} \quad (2.9b)$$

Where δ_{ij} is the Kronecker delta such that

$$\delta_{ij} = \begin{cases} 1, & i=j \\ 0, & i \neq j \end{cases} \quad (2.9c)$$

Ellipsoidal model had be proof better than BGK model in solve some shock structure problems. However, A disadvantage of this model is that it has not been possible to prove (or disprove) the H theory.

2.2.3 Shakov model



In order to have a correct value for the Prandtl number, higher-order equation, namely, the Shakhov equation, as well as the complete Boltzmann equation, is usually used in the numerical solution. Neglect external force after the function, the Boltzmann equation become;

$$\frac{\partial f}{\partial t} + \vec{v} \cdot \frac{\partial f}{\partial \vec{r}} = \left[\frac{\partial f}{\partial t} \right]_{\text{coll.}} = \nu (f^+ - f) \quad (2.10)$$

$$\nu = \int f_1 v_r \sigma d\vec{v}_1 \quad (2.10a)$$

$$f^+ = \frac{J^+}{\nu} \quad (2.10b)$$

$$f^+ = \int f^* f_1^* v_r d\Omega dv_1 \quad (2.10c)$$

If the molecule model considering colliding in the section σ in inverse

proportion to relative velocity among the molecules v_r , namely collide frequency is not the function of the molecule velocity, the model Shakhov equation can be write this type;

$$\frac{\partial f}{\partial t} + \bar{v} \cdot \frac{\partial f}{\partial \bar{r}} = \nu (f^S - f) \quad (2.11)$$

Where f^S is the local Maxwellian equilibrium distribution function given by

$$f^S(\bar{r}, \bar{v}, t) = f^M(\bar{r}, \bar{v}, t) [1 + (1 - Pr) c \cdot q (\frac{c^2}{RT} - 5) / (5pRT)] \quad (2.12)$$

If moment equation for Eq. (2.11) is same as moment equation for Eq. (2.10), which model equation (2.11) is similar equation for Boltzmann equation (2.10).

$$\int \nu (f^S - f) \psi d\bar{v} = \int [\frac{\partial f}{\partial t}]_{coll.} \psi d\bar{v} \quad (2.13)$$

Where $\psi = \psi(\bar{v}) = 1, v_i, v_i v_j, v_i v_j v_k, \dots$ (2.14a)

Alternatively one can use $\psi = \psi(\bar{v}) = 1, c_i, c_i c_j, c_i c_j c_k, \dots$ (2.14b)

We assume that

$$f^S = f^M \{ a^{(0)} + a_i^{(1)} c_i + a_{ij}^{(2)} c_{ij} + a_{ijk}^{(3)} c_{ijk} + \dots \} \quad (2.15)$$

We consider Eq. (2.15) reduced

The Shakhov model kinetic equation is a generalization of the Krook model equation in that the approximation condition is satisfied not only for $1, v_i, v^2, v_i v_j$ but also for $v_i v^2$. This ensures the correct relaxation of both the heat flux and stresses, leading thus to the correct continuum limit in the case of small Knudsen numbers. In particular, the model gives the correct Prandtl number. Comparisons of different monatomic model equations with experimental data and the finite-difference solution of the Boltzmann equation with the exact collision integral shows the Shakhov model

to be more accurate than the BGK model and Ellipsoidal models.

2.3 Discrete Ordinate Method

We consider accurate numerical methods for solving the kinetic model Boltzmann equations. The approach taken here is to apply the discrete ordinate method to the distribution function to replace its continuous dependency on the velocity space by a set of distribution functions which are continuous function in physical space and time but point function in velocity space. The resulting set of partial differential equations are of hyperbolic type and can be cast into hyperbolic conservation laws from with nonlinear source terms.

Its main idea is to replace the exact integration with respect to molecular velocity v over all velocity space by an approximate numerical integration over a finite domain using a discrete set of points. Let β be an index of the three-dimensional molecular velocity mesh, v_β be a node in this mesh, $f_\beta = f(t, \vec{r}, v_\beta)$.

Then the model kinetic equation is replaced by a system of equations for f_β .

2.4 Finite-difference Discretization of the Two-Dimensional MBE

We consider a class of model Boltzmann equations of the form

$$\frac{\partial f}{\partial t} + \vec{v} \cdot \frac{\partial f}{\partial \vec{r}} = \nu (f^N - f) \quad (2.16)$$

where $f(\bar{r}, \bar{v}, t)$ is the velocity distribution function which depends on space, \bar{r} , molecular velocity, \bar{v} , and time, t ; ν is the collision frequency and f^N is an appropriate distribution function depending on the model selected. The number density, macroscopic flow velocity, and temperature of the gas are the first three moments of the distribution function

$$n(\bar{r}, t) = \int f(\bar{r}, \bar{v}, t) d^3v \quad (2.17)$$

$$nu_i(\bar{r}, t) = \int v_i f(\bar{r}, \bar{v}, t) d^3v, \quad i = 1, 2, 3 \quad (2.18)$$

$$\frac{3nRT(\bar{r}, t)}{2} = \int \frac{c^2}{2} f(\bar{r}, \bar{v}, t) d^3v \quad (2.19)$$

Here, R is the gas constant, $c = \bar{v} - u(\bar{r}, t)$ is the peculiar velocity of the molecule.

The gas pressure p and the stress tensor τ_{ij} are defined by

$$p(\bar{r}, t) = n(\bar{r}, t)kT(\bar{r}, t) \quad (2.20)$$

$$\tau_{ij}(\bar{r}, t) = \int c_i c_j f(\bar{r}, \bar{v}, t) d^3v - p \delta_{ij} \quad (2.21)$$

where k is the Boltzmann constant and δ_{ij} is the Kronecker delta. The heat flux vector q is

$$q_i(\bar{r}, t) = \int \frac{c^2}{2} c_i f(\bar{r}, \bar{v}, t) d^3v \quad (2.22)$$

The elastic collision frequency is of the form

$$\nu = nkT/\mu \quad (2.23)$$

where μ is the viscosity and is assumed to have a temperature dependence

$$\mu/\mu_\infty = (T/T_\infty)^\lambda \quad (2.24)$$

Here χ is a constant for a given gas. If we assume the dependence of the viscosity on the temperature as for the Chapman-Enskog gas of inverse ζ power law, we have $\chi = \frac{\zeta + 3}{2(\zeta - 1)}$. For Maxwell molecules, $\zeta = 5$ then $\chi = 1$; thus the collision frequency is independent of temperature. The viscosity coefficient μ_∞ is related to the freestream mean free path λ_∞ by the relation

$$\mu_\infty = \frac{16}{5} \frac{\lambda_\infty}{mn_\infty \sqrt{2\pi RT_\infty}} \quad (2.25)$$

In this study we consider two kinetic models for f^N ; one is the BGK model and the other is the Shakov model. For the BGK model, we have f^N equal to the Maxwellian distribution f^M :

$$f^N = f^M(\bar{r}, \bar{v}, t) = \frac{n(\bar{r}, t)}{(2\pi RT(\bar{r}, t))^{3/2}} \exp\left[-\frac{(\bar{v} - u(\bar{r}, t))^2}{2RT(\bar{r}, t)}\right] \quad (2.26)$$

For the Shakov model, we have

$$f^N = f^S(\bar{r}, \bar{v}, t) = f^M(\bar{r}, \bar{v}, t) \left[1 + (1 - \text{Pr})c \cdot q \left(\frac{c^2}{RT} - 5\right) / (5pRT)\right] \quad (2.27)$$

Here, Pr is the prandtl number and is equal to $\frac{2}{3}$ for a monatomic gas.

We note that the derivation of the continuum Navier-Stokes equations from the BGK model or the Shakov model can be obtained using a Chapman-Enskog procedure.

To illustrate the numerical approach, we describe in detail the relevant equations for two-dimensional problem, for the purpose of reduction in computer storage requirements, the following reduced distribution functions (Chu 1965) are introduced:

$$g(v_x, v_y, x, y, t) = \int_{-\infty}^{\infty} f(\bar{v}, x, y, t) dv_z \quad (2.28a)$$

$$h(v_x, v_y, x, y, t) = \int_{-\infty}^{\infty} v_z^2 f(\bar{v}, x, y, t) dv_z \quad (2.28b)$$

Define the reference velocity and time as $C_\infty = \sqrt{2RT_\infty}$ $t_\infty = L/C_\infty$

Where L is the reference length, T_∞ is the reference temperature. Then, the

non-dimensional variables can be defined as follows:

$$\begin{aligned} \hat{t} &= t/t_\infty, & \hat{u}_x &= u_x/C_\infty, & \hat{u}_y &= u_y/C_\infty, & \hat{v}_i &= v_i/C_\infty, & \hat{n} &= n/n_\infty \\ \hat{T} &= T/T_\infty, & \hat{P} &= P/\left(\frac{1}{2}mn_\infty C_\infty^2\right), & \hat{q}_x &= q/\left(\frac{1}{2}mn_\infty C_\infty^3\right), \\ \hat{\tau}_{ij} &= \tau_{ij}/(mn_\infty C_\infty^2), & \hat{x} &= x/L, & \hat{y} &= y/L \\ \hat{g} &= g/\left(\frac{n_\infty}{C_\infty^2}\right), & \hat{h} &= h/n_\infty, & \hat{G} &= G/\left(\frac{n_\infty}{C_\infty^2}\right), & \hat{H} &= H/n_\infty \end{aligned} \quad (2.29)$$

After the process of non-dimensionalization and integrating out the v_z dependence in Eq. (2.16) using Eq. (2.28), the single model Boltzmann equation in three space dimensions reduces to the following two simultaneous equations in two space dimensions and then we neglect the signal " \wedge ".

$$\frac{\partial g}{\partial t} + v_x \cdot \frac{\partial g}{\partial x} + v_y \cdot \frac{\partial g}{\partial y} = \nu(G - g) \quad (2.30a)$$

$$\frac{\partial h}{\partial t} + v_x \cdot \frac{\partial h}{\partial x} + v_y \cdot \frac{\partial h}{\partial y} = \nu(H - h) \quad (2.30b)$$

If $G = G^M$, $H = H^M$, we can get the BGK model reduced fuctions

$$G^M = n \left(\frac{1}{\pi T}\right) \exp \left\{ -\frac{1}{T} [(v_x - u_x)^2 + (v_y - u_y)^2] \right\} \quad (2.31a)$$

$$H^M = \frac{1}{2} T G^M \quad (2.31b)$$

If $G = G^S$, $H = H^S$, we can get the Shakov model reduced fuctions

$$G^S = G^M [1 + (1 - \text{Pr})c_i q_i (\frac{2c^2}{T} - 4) / (\frac{5}{2} pT)] \quad (2.32a)$$

$$H^S = H^M [1 + (1 - \text{Pr})c_i q_i (\frac{2c^2}{T} - 2) / (\frac{5}{2} pT)] \quad (2.32b)$$

Without causing any confusion we shall drop the hat in the equations in the following.

The macroscopic moments are found as follows:

$$n = \int_{-\infty}^{\infty} \int_{-\infty}^{\infty} g \, dv_x \, dv_y \quad (2.33a)$$

$$nu_x = \int_{-\infty}^{\infty} \int_{-\infty}^{\infty} v_x g \, dv_x \, dv_y, \quad (2.33b)$$

$$nu_y = \int_{-\infty}^{\infty} \int_{-\infty}^{\infty} v_y g \, dv_x \, dv_y, \quad (2.33c)$$

$$\frac{3}{2} nT = \int_{-\infty}^{\infty} \int_{-\infty}^{\infty} h \, dv_x \, dv_y + \int_{-\infty}^{\infty} \int_{-\infty}^{\infty} [(v_x - u_x)^2 + (v_y - u_y)^2] g \, dv_x \, dv_y \quad (2.33d)$$

$$p = nT \quad (2.33e)$$

$$q_x = \int_{-\infty}^{\infty} \int_{-\infty}^{\infty} v_x [h + (v_x^2 + v_y^2) g] \, dv_x \, dv_y - 2u_x \int_{-\infty}^{\infty} \int_{-\infty}^{\infty} v_x^2 g \, dv_x \, dv_y - 2u_y \int_{-\infty}^{\infty} \int_{-\infty}^{\infty} v_x v_y g \, dv_x \, dv_y + nu_x (u_x^2 + u_y^2) - \frac{3}{2} nTu_x \quad (2.33f)$$

$$q_y = \int_{-\infty}^{\infty} \int_{-\infty}^{\infty} v_y [h + (v_x^2 + v_y^2) g] \, dv_x \, dv_y - 2u_x \int_{-\infty}^{\infty} \int_{-\infty}^{\infty} v_x v_y g \, dv_x \, dv_y - 2u_y \int_{-\infty}^{\infty} \int_{-\infty}^{\infty} v_y^2 g \, dv_x \, dv_y + nu_y (u_x^2 + u_y^2) - \frac{3}{2} nTu_x \quad (2.33g)$$

$$\tau_{xx} = \int_{-\infty}^{\infty} \int_{-\infty}^{\infty} v_x v_y g \, dv_x \, dv_y - nu_x u_y - \frac{1}{2} p, \quad (2.33h)$$

$$\tau_{xy} = \int_{-\infty}^{\infty} \int_{-\infty}^{\infty} v_x v_y g \, dv_x \, dv_y - nu_x u_y \quad (2.33i)$$

$$\tau_{yy} = \int_{-\infty}^{\infty} \int_{-\infty}^{\infty} v_x v_y g \, dv_x \, dv_y - nu_y^2 - \frac{1}{2} p \quad (2.33j)$$

It is noted that the set of partial differential equations (2.30) can be cast into the

strong conservation law from with stiff source terms as follows:

$$\frac{\partial Q}{\partial t} + \frac{\partial F^x}{\partial x} + \frac{\partial F^y}{\partial y} = S \quad (2.34)$$

Where

$$Q = \begin{pmatrix} \mathbf{g}(x, y, t, v_x, v_y) \\ \mathbf{h}(x, y, t, v_x, v_y) \end{pmatrix}, F^x = \begin{pmatrix} v_x \mathbf{g} \\ v_x \mathbf{h} \end{pmatrix}, F^y = \begin{pmatrix} v_y \mathbf{g} \\ v_y \mathbf{h} \end{pmatrix}, S = \begin{pmatrix} \nu(\mathbf{G}^M - \mathbf{g}) \\ \nu(\mathbf{H}^M - \mathbf{h}) \end{pmatrix} \quad (2.35)$$

To treat general geometry we consider the conservation equation of the two-dimensional rarefied gasdynamics in general coordinates (ξ, η)

$$\frac{\partial Q}{\partial t} + \frac{\partial F^\xi}{\partial \xi} + \frac{\partial F^\eta}{\partial \eta} = S \quad (2.36)$$

Where

$$Q = J^{-1} \begin{pmatrix} \mathbf{g} \\ \mathbf{h} \end{pmatrix}, F^\xi = J^{-1} \begin{pmatrix} U \mathbf{g} \\ U \mathbf{h} \end{pmatrix}, F^\eta = J^{-1} \begin{pmatrix} V \mathbf{g} \\ V \mathbf{h} \end{pmatrix} \quad (2.37)$$

With $U = \xi_x v_x - \xi_y v_y, V = \eta_x v_x - \eta_y v_y$

The metric Jacobian and the metric terms are given by

$$\begin{aligned} J &= \xi_x \eta_y - \xi_y \eta_x \\ \xi_x &= J y_\eta, \eta_x = -J y_\xi \\ \xi_y &= -J x_\eta, \eta_y = J x_\xi \end{aligned} \quad (2.38)$$

The Jacobian coefficient matrices $A^\xi = \frac{\partial F^\xi}{\partial Q}$ and $B^\eta = \frac{\partial F^\eta}{\partial Q}$ of the transformed equations have real eigenvalues

$$\lambda_1^\xi = \lambda_2^\xi = U, \quad \lambda_1^\eta = \lambda_2^\eta = V. \quad (2.39)$$

It is noted that both A^ξ and B^η are diagonal matrices

$$A^\xi = \Lambda^\xi = \text{diag}\{\lambda_1^\xi\}, \quad B^\eta = \Lambda^\eta = \text{diag}\{\lambda_1^\eta\} \quad (2.40)$$

Each of the reduced distribution functions is still a function of five independent

variables (for two-dimensional case). To remove the functional dependency on the velocity space of the equations, the discrete ordinate method [10] is applied. This method, which consists of replacing the integration over velocity space of the distribution function by an appropriate quadrature, requires the values of the distribution function only at certain discrete velocities. The choice of the discrete values of velocity point is dictated by the consideration that our final interest is not in the distribution functions themselves but in the moments. Hence, the macroscopic moments given by integrals over molecular velocity space can be evaluated by the same quadrature. The discrete ordinate method is then applied the set of Eq. (2.36) for the (v_x, v_y) velocity space. That is the value of $g(\xi, \eta, t, v_x, v_y)$ become $g_{\sigma, \delta}(\xi, \eta, t) = g(\xi, \eta, t, v_\sigma, v_\delta)$ and Eq. (2.36) in phase space is reduced to a set of hyperbolic partial differential equations with source terms in the physical space

$$\frac{\partial Q_{\sigma, \delta}}{\partial t} + \frac{\partial F_{\sigma, \delta}^\xi}{\partial \xi} + \frac{\partial F_{\sigma, \delta}^\eta}{\partial \eta} = S_{\sigma, \delta} \quad (2.41)$$

$$\sigma = -N_1, \dots, -1, 1, \dots, N_1, \delta = -N_2, \dots, -1, 1, \dots, N_2$$

where

$$Q_{\sigma, \delta} = \frac{1}{J} \begin{pmatrix} g_{\sigma, \delta}(\xi, \eta, t) \\ h_{\sigma, \delta}(\xi, \eta, t) \end{pmatrix}, \quad F_{\sigma, \delta}^\xi = \frac{1}{J} \begin{pmatrix} U_{\sigma, \delta} g_{\sigma, \delta} \\ U_{\sigma, \delta} h_{\sigma, \delta} \end{pmatrix}$$

$$F_{\sigma, \delta}^\eta = \frac{1}{J} \begin{pmatrix} V_{\sigma, \delta} g_{\sigma, \delta} \\ V_{\sigma, \delta} h_{\sigma, \delta} \end{pmatrix}; \quad S_{\sigma, \delta} = \begin{pmatrix} \nu(G_{\sigma, \delta}^+ - g_{\sigma, \delta}) \\ \nu(H_{\sigma, \delta}^+ - h_{\sigma, \delta}) \end{pmatrix} \quad (2.42)$$

Here, $g_{\sigma, \delta}$, $h_{\sigma, \delta}$, $G_{\sigma, \delta}$ and $H_{\sigma, \delta}$ represent values of g , h , G , and H evaluated at the

discrete velocity point (v_σ, v_δ) respectively, where $\sigma = -N_1, \dots, -1, 1, \dots, N_1$, and $\delta = -N_2, \dots, -1, 1, \dots, N_2$. Also to apply the discrete ordinate method, the integrals appeared in Eq. (2.33) are expressed as finite sums according to the quadrature define as

$$\int_0^\infty \exp(-\beta v^2) f(v) dv = \sum_{\sigma=1}^N W_\sigma f(v_\sigma) \quad (2.43)$$

Where $v_\sigma (\sigma = 1, \dots, N)$ are the positive roots of Hermite polynomial of degree N and W_σ s are the corresponding weights of the Gauss-Hermite quadrature. Both full-range and half-range Gauss-Hermite quadrature are needed. It can be shown that above quadrature formula is equivalent to approximate the Maxwellian distribution by the discrete distribution

$$e^{-u^2} \cong \sum_{\sigma=1}^N W_\sigma \bar{\delta}(u - u_i) \quad (2.44)$$

Where $\bar{\delta}$ is the Dirac delta function. This can be considered as the optimum discrete approximation in the sense that the first $2N$ moments of the Maxwellian can be exactly duplicated

$$\int_0^\infty e^{-u^2} u^l du = \int_0^\infty \sum_{i=1}^N W_i \bar{\delta}(u - u_i) u^l du, \quad l = 0, 1, 2, \dots, 2N - 1. \quad (2.45)$$

Performing the integrations gives

$$\sum_{i=1}^N W_i v_i^l = \frac{1}{2} \Gamma\left(\frac{l+1}{2}\right) \quad (2.46)$$

Where Γ represents the usual Gamma function. The discrete velocity points and the corresponding weights can be obtained using the algorithms described by Huang &

Giddens (1968) and by Shizgal (1981).

Once the discrete distribution functions $g_{\sigma,\delta}$ and $h_{\sigma,\delta}$ are solved, one can obtain

all the moment integrals as

$$n = \int_{-\infty}^{\infty} \int_{-\infty}^{\infty} [g(v_x, v_y, x, y, t) e^{v_x^2} e^{v_y^2}] e^{-v_x^2} e^{-v_y^2} dv_x dv_y = \sum_{\sigma=-N_1}^{N_1} \sum_{\delta=-N_2}^{N_2} W_{\sigma} W_{\delta} (g_{\sigma,\delta} e^{v_{\sigma}^2} e^{v_{\delta}^2}) \quad (2.47a)$$

$$u_x = \frac{1}{n} \sum_{\sigma=-N_1}^{N_1} \sum_{\delta=-N_2}^{N_2} W_{\sigma} W_{\delta} (v_{\sigma} g_{\sigma,\delta} e^{v_{\sigma}^2} e^{v_{\delta}^2}) \quad (2.47b)$$

$$u_y = \frac{1}{n} \sum_{\sigma=-N_1}^{N_1} \sum_{\delta=-N_2}^{N_2} W_{\sigma} W_{\delta} (v_{\delta} g_{\sigma,\delta} e^{v_{\sigma}^2} e^{v_{\delta}^2}) \quad (2.47c)$$

$$\frac{3}{2} nT = \sum_{\sigma=-N_1}^{N_1} \sum_{\delta=-N_2}^{N_2} W_{\sigma} W_{\delta} [h_{\sigma,\delta} + (v_{\sigma}^2 + v_{\delta}^2) g_{\sigma,\delta}] e^{v_{\sigma}^2} e^{v_{\delta}^2} - n(v_x^2 + v_y^2) \quad (2.47d)$$

$$p = nT \quad (2.47e)$$

$$q_x = \sum_{\sigma=-N_1}^{N_1} \sum_{\delta=-N_2}^{N_2} W_{\sigma} W_{\delta} v_{\sigma} [h_{\sigma,\delta} + (v_{\sigma}^2 + v_{\delta}^2) g_{\sigma,\delta}] e^{v_{\sigma}^2} e^{v_{\delta}^2} - 2u_x \sum_{\sigma=-N_1}^{N_1} \sum_{\delta=-N_2}^{N_2} W_{\sigma} W_{\delta} (v_{\sigma}^2 g_{\sigma,\delta} e^{v_{\sigma}^2} e^{v_{\delta}^2})$$

$$- 2u_y \sum_{\sigma=-N_1}^{N_1} \sum_{\delta=-N_2}^{N_2} W_{\sigma} W_{\delta} (v_{\delta}^2 g_{\sigma,\delta} e^{v_{\sigma}^2} e^{v_{\delta}^2}) + nu_x (v_x^2 + v_y^2) - \frac{3}{2} nT u_x, \quad (2.47f)$$

$$\tau_{xx} = \sum_{\sigma=-N_1}^{N_1} \sum_{\delta=-N_2}^{N_2} W_{\sigma} W_{\delta} (v_{\sigma}^2 g_{\sigma,\delta} e^{v_{\sigma}^2} e^{v_{\delta}^2}) - nu_x^2 - \frac{1}{2} p \quad (2.47g)$$

$$\tau_{xy} = \sum_{\sigma=-N_1}^{N_1} \sum_{\delta=-N_2}^{N_2} W_{\sigma} W_{\delta} (v_{\sigma} v_{\delta} g_{\sigma,\delta} e^{v_{\sigma}^2} e^{v_{\delta}^2}) - nu_x u_y \quad (2.47h)$$

$$\tau_{yy} = \sum_{\sigma=-N_1}^{N_1} \sum_{\delta=-N_2}^{N_2} W_{\sigma} W_{\delta} (v_{\delta}^2 g_{\sigma,\delta} e^{v_{\sigma}^2} e^{v_{\delta}^2}) - nu_y^2 - \frac{1}{2} p \quad (2.47i)$$

inviscid Euler equations. In this work, we not only need to solve the discrete distribution functions (not in equilibrium) but also to use them to evaluate the

macroscopic moment by numerical quadratures. The selection of the discrete velocity point and the range of velocity space in the Newton-Cotes formulas are somewhat

2.5 Numerical Algorithm in solving the MBE

In this section we describe the numerical algorithm for solving the set of Eq. (2.41). Both the time-accurate explicit method using operator splitting for unsteady flow problems and implicit method using lower-upper (LU) factorization for steady-state calculations are considered. We follow and extend our previous high resolution non-oscillatory scheme for hyperbolic system of conservation laws to include a source term. Some general remarks can be given here. When explicit methods are used to integrate the equations for $g_{\sigma,\delta}$ and $h_{\sigma,\delta}$, one can decouple the equations and solve them separately. When implicit methods are employed, the equations in general are coupled through the jacobian of the source terms since the source terms are functionals of $g_{\sigma,\delta}$ and $h_{\sigma,\delta}$. In the following we still keep the equations in vector-matrix form and with the understanding that they can be coupled into scalar form and solved in scalar manner.

Define a uniform computational mesh system (ξ_j, η_k) with mesh sizes $\Delta\xi, \Delta\eta=1$ and let $Q_{j,k,\sigma,\delta}^n$ denote the value of Q at time level $n \Delta t$, position $(j \Delta\xi, k \Delta\eta)$ and discrete velocity point (v_σ, v_δ) . Define the difference of the characteristic variables in the local ξ -direction and η -direction respectively as

$$\alpha_{j+\frac{1}{2},k,\sigma,\delta}^\xi = (Q_{j+1,k,\sigma,\delta} - Q_{j,k,\sigma,\delta}) J_{j+\frac{1}{2},k} \quad (2.48a)$$

$$\alpha_{j,k+\frac{1}{2},\sigma,\delta}^\xi = (Q_{j,k+1,\sigma,\delta} - Q_{j,k,\sigma,\delta}) J_{j,k+\frac{1}{2}} \quad (2.48b)$$

where $J_{j+\frac{1}{2},k} = (J_{j,k} + J_{j+1,k}) / 2$

Explicit Method

To integrate the set of Eq. (2.41), we use time splitting as follow:

$$\frac{\partial Q_{\sigma,\delta}}{\partial t} + \frac{\partial F_{\sigma,\delta}^{\xi}}{\partial \xi} = 0 \quad (2.49a)$$

$$\frac{\partial Q_{\sigma,\delta}}{\partial t} + \frac{\partial F_{\sigma,\delta}^{\eta}}{\partial \eta} = 0 \quad (2.49b)$$

$$\frac{\partial Q_{\sigma,\delta}}{\partial t} = S_{\sigma,\delta} \quad (2.49c)$$

The time-splitting method described above closely patterns the procedure first proposed by Bird and used in particles schemes, in which free molecular motion and the intermolecular collisions are two independent stages of the algorithm that update the particle position and velocity.

In terms of operator form we have the time integration schemes as

$$Q_{\sigma,\delta}(t + 2\Delta t) = L_s(\Delta t)L_{\xi}(\Delta t)L_{\eta}(\Delta t)L_{\eta}(\Delta t)L_{\xi}(\Delta t)L_s(\Delta t)Q_{\sigma,\delta}(t) \quad (2.50)$$

Where the time step Δt is chosen to be less than the local mean collision time, τ . The time integration of the governing equations is carried out on each pair of discrete velocity point (v_{σ}, v_{δ}) with finite difference approximations. Without causing any ambiguity, we omit the subscripts (σ, δ) in the time integration operators L_s, L_{ξ} , and L_{η} described below.

The integration of the source term is done using a multistage Runge-Kutta

method

$$Q_{j,k}^* = L_S(\Delta t)Q_{j,k}^n = Q_{j,k}^n + \Delta t S_{j,k}^n \quad (2.51a)$$

$$Q_{j,k}^{n+1} = Q_{j,k} + \frac{1}{2}\Delta t(L_S Q_{j,k}^n + L_S Q_{j,k}^*) \quad (2.51b)$$

The one-dimensional space operator is defined by

$$Q_{j,k}^{n+1} = L_\xi(\Delta t)Q_{j,k}^n = Q_{j,k}^n - \Delta t (F_{j+\frac{1}{2},k}^N - F_{j-\frac{1}{2},k}^N) \quad (2.52)$$

with

$$F_{j+\frac{1}{2},k}^N = \frac{1}{2}[F_{j,k} + F_{j+1,k} + \Phi_{j+\frac{1}{2},k}^N / J_{j+\frac{1}{2},k}] \quad (2.53)$$

Where all the metric terms such as $(\xi_x)_{j+\frac{1}{2},k}$, $(\xi_y)_{j+\frac{1}{2},k}$ and $j+\frac{1}{2},k$ are evaluated

using simple averages. The components of $\Phi_{j+\frac{1}{2},k}^N$ are given by

$$\begin{aligned} \phi_{j+\frac{1}{2},k}^1 &= \bar{\sigma}(\lambda_{j+\frac{1}{2},k}^1)(e_{j,k}^1 + e_{j+1,k}^1) + \omega\tilde{\sigma}(\lambda_{j+\frac{1}{2},k}^1)(d_{j,k}^1 + d_{j+1,k}^1) \\ &\quad - \psi(\lambda_{j+\frac{1}{2},k}^1 + \beta_{j+\frac{1}{2},k}^1 + \omega\tilde{\beta}_{j+\frac{1}{2},k}^1)\alpha_{j+\frac{1}{2},k}^1 \end{aligned} \quad (2.54)$$

$$\begin{aligned} e_{j,k}^1 &= m[\alpha_{j+\frac{1}{2},k}^1 - \mathcal{G}\bar{m}(\Delta_- \alpha_{j+\frac{1}{2},k}^1, \Delta_+ \alpha_{j+\frac{1}{2},k}^1), \\ &\quad \alpha_{j-\frac{1}{2},k}^1 + \mathcal{G}\bar{m}(\Delta_- \alpha_{j-\frac{1}{2},k}^1, \Delta_+ \alpha_{j-\frac{1}{2},k}^1)] \end{aligned} \quad (2.55)$$

$$d_{j,k}^1 = \begin{cases} \bar{m}(\Delta_- \alpha_{j-\frac{1}{2},k}^1, \Delta_+ \alpha_{j-\frac{1}{2},k}^1), & \text{if } \left| \alpha_{j-\frac{1}{2},k}^1 \right| \leq \left| \alpha_{j+\frac{1}{2},k}^1 \right| \\ \bar{m}(\Delta_- \alpha_{j+\frac{1}{2},k}^1, \Delta_+ \alpha_{j+\frac{1}{2},k}^1), & \text{if } \left| \alpha_{j+\frac{1}{2},k}^1 \right| > \left| \alpha_{j-\frac{1}{2},k}^1 \right| \end{cases} \quad (2.56)$$

$$\beta_{j+\frac{1}{2},k}^1 = \begin{cases} \bar{\sigma}(\lambda_{j+\frac{1}{2},k}^1)(e_{j+1,k}^1 - e_{j,k}^1)/\alpha_{j+\frac{1}{2},k}^1, & \text{if } \alpha_{j+\frac{1}{2},k}^1 \neq 0 \\ 0, & \text{otherwise} \end{cases} \quad (2.57)$$

$$\tilde{\beta}_{j+\frac{1}{2},k}^1 = \begin{cases} \tilde{\sigma}(\lambda_{j+\frac{1}{2},k}^1)(d_{j+1,k}^1 - d_{j,k}^1)/\alpha_{j+\frac{1}{2},k}^1, & \text{if } \alpha_{j+\frac{1}{2},k}^1 \neq 0 \\ 0, & \text{otherwise} \end{cases} \quad (2.58)$$

where

$$\bar{\sigma}(z) = \frac{1}{2}[\psi(z) - \Delta t z^2] \quad (2.59)$$

$$\tilde{\sigma}(z) = \begin{cases} \frac{1}{6}(2|z| - 3\Delta t|z|^2 + \Delta t^2|z|^3), & \text{if } \left| \alpha_{j-\frac{1}{2},k}^1 \right| \leq \left| \alpha_{j+\frac{1}{2},k}^1 \right| \\ \frac{1}{6}(\Delta t^2|z|^3 - |z|), & \text{if } \left| \alpha_{j-\frac{1}{2},k}^1 \right| > \left| \alpha_{j+\frac{1}{2},k}^1 \right| \end{cases} \quad (2.60)$$

$$\psi(z) = \begin{cases} |z|, & \text{if } |z| \geq \varepsilon \\ (z^2 + \varepsilon^2)/2\varepsilon, & \text{if } |z| < \varepsilon \end{cases} \quad (2.61)$$

Here ε is a small value and is taken to be 0.01 in all the calculations reported later. The m and \bar{m} functions are given by

$$m(y,z) = \begin{cases} s \min(|y|, |z|), & \text{if } \text{sgn } y = \text{sgn } z = s \\ z, & \text{if } |y| > |z| \end{cases} \quad (2.62)$$

$$\bar{m}(y,z) = \begin{cases} y, & \text{if } |y| \leq |z| \\ z, & \text{if } |y| > |z| \end{cases} \quad (2.63)$$

Similar expressions for the $L_\eta(\Delta t)$ operator can be defined.

The class of schemes covered by Eq. (2.54) includes the total variation diminishing (TVD) and essentially nonoscillatory (ENO) scheme. For $\omega = 0$ and $\mathcal{G} = 0$ one has a second-order TVD scheme and is denoted as TVD2; for $\omega = 0$ and $\mathcal{G} = \frac{1}{2}$, one has a second-order ENO scheme, denoted as ENO2; for $\omega = 1$ and $\mathcal{G} = 0$, one has a third-order ENO scheme, denoted as ENO3. a first-order upwind scheme, denoted as UW1, can be deduced from Eq. (2.54) by setting all the elements $e_{j,k}^1$ and $d_{j,k}^1$ equal to zero. The accuracy and Fourier stability of schemes defined by Eq. (2.54) can be analyzed by looking at different possible combinations of the

arguments in the m and \bar{m} limiter functions.

Implicit Method

Using the Euler implicit time-differencing formula, Eq. (2.41) can be written as

$$[I + \Delta t(\partial_{\xi} \Lambda^{\xi} + \partial_{\eta} \Lambda^{\eta} + C)] \Delta Q_{j,k}^{n+1} = \text{RHS}_{j,k}^n \quad (2.64)$$

where

$$\text{RHS}_{j,k}^n = -\Delta t \left(\frac{\partial F^{\xi}}{\partial \xi} + \frac{\partial F^{\eta}}{\partial \eta} - S \right)_{j,k}^n \quad (2.65)$$

Equation (2.64) can be approximately factored in several different ways. Here we adopt the lower-upper method and Eq. (2.64) become

$$[I + \Delta t(L + U + C)] \Delta Q_{j,k}^{n+1} = \text{RHS}_{j,k}^n \quad (2.66a)$$

where

$$L = \delta_{\xi}^b \Lambda^{\xi^+} + \delta_{\eta}^b \Lambda^{\eta^+}, \quad U = \delta_{\xi}^f \Lambda^{\xi^-} + \delta_{\eta}^f \Lambda^{\eta^-}, \quad (2.66b)$$

$$\text{RHS}_{j,k}^n = -\Delta t \left[(F_{j+\frac{1}{2},k}^N - F_{j-\frac{1}{2},k}^N) + (F_{j,k+\frac{1}{2}}^N - F_{j,k-\frac{1}{2}}^N) \right] + \Delta t S_{j,k}^n$$

In Eq. (2.66) denote the backward and forward difference operators, respectively.

The split jacobian matrices are $\Lambda^{\pm} = \text{diag}\{\lambda^{\pm}\}$, where $\lambda^{\pm} = (\lambda^1 \pm |\lambda^1|)/2$. The

numerical fluxes $F_{j+\frac{1}{2},k}^N$ and $F_{j,k+\frac{1}{2}}^N$ are defined analogously by Eq. (2.53). for

steady-state calculation, the use of Eq. (2.58) and (2.59) can lead to the undesirable

results that the steady state depends on the time step Δt and causes slow

convergence. We use the following approximation which still maintains the spatial

accuracy:

$$\bar{\sigma}(z) = \frac{1}{2} \psi(z)$$

$$\tilde{\sigma}(z) = \begin{cases} |z|/3, & \text{if } \left| \alpha_{j-\frac{1}{2},k}^1 \right| \leq \left| \alpha_{j+\frac{1}{2},k}^1 \right| \\ -|z|/6, & \text{if } \left| \alpha_{j-\frac{1}{2},k}^1 \right| > \left| \alpha_{j+\frac{1}{2},k}^1 \right| \end{cases} \quad (2.67)$$

An approximate L factorization for Eq. (2.66) can be given as

$$[D + \Delta t L] D^{-1} [D + \Delta t U] \Delta Q_{j,k}^{n+1} = \text{RHS}_{j,k}^n \quad (2.68a)$$

$$D = I + \Delta t C \quad (2.68b)$$

and it is implemented in the sequence:

$$[D + \Delta t L] \Delta Q_{j,k}^* = \text{RHS}_{j,k}^n \quad (2.69a)$$

$$[D + \Delta t U] \Delta Q_{j,k}^{n+1} = D \Delta Q_{j,k}^* \quad (2.69b)$$

$$Q_{j,k}^{n+1} = Q_{j,k}^n + \Delta Q_{j,k}^{n+1} \quad (2.69c)$$

The approximation factorization error of Eq. (2.68) is

$$E_{LU} = \Delta t^2 L D^{-1} U \Delta Q^{n+1} \quad (2.70)$$

which can be show to produce the least amount of error among several possible factorizations, particularly when the norms of the source terms are large. The collision source term, S , of the model equation in general is a functional of the reduced distribution functions $g_{\sigma,\delta}$ and $h_{\sigma,\delta}$. The exact evaluation of the jacobian matrix of the source term, C , is difficult. In this work, we approximate the jacobian of the source term by

$$C \approx \nu \begin{pmatrix} -1 & 0 \\ 0 & -1 \end{pmatrix} = \Lambda^S \quad (2.71)$$

With this simplified approximation the equations become diagonal and completely decoupled and the solution procedure becomes rather simple and can be solved scalarly. The numerical experience indicates that such an approximation works well.

Boundary Conditions

To specify the interaction of the molecules with the solid surface, it is assumed that molecules which strike the surface are subsequently emitted with a Maxwellian velocity distribution characterized by the surface temperature T_w and zero net tangential velocity. The two-stream concept is also applied here by defining the half-range distribution functions

$$g^+(\xi, \eta; v_x, v_y) = 0, \quad \text{for } v_n < 0$$

$$g^-(\xi, \eta; v_x, v_y) = 0, \quad \text{for } v_n > 0$$

where $v_n = \mathbf{v} \cdot \mathbf{n}$, and \mathbf{n} is the outward unit normal to the solid surface. On the solid wall, the wall distribution function is given by

$$\begin{aligned} g_w^+ &= \frac{n_w}{\pi T_w} \exp\left[-\frac{1}{T_w}(\mathbf{v} - \mathbf{u}_w)^2\right], \quad \text{if } \mathbf{v} \cdot \mathbf{n} > 0, \\ h_w^+ &= \frac{1}{2} T_w g_w^+. \end{aligned} \quad (2.72)$$

The density of the molecules diffusing from the surface, n_w , is not known a priori and may be found by applying the condition of zero mass flux normal to the surface at the wall. One has

$$n_w = -2 \left(\frac{\pi}{T_w}\right)^{1/2} \int_{-\infty}^{\infty} \int_{-\infty}^{\infty} v_n^- g^-(x, y, t, v_x, v_y) dv_x dv_y \quad (2.73)$$

where $v_n^- = (v_n - |v_n|)/2$

The farfield boundary condition at the freestream is given by the Maxwellian distribution

$$g_\infty = \frac{n_\infty}{\pi T_\infty} \exp\left\{-\frac{1}{T_\infty}[(v_x - U_\infty \cos\alpha)^2 + (v_y - U_\infty \sin\alpha)^2]\right\} \quad (2.74)$$

where U_∞ is the freestream velocity and α is the angle of attack.

The inflow and outflow boundary conditions are treated using characteristics-

based boundary conditions which are in accord with the upwind nature of the interior point scheme. For problems with symmetry, only half plane is computed and the symmetry condition is assigned to the distribution function for

$$g(\xi, -\eta, t, v_x, v_y) = g(\xi, \eta, t, v_x, -v_y) \quad (2.75)$$



Chapter 3. Preliminary Results and Discussion

3.1 Comparison of MBE Results with DSMC Numerical Method

The computed results using MBE are found to compare well with those using the DSMC(direct simulation Monte Carlo) in the Near-continuum regime flows .

We using DSMC to simulated for $M=2$, and $Kn=0.0033$. In Fig. 3.114, we show the simulated results include, number density, temperature, Mach number, u-velocity, v-velocity, and velocity streamlines.


To compare with MBE simulated results. In Fig. 3.114 (a), an ultra high-density region appears at the very right-hand upper corner due to the moving plate at the top of the cavity, but smaller than MBE simulated results. In Fig. 3.114 (b), there is a temperature increased region in the cavity, the right-hand upper corner which temperature increased obvious as a result of density increased, but smaller than MBE simulated results. In Fig. 3.114 (c), (d), (e), and (f), The MBE simulated results about u-direction and v-direction negative speed also are all bigger slightly than the DSMC simulated results. Therefore, we may discover that smaller secondary eddies have been created at the two bottom corners and the center of the top vortex is moved slightly to right-side and toward the moving plane.

3.2 Driven Cavity Flows

3.2.1 Problem Description and Test Conditions

Fig. 3.1 sketch of the 2D square ($L/H=1$) driven cavity flow with moving top plate. Initially, we use argon gas at rest inside the cavity and at the same uniform temperature 300K. At time $t=0$ the upper plate begins moving instantaneously at speed $Ma=0.5-2$ and $Kn=10-0.0033$ based on the mean free path of wall temperature and size of the cavity. Table I -III shows the all cases which we simulates with different parameters .

3.2.2 Grid Convergence Tests



In order to must test the different grid to the result influence. We have used four kind of different grids (Fig. 3.2-5 to show) in the case ($M=0.9$, $Kn=0.01$). In Fig. 3.6, we found that the convergence is better while grid size becomes smaller towards the diffuse wall. However, when grid size nearby the diffuse wall is the same, the large number of mesh doesn't result in better convergence. In Fig. 3.7, we compare BGK and the Shakov these two kind of different models. Although in each kind of parameter result comparison all almost, but the Shakov MODEL convergence speed is faster.

3.2.3 Effects of Knudsen Number

In this section, we were observed effects of Mach number in different Knudsen numbers ($Kn=10-0.0033$). First, we were showed general simulation results include density, temperature, Mach number, u-direction, v-direction and streamline. Second, we were showed property distributions across cavity geometric center for $x =0.5m$, $y=0$ to $-1m$ and $y=-0.5m$, $x=0$ to $1m$. Third, we showed property distributions near the solid walls. Finally, we were observed the recirculation center position in different cases.

3.2.3.1 General Simulation Results

3.2.3.1.1 Subsonic Moving Plate ($M=0.5, 0.9$)

Fig. 3.7 shows that number density contour for $Ma=0.5$ and Knudsen number 10, 1, 0.1, 0.01, and 0.0033 respectively. Driven plate takes particles to the right-hand upper corner. An ultra high-density region appears at the very right-hand upper corner due to the moving plate at the top of the cavity. Therefore the particles are larger than initial value. In addition, there are low densities at the left-hand upper corner. In the other series, fixed $M=0.9$ Fig. 3.12.

Fig. 3.8 show that temperature contour for $Ma=0.5$, and Knudsen number 10, 1, 0.1, 0.01, and 0.0033 respectively. We normalize temperature to divide the initial

temperature 300K. When the Knudsen number is decrease, there are two ultra temperatures region in the cavity. One of them is the right-hand upper corner which temperature increased as a result of density increased; the other one is left-hand upper corner which temperature increased due to high vertical speed. Therefore, the temperature increase more seriously as Knudsen number decreased. In the other series, fixed $M=0.9$ is showed in Fig. 3.13.

Fig. 3.9 show that Mach contour for $Ma=0.5$, and Knudsen number 10, 1, 0.1, 0.01, and 0.0033 respectively. In the other series, fixed $M=0.9$ is showed in Fig. 3.14.

Fig. 3.10 show that u-velocity contour for $Ma=0.5$, and Knudsen number 10, 1, 0.1, 0.01, and 0.0033 respectively. The maximum u-velocity values are 0.35, 0.4, 0.6, 0.9, and 0.9 with Knudsen number 10, 1, 0.1, 0.01, and 0.0033, respectively. Because of rarefaction effect caused slip phenomenon and the slip velocity along the solid walls increase with Knudsen number at the same Mach number. We normalize u-velocity to divide the upper plate velocity. The velocity is more and more decrease when Knudsen number increase. In the other series, fixed $M=0.9$ is showed in Fig. 3.15.

Fig. 3.11 show that v-velocity contour for $Ma=0.5$, and Knudsen number 10, 1, 0.1, 0.01, and 0.0033 respectively. We normalize v-velocity to divide the upper plate velocity. An ultra high-speed region appears at the left-hand and right-hand upper

region. The velocity of right-hand upper region is increase when Knudsen number decrease. In the other series, fixed $M=0.9$ is showed in Fig. 3.16.

As mentioned above, we can be briefly summarized as follows:

1. The slip velocity is more and more decrease when Knudsen number increase.
2. An ultra high-density region appears at the very right-hand upper corner due to the moving plate at the upper of the cavity
3. There are two ultra temperatures region in the right and left upper corner in cavity.

3.2.3.1.2 Supersonic Moving Plate ($M=1.1, 2$)

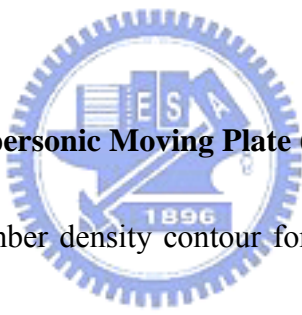


Fig. 3.17 shows that number density contour for $Ma=1.1$ and Knudsen number 10, 1, 0.1, 0.01, and 0.0033 respectively. Driven plate takes particles to the right-hand upper corner. An ultra high-density region appears at the very right-hand upper corner due to the high-speed moving plate at the top of the cavity. Therefore the particles are larger than initial value. In addition, there are low densities at the left-hand upper corner. In the other series, fixed $M=2$ Fig. 3.22.

Fig. 3.18 show that temperature contour for $Ma=1.1$, and Knudsen number 10, 1, 0.1, 0.01, and 0.0033 respectively. We normalize temperature to divide the initial temperature 300K. When the Knudsen number is decrease, there are two ultra

temperatures region in the cavity. One of them is the right-hand upper corner which temperature increased as a result of density increased; the other one is left-hand upper corner which temperature increased due to high vertical speed. Therefore, the temperature increase more seriously as Knudsen number decreased. In the other series, fixed $M=2$ is showed in Fig. 3.23.

Fig. 3.19 show that Mach contour for $Ma=1.1$, and Knudsen number 10, 1, 0.1, 0.01, and 0.0033 respectively. In the other series, fixed $M=2$ is showed in Fig. 3.24.

Fig. 3.20 show that u-velocity contour for $Ma=1.1$, and Knudsen number 10, 1, 0.1, 0.01, and 0.0033 respectively. The maximum u-velocity values are 0.35, 0.4, 0.6, 0.9, and 0.9 with Knudsen number 10, 1, 0.1, 0.01, and 0.0033, respectively. Because of rarefaction effect caused slip phenomenon and the slip velocity along the solid walls increase with Knudsen number at the same Mach number. We normalize u-velocity to divide the upper plate velocity. The velocity is more and more decrease when Knudsen number increase. In the other series, fixed $M=2$ is showed in Fig. 3.25.

Fig. 3.21 show that v-velocity contour for $Ma=1.1$, and Knudsen number 10, 1, 0.1, 0.01, and 0.0033 respectively. We normalize v-velocity to divide the upper plate velocity. An ultra high-speed region appears at the left-hand and right-hand upper region. The velocity of right-hand upper region is increase when Knudsen number decrease. In the other series, fixed $M=2$ is showed in Fig. 3.26.

As mentioned above, we can be briefly summarized as follows:

1. The slip velocity is more and more decrease when Knudsen number increase.
2. An ultra high-density region appears at the very right-hand upper corner due to the **high-speed** moving plate at the upper of the cavity
3. There are two ultra temperatures region in the right and left upper corner in cavity.

3.2.3.2 Property Distributions Across Cavity Centroid

Fig. 3.27 present the profiles of the number density along vertical line through geometry center($x/L=0.5$) for $Ma=0.5-2$, and Knudsen number 10, 1, 0.1, 0.01, and 0.0033 respectively. In the other series, the number density have replaced by temperature, u-velocity and velocity is showed in Fig. 3.28-30.

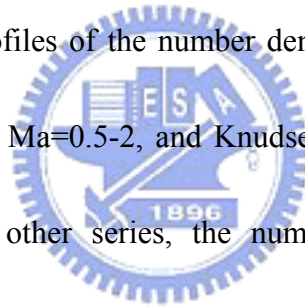


Fig. 3.31 present the profiles of the number density along vertical line through geometry center($y/L=-0.5$) for $Ma=0.5-2$, and Knudsen number 10, 1, 0.1, 0.01, and 0.0033 respectively. In the other series, the number density have replaced by temperature, u-velocity and velocity is showed in Fig. 3.32-34.

3.2.3.3 Property Distributions Near Solid Walls

Fig. 3.35 present the profiles of the number density along vertical line through

geometry center($x/L=0$) for $Ma=0.5-2$, and Knudsen number 10, 1, 0.1, 0.01, and 0.0033 respectively. In the other series, the number density have replaced by temperature, u-velocity and velocity is showed in Fig. 3.36-38.

Fig. 3.39 present the profiles of the number density along vertical line through geometry center($x/L=1$) for $Ma=0.5-2$, and Knudsen number 10, 1, 0.1, 0.01, and 0.0033 respectively. In the other series, the number density have replaced by temperature, u-velocity and velocity is showed in Fig. 3.40-43.

Fig. 3.44 present the profiles of the number density along vertical line through geometry center($y/L=-1$) for $Ma=0.5-2$, and Knudsen number 10, 1, 0.1, 0.01, and 0.0033 respectively. In the other series, the number density have replaced by temperature, u-velocity and velocity is showed in Fig. 3.45-Fig. 3.47.

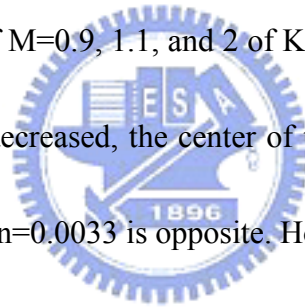
Fig. 3.48 present the profiles of the number density along vertical line through geometry center($y/L=0$) for $Ma=0.5-2$, and Knudsen number 10, 1, 0.1, 0.01, and 0.0033, respectively. In the other series, the number density have replaced by temperature, u-velocity and velocity is showed in Fig. 3.49-Fig. 3.51.

3.2.3.4 Recirculation Center Position

Fig. 3. 51-54 show plots of the velocity streamlines for $M=0.5, 0.9, 1.1, \text{ and } 2$, respectively, and in each figure results are provided for various values of Knudsen

number. The corresponding velocity streamlines for $M=0.5, 0.9,$ and $1.1,$ are given in Fig. 3.51-53. It is seen that while for $Kn=10, 1,$ and 0.1 there is only one vortex, for $Kn=0.01,$ and $0.0033,$ under the main vortex secondary eddies have been created at the two bottom corners. In Fig. 3.54, it is seen that while for $Kn=1,$ and 0.1 there is only one vortex, for $Kn=10$ one additional vortex, for $Kn=0.01,$ and 0.0033 two additional vortices, under the first one, have been developed. As the Knudsen number is increased further, these secondary eddies grow under the first one.

In Fig. 3.55, we show the relative vertical distance (x/L) of the center of the top vortex of the cavity in term of $M=0.9, 1.1,$ and 2 of $Kn=10, 1, 0.1,$ and 0.01 . It is seen that in these cases, as Kn is decreased, the center of the top vortex is moved slightly toward the right wall, when $Kn=0.0033$ is opposite. However, $M=0.5$ of $Kn=10, 1, 0.1,$ $0.01,$ and 0.0033 . It is seen that in these cases, as Kn is decreased, the center of the top vortex is moved slightly toward the right wall.



In Fig. 3.56, we show the relative vertical distance (y/L) of the center of the top vortex of the cavity in term of $M=0.5, 0.9,$ and 1.1 of $Kn=10, 1, 0.1,$ and 0.01 . It is seen that in these cases, as Kn is increased, the center of the top vortex is moved slightly reversely the moving wall, when $Kn=0.0033$ is opposite. However, $M=2$ of $Kn=10, 1, 0.1, 0.01,$ and 0.0033 . It is seen that in these cases, as Kn is increased, the center of the top vortex is moved slightly toward the moving wall.

3.2.4 Effect of Mach Number of the Driven Plate

In this section, we were observed effects of Knudsen number in different Mach numbers ($Ma=0.5-2$). First, we were showed general simulation results include density, temperature, Mach number, u-direction, v-direction and streamline. Second, we were showed property distributions across cavity geometric center for $x =0.5m$, $y= 0$ to $-1m$ and $y=-0.5m$, $x=0$ to $1m$. Third, we showed property distributions near the solid walls. Finally, we were observed the recirculation center position in different cases.

3.2.4.1 General Simulation Results

3.2.4.1.1 Free Molecular Regime ($Kn=10$)

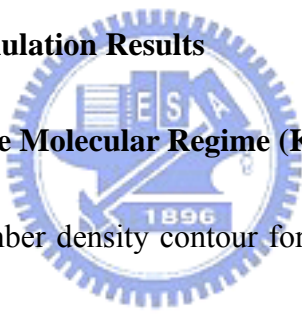


Fig. 3.57 shows that number density contour for $Kn=10$ and Mach number 0.5, 0.9, 1.1, and 2, respectively. Driven plate takes particles to the right-hand upper corner. An ultra high-density region appears at the very right-hand upper corner due to the moving plate at the top of the cavity. Therefore the particles are larger than initial value. In addition, there are low densities at the left-hand upper corner.

Fig. 3.58 show that temperature contour for $Kn=10$ and Mach number 0.5, 0.9, 1.1, and 2, respectively. We normalize temperature to divide the initial temperature 300K. When the Mach number is increase, there is a ultra temperatures region in the cavity. It is the upper moving plane which temperature increased due to high speed.

Therefore, the temperature increase as Mach number is increased.

Fig. 3.59 show that Mach contour for $Kn=10$ and Mach number 0.5, 0.9, 1.1, and 2, respectively.

Fig. 3.60 show that u-velocity contour for $Kn=10$ and Mach number 0.5, 0.9, 1.1, and 2, respectively. The maximum u-velocity values are all equal 0.35 with various values Mach number. When $Kn=10$, the various values Mach number about the slip phenomenon without influence.

Fig. 3.61 show that v-velocity contour for $Kn=10$ and Mach number 0.5, 0.9, 1.1, and 2, respectively. We normalize v-velocity to divide the upper plate velocity. When $Kn=10$, the various values Mach number about the v-velocity with slightly effect.

As mentioned above, we can be briefly summarized as follows:

1. The slip phenomenon without influence when Mach number increase.
2. An ultra high-density region appears at the very right-hand upper corner due to the moving plate at the upper of the cavity
3. There is high temperatures region in the upper moving plane in cavity.

3.2.4.1.2 Transitional Regime ($Kn=1, 0.1, 0.01$)

Fig. 3.62 shows that number density contour for $Kn=1$ and Mach number 0.5, 0.9, 1.1, and 2, respectively. Driven plate takes particles to the right-hand upper corner.

An ultra high-density region appears at the very right-hand upper corner due to the moving plate at the top of the cavity. Therefore the particles are larger than initial value. In addition, there are low densities at the left-hand upper corner. In the other series, fixed $Kn=0.1$, and 0.01 are showed in Fig. 3.67 and Fig. 3.72.

Fig. 3.63 show that temperature contour for $Kn=1$ and Mach number 0.5 , 0.9 , 1.1 , and 2 , respectively. We normalize temperature to divide the initial temperature $300K$. When the Mach number is increase, there are two ultra temperatures region in the cavity. One of them is the right-hand upper corner which temperature increased as a result of density increased; the other one is left-hand upper corner which temperature increased due to high vertical speed. Therefore, the temperature increase more seriously as Mach number decreased. In the other series, fixed $Kn=0.1$, and 0.01 are showed in Fig. 3.68 and Fig. 3.73.

Fig. 3.64 show that Mach contour for $Kn=1$ and Mach number 0.5 , 0.9 , 1.1 , and 2 , respectively. In the other series, fixed $Kn=0.1$, and 0.01 are showed in Fig. 3.69 and Fig. 3.74.

Fig. 3.65 show that u-velocity contour for $Kn=1$ and Mach number 0.5 , 0.9 , 1.1 , and 2 , respectively. The maximum u-velocity values are all equal 0.4 with various values Mach number. When $Kn=1$, the various values Mach number about the slip phenomenon without influence. In the other series, fixed $Kn=0.1$, and 0.01 are

showed in Fig. 3.70 and Fig. 3.75.

Fig. 3.66 show that v -velocity contour for $Kn=1$ and Mach number 0.5, 0.9, 1.1, and 2, respectively. We normalize v -velocity to divide the upper plate velocity. When $Kn=1$, the various values Mach number about the v -velocity with slightly effect. In the other series, fixed $Kn=0.1$, and 0.01 are showed in Fig. 3.71 and Fig. 3.76.

1. The slip phenomenon without influence when Mach number increase.
2. An ultra high-density region appears at the very right-hand upper corner due to the moving plate at the upper of the cavity
3. There are two ultra temperatures region in the right and left upper corner in cavity.



3.2.4.1.3 Near-continuum Regime ($Kn=0.0033$)

Fig. 3.77 shows that number density contour for $Kn=0.0033$ and Mach number 0.5, 0.9, 1.1, and 2, respectively. Driven plate takes particles to the right-hand upper corner. An ultra high-density region appears at the very right-hand upper corner due to the moving plate at the top of the cavity. Therefore the particles are larger than initial value. In addition, there are low densities at the left-hand upper corner.

Fig. 3.78 show that temperature contour for $Kn=0.0033$ and Mach number 0.5, 0.9, 1.1, and 2, respectively. We normalize temperature to divide the initial

temperature 300K. When the Mach number is increase, there are two ultra temperatures region in the cavity. One of them is the right-hand upper corner which temperature increased as a result of density increased; the other one is left-hand upper corner which temperature increased due to high vertical speed. Therefore, the temperature increase more seriously as Mach number decreased.

Fig. 3.79 show that Mach contour for $Kn=0.0033$ and Mach number 0.5, 0.9, 1.1, and 2, respectively.

Fig. 3.80 show that u-velocity contour for $Kn=1$ and Mach number 0.5, 0.9, 1.1, and 2, respectively. The maximum u-velocity values are all equal 0.4 with various values Mach number. When $Kn=1$, the various values Mach number about the slip phenomenon without influence.

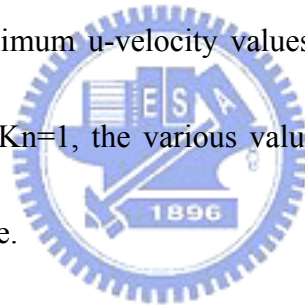


Fig. 3.81 show that v-velocity contour for $Kn=0.0033$ and Mach number 0.5, 0.9, 1.1, and 2, respectively. We normalize v-velocity to divide the upper plate velocity. An ultra high-speed region appears at the left-hand and right-hand upper region. The velocity of right-hand upper region is increase when Mach number increased.

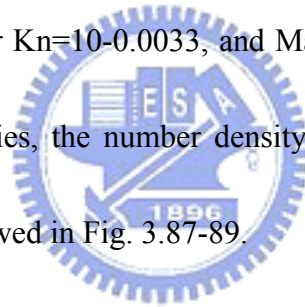
1. The slip phenomenon without influence when Mach number increase.
2. An ultra high-density region appears at the very right-hand upper corner due to the moving plate at the upper of the cavity
3. There are two ultra temperatures region in the right and left upper corner in

cavity.

3.2.4.2 Property Distributions Across Cavity Centroid

Fig. 3.82 present the profiles of the number density along vertical line through geometry center($x/L=0.5$) for $Kn=10-0.0033$, and Mach number 0.5, 0.9, 1.1, and 2, respectively. In the other series, the number density have replaced by temperature, u-velocity and velocity is showed in Fig. 3.83-85.

Fig. 3.86 present the profiles of the number density along vertical line through geometry center($y/L=-0.5$) for $Kn=10-0.0033$, and Mach number 0.5, 0.9, 1.1, and 2, respectively. In the other series, the number density have replaced by temperature, u-velocity and velocity is showed in Fig. 3.87-89.



3.2.4.3 Property Distributions Near Solid Walls

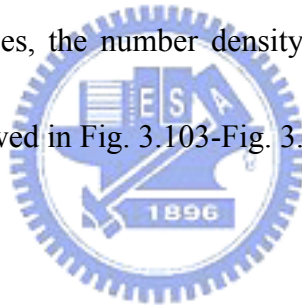
Fig. 3.90 present the profiles of the number density along vertical line through geometry center($x/L=0$) for $Kn=10-0.0033$, and Mach number 0.5, 0.9, 1.1, and 2, respectively. In the other series, the number density have replaced by temperature, u-velocity and velocity is showed in Fig. 3.91-93.

Fig. 3.94 present the profiles of the number density along vertical line through geometry center($x/L=1$) for $Kn=10-0.0033$, and Mach number 0.5, 0.9, 1.1, and 2,

respectively. In the other series, the number density have replaced by temperature, u-velocity and velocity is showed in Fig. 3.95-97.

Fig. 3.98 present the profiles of the number density along vertical line through geometry center($y/L=-1$) for $Kn=10-0.0033$, and Mach number 0.5, 0.9, 1.1, and 2, respectively. In the other series, the number density have replaced by temperature, u-velocity and velocity is showed in Fig. 3.99-Fig. 3.101.

Fig. 3.102 present the profiles of the number density along vertical line through geometry center($y/L=0$) for $Kn=10-0.0033$, and Mach number 0.5, 0.9, 1.1, and 2, respectively. In the other series, the number density have replaced by temperature, u-velocity and velocity is showed in Fig. 3.103-Fig. 3.105.



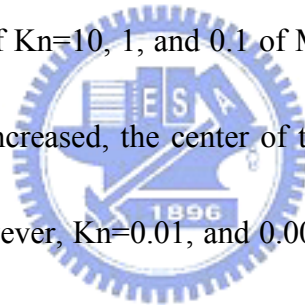
3.2.4.4 Recirculation Center Position

Fig. 3. 106-110 show plots of the velocity streamlines for $Kn=10, 1, 0.1, 0.01,$ and 0.0033 , respectively, and in each figure results are provided for various values of Mach number number. The corresponding velocity streamlines for $Kn=0.01$, and 0.0033 , are given in Fig. 3.108-110. It is seen that under the main vortex secondary eddies have been created at the two bottom corners. In Fig. 3.107 , it is seen that while for $Kn=1$, there is only one vortex, for $M=2$ one additional vortex, under the first one, have been developed. As the Mach number is increased further, these secondary

eddies grow under the first one.

In Fig. 3.111, we show the relative vertical distance (x/L) of the center of the top vortex of the cavity in term of $Kn=10, 1, \text{ and } 0.1$ of $M=0.5, 0.9, 1.1, \text{ and } 2$. It is seen that in these cases, as M is increased, the center of the top vortex is moved slightly toward the right wall, when $Kn=0.0033$ is opposite. However, $Kn=0.01$ of $M=0.5, 0.9, \text{ and } 1.1$. It is seen that in these cases, as M is increased, the center of the top vortex is moved slightly toward the right wall, when $M=2$ is opposite

In Fig. 3.112, we show the relative vertical distance (y/L) of the center of the top vortex of the cavity in term of $Kn=10, 1, \text{ and } 0.1$ of $M=0.5, 0.9, 1.1, \text{ and } 2$. It is seen that in these cases, as M is increased, the center of the top vortex is moved slightly toward the moving wall. However, $Kn=0.01, \text{ and } 0.0033$ of $M=0.5, 0.9, 1.1, \text{ and } 2$. It is seen that in these cases, as M is increased, the center of the top vortex is moved slightly reversely the moving wall.



Chapter 4. Conclusions and Recommendation of Future

Work

4.1 Conclusion

Work progress in this period can be briefly summarized as follows:

1. In the work, accurate numerical methods, which combine features of the modern high resolution upwind method in computational fluid dynamics and the discrete ordinate method in kinetic theory, have been proposed for the computations of rarefied gas flows using the nonlinear model Boltzmann equations. Two kinetic model are employed. One is the BGK model and the other is the Shakov model.
2. We found that the convergence is better while grid size becomes smaller towards the diffuse wall. However, when grid size nearby the diffuse wall is the same, the large number of mesh doesn't result in better convergence.
3. Velocity slips and temperature jumps increase at the solid walls with increasing rarefaction at the same Mach number.
4. Results show that vortex center move toward left and down as Knudsen number ($Kn=10, 1, 0.1, 0.01$) decreasing for $M=0.5, 0.9, 1.1, \text{ and } 2$, when $Kn=0.0033$ is opposite. But the vortex center move toward the opposite way for $M=0.5, Kn=0.0033$ and $M=2, Kn=0.0033..$
5. For $Kn=0.01, \text{ and } 0.0033$, under the main vortex secondary eddies have been

created at the two bottom corners. Only in this special example for $M=2$, $Kn=10$, unnder the main vortex secondary eddie have been created at the right bottom corners.

6. To compare our computations with DSMC calculations and Navier-Stokes equation calculations.

4.2 Recommendation of Future Work

Based on this study, future work is suggested as follows:

1. To simulate the flows in detail by changing the ratio of height to width of the cavity;
2. To simulate the flows in detail by changing the wall temperatures and to focus on the discussion of heat transfer along the solid walls;
3. To simulate the driven cavity flow with oscillatory top moving plate.
4. To simulate the driven cavity flows with gas mixture and discuss the effects of moving plate speed and oscillation to the mixing of different species within the cavity.

References

- [1] 吳大猷, 熱力學, 氣體動力學, 統計力學, 理論物理第五冊, 聯經出版事業公司, 民國 67 年。
- [2] Bhatnagar, M. O. and Gross, E. P. and Krook, M., “A model collision processes in gases. I. Small amplitude processes in charged and neutral one-component system”, *Phys. Rev.* 94, 511-525, 1954.
- [3] Bird, G. A., Molecular gas dynamics and the direct simulation of gas flows, Oxford university press, New York, 1994.
- [4] Cercignani, C., The Boltzmann Equation and Its Applications, Springer, New York, 1988.
- [5] Chapman, S. and Cowling. T. G., “The Mathematical Theory of Non-Uniform Gases”, Cambridge University Press, 1970.
- [6] Chung, C. H. and Jeng, D. R., “Numerical Simulation of Rarefied Gas Flow through a Slit”, *JOURNAL OF THERMOPHYSICS AND HEAT TRANSFER*, Vol. 6, No.1, Jan.-March 1992.
- [7] Chung, C. H., “Numerical Simulation of Low-Speed Gas Flows in a Microfluidic System”, *JOURNAL OF THERMOPHYSICS AND HEAT TRANSFER*, Vol. 19, No. 3, July.-September 2005.
- [8] Erturk, E, Corke,. T. C. and Gokcol, C., “Numerical solutions of 2-D steady incompressible driven cavity flow at high Reynolds numbers”, *Int. J. Numer. Meth. Fluids* 2005; 48:747-774.
- [9] Harris, S., “An Introduction to the Theory of the Boltzmann Equation”, Dover Publications, Inc. Mineola, New York, 2004.
- [10] Holway, L. H. Jr., “New Statistical Model for Kinetic Theory, method of construction”, *phys. Fluids* 9, 1658-1673, 1966.
- [11] Huang, A. B. and Giddens, D. P., “The discrete ordinate method for the boundary value problems in kinetic theory of gases. In rarefied gas dynamics (ed. C. L. Brundin)”, Academic Press, pp. 481-505, New York, 1967.
- [12] Huang, A. B. and Giddens, D. P., “A new table for a modified (half-range) Gauss-Hermite quadrature with an evaluation of the integral $\int_0^{\infty} e^{-u^2 - x/u} du$ ”, *Journal of Mathematics Physics*, vol. 47, No. 2, 213-218, 1968.
- [13] Li, Z. H. and Zhang, H. X., “Study on gas kinetic unified algorithm for flows from rarefied transition to continuum”, *Journal of Computational Physics* 193, 708–738, 2004.
- [14] Li, Z. H. and Zhang, H. X., “Gas kinetic algorithm using Boltzmann model equation”, *Computers & Fluids* 33, 967–991, 2004.
- [15] Kogan, M. N., Rarefied Gas Dynamics, Plenum Press, New York, 1969

- [16] Nanbu, K., "Theoretical Basis on the Direct Monte Carlo Method", Rarefied Gas Dynamics, 1, Boffi, V. and Cercignani, C. (editor), Teubner, Stuttgart, 1986.
- [17] Nairs, S. and Valougeorgis, D., "The driven cavity flow over the whole range of the Knudsen number", PHYSICS OF FLUIDS 17, 097106 (2005).
- [18] Titarev, V. A., "Conservative Numerical Methods For Advanced Model Kinetic Equations", European Conference on Computational Fluid Dynamics, 2006.
- [19] Wagner, W., "A convergence proof for Bird's Direct simulation Monte Carlo method for the Boltzmann equation", Journal State Physics, 66(3/4), pp. 1011-1044, 1992.
- [20] Wu, J. S. and Lian, Y. Y., "Development and Verification of a Coupled DSMC-NS Scheme Using Unstructured Mesh", Journal of Computational Physics, Vol. 219, No.2, pp. 579-607, 2006.
- [21] Yang, J. Y. and Huang, J. C., "Rarefied Flow Computations Using Nonlinear Model Boltzmann Equations", Journal of Computational Physics 120, 323-339, 1995.
- [22] Yang, J. Y. and Huang, J. C., "Numerical solutions of the nonlinear model Boltzmann equations", Proc. R. Soc. Lond. A (1995) 448, 55-80.



Table. I All the Simulation cases.

M \ Kn	Kn=0.0033	Kn=0.01	Kn=0.1	Kn=1	Kn=10
M=0.5	Case A	Case B	Case C	Case D	Case E
M=0.9	Case F	Case G	Case H	Case I	Case J
M=1.1	Case K	Case L	Case M	Case N	Case O
M=2.0	Case P	Case Q	Case R	Case S	Case T



Table. II Mesh information

Knudsen number	Mach number	Mesh	Grid size of the smallest cell	model
10	2	101 x 101	0.01	BGK / Shakov
10	1.1	101 x 101	0.01	BGK / Shakov
10	0.9	101 x 101	0.01	BGK / Shakov
10	0.5	101 x 101	0.01	BGK / Shakov
1	2	101 x 101	0.01	BGK / Shakov
1	1.1	101 x 101	0.01	BGK / Shakov
1	0.9	101 x 101	0.01	BGK / Shakov
1	0.5	101 x 101	0.01	BGK / Shakov
0.1	2	101 x 101	0.01	BGK / Shakov
0.1	1.1	101 x 101	0.01	BGK / Shakov
0.1	0.9	101 x 101	0.01	BGK / Shakov
0.1	0.5	101 x 101	0.01	BGK / Shakov
0.01	2	101 x 101	0.001	BGK / Shakov
0.01	1.1	101 x 101	0.001	BGK / Shakov
0.01	0.9	101 x 101	0.001	BGK / Shakov
0.01	0.5	101 x 101	0.001	BGK / Shakov
0.0033	2	101 x 101	0.001	BGK / Shakov
0.0033	1.1	101 x 101	0.001	BGK / Shakov
0.0033	0.9	101 x 101	0.001	BGK / Shakov
0.0033	0.5	101 x 101	0.001	BGK / Shakov

Table. III Simulation condition

Knudsen number	Mach number	Re number	Driven plate velocity	Initial wall and gas temperature
10	2	0.33	644	300
10	1.1	0.18	354.2	300
10	0.9	0.15	289.8	300
10	0.5	0.08	161	300
1	2	3.3	644	300
1	1.1	1.8	354.2	300
1	0.9	1.5	289.8	300
1	0.5	0.8	161	300
0.1	2	33	644	300
0.1	1.1	18	354.2	300
0.1	0.9	15	289.8	300
0.1	0.5	8	161	300
0.01	2	330	644	300
0.01	1.1	180	354.2	300
0.01	0.9	150	289.8	300
0.01	0.5	80	161	300
0.0033	2	999	644	300
0.0033	1.1	550	354.2	300
0.0033	0.9	450	289.8	300
0.0033	0.5	250	161	300

Table. IV Location of the center of the top vortex for various values of Ma and Kn.

M\Kn	10	1	0.1	0.01	0.0033
0.5	(0.5267, -0.3075)	(0.5274, -0.3001)	(0.5305, -0.2691)	(0.5823, -0.2442)	(0.6323, -0.2826)
0.9	(0.5448, -0.2878)	(0.5457, -0.2840)	(0.5513, -0.2679)	(0.6156, -0.2549)	(0.6008, -0.3488)
1.1	(0.5530, -0.2752)	(0.5540, -0.2735)	(0.5602, -0.2664)	(0.6225, -0.2611)	(0.5850, -0.3697)
2	(0.5810, -0.2216)	(0.5831, -0.2247)	(0.5934, -0.2497)	(0.6213, -0.2879)	(0.5414, -0.4203)



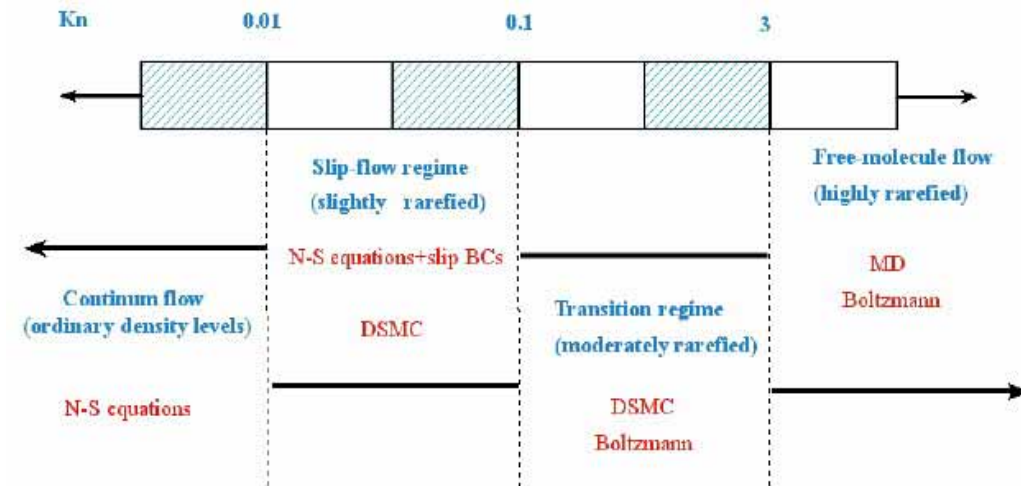


Fig. 1.1 Flow Regime and solution method

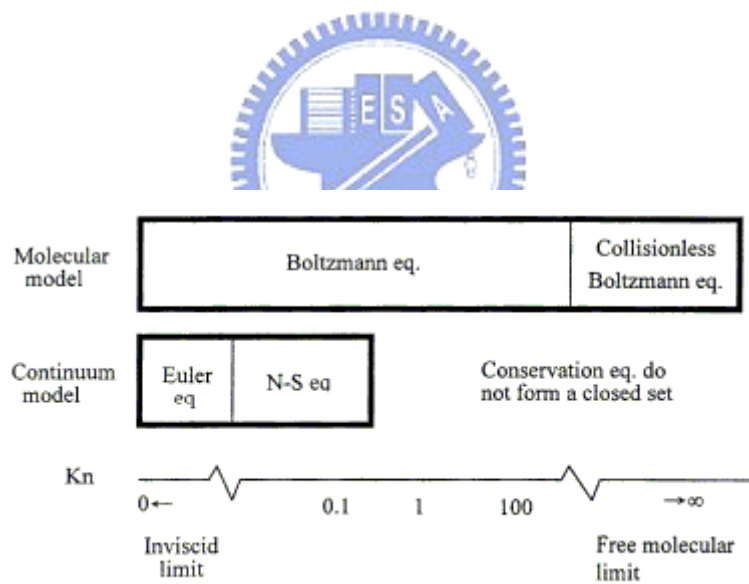


Fig. 2.1 The Knudsen number limits on the mathematical models.

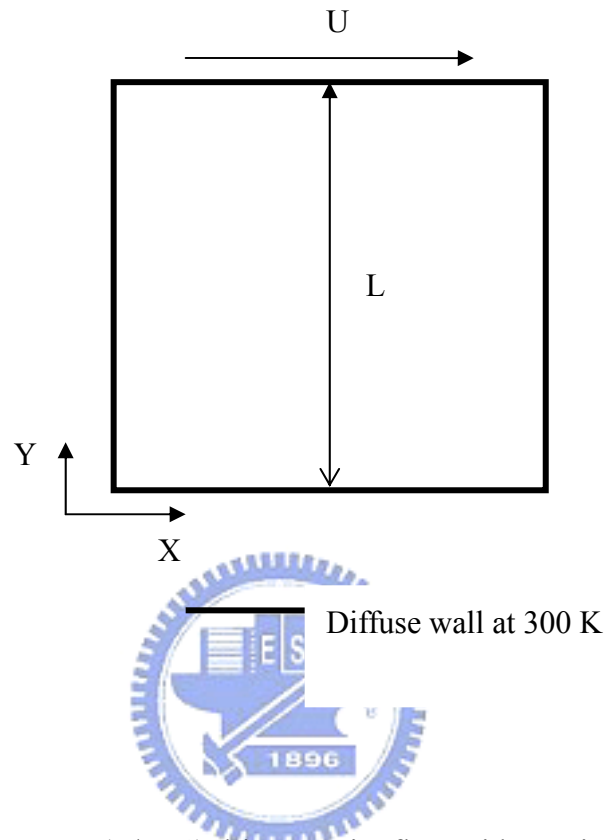


Fig. 3.1 The 2D square ($L/H=1$) driven cavity flow with moving top plate

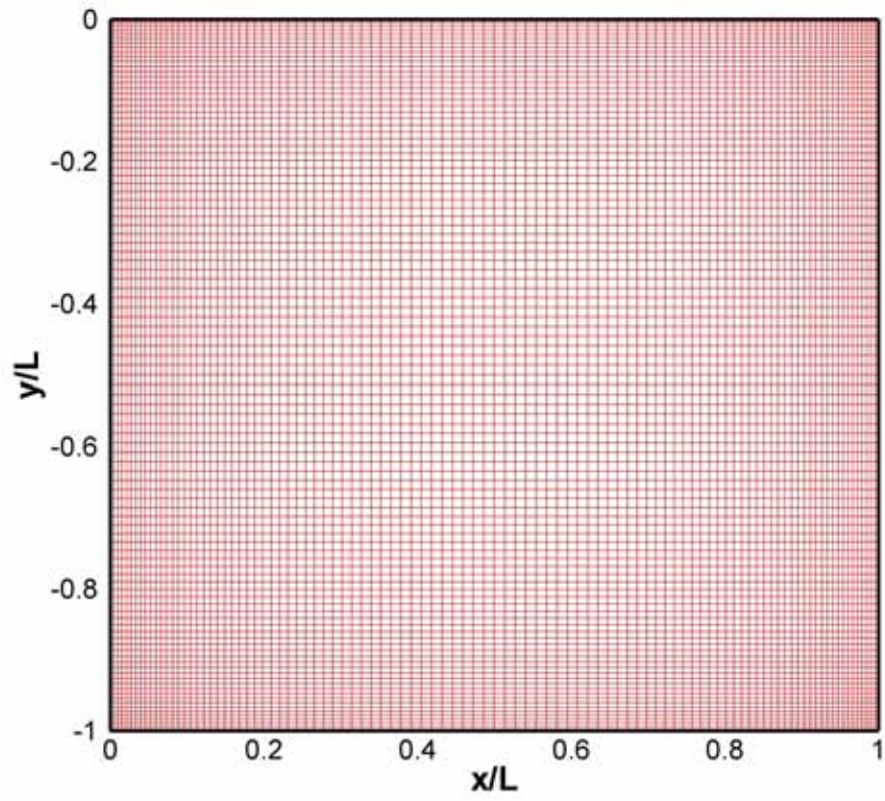


Fig. 3.2 Grid. 1 is grid mesh of 101 by 101 and smallest grid size is 5×10^{-3} .

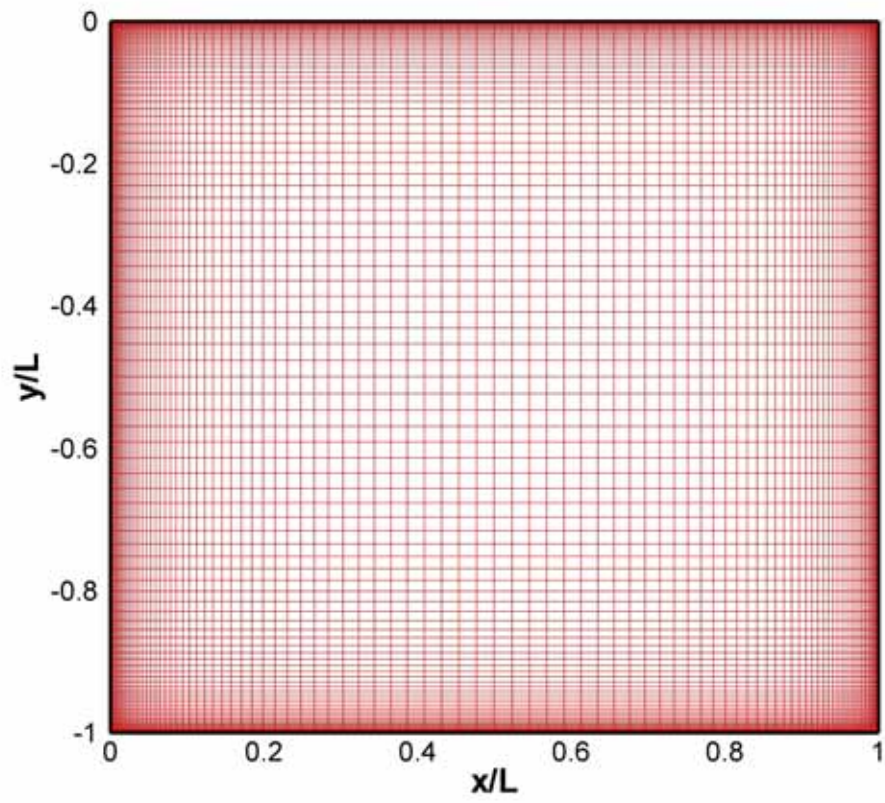


Fig. 3.3 Grid. 2 is grid mesh of 101 by 101 and smallest grid size is 1×10^{-3}

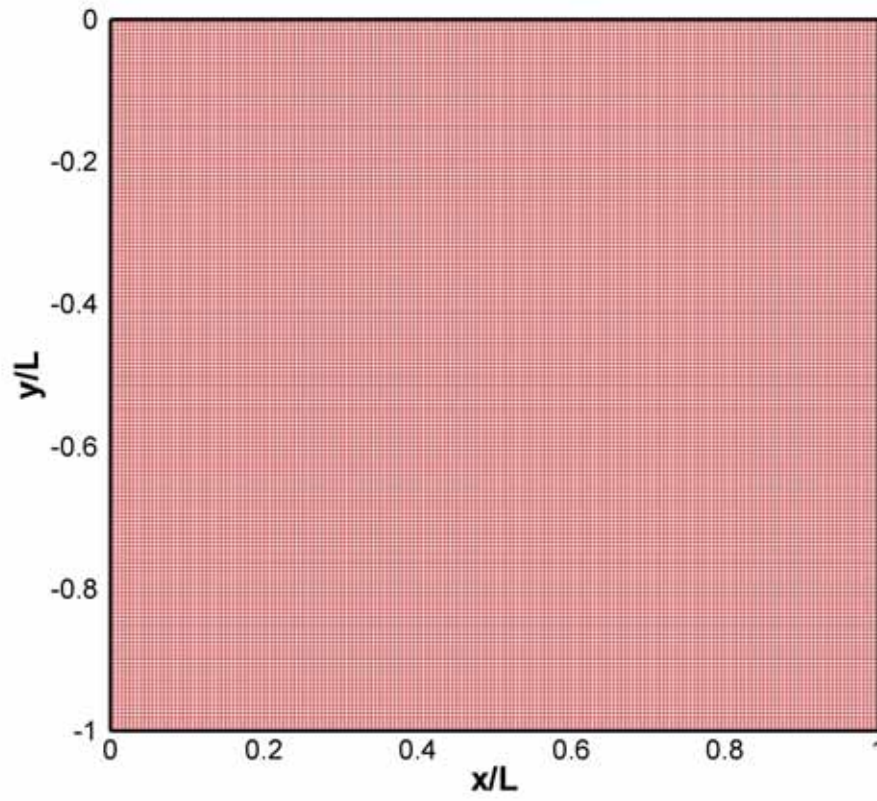


Fig. 3.4 Grid. 3 is grid mesh of 201 by 201 and smallest grid size is 5×10^{-3}

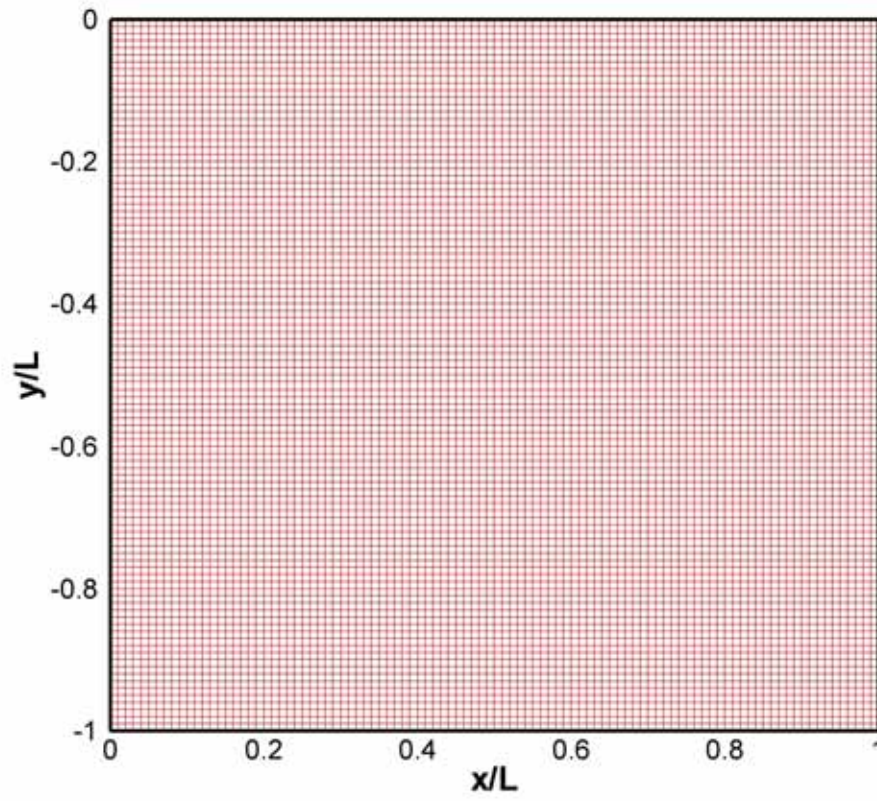
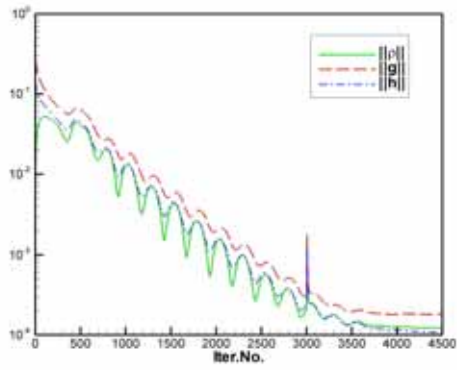
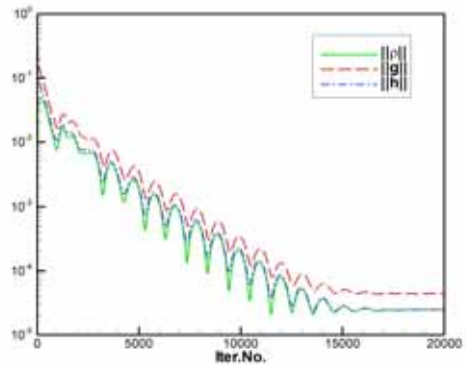


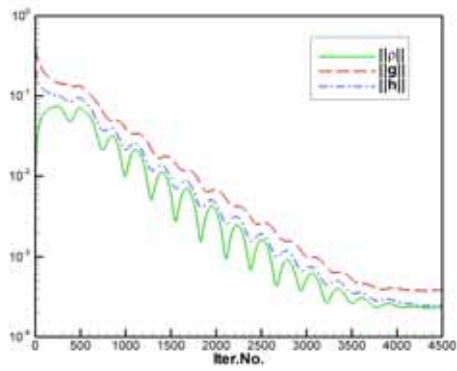
Fig. 3.5 Grid. 4 is grid mesh of 101 by 101 and smallest grid size is 1×10^{-2}



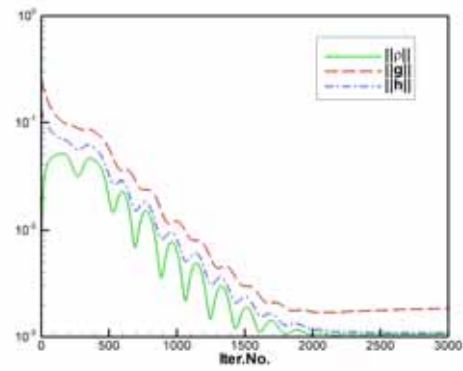
(a)



(b)



(c)



(d)

Fig. 3.6 The residual functions for different grids (a) Grid. 1, (b) Grid. 2, (c) Grid. 3, (d)Grid. 4.

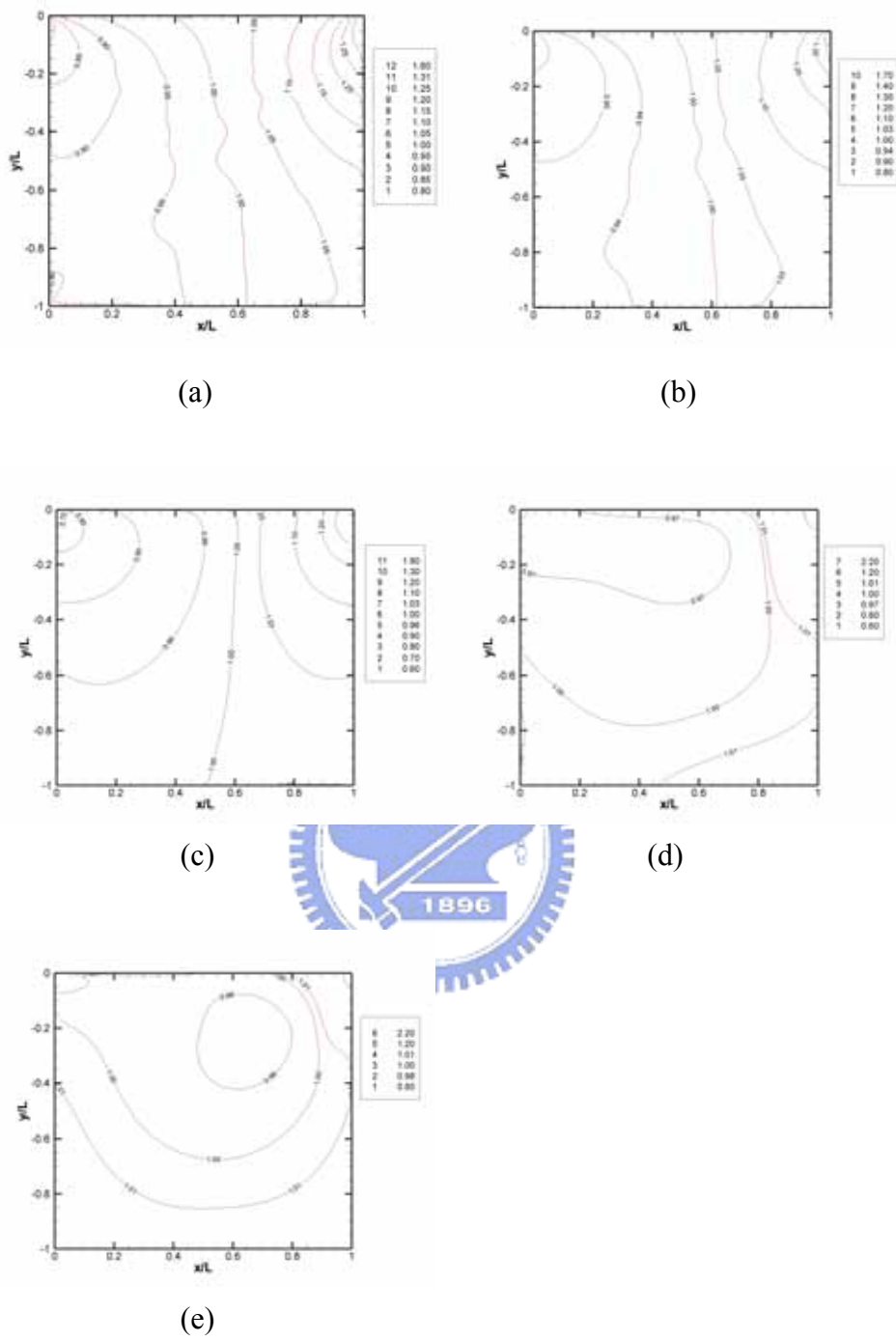
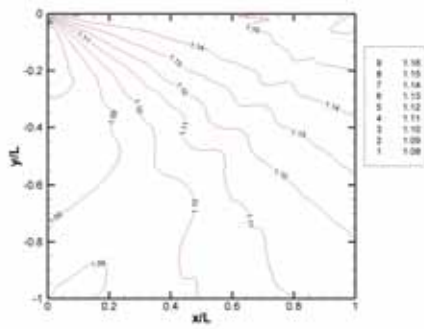
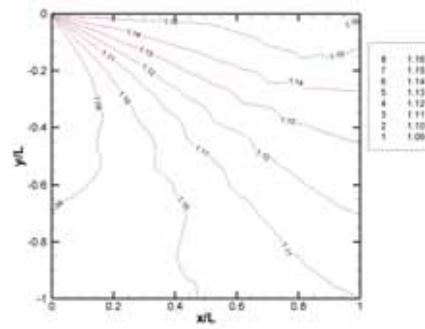


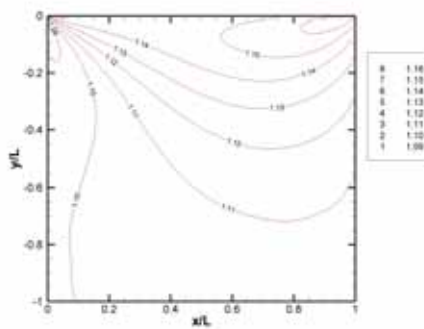
Fig. 3.7 Contours of number Density for $M=0.5$, (a) $Kn=10$; (b) $Kn=1$; (c) $Kn=0.1$; (d) $Kn=0.01$; (e) $Kn=0.0033$



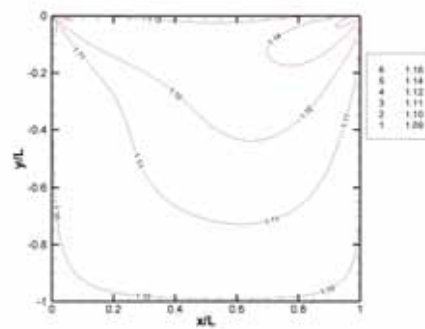
(a)



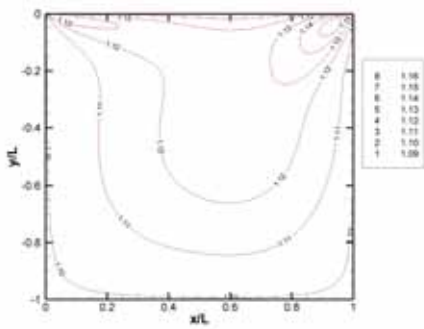
(b)



(c)



(d)



(e)



Fig. 3.8 Contours of Temperature for $M=0.5$, (a) $Kn=10$; (b) $Kn=1$; (c) $Kn=0.1$; (d) $Kn=0.01$; (e) $Kn=0.0033$

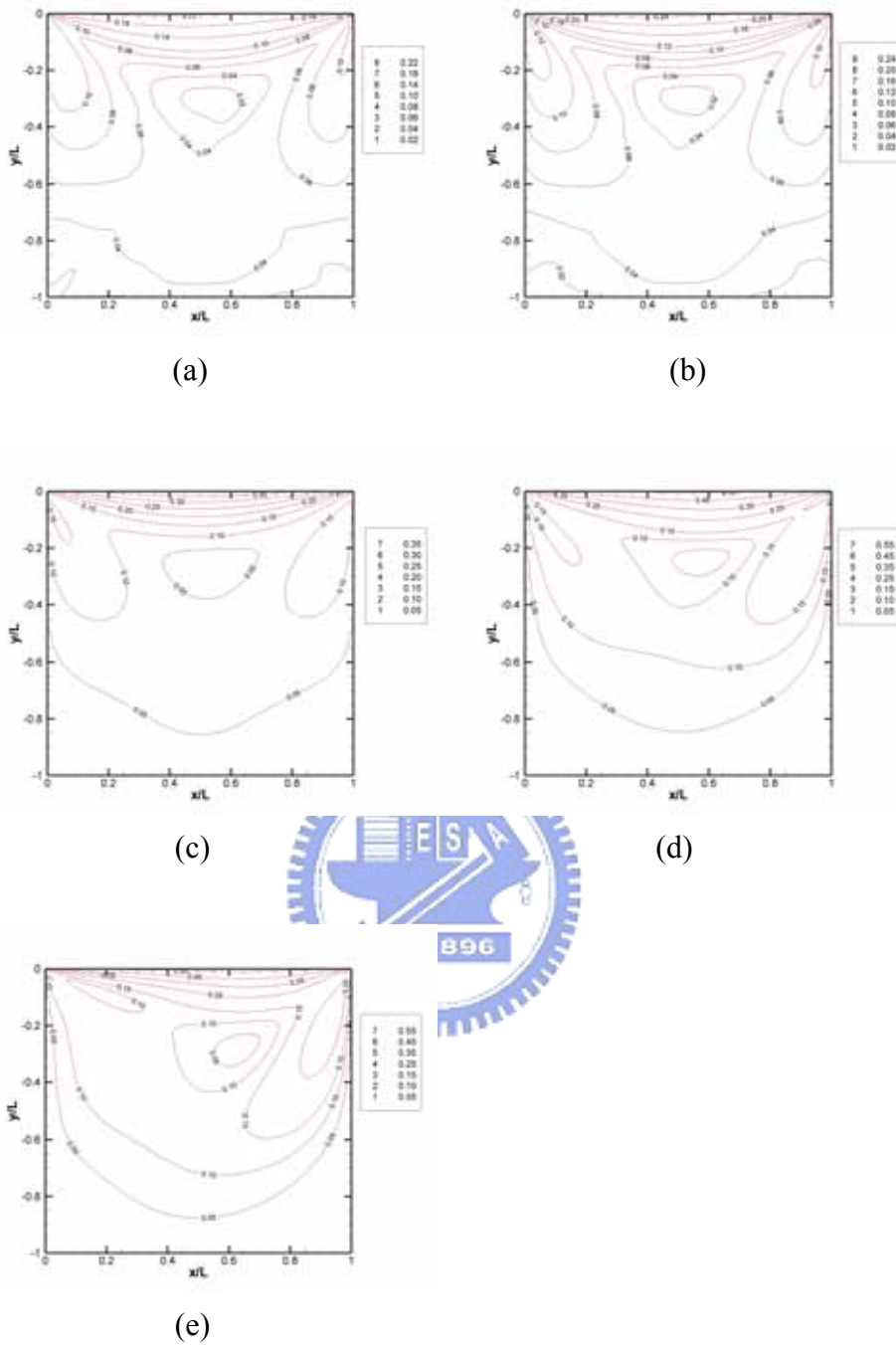
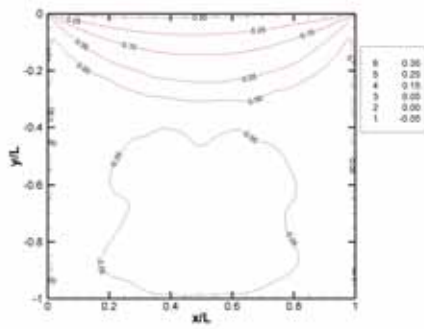
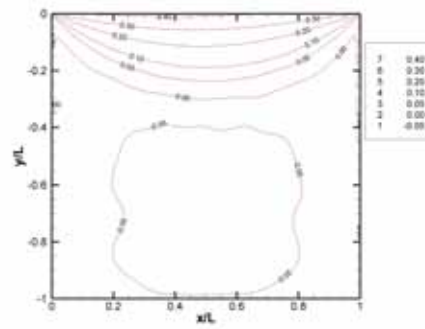


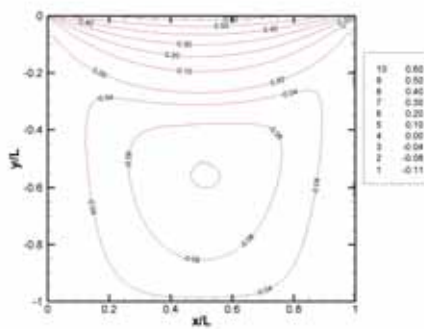
Fig. 3.9 Contours of Mach number for $M=0.5$, (a) $Kn=10$; (b) $Kn=1$; (c) $Kn=0.1$; (d) $Kn=0.01$; (e) $Kn=0.0033$



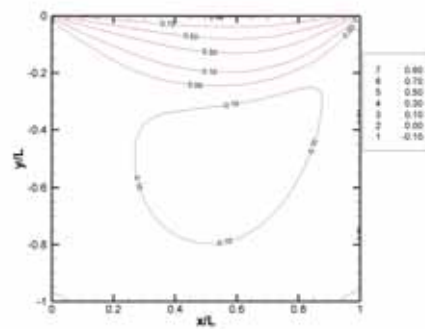
(a)



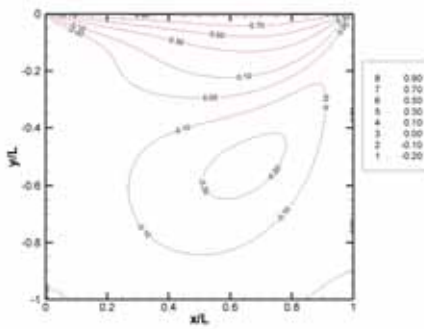
(b)



(c)



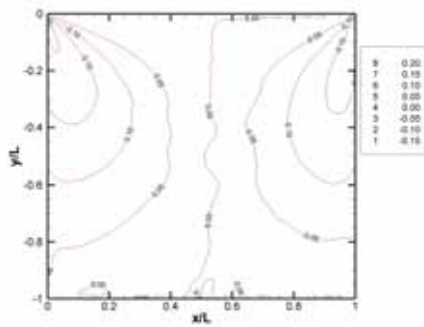
(d)



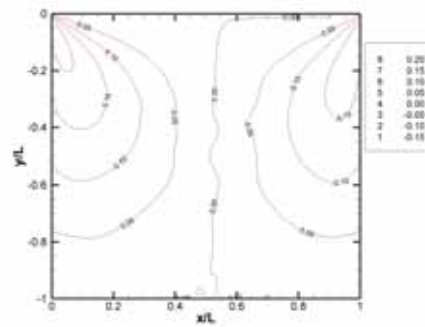
(e)



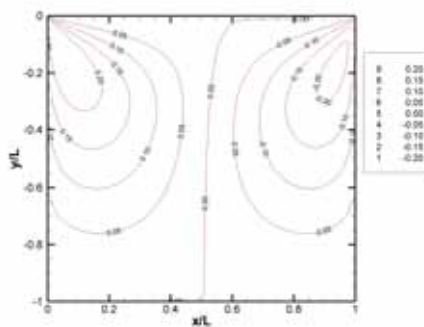
Fig. 3.10 Contours of U-velocity for $M=0.5$, (a) $Kn=10$; (b) $Kn=1$; (c) $Kn=0.1$; (d) $Kn=0.01$; (e) $Kn=0.0033$



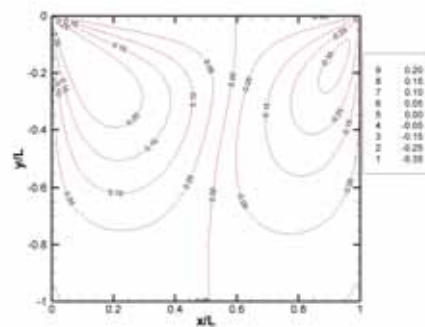
(a)



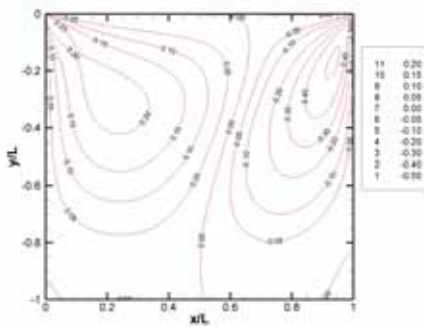
(b)



(c)



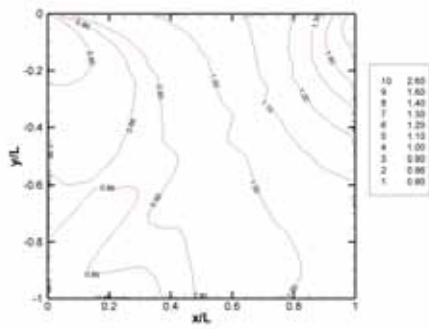
(d)



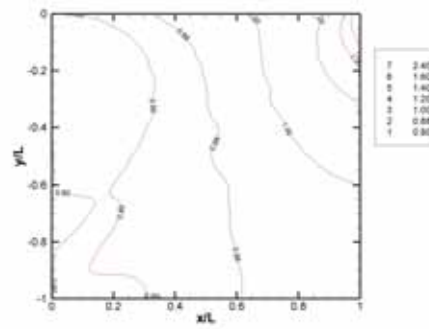
(e)



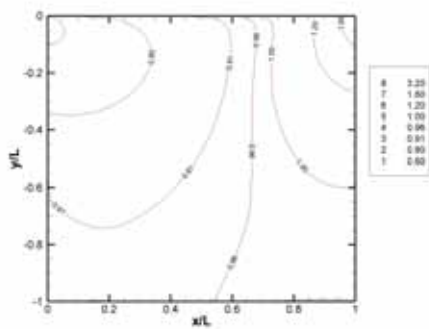
Fig. 3.11 Contours of V-velocity for $M=0.5$, (a) $Kn=10$; (b) $Kn=1$; (c) $Kn=0.1$; (d) $Kn=0.01$; (e) $Kn=0.0033$



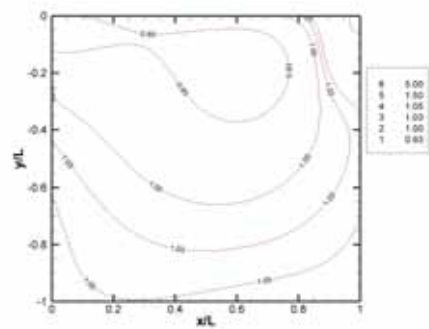
(a)



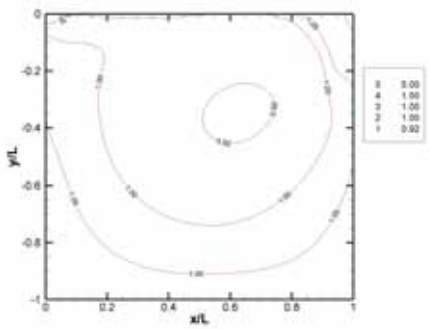
(b)



(c)



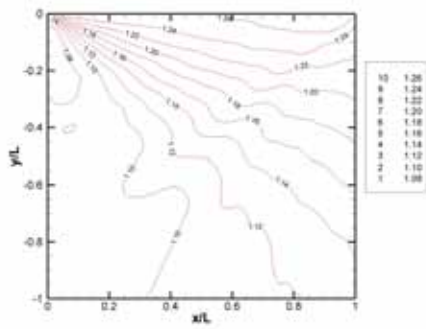
(d)



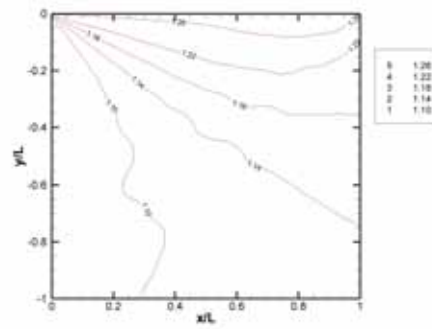
(e)



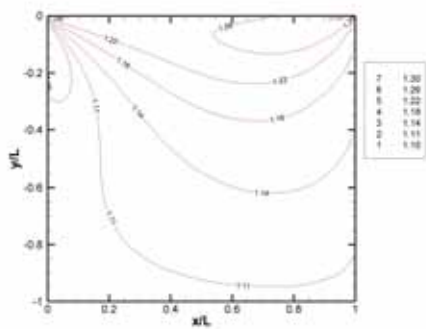
Fig. 3.12 Contours of number Density for $M=0.9$, (a) $Kn=10$; (b) $Kn=1$; (c) $Kn=0.1$; (d) $Kn=0.01$; (e) $Kn=0.0033$



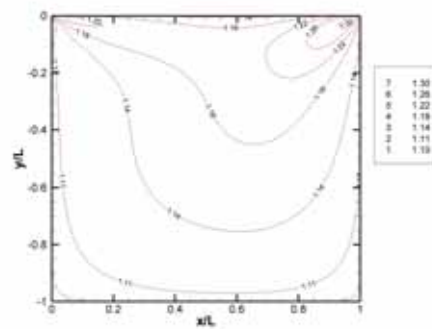
(a)



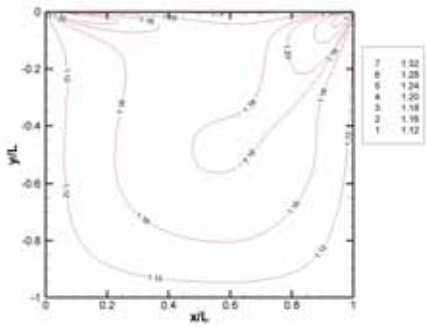
(b)



(c)



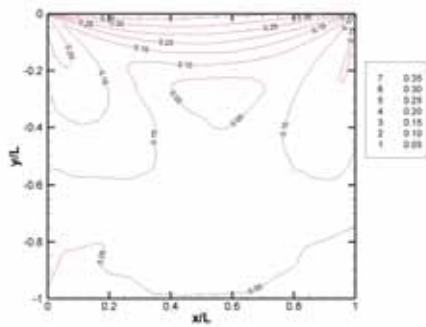
(d)



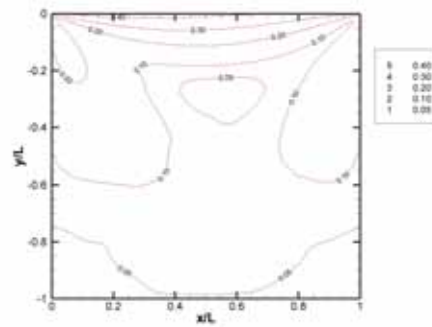
(e)



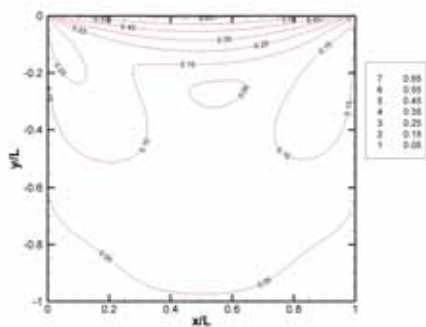
Fig. 3.13 Contours of Temperature for $M=0.9$, (a) $Kn=10$; (b) $Kn=1$; (c) $Kn=0.1$; (d) $Kn=0.01$; (e) $Kn=0.0033$



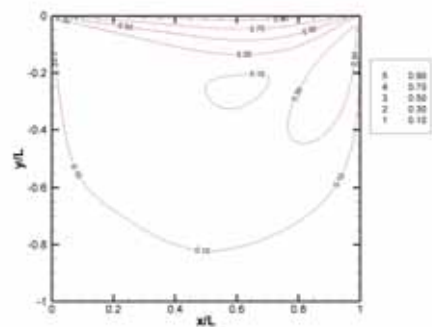
(a)



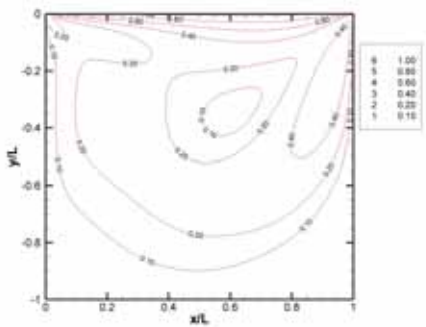
(b)



(c)



(d)



(e)



Fig. 3.14 Contours of Mach number for $M=0.9$, (a) $Kn=10$; (b) $Kn=1$; (c) $Kn=0.1$; (d) $Kn=0.01$; (e) $Kn=0.0033$

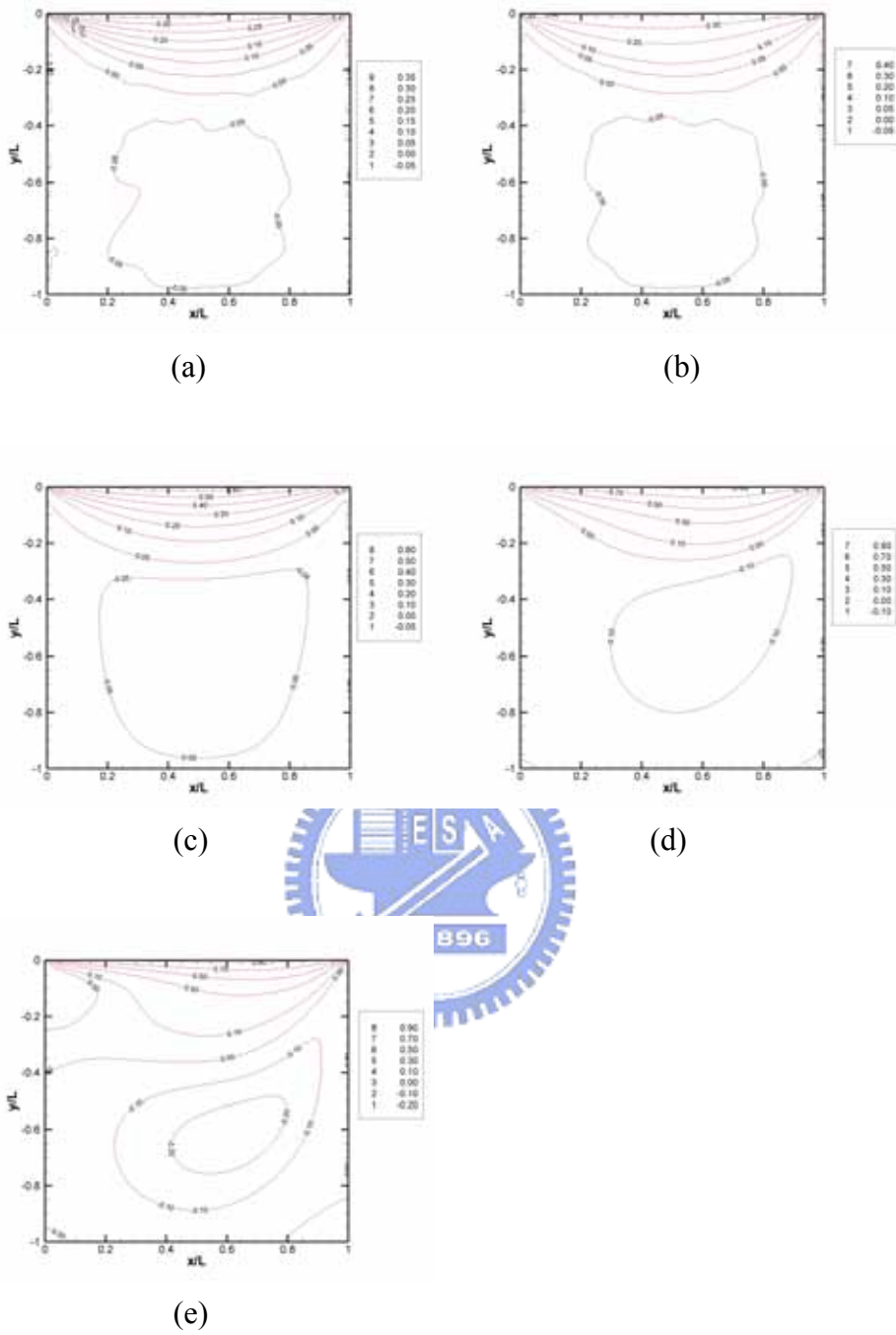


Fig. 3.15 Contours of U-velocity for $M=0.9$, (a) $Kn=10$; (b) $Kn=1$; (c) $Kn=0.1$; (d) $Kn=0.01$; (e) $Kn=0.0033$

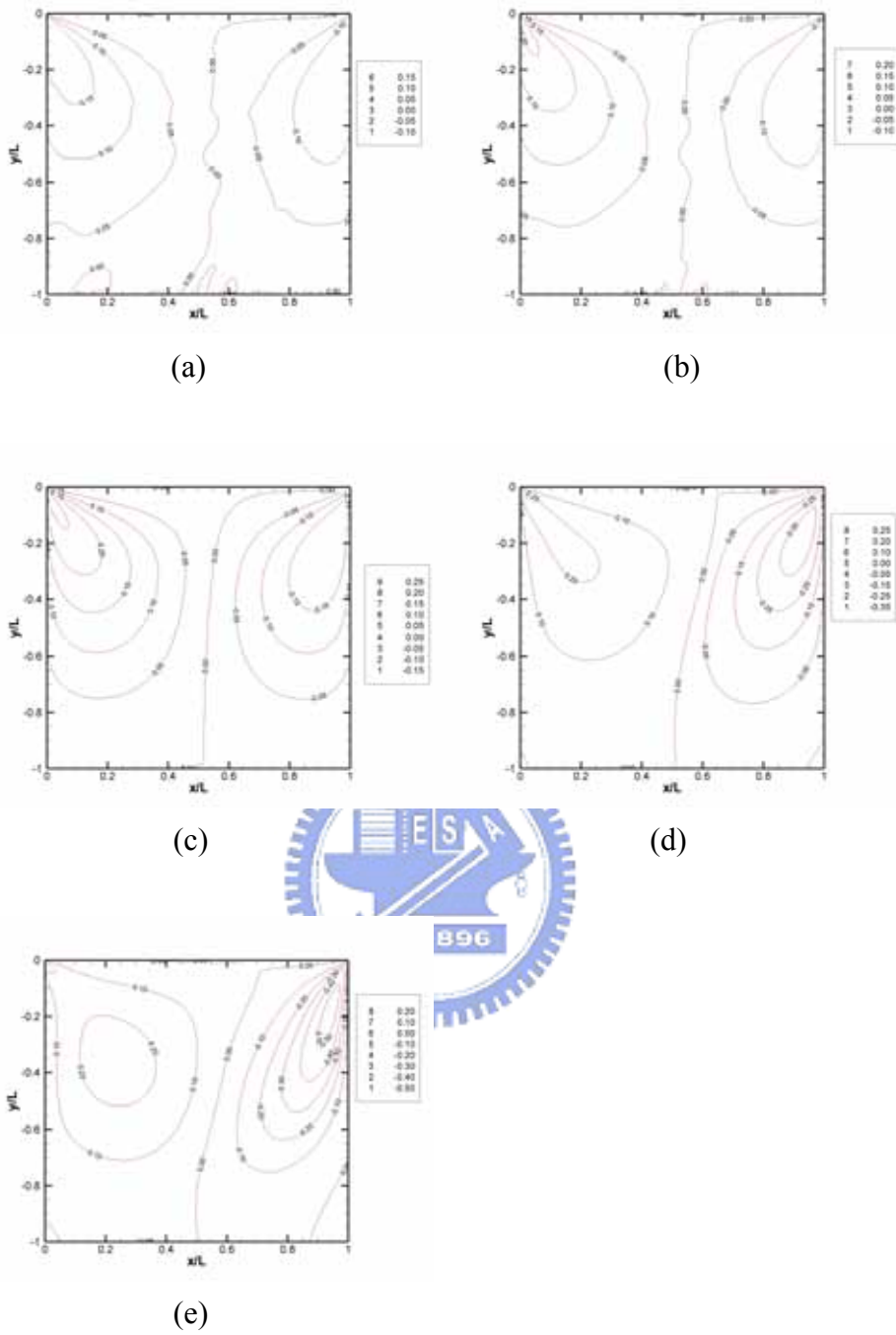
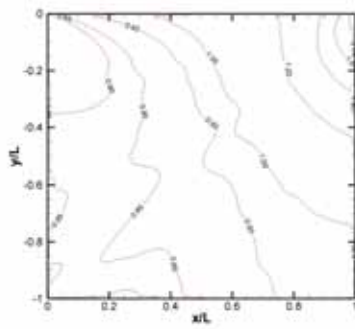
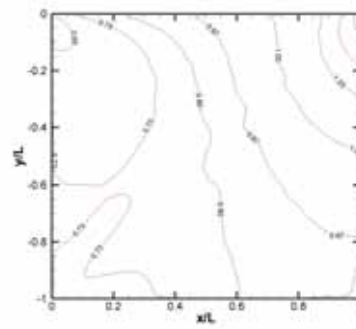


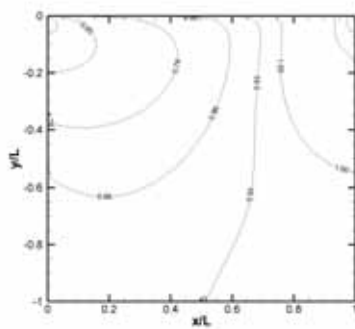
Fig. 3.16 Contours of V-velocity for $M=0.9$, (a) $Kn=10$; (b) $Kn=1$; (c) $Kn=0.1$; (d) $Kn=0.01$; (e) $Kn=0.0033$



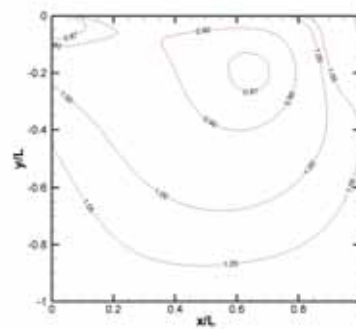
(a)



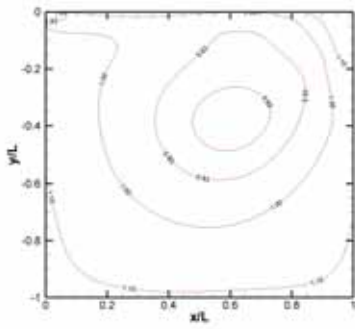
(b)



(c)

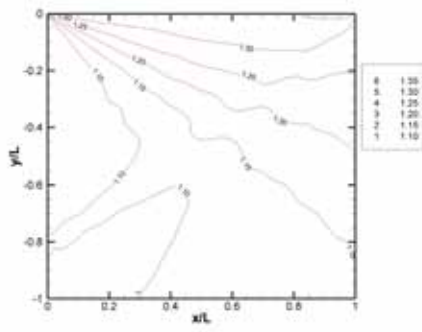


(d)

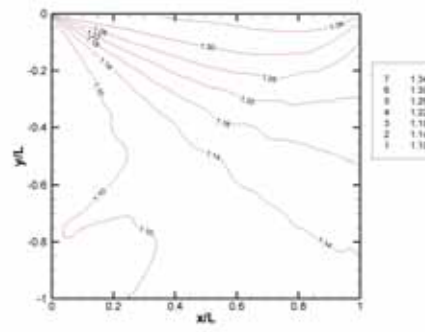


(e)

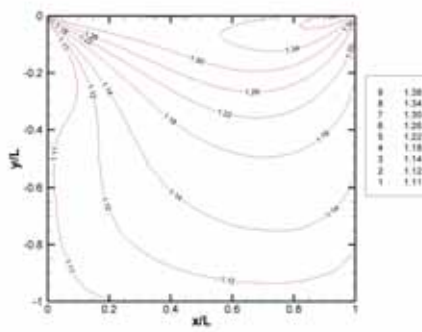
Fig. 3.17 Contours of number Density for $M=1.1$, (a) $Kn=10$; (b) $Kn=1$; (c) $Kn=0.1$; (d) $Kn=0.01$; (e) $Kn=0.0033$



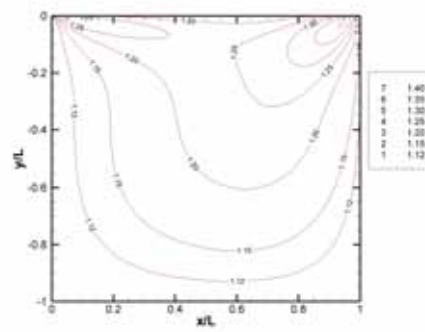
(a)



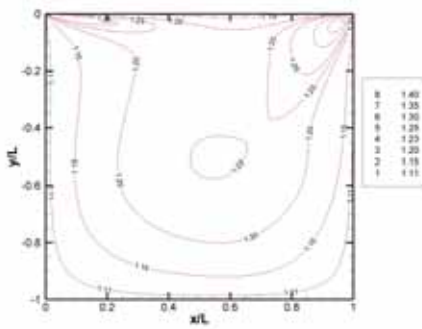
(b)



(c)



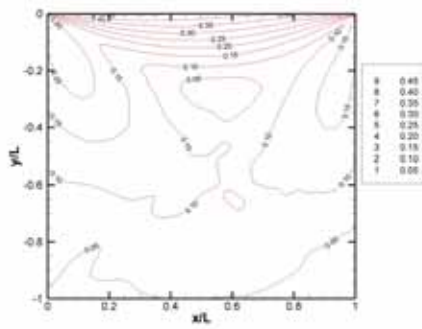
(d)



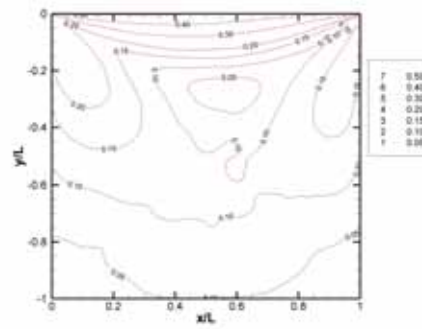
(e)



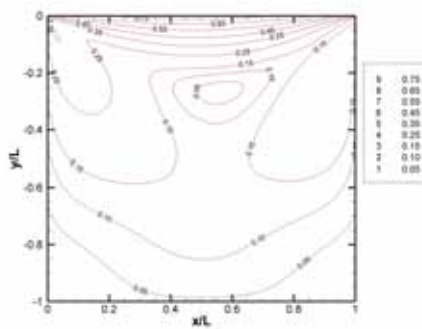
Fig. 3.18 Contours of Temperature for $M=1.1$, (a) $Kn=10$; (b) $Kn=1$; (c) $Kn=0.1$; (d) $Kn=0.01$; (e) $Kn=0.0033$



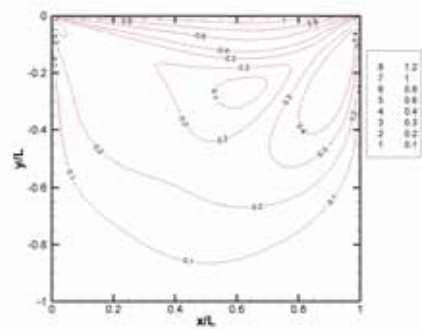
(a)



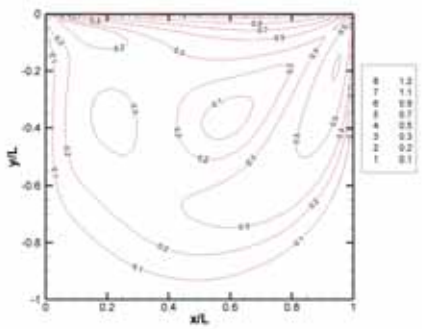
(b)



(c)



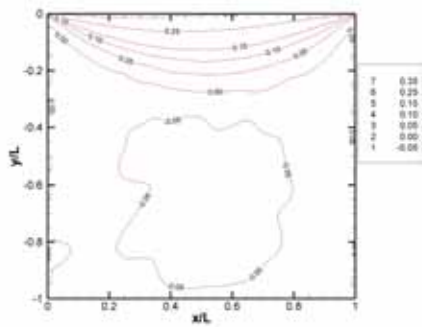
(d)



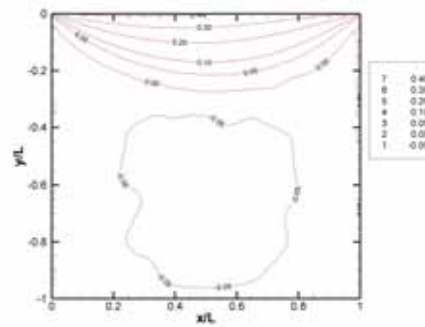
(e)



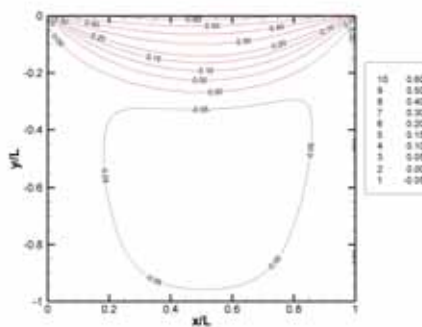
Fig. 3.19 Contours of Mach number for $M=1.1$, (a) $Kn=10$; (b) $Kn=1$; (c) $Kn=0.1$; (d) $Kn=0.01$; (e) $Kn=0.0033$



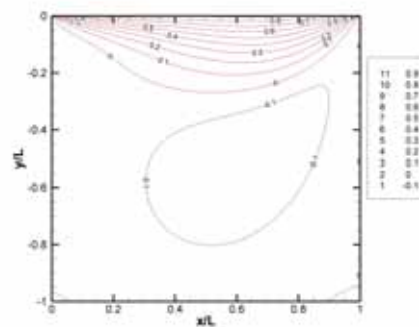
(a)



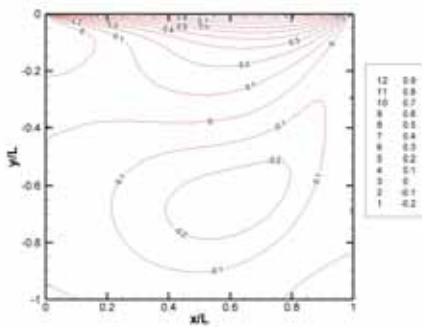
(b)



(c)



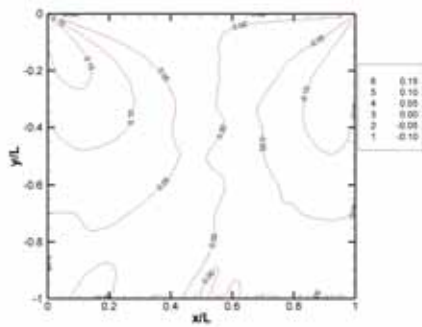
(d)



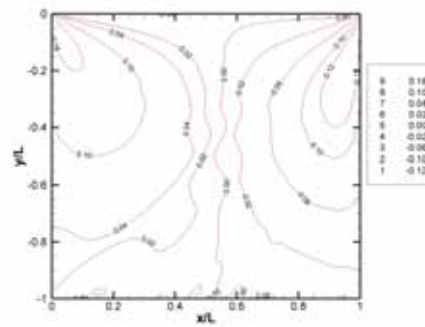
(e)



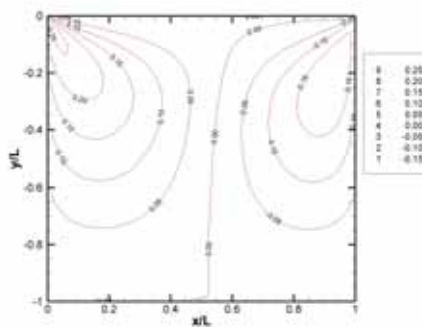
Fig. 3.20 Contours of U-velocity for $M=1.1$, (a) $Kn=10$; (b) $Kn=1$; (c) $Kn=0.1$; (d) $Kn=0.01$; (e) $Kn=0.0033$



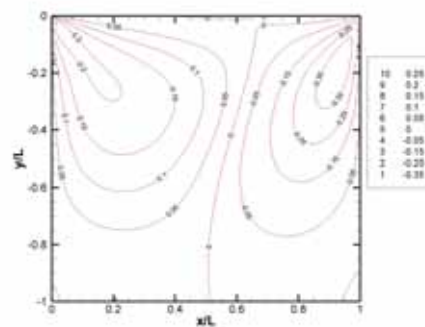
(a)



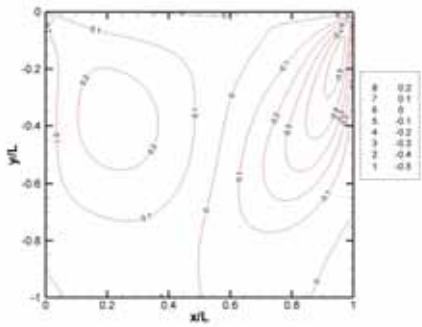
(b)



(c)



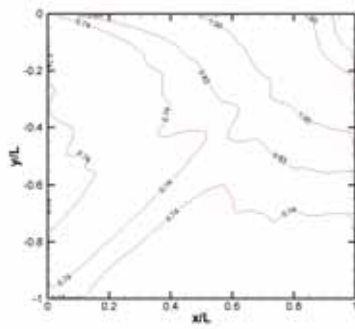
(d)



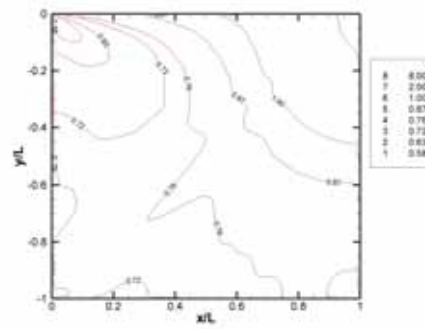
(e)



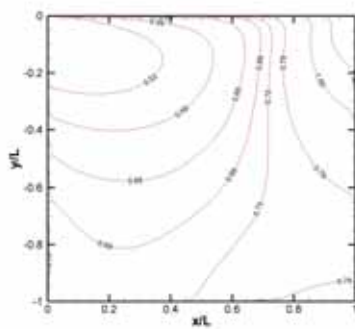
Fig. 3.21 Contours of V-velocity for $M=1.1$, (a) $Kn=10$; (b) $Kn=1$; (c) $Kn=0.1$; (d) $Kn=0.01$; (e) $Kn=0.0033$



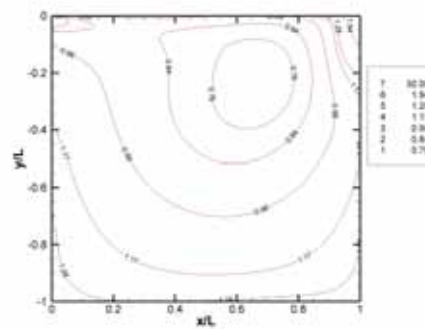
(a)



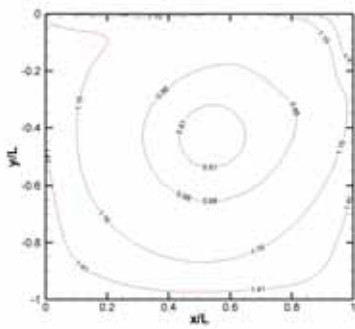
(b)



(c)



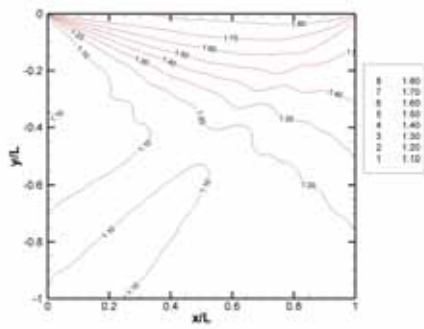
(d)



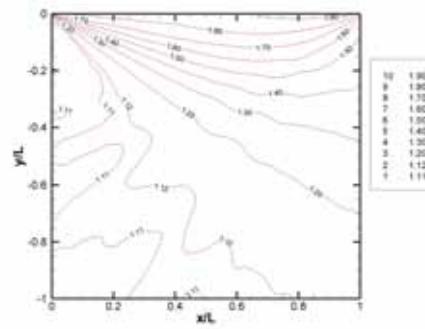
(e)



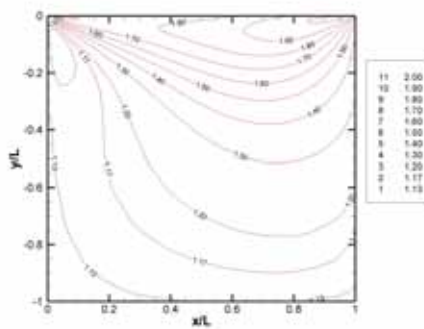
Fig. 3.22 Contours of number Density for $M=2.0$, (a) $Kn=10$; (b) $Kn=1$; (c) $Kn=0.1$; (d) $Kn=0.01$; (e) $Kn=0.0033$



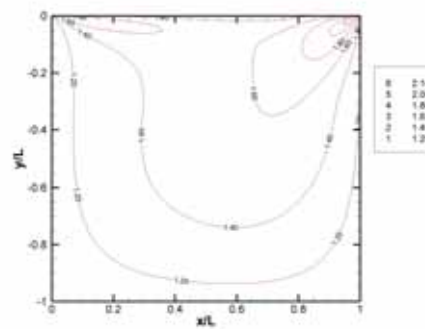
(a)



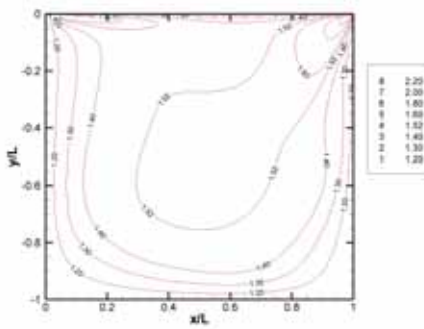
(b)



(c)



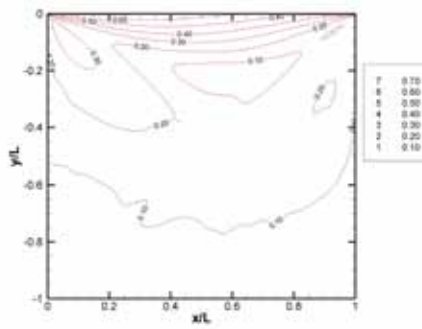
(d)



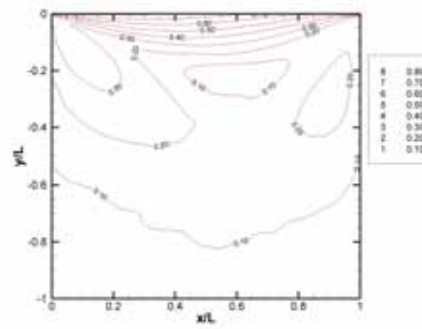
(e)



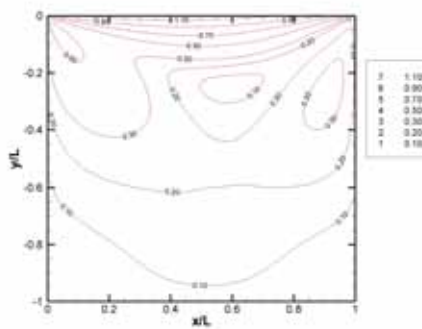
Fig. 3.23 Contours of Temperature for $M=2.0$, (a) $Kn=10$; (b) $Kn=1$; (c) $Kn=0.1$; (d) $Kn=0.01$; (e) $Kn=0.0033$



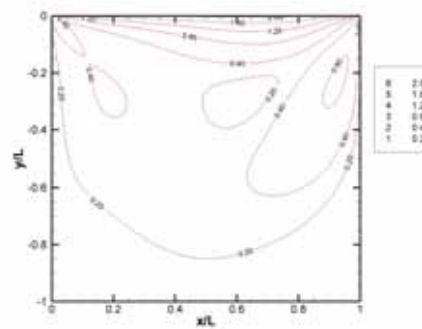
(a)



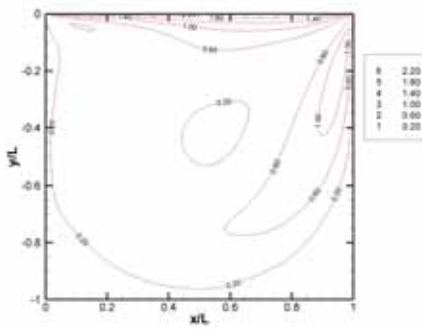
(b)



(c)



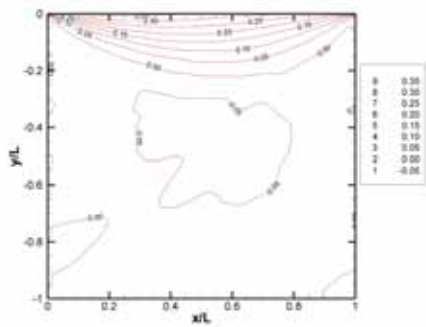
(d)



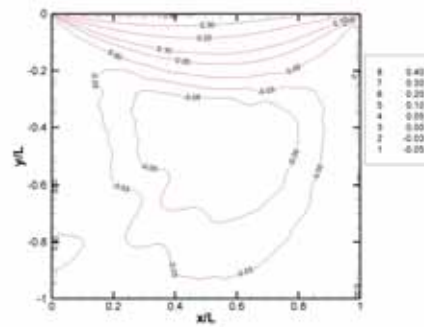
(e)



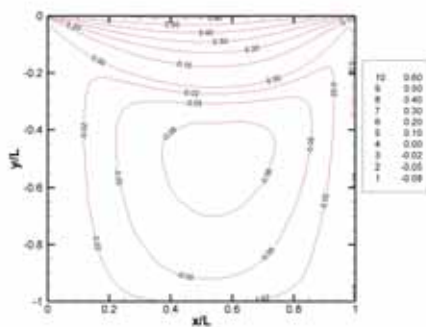
Fig. 3.24 Contours of Mach number for $M=2.0$, (a) $Kn=10$; (b) $Kn=1$; (c) $Kn=0.1$; (d) $Kn=0.01$; (e) $Kn=0.0033$



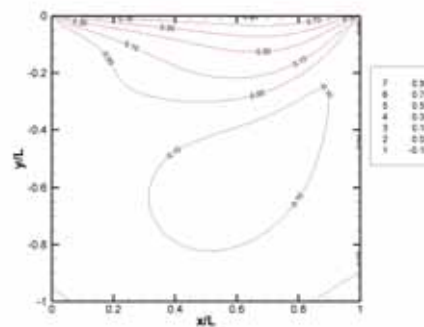
(a)



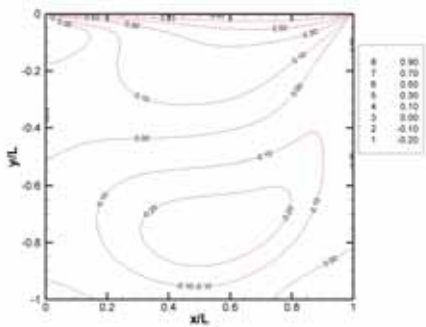
(b)



(c)



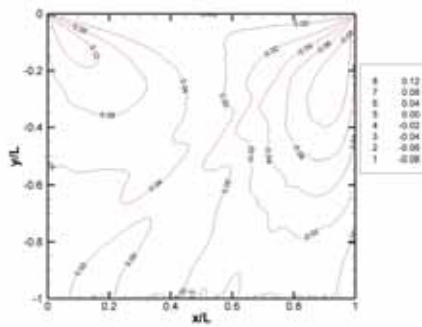
(d)



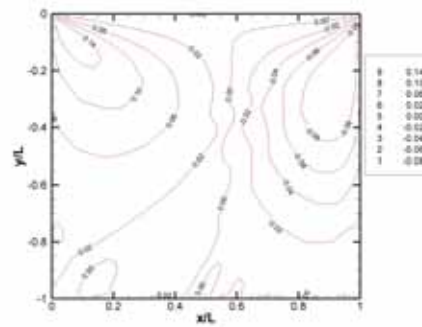
(e)



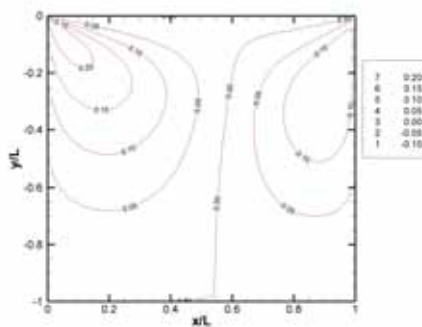
Fig. 3.25 Contours of U-velocity for $M=2.0$, (a) $Kn=10$; (b) $Kn=1$; (c) $Kn=0.1$; (d) $Kn=0.01$; (e) $Kn=0.0033$



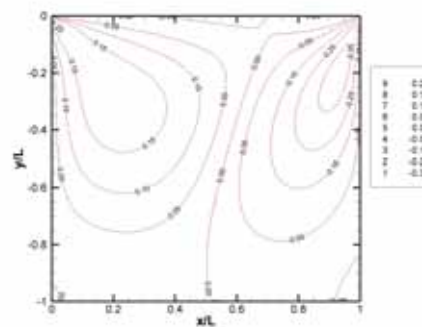
(a)



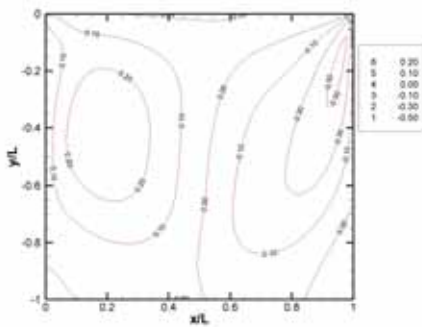
(b)



(c)



(d)



(e)



Fig. 3.26 Contours of V-velocity for $M=2.0$, (a) $Kn=10$; (b) $Kn=1$; (c) $Kn=0.1$; (d) $Kn=0.01$; (e) $Kn=0.0033$

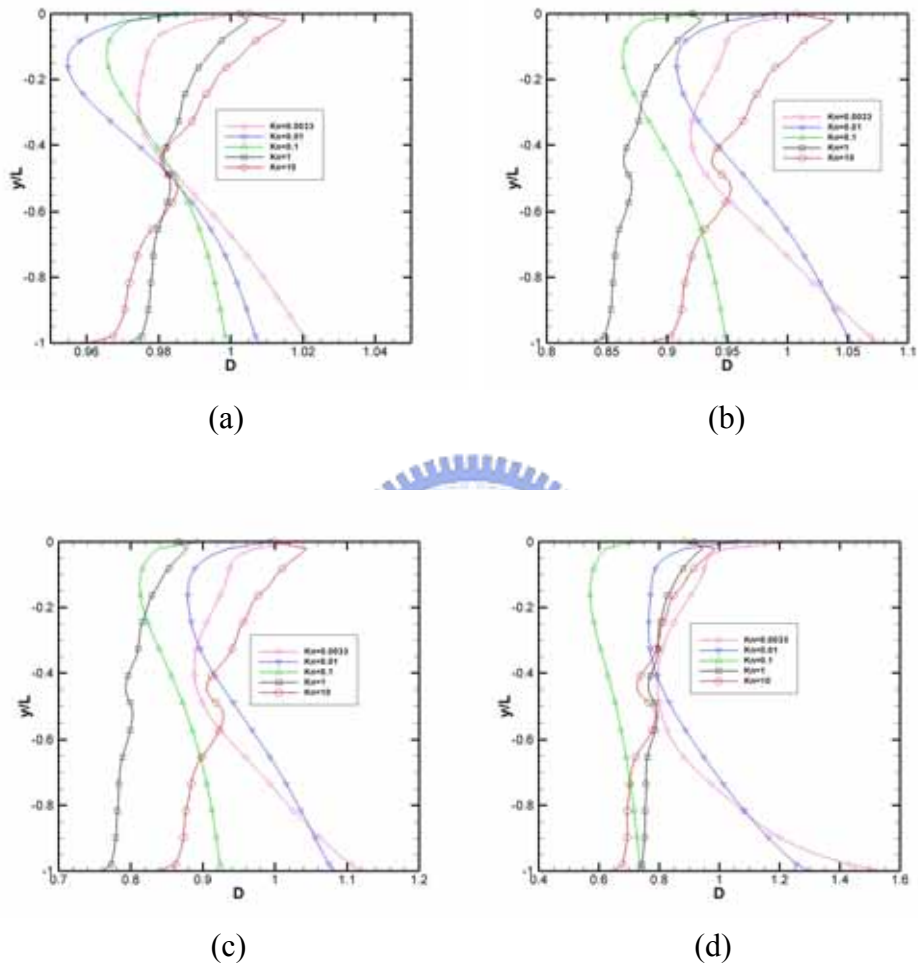


Fig. 3.27 Profile of the number Density on a vertical plane $x=0.5$ for (a) $M=0.5$; (b) $M=0.9$; (c) $M=1.1$; (d) $M=2$

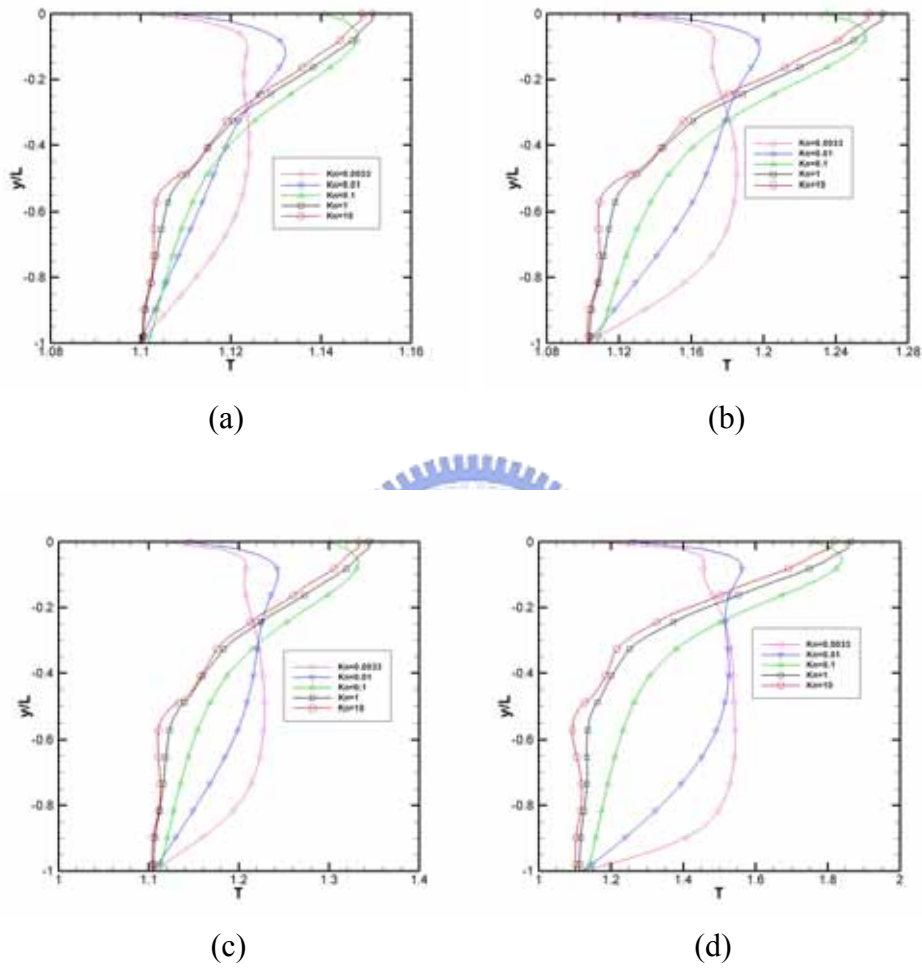


Fig. 3.28 Profile of the Temperature on a vertical plane $x=0.5$ for (a) $M=0.5$; (b) $M=0.9$; (c) $M=1.1$; (d) $M=2$

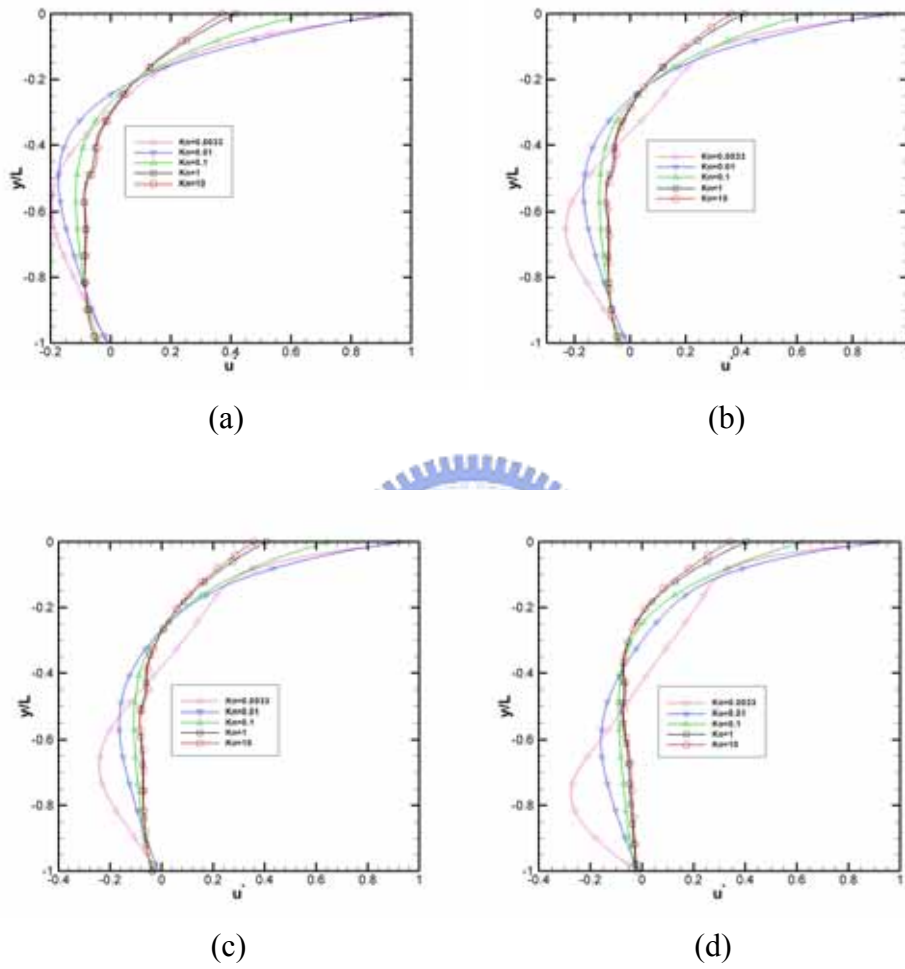


Fig. 3.29 Profile of the U-velocity on a vertical plane $x=0.5$ for (a) $M=0.5$; (b) $M=0.9$; (c) $M=1.1$; (d) $M=2$

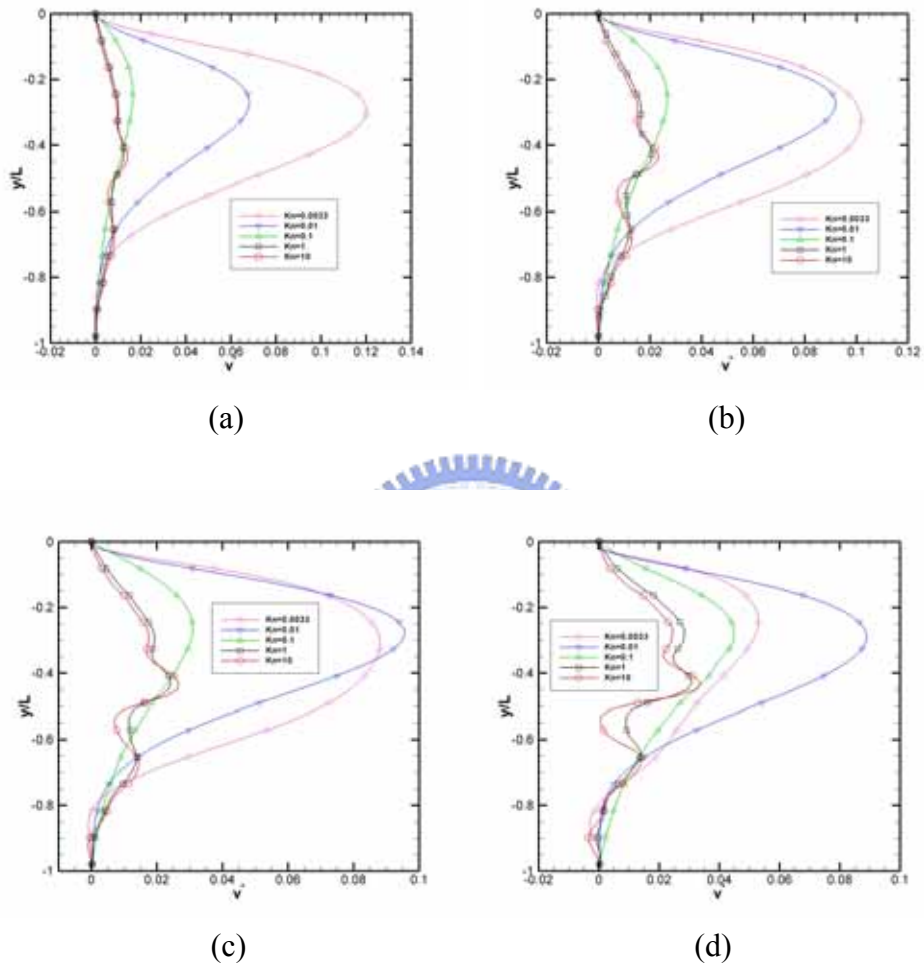


Fig. 3.30 Profile of the V-velocity on a vertical plane $x=0.5$ for (a) $M=0.5$; (b) $M=0.9$; (c) $M=1.1$; (d) $M=2$

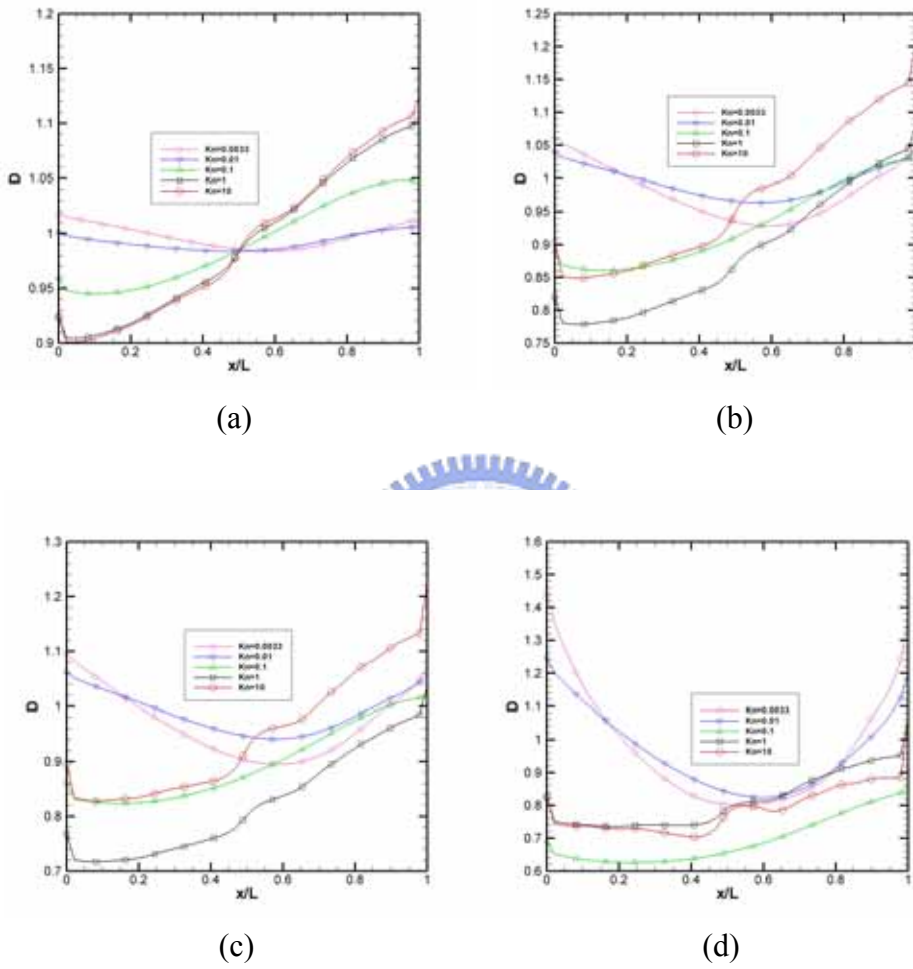


Fig. 3.31 Profile of the number Density on a horizontal plane $y=-0.5$ for (a) $M=0.5$; (b) $M=0.9$; (c) $M=1.1$; (d) $M=2$

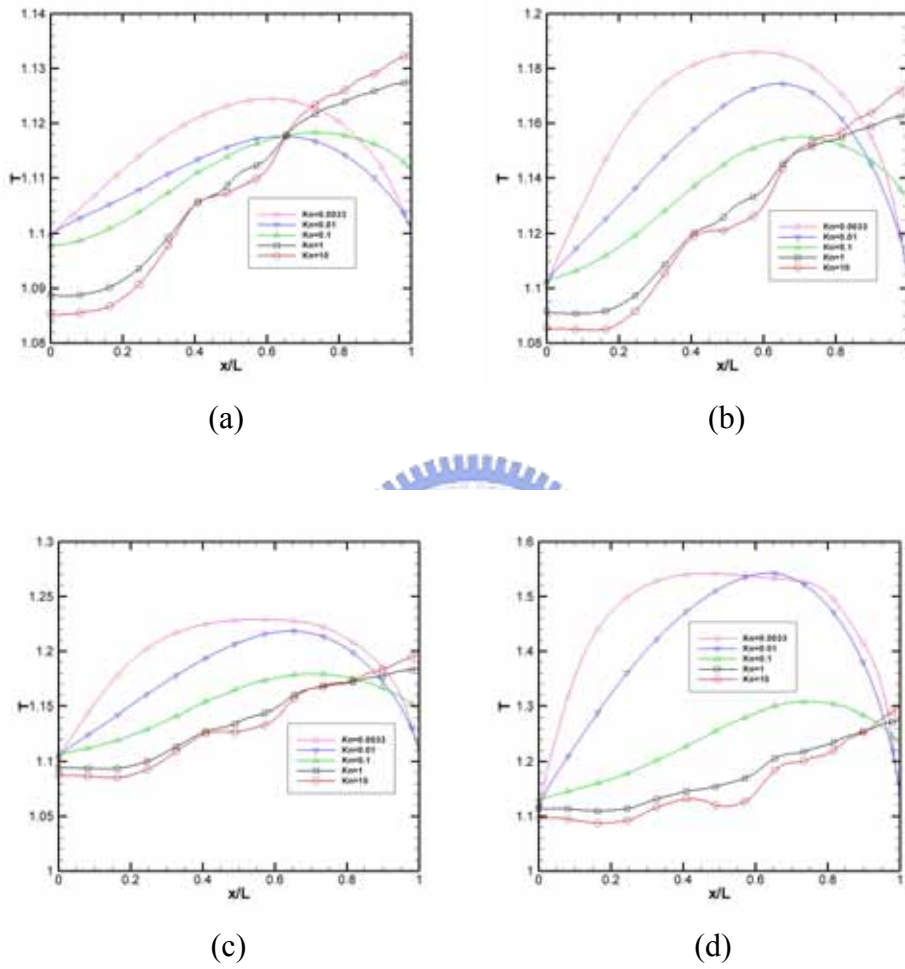


Fig. 3.32 Profile of the Temperature on a horizontal plane $y = -0.5$ for (a) $M = 0.5$; (b) $M = 0.9$; (c) $M = 1.1$; (d) $M = 2$

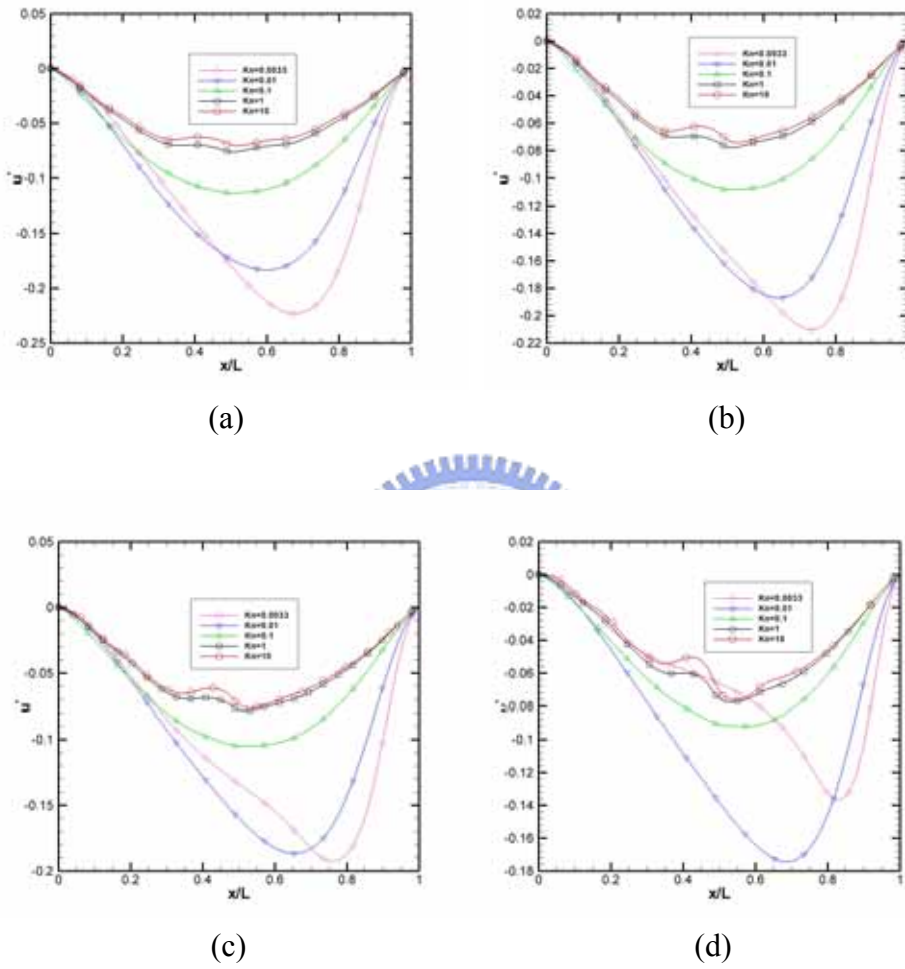
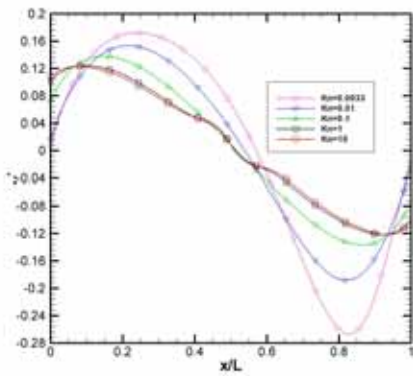
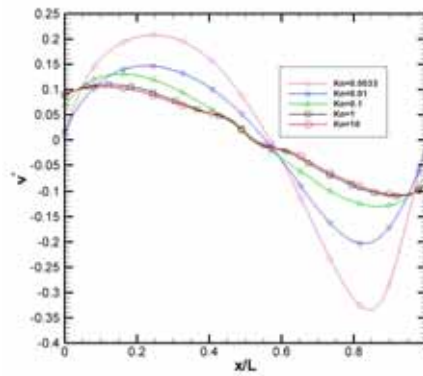


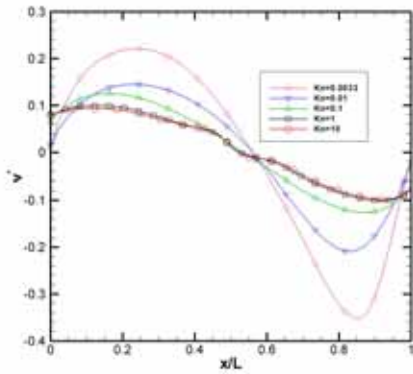
Fig. 3.33 Profile of the U-velocity on a horizontal plane $y=-0.5$ for (a) $M=0.5$; (b) $M=0.9$; (c) $M=1.1$; (d) $M=2$



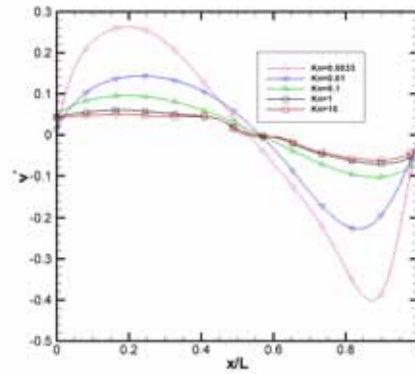
(a)



(b)



(c)



(d)

Fig. 3.34 Profile of the V-velocity on a horizontal plane $y=-0.5$ for (a) $M=0.5$; (b) $M=0.9$; (c) $M=1.1$; (d) $M=2$

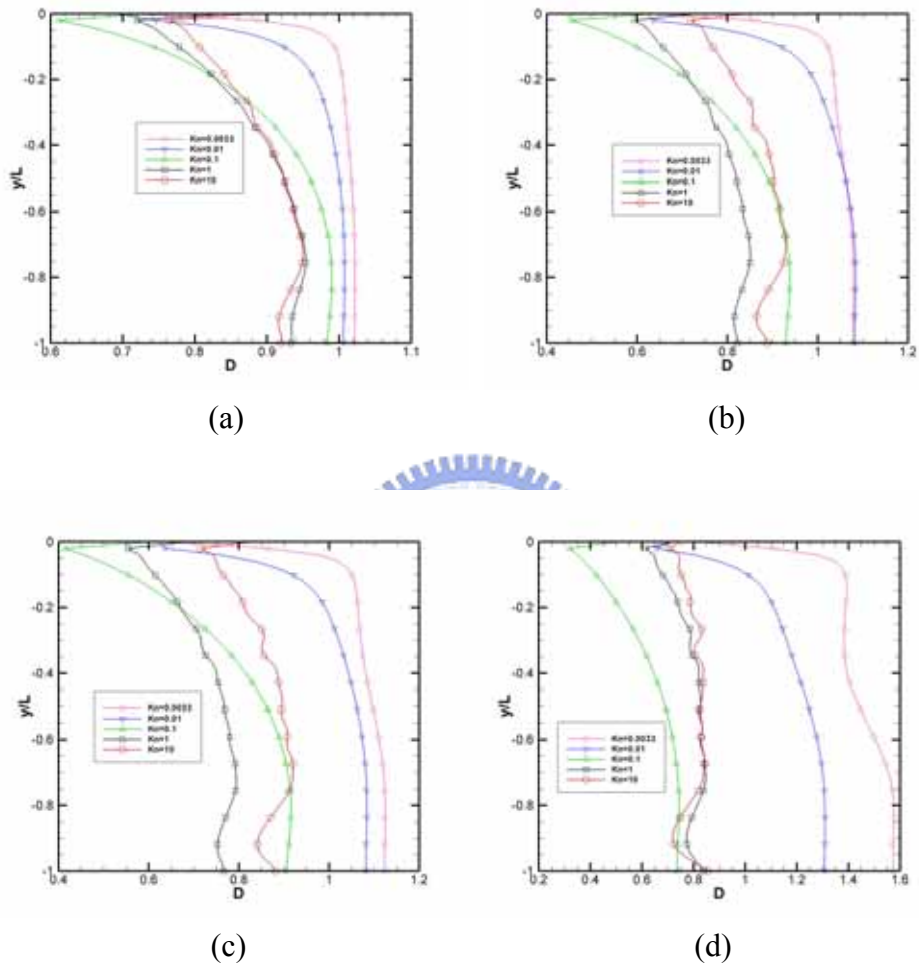


Fig. 3.35 Profile of the number Density on a vertical plane $x=0$ for (a) $M=0.5$; (b) $M=0.9$; (c) $M=1.1$; (d) $M=2$

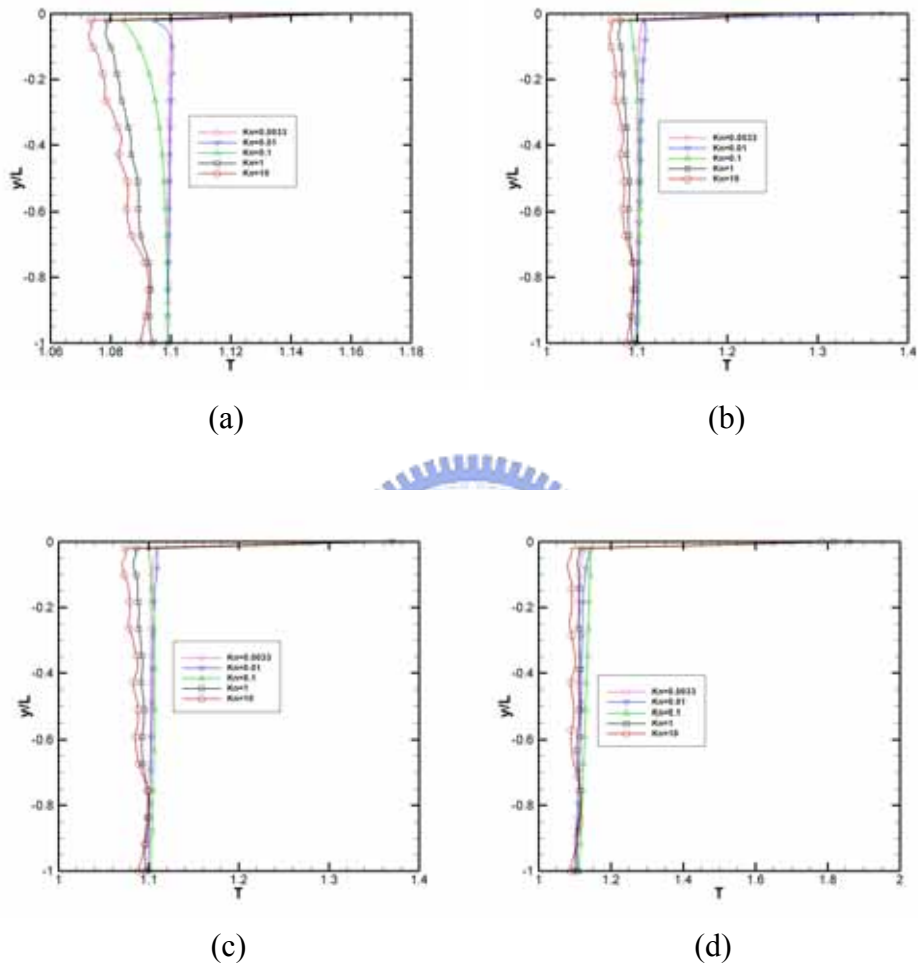


Fig. 3.36 Profile of the Temperature on a vertical plane $x=0$ for (a) $M=0.5$; (b) $M=0.9$; (c) $M=1.1$; (d) $M=2$

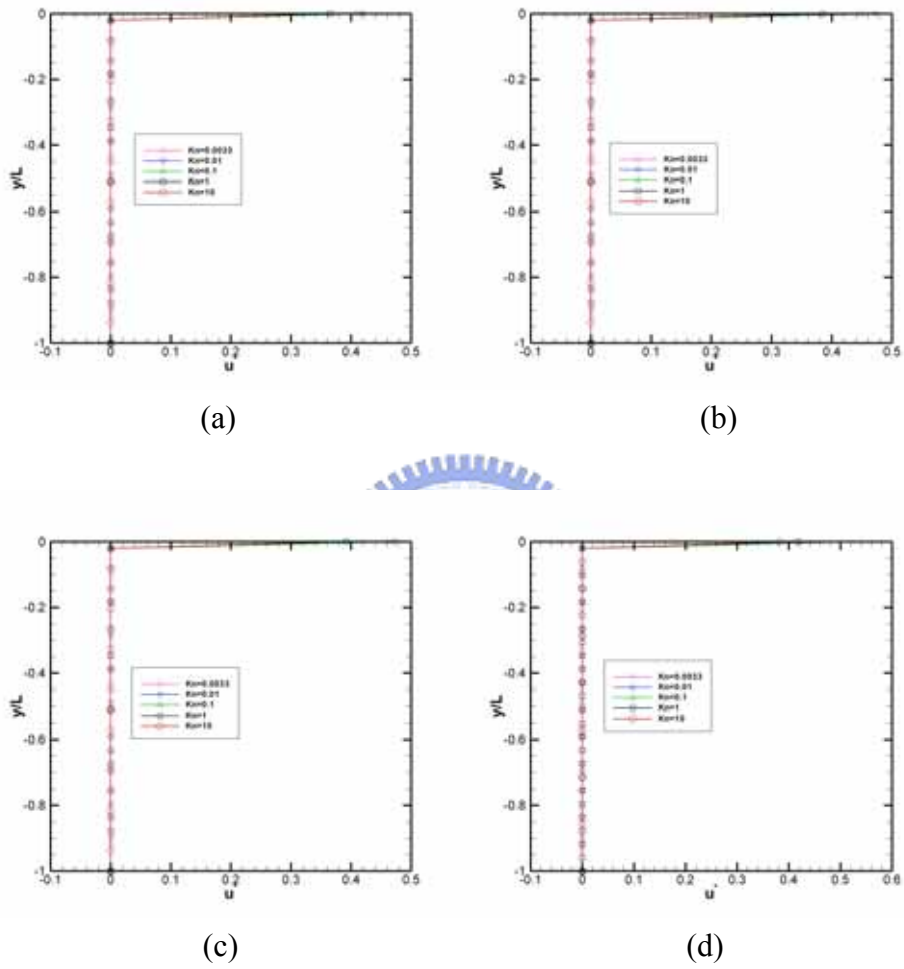


Fig. 3.37 Profile of the U-velocity on a vertical plane $x=0$ for (a) $M=0.5$; (b) $M=0.9$; (c) $M=1.1$; (d) $M=2$

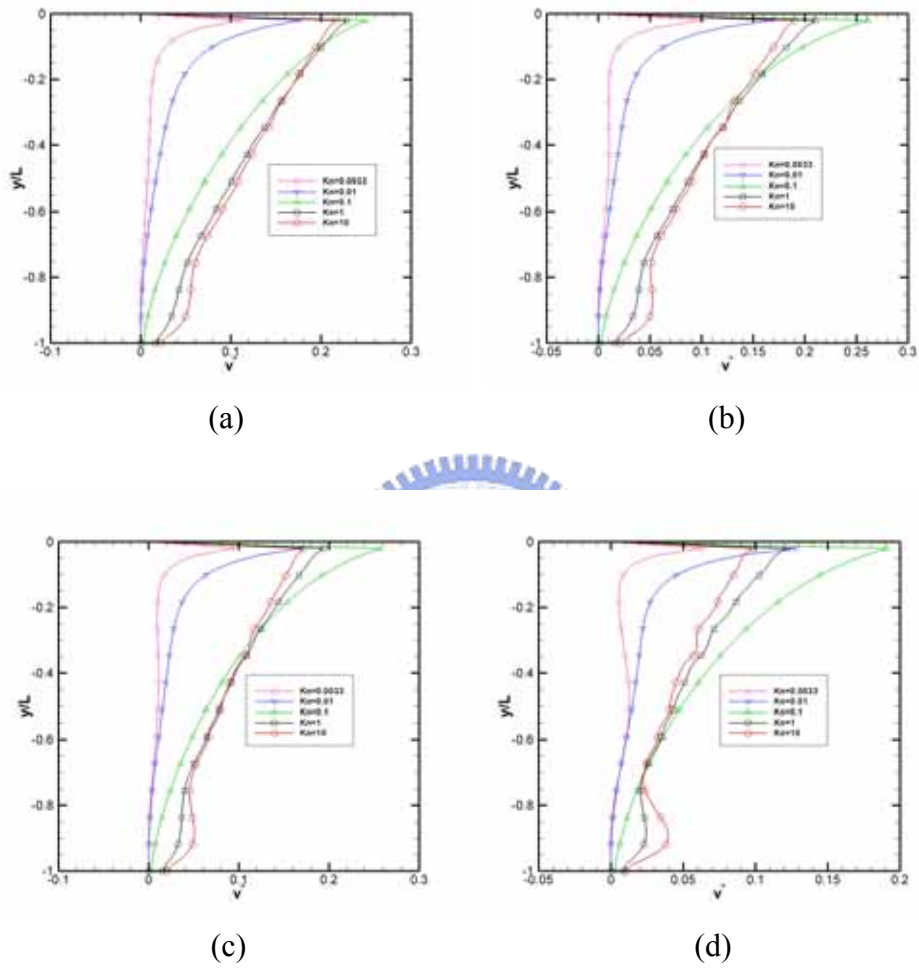


Fig. 3.38 Profile of the V-velocity on a vertical plane $x=0$ for (a) $M=0.5$; (b) $M=0.9$; (c) $M=1.1$; (d) $M=2$

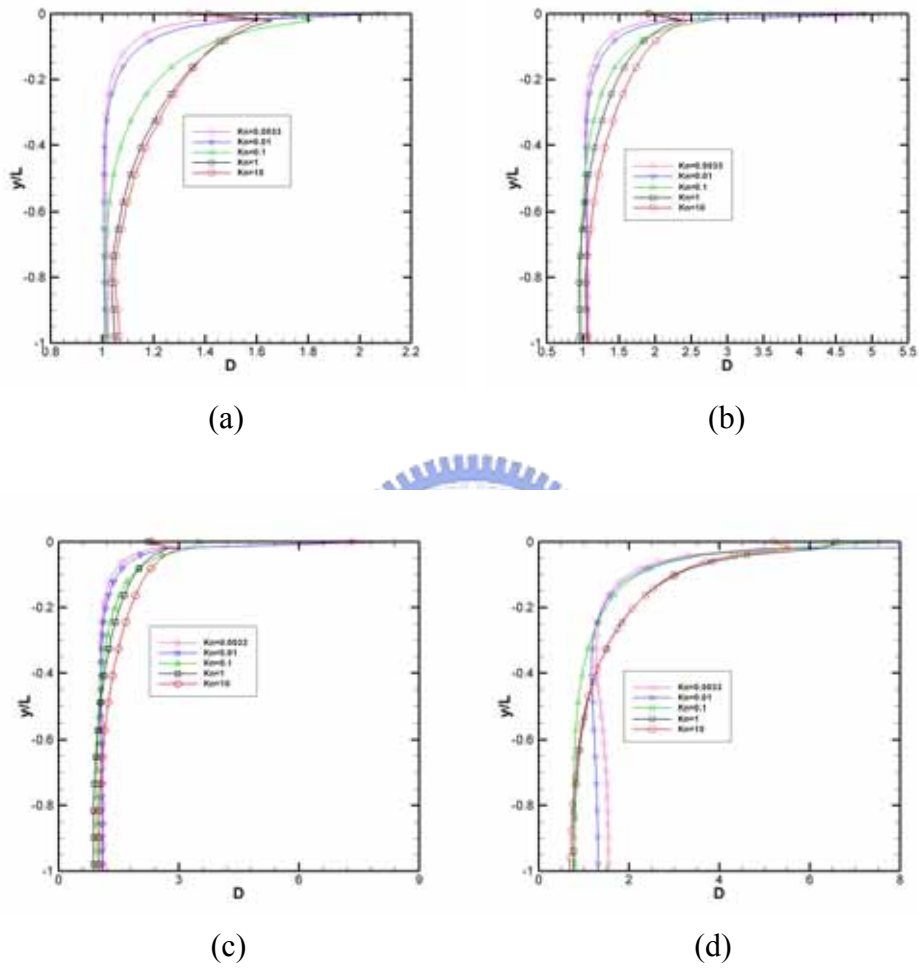


Fig. 3.39 Profile of the number Density on a vertical plane $x=1$ for (a) $M=0.5$; (b) $M=0.9$; (c) $M=1.1$; (d) $M=2$

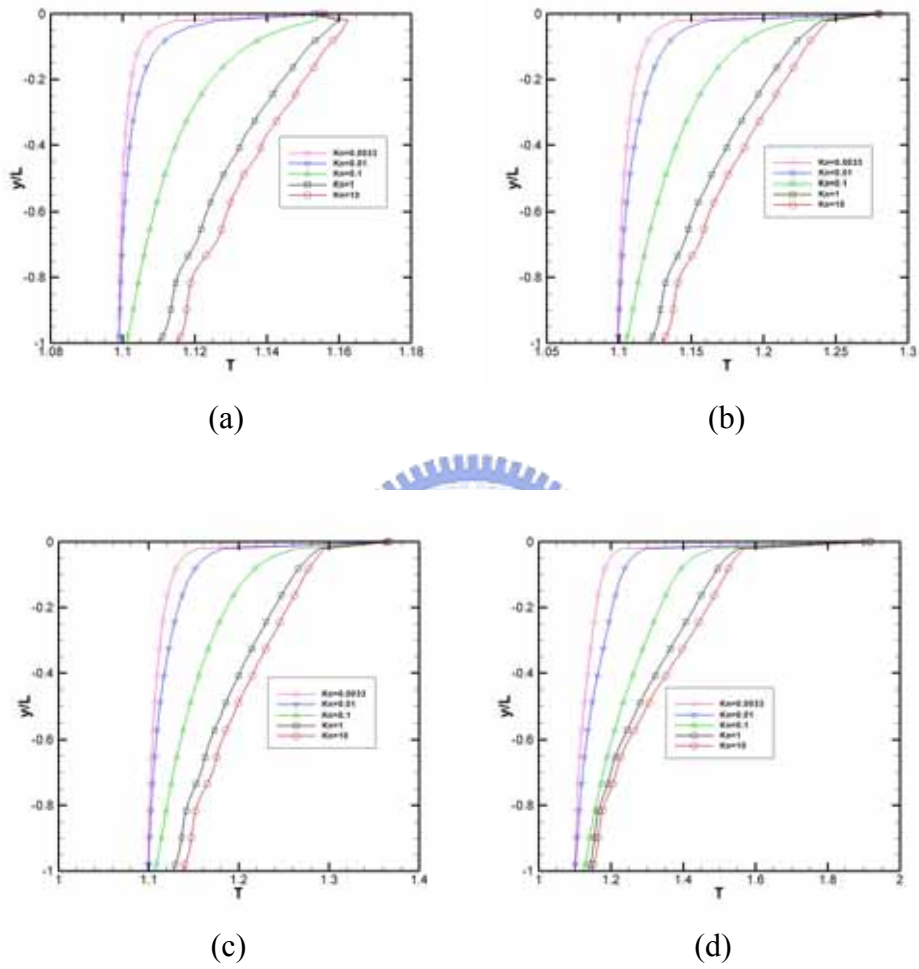


Fig. 3.40 Profile of the Temperature on a vertical plane $x=1$ for (a) $M=0.5$; (b) $M=0.9$; (c) $M=1.1$; (d) $M=2$

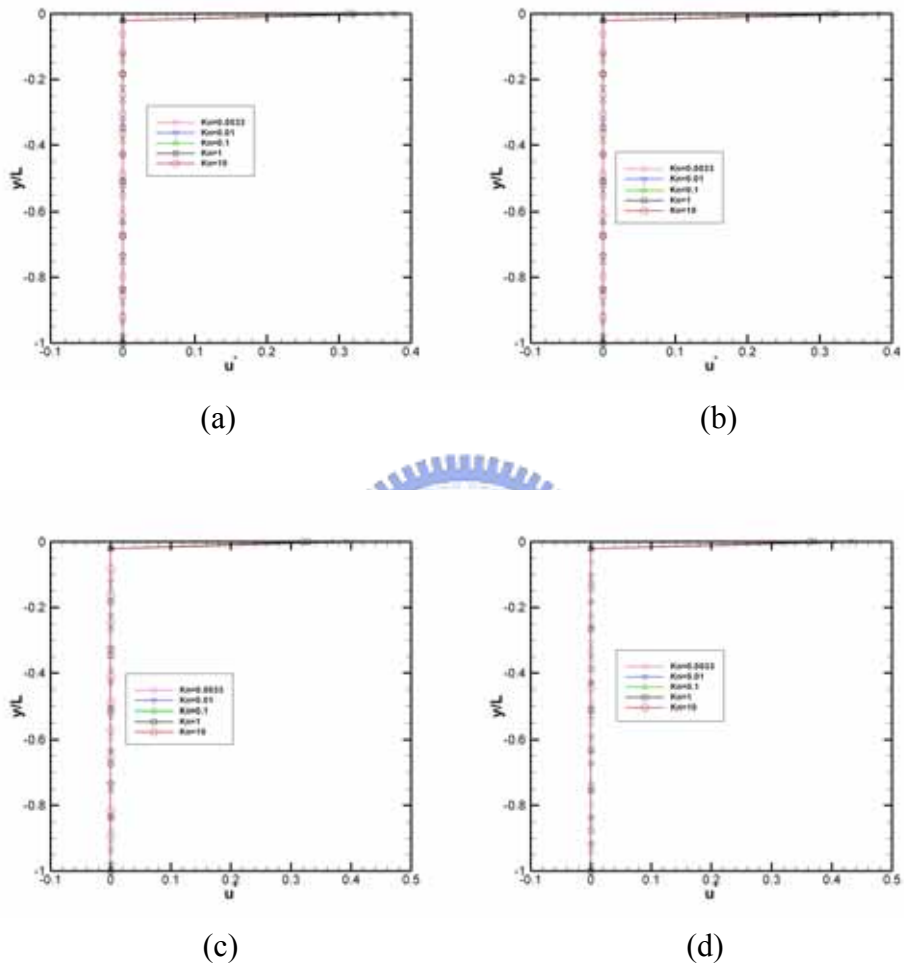


Fig. 3.41 Profile of the U-velocity on a vertical plane $x=1$ for (a) $M=0.5$; (b) $M=0.9$; (c) $M=1.1$; (d) $M=2$

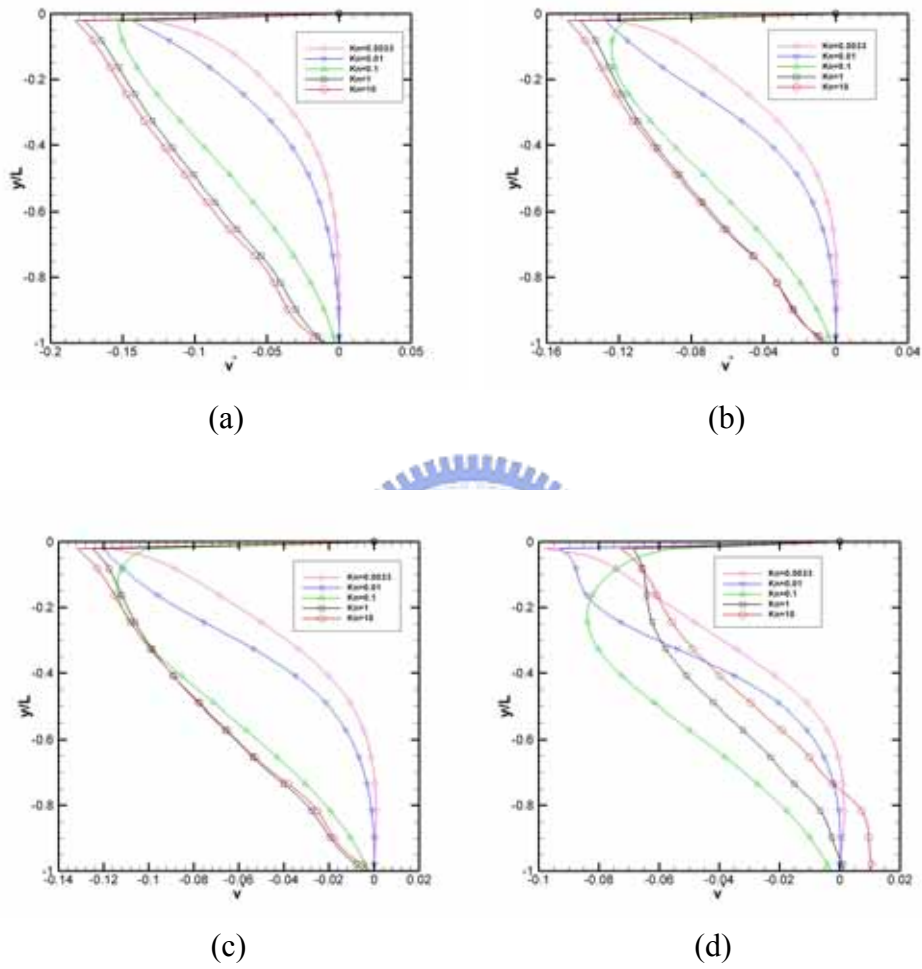


Fig. 3.42 Profile of the V-velocity on a vertical plane $x=1$ for (a) $M=0.5$; (b) $M=0.9$; (c) $M=1.1$; (d) $M=2$

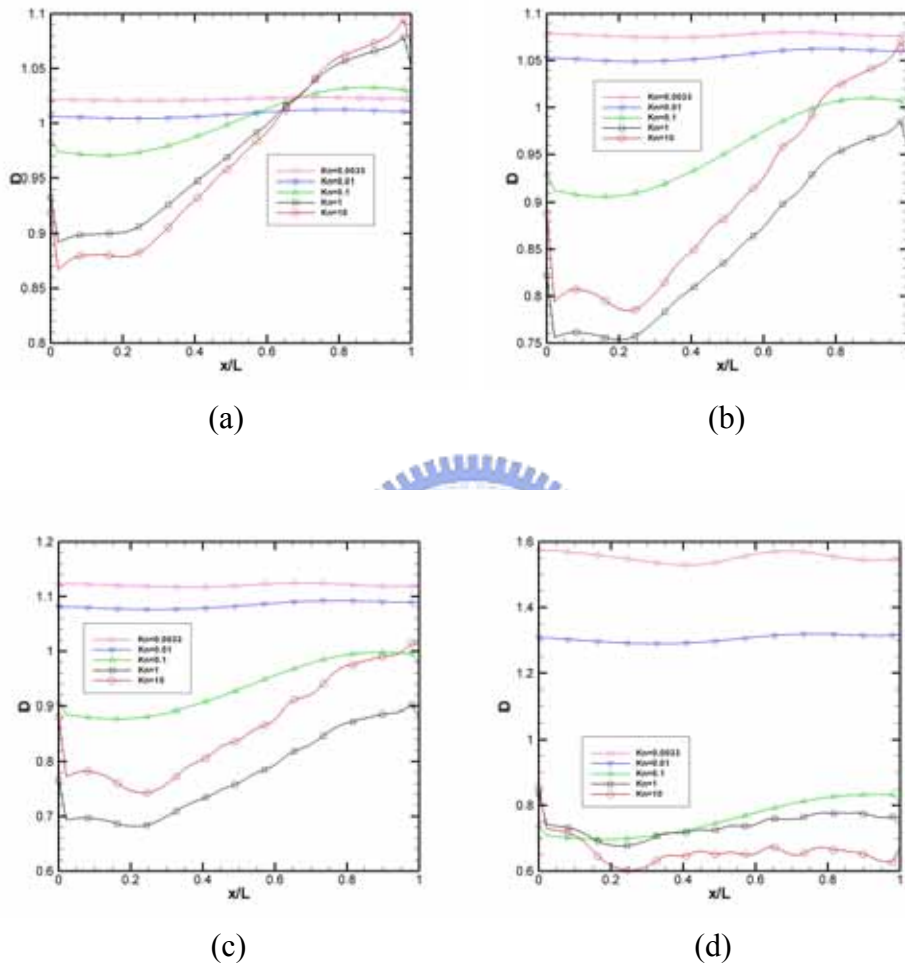


Fig. 3.43 Profile of the number Density on a horizontal plane $y=-1$ for (a) $M=0.5$; (b) $M=0.9$; (c) $M=1.1$; (d) $M=2$

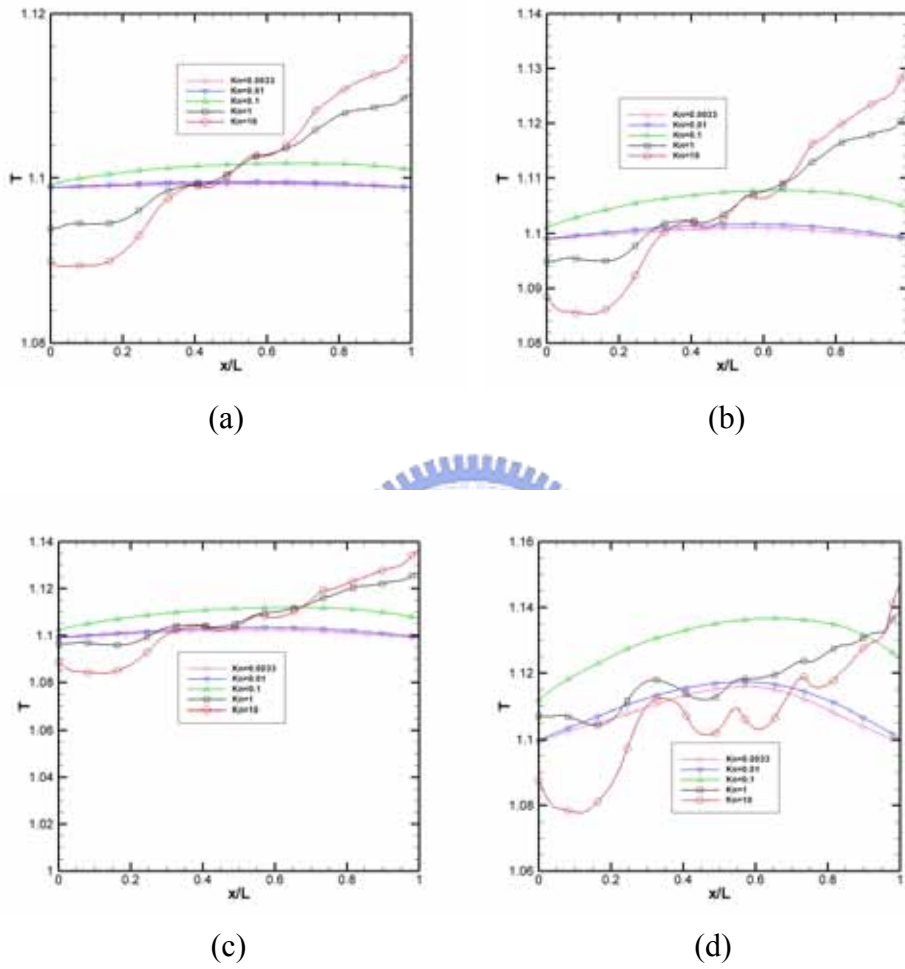


Fig. 3.44 Profile of the Temperature on a horizontal plane $y=-1$ for (a) $M=0.5$; (b) $M=0.9$; (c) $M=1.1$; (d) $M=2$

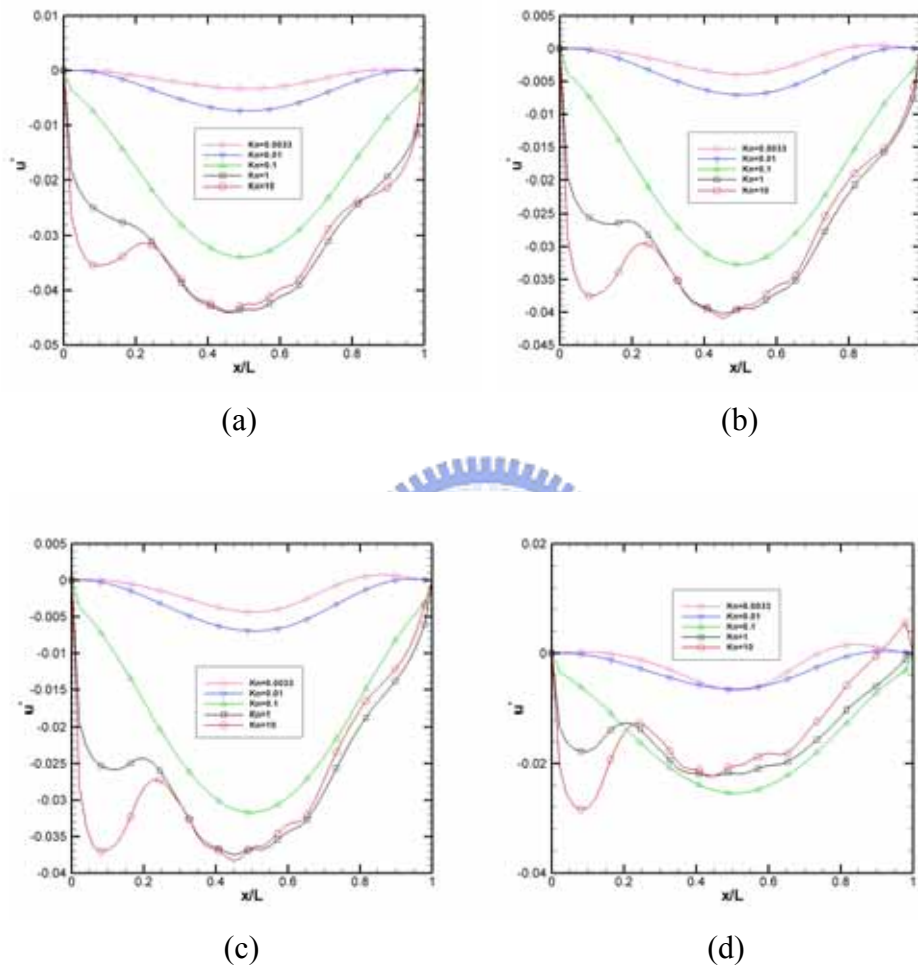


Fig. 3.45 Profile of the U-velocity on a horizontal plane $y=-1$ for (a) $M=0.5$; (b) $M=0.9$; (c) $M=1.1$; (d) $M=2$

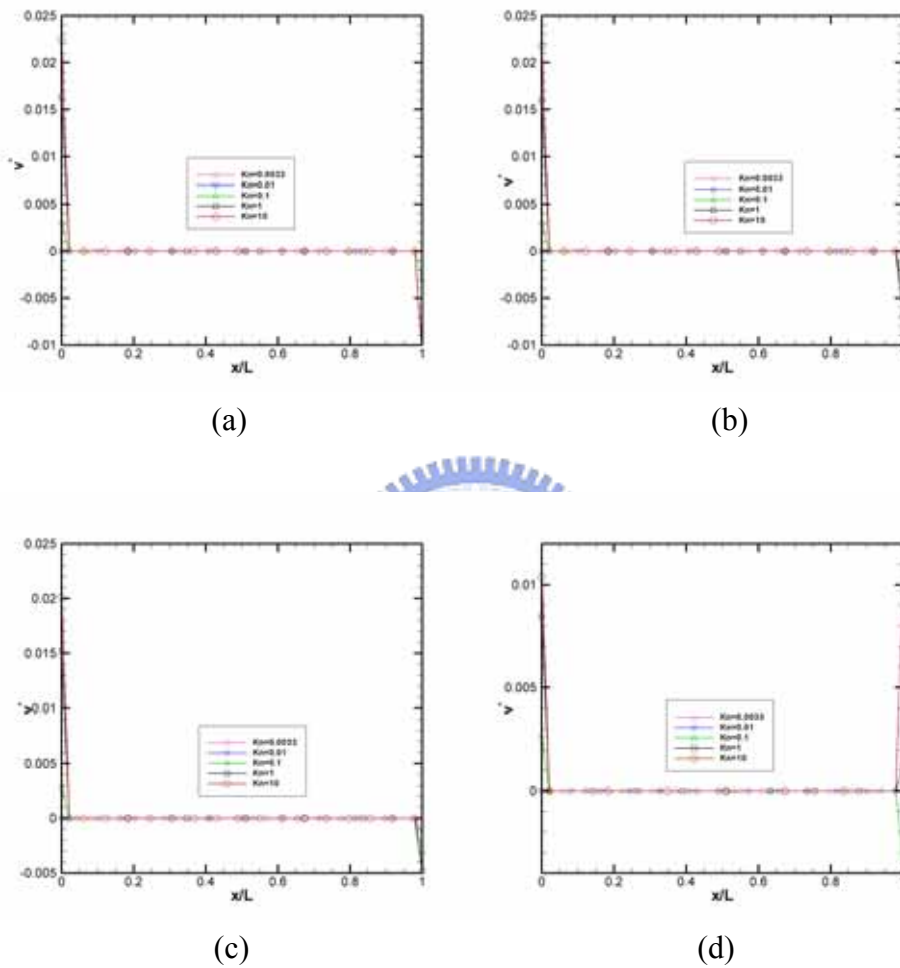


Fig. 3.46 Profile of the V-velocity on a horizontal plane $y=-1$ for (a) $M=0.5$; (b) $M=0.9$; (c) $M=1.1$; (d) $M=2$

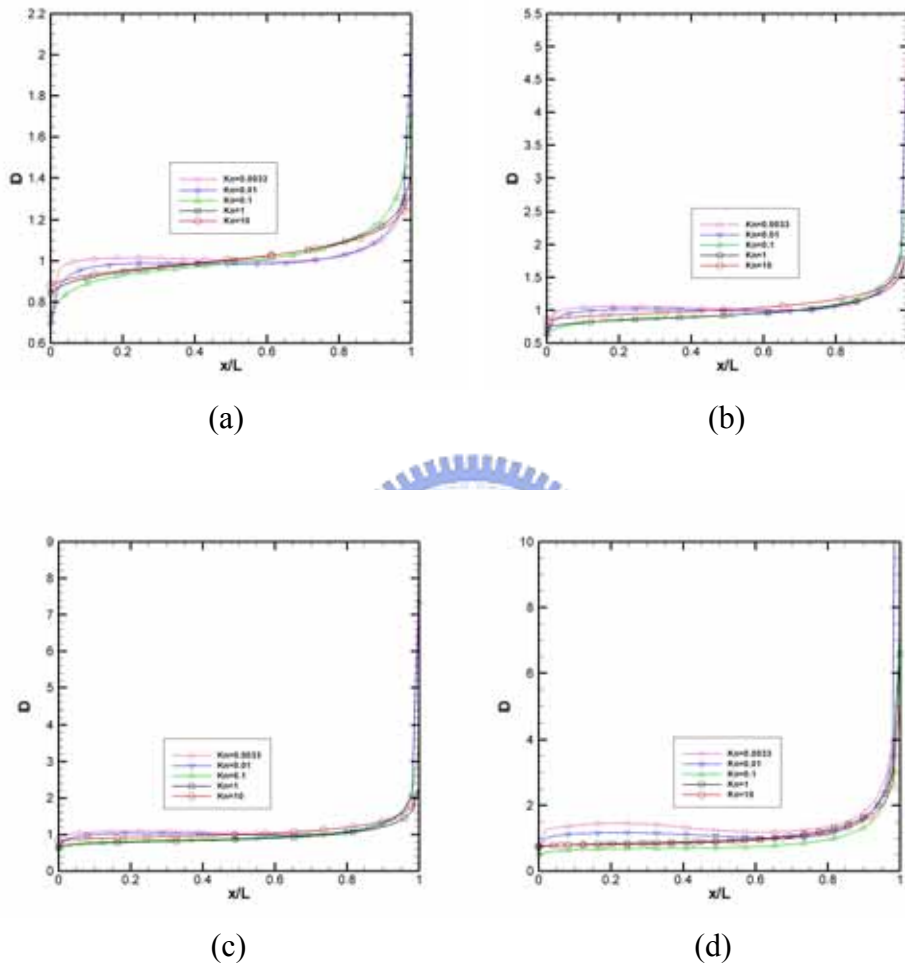


Fig. 3.47 Profile of the number Density on a horizontal plane $y=0$ for (a) $M=0.5$; (b) $M=0.9$; (c) $M=1.1$; (d) $M=2$

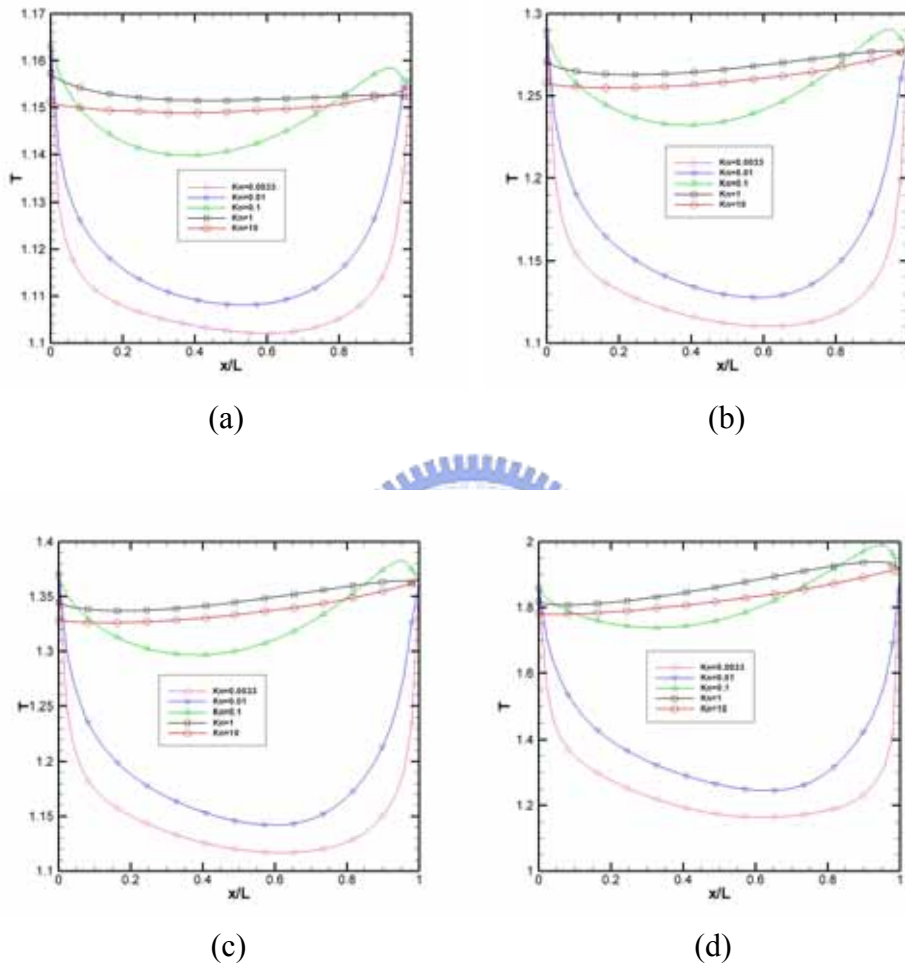


Fig. 3.48 Profile of the Temperature on a horizontal plane $y=0$ for (a) $M=0.5$; (b) $M=0.9$; (c) $M=1.1$; (d) $M=2$

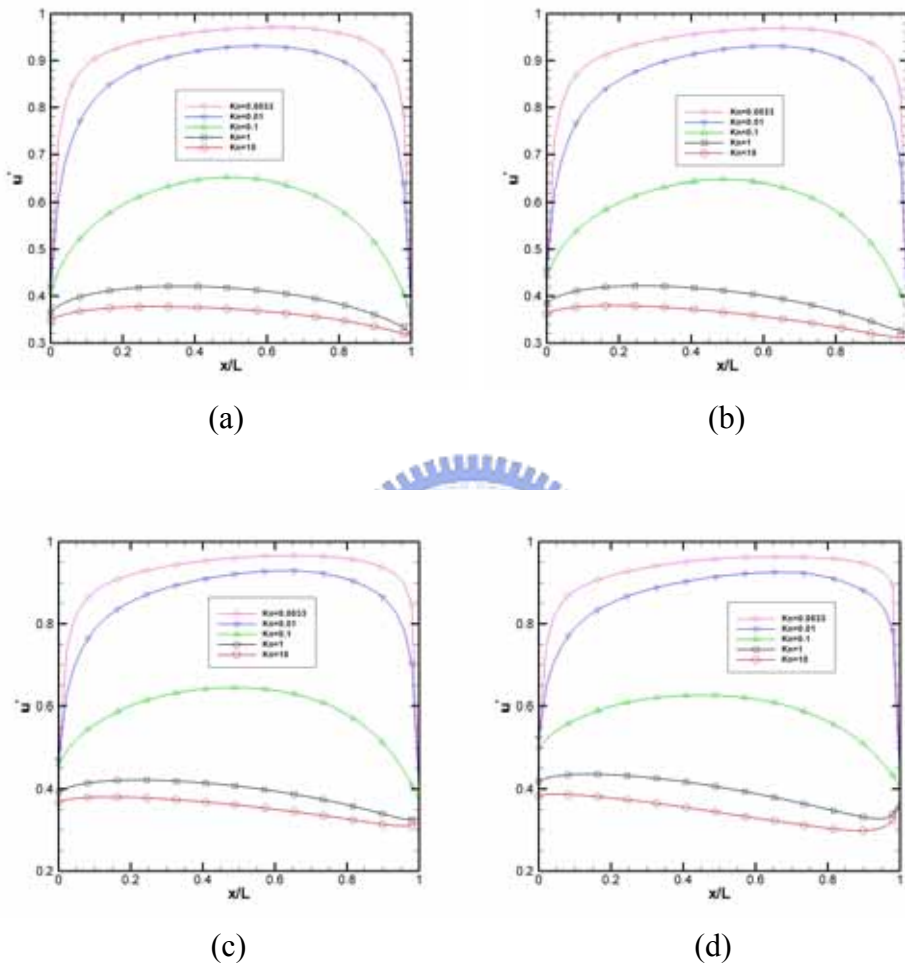
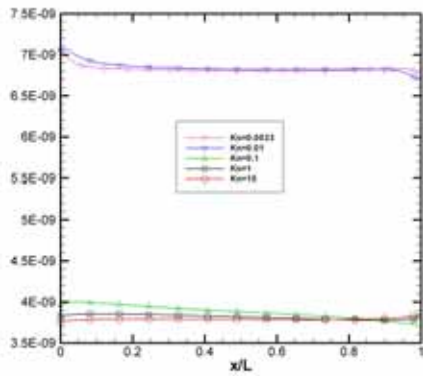
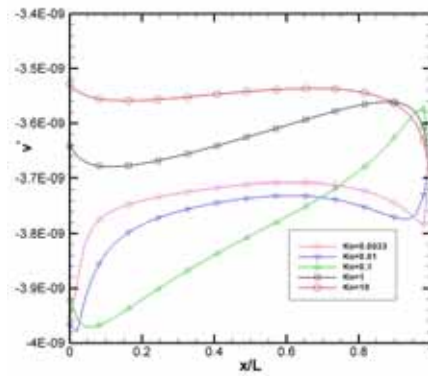


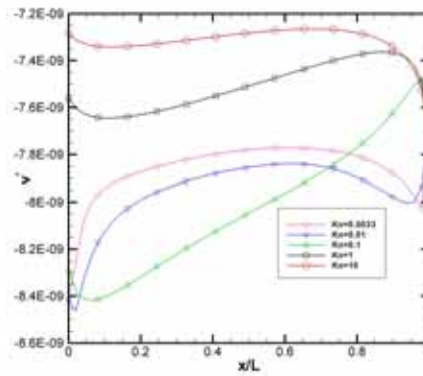
Fig. 3.49 Profile of the U-velocity on a horizontal plane $y=0$ for (a) $M=0.5$; (b) $M=0.9$; (c) $M=1.1$; (d) $M=2$



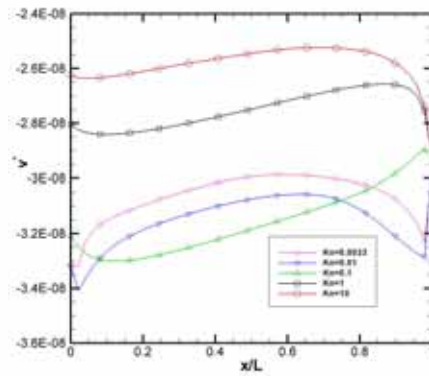
(a)



(b)

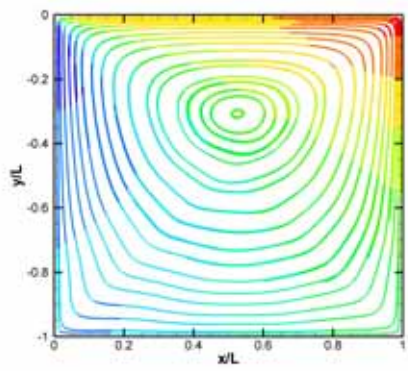


(c)

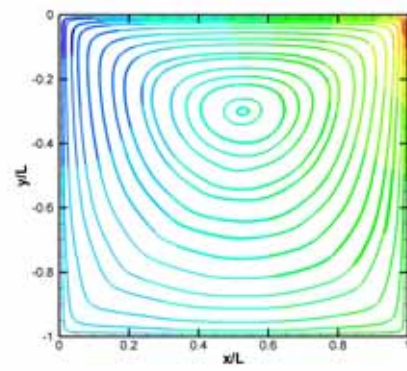


(d)

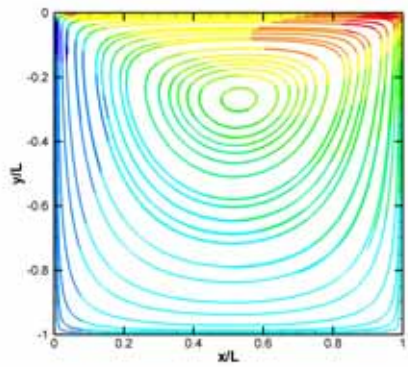
Fig. 3.50 Profile of the V-velocity on a horizontal plane $y=0$ for (a) $M=0.5$; (b) $M=0.9$; (c) $M=1.1$; (d) $M=2$



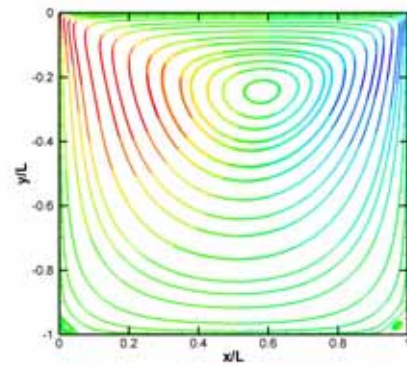
(a)



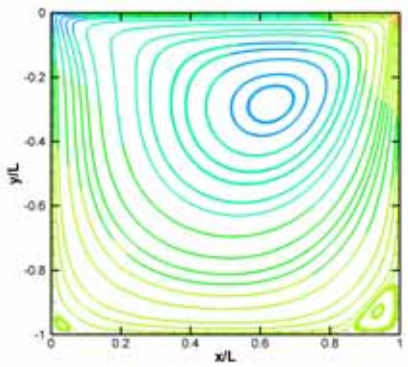
(b)



(c)



(d)



(e)

Fig. 3.51 Velocity streamlines for $M=0.5$, and (a) $Kn=10$; (b) $Kn=1$; (c) $Kn=0.1$; (d) $Kn=0.01$; (e) $Kn=0.0033$

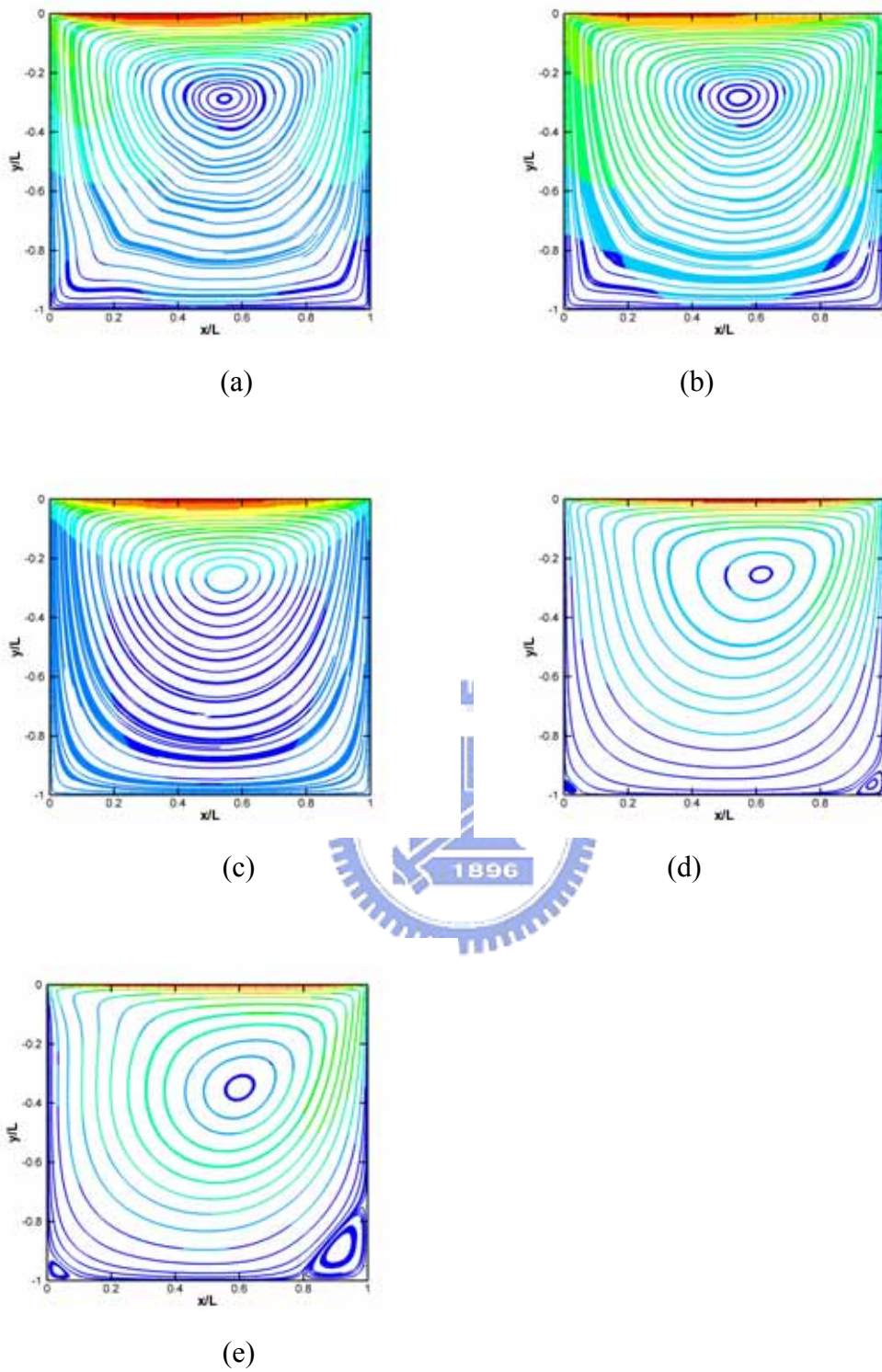


Fig. 3.52 Velocity streamlines for $M=0.9$, and (a) $Kn=10$; (b) $Kn=1$; (c) $Kn=0.1$; (d) $Kn=0.01$; (e) $Kn=0.0033$

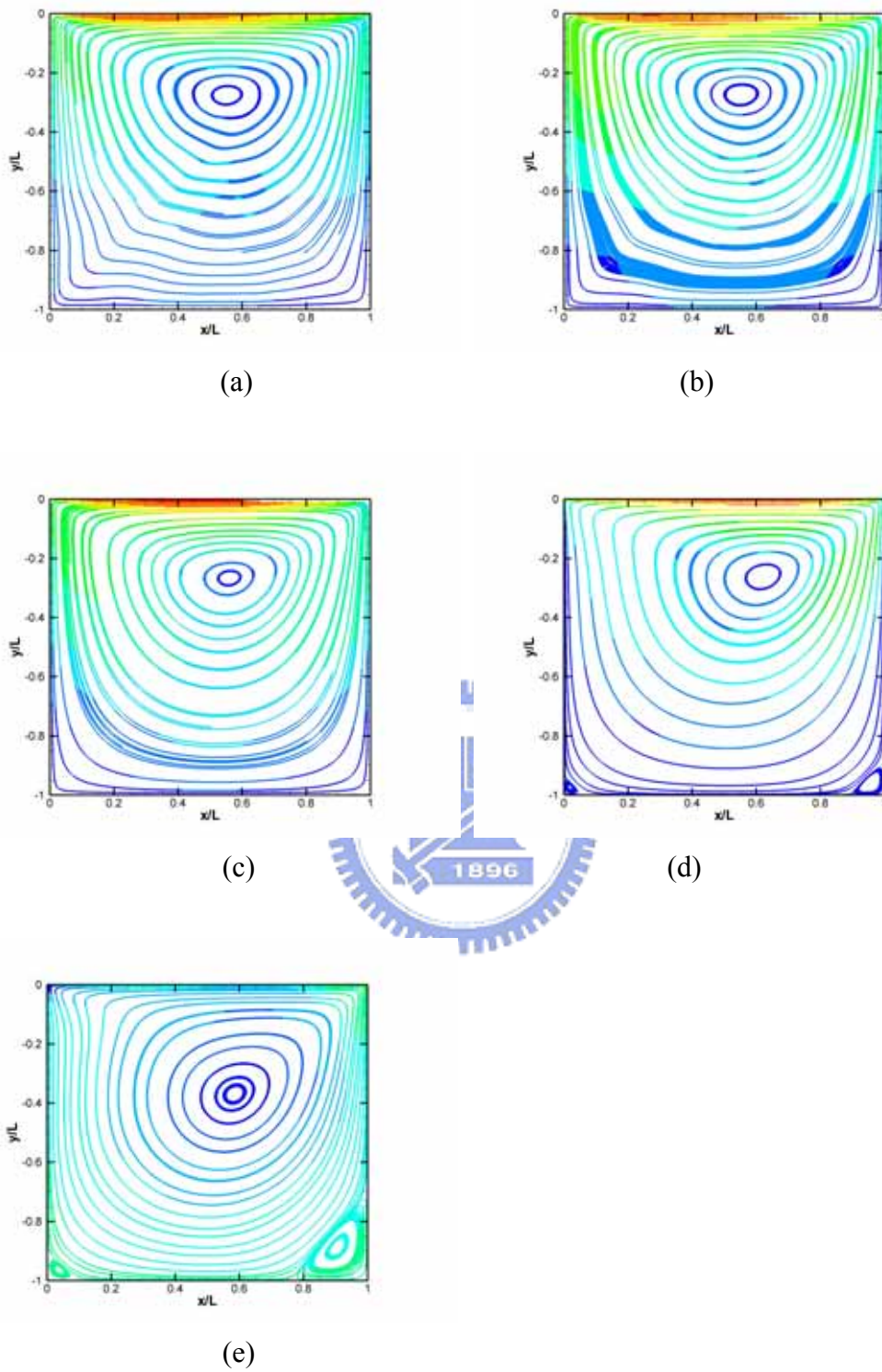


Fig. 3.53 Velocity streamlines for $M=1.1$, and (a) $Kn=10$; (b) $Kn=1$; (c) $Kn=0.1$; (d) $Kn=0.01$; (e) $Kn=0.0033$

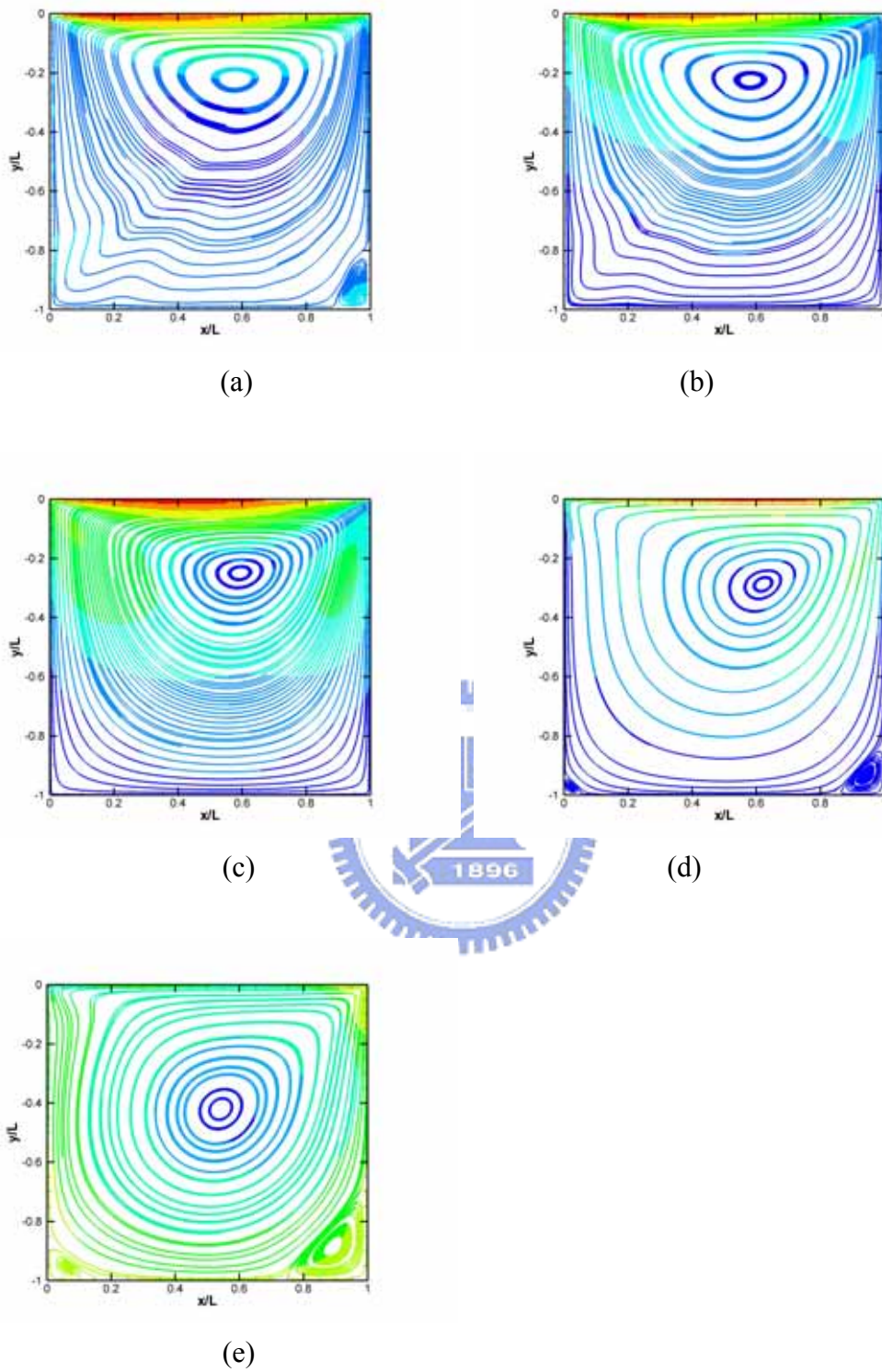


Fig. 3.54 Velocity streamlines for $M=2$, and (a) $Kn=10$; (b) $Kn=1$; (c) $Kn=0.1$; (d) $Kn=0.01$; (e) $Kn=0.0033$

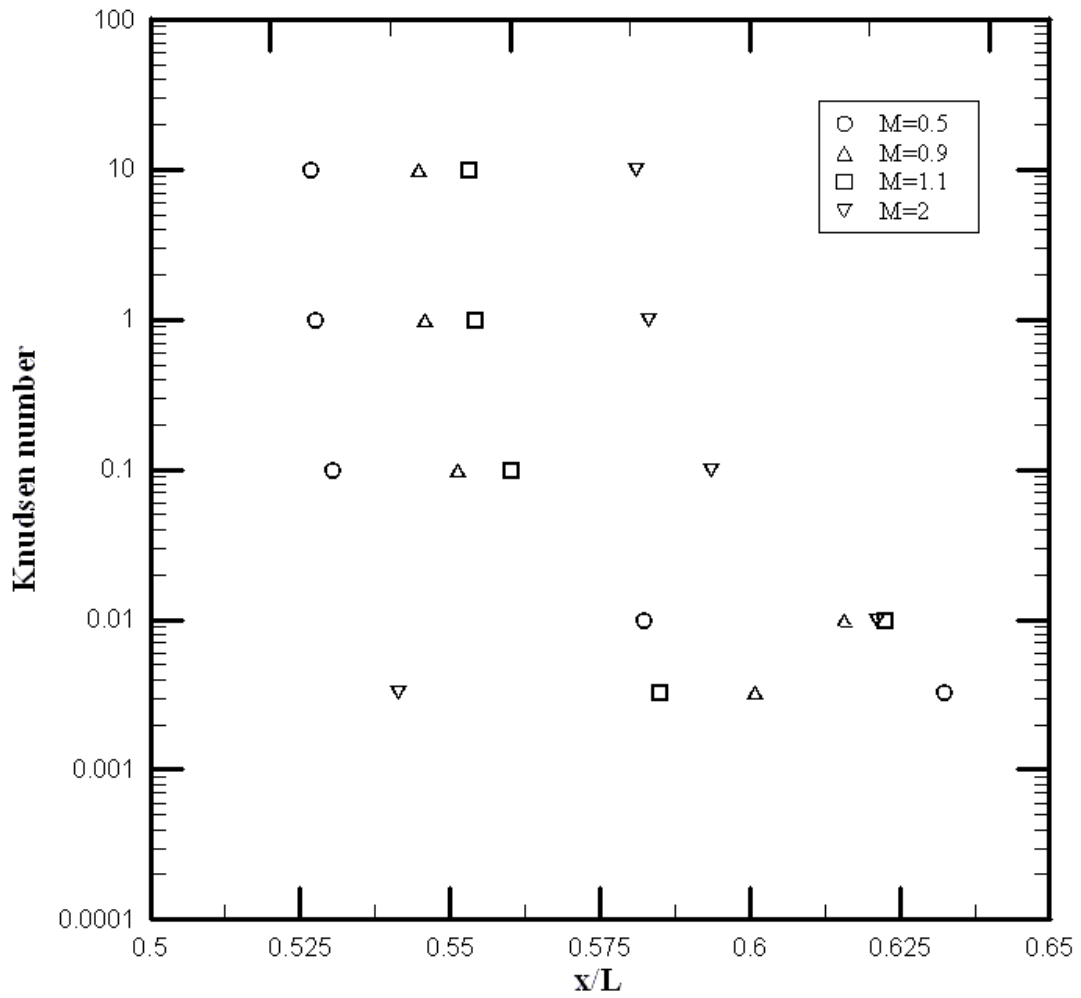


Fig. 3.55 Location of the center for x/L of the top vortex for various values of Mach number and Knudsen number.

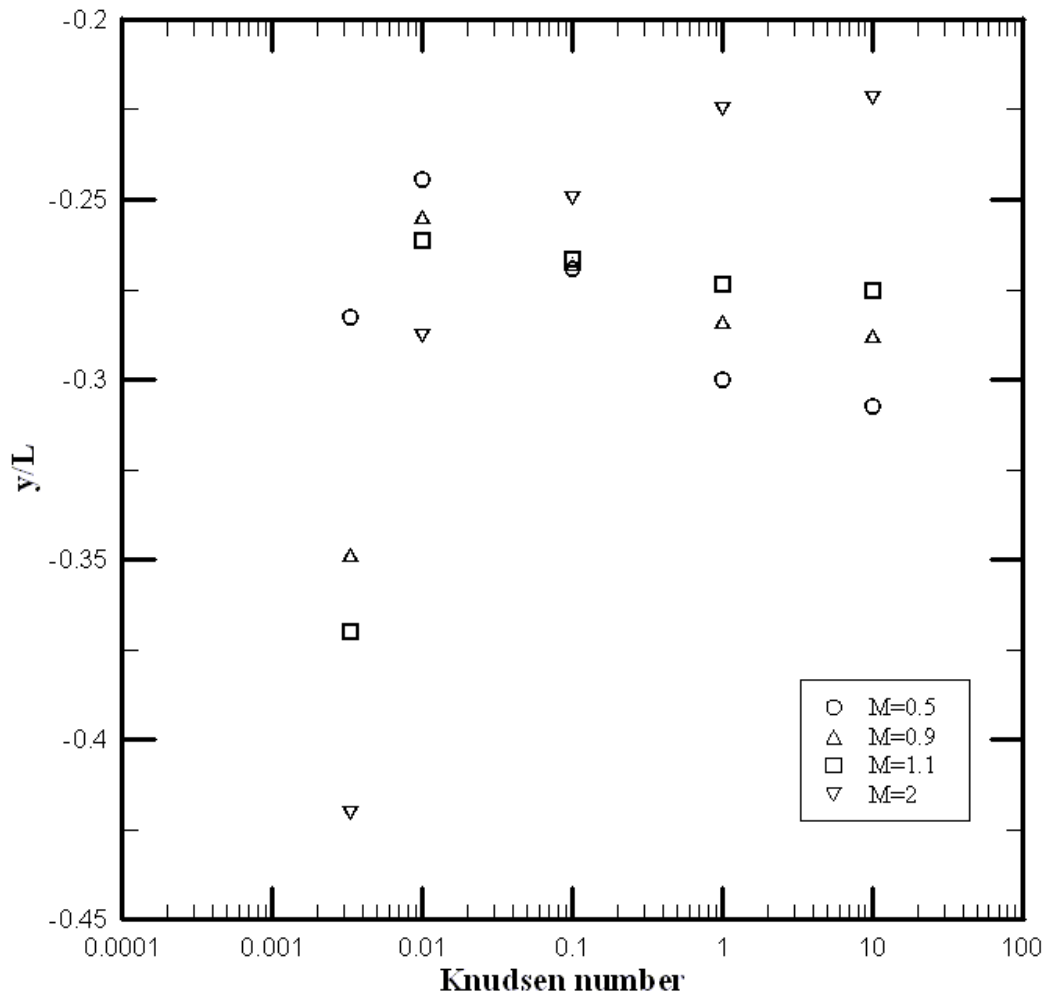


Fig. 3.56 Location of the center for y/L of the top vortex for various values of Mach number and Knudsen number.

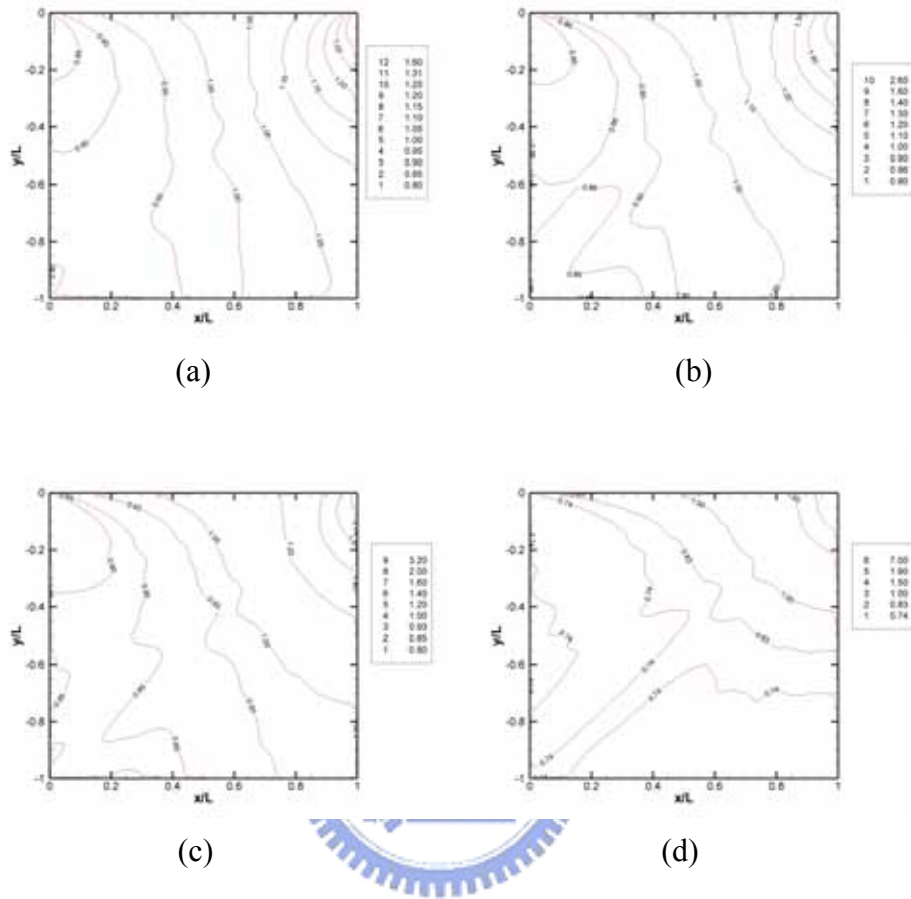


Fig. 3.57 Contours of number Density for $Kn=10$, (a) $M=0.5$; (b) $M=0.9$; (c) $M=1.1$; (d) $M=2.0$

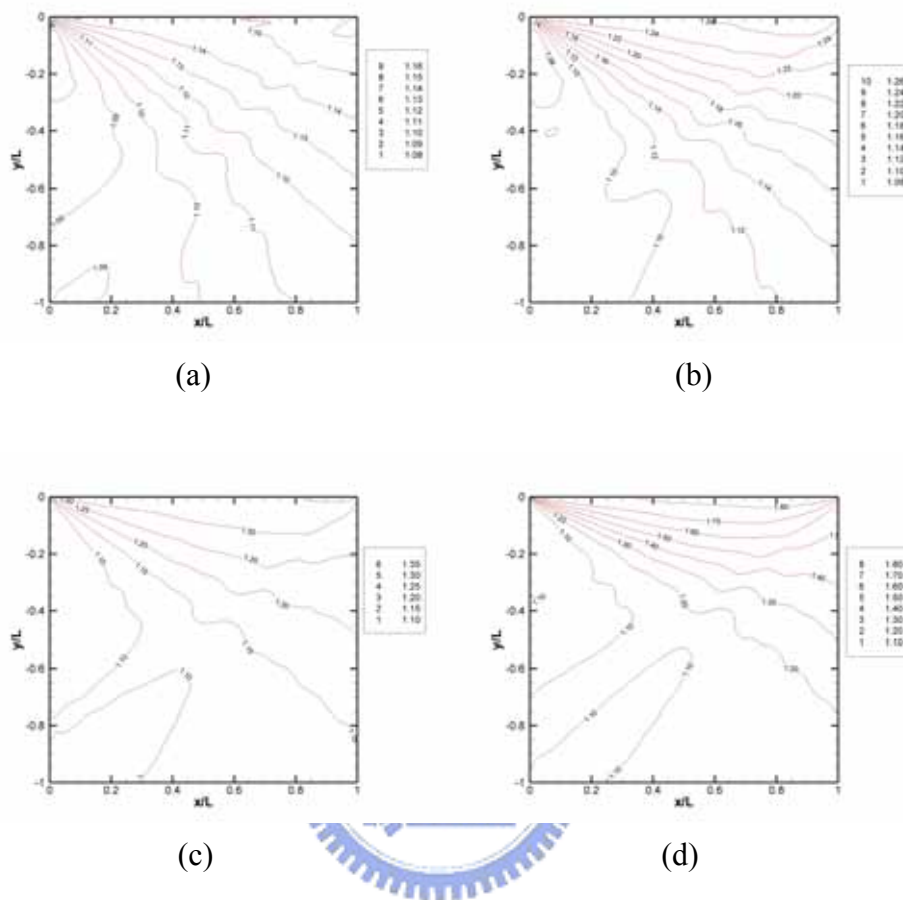


Fig. 3.58 Contours of Temperature for $Kn=10$, (a) $M=0.5$; (b) $M=0.9$; (c) $M=1.1$; (d) $M=2.0$

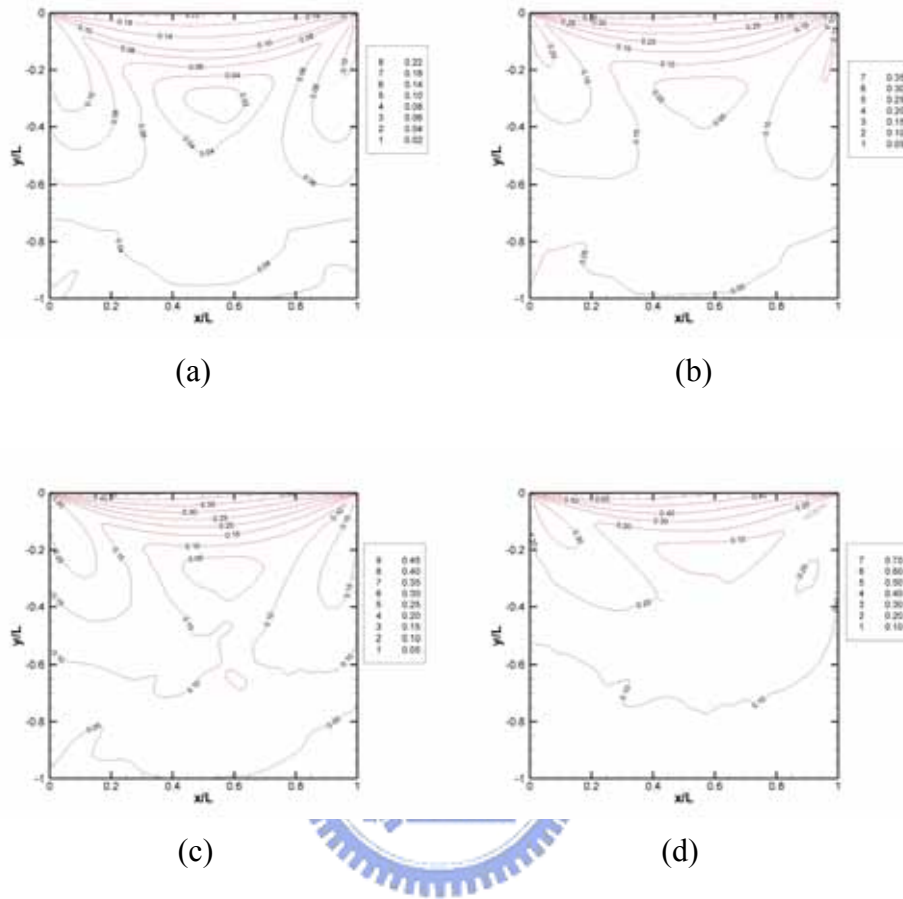


Fig. 3.59 Contours of Mach number for $Kn=10$, (a) $M=0.5$; (b) $M=0.9$; (c) $M=1.1$; (d) $M=2.0$

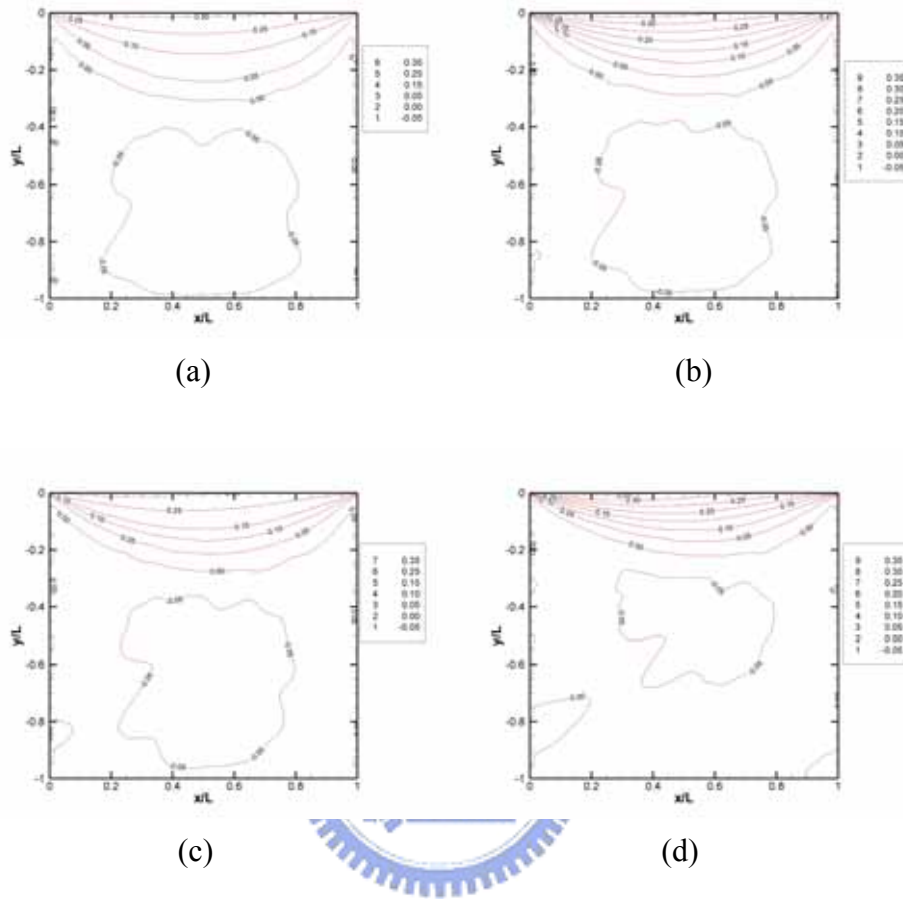


Fig. 3.60 Contours of U-velocity for $Kn=10$, (a) $M=0.5$; (b) $M=0.9$; (c) $M=1.1$; (d) $M=2.0$

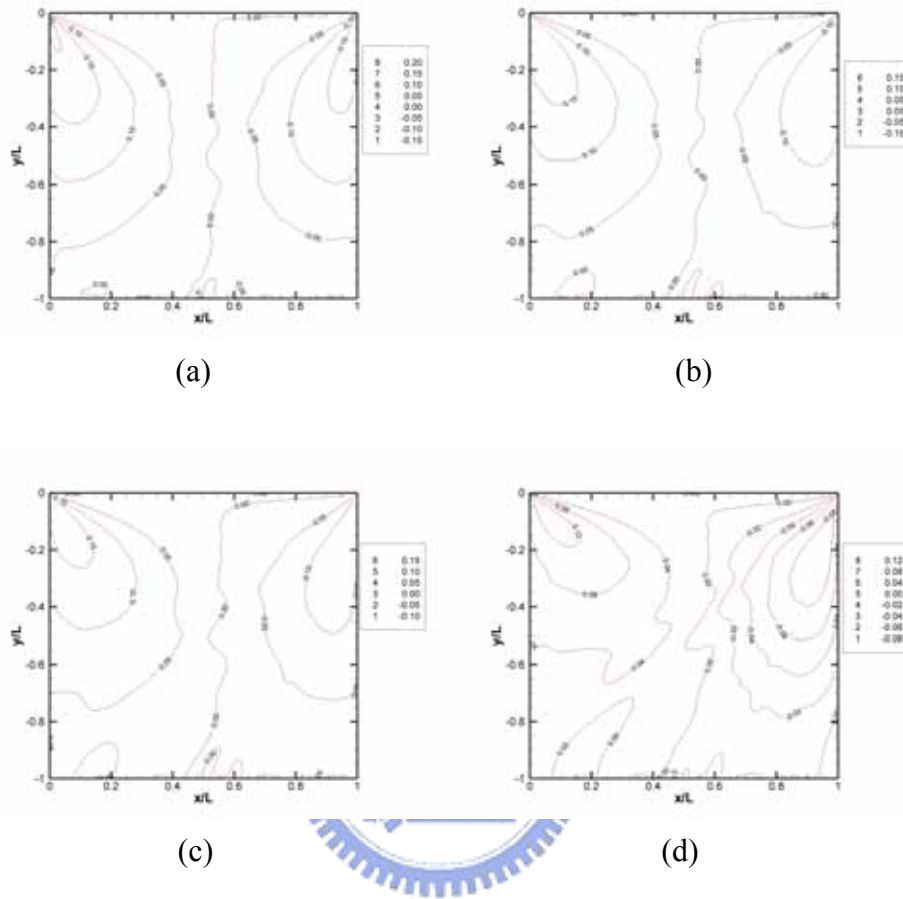


Fig. 3.61 Contours of V-velocity for $Kn=10$, (a) $M=0.5$; (b) $M=0.9$; (c) $M=1.1$; (d) $M=2.0$

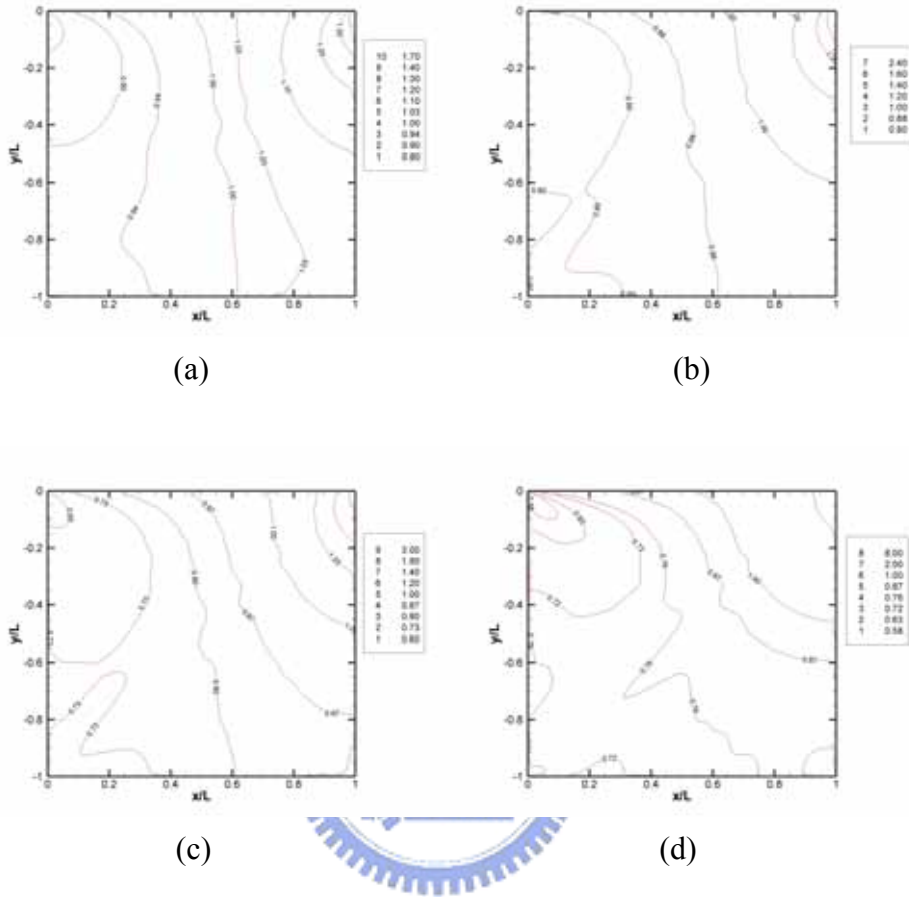


Fig. 3.62 Contours of number Density for $Kn=1$, (a) $M=0.5$; (b) $M=0.9$; (c) $M=1.1$; (d) $M=2.0$

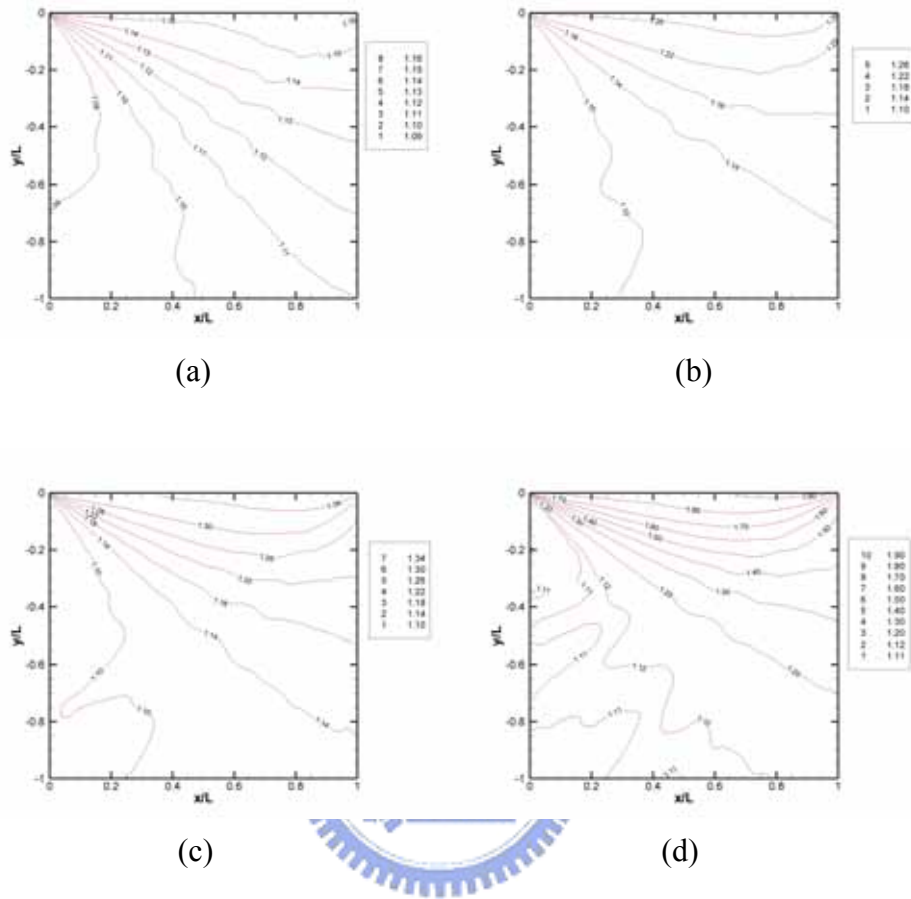


Fig. 3.63 Contours of Temperature for $Kn=1$, (a) $M=0.5$; (b) $M=0.9$; (c) $M=1.1$; (d) $M=2.0$

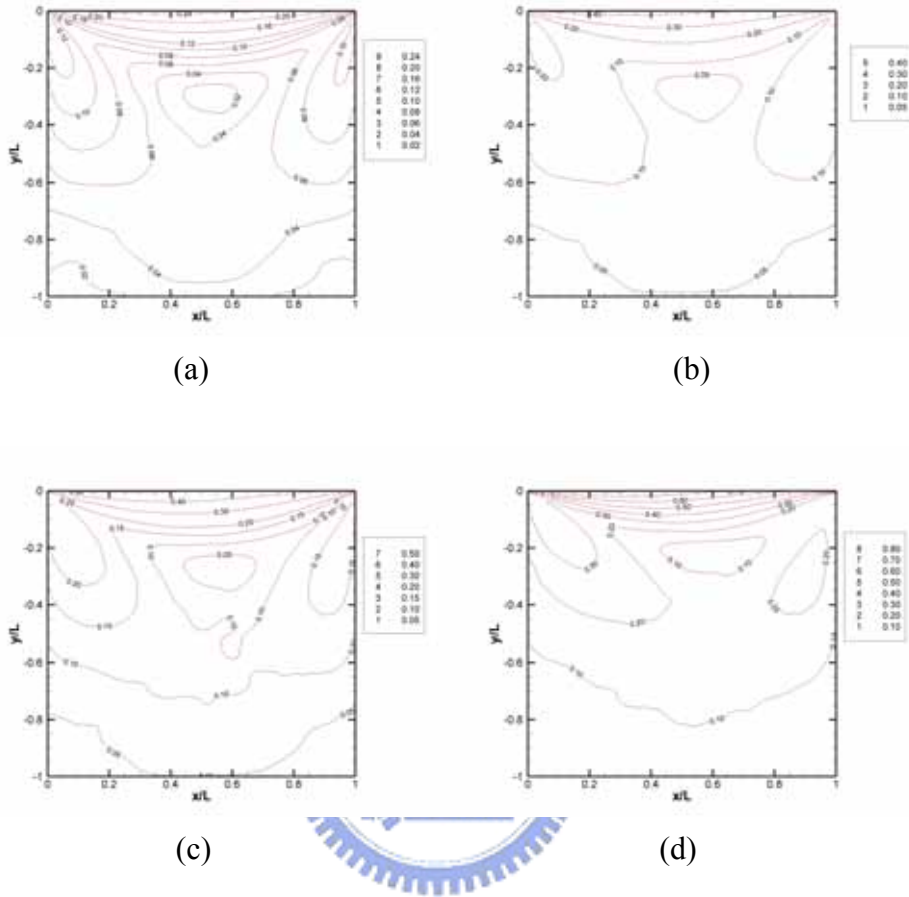


Fig. 3.64 Contours of Mach number for $Kn=1$, (a) $M=0.5$; (b) $M=0.9$; (c) $M=1.1$; (d) $M=2.0$

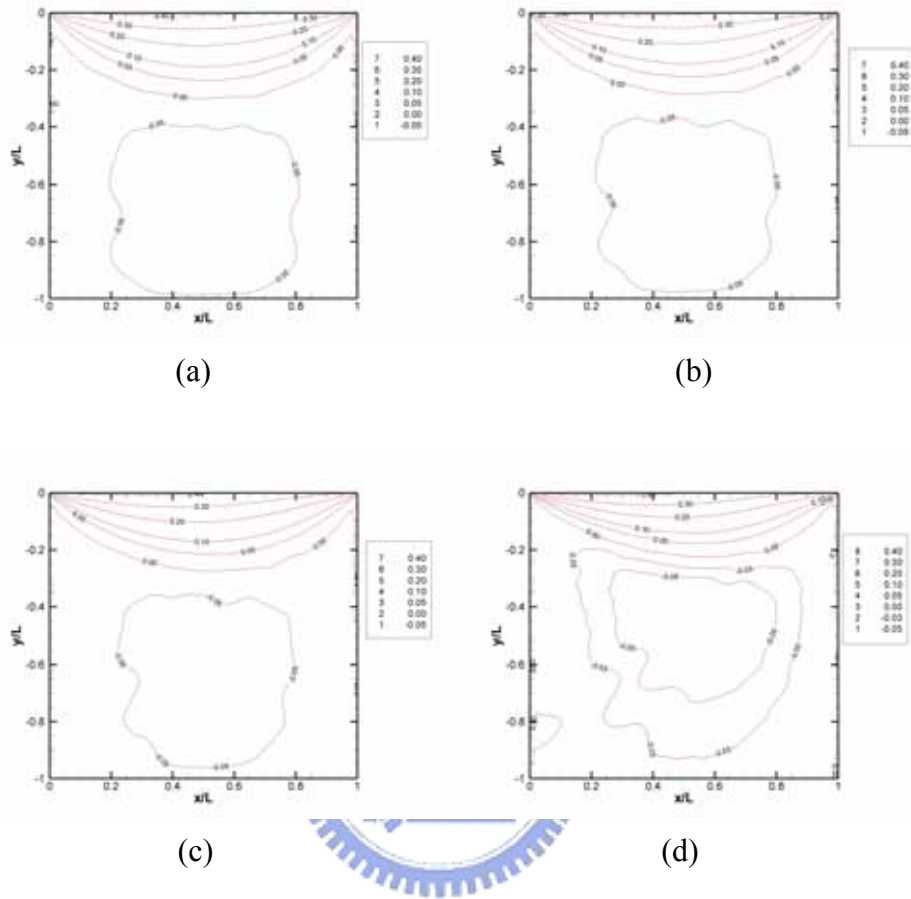


Fig. 3.65 Contours of U-velocity for $Kn=1$, (a) $M=0.5$; (b) $M=0.9$; (c) $M=1.1$; (d) $M=2.0$

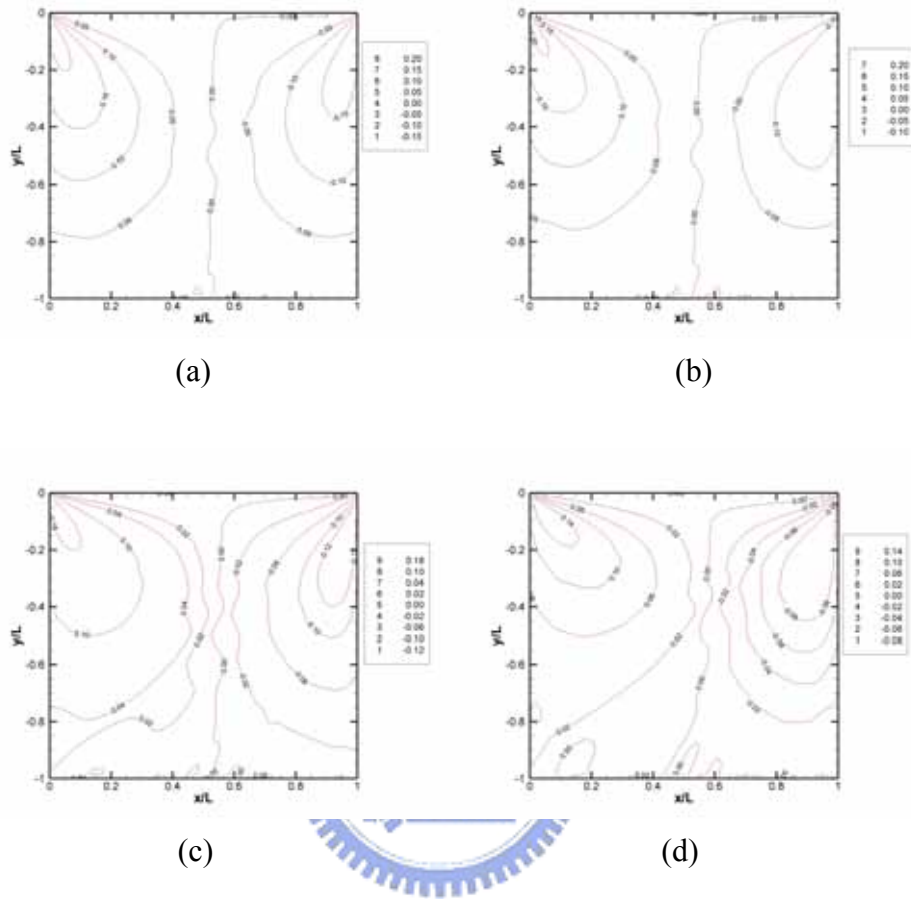


Fig. 3.66 Contours of V-velocity for $Kn=1$, (a) $M=0.5$; (b) $M=0.9$; (c) $M=1.1$; (d) $M=2.0$

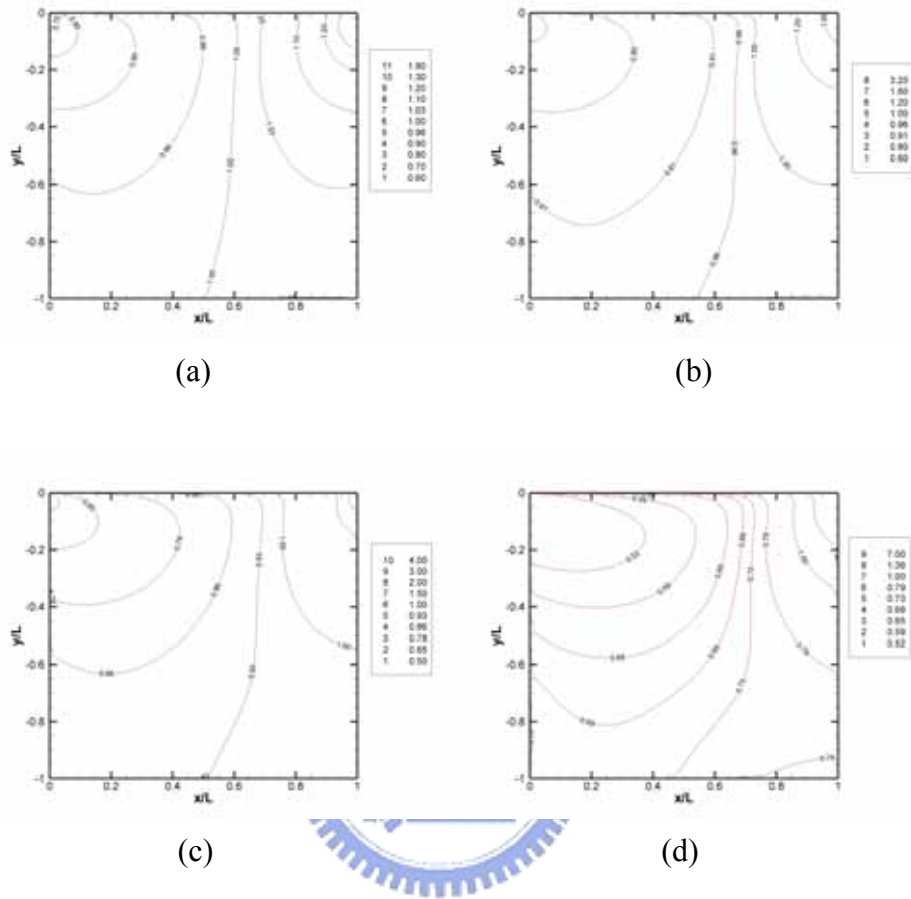


Fig. 3.67 Contours of number Density for $Kn=0.1$, (a) $M=0.5$; (b) $M=0.9$; (c) $M=1.1$; (d) $M=2.0$

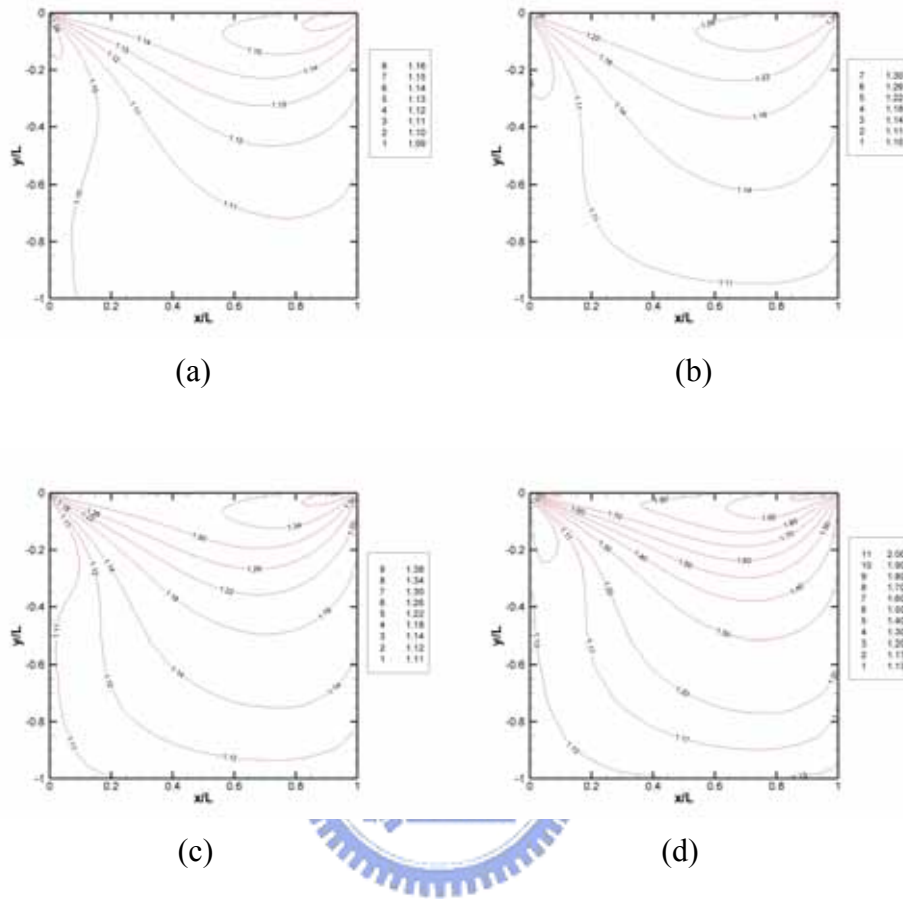


Fig. 3.68 Contours of Temperature for $Kn=0.1$, (a) $M=0.5$; (b) $M=0.9$; (c) $M=1.1$; (d) $M=2.0$

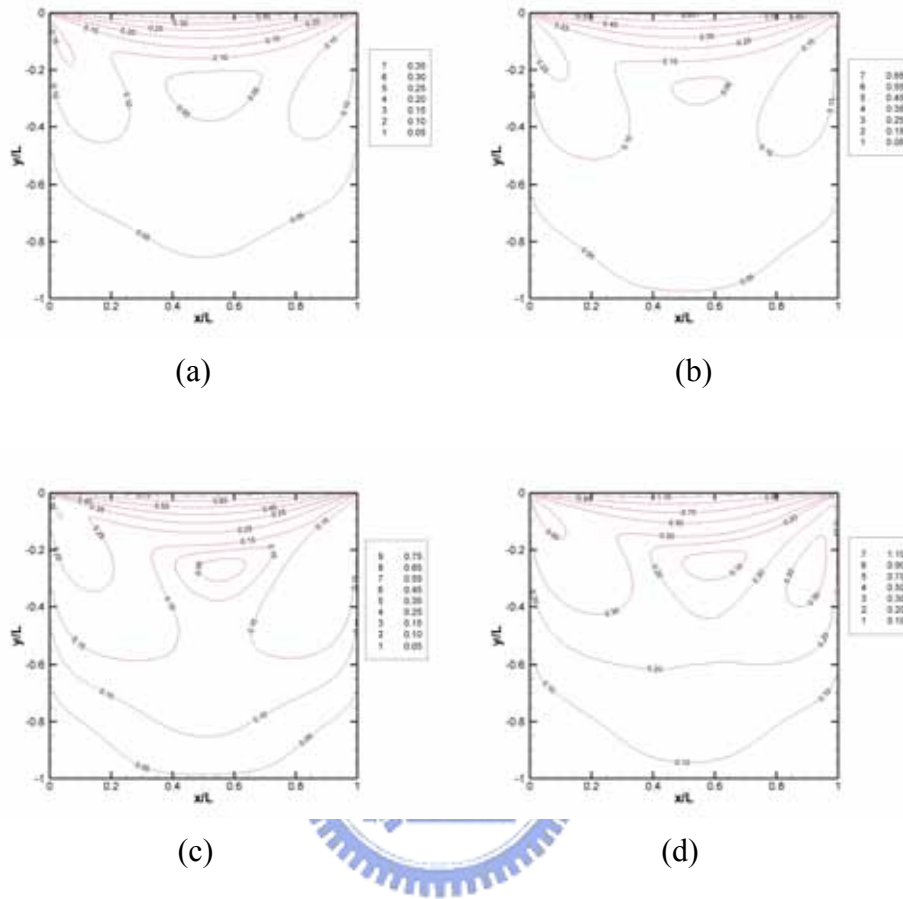


Fig. 3.69 Contours of Mach number for $Kn=0.1$, (a) $M=0.5$; (b) $M=0.9$; (c) $M=1.1$; (d) $M=2.0$

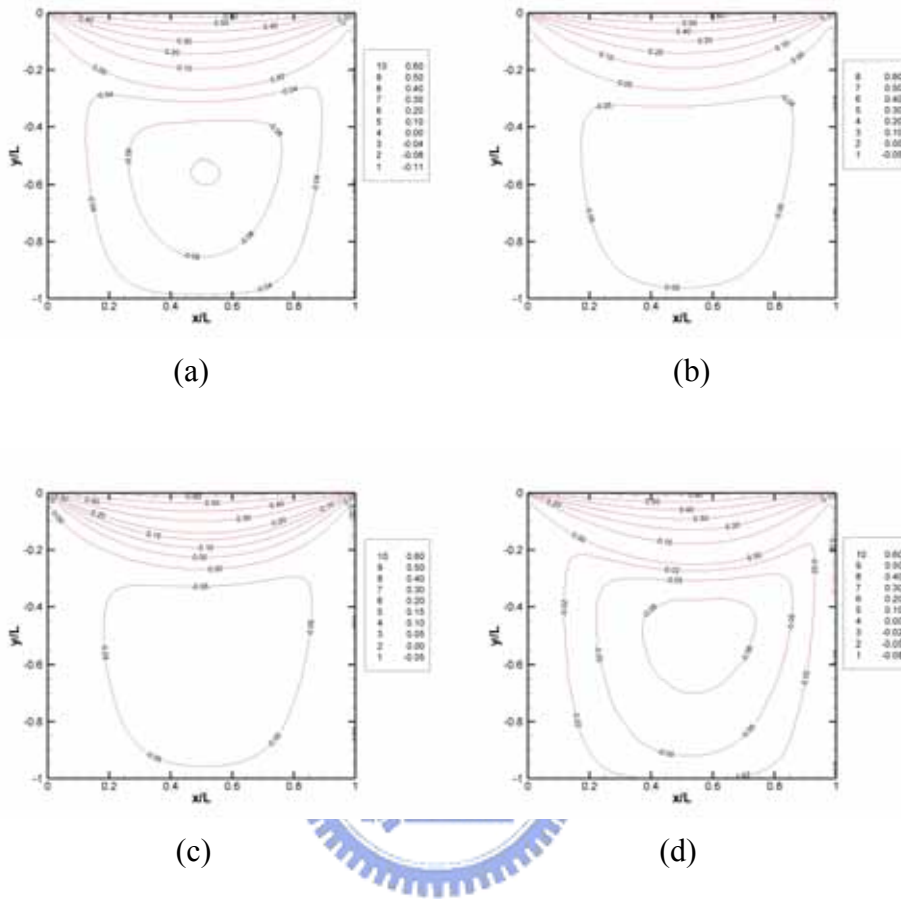


Fig. 3.70 Contours of U-velocity for $Kn=0.1$, (a) $M=0.5$; (b) $M=0.9$; (c) $M=1.1$; (d) $M=2.0$

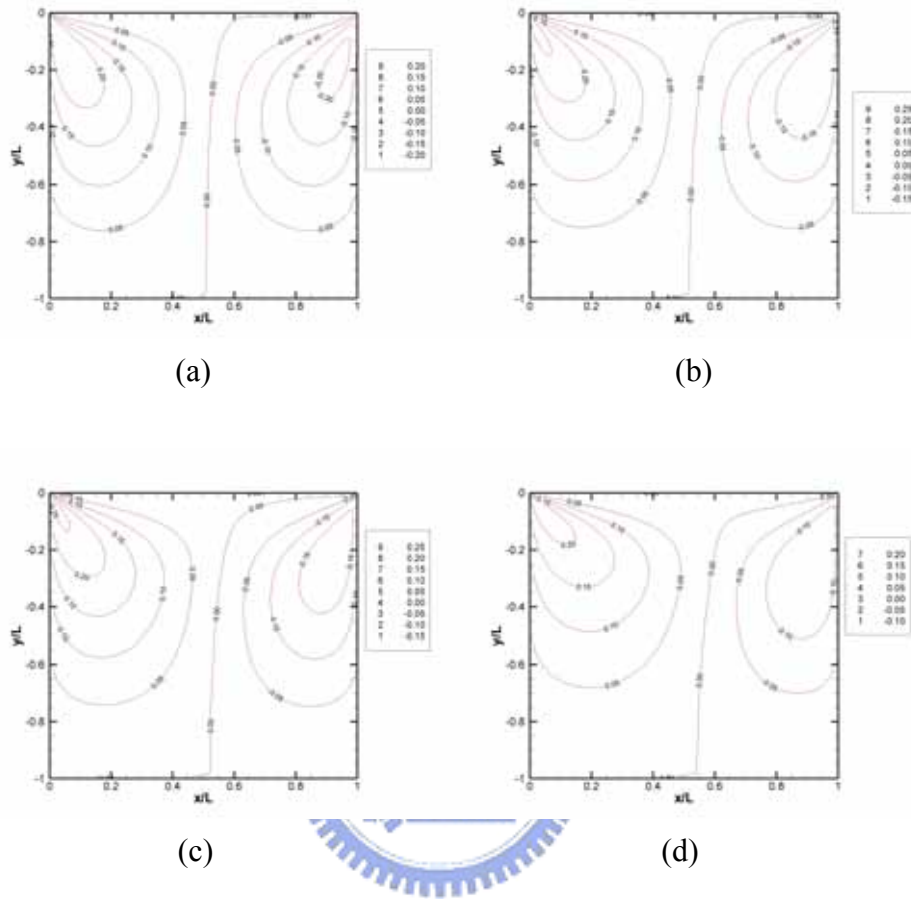


Fig. 3.71 Contours of V-velocity for $Kn=0.1$, (a) $M=0.5$; (b) $M=0.9$; (c) $M=1.1$; (d) $M=2.0$

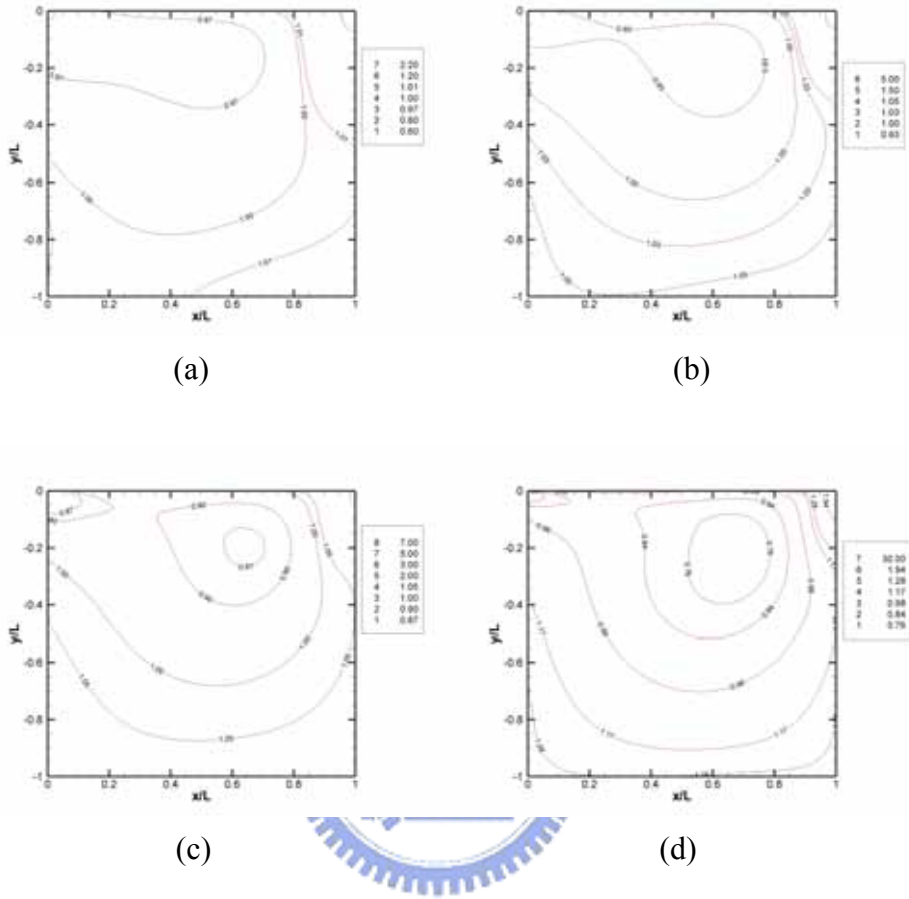


Fig. 3.72 Contours of number Density for $Kn=0.01$, (a) $M=0.5$; (b) $M=0.9$; (c) $M=1.1$; (d) $M=2.0$

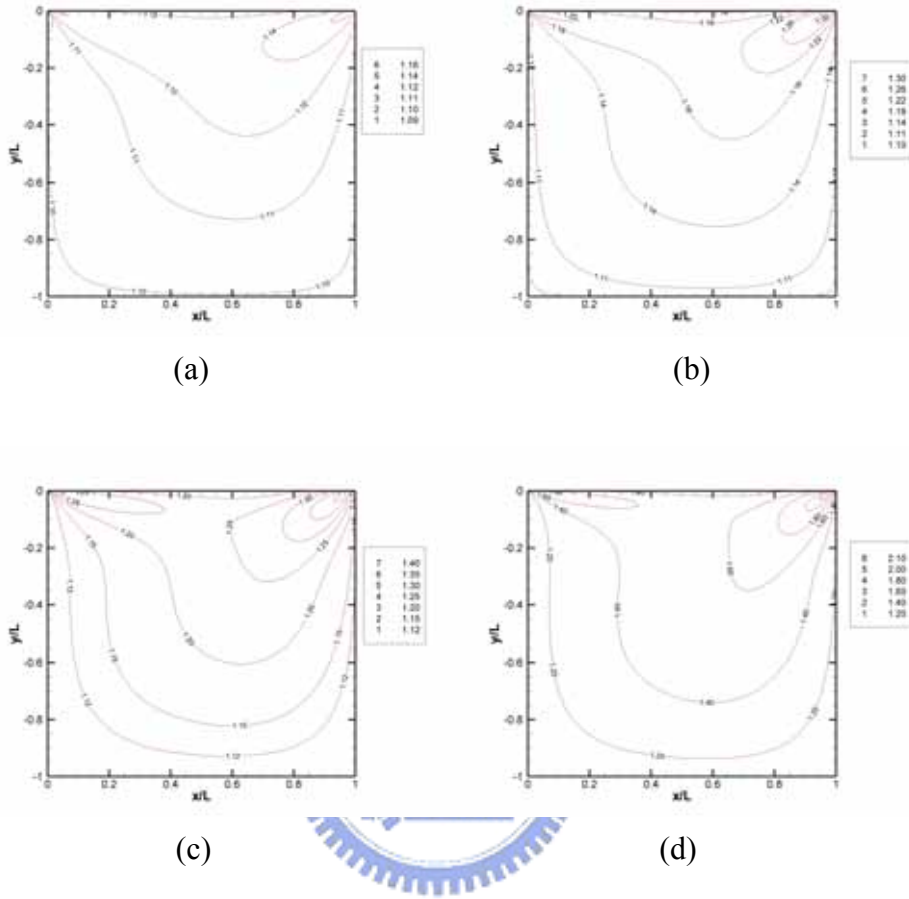


Fig. 3.73 Contours of Temperature for $Kn=0.01$, (a) $M=0.5$; (b) $M=0.9$; (c) $M=1.1$; (d) $M=2.0$

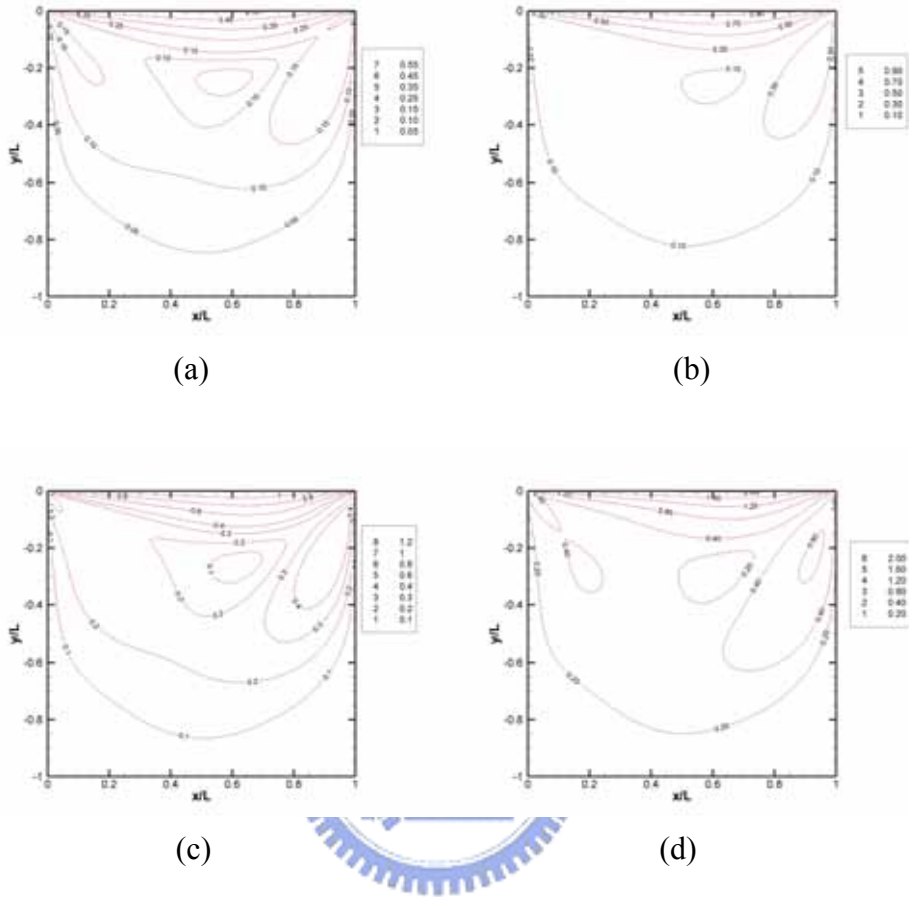


Fig. 3.74 Contours of Mach number for $Kn=0.01$, (a) $M=0.5$; (b) $M=0.9$; (c) $M=1.1$; (d) $M=2.0$

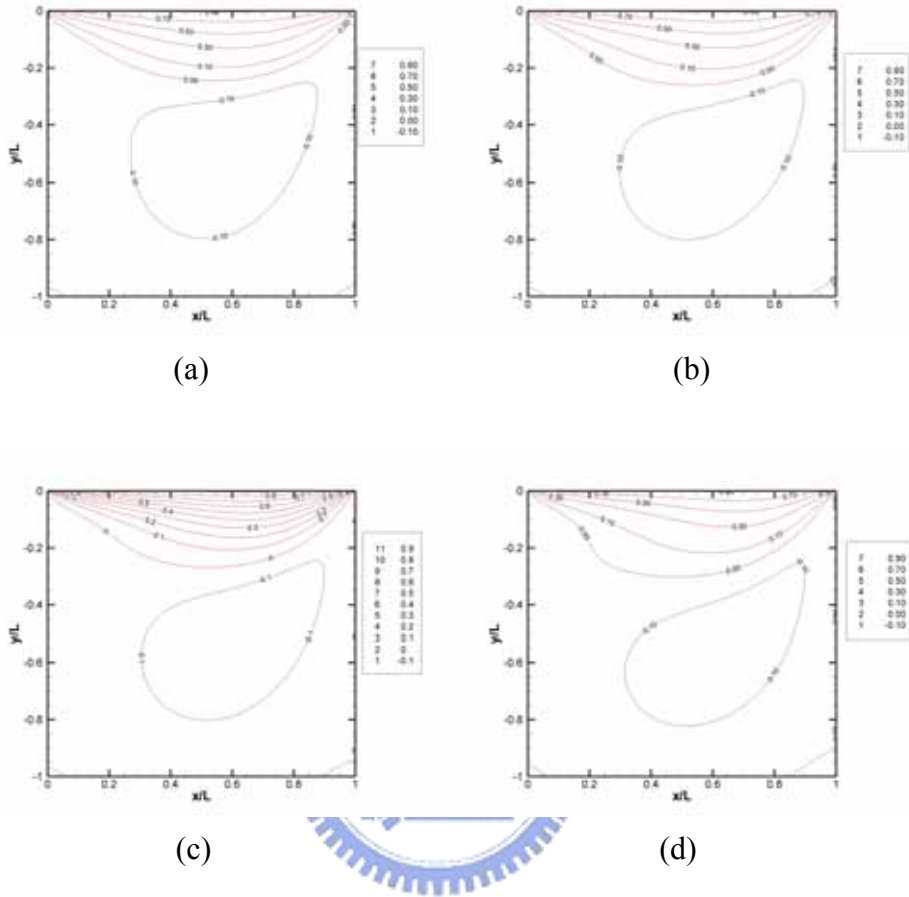


Fig. 3.75 Contours of U-velocity for Kn=0.01, (a) M=0.5; (b) M=0.9; (c) M=1.1; (d) M=2.0

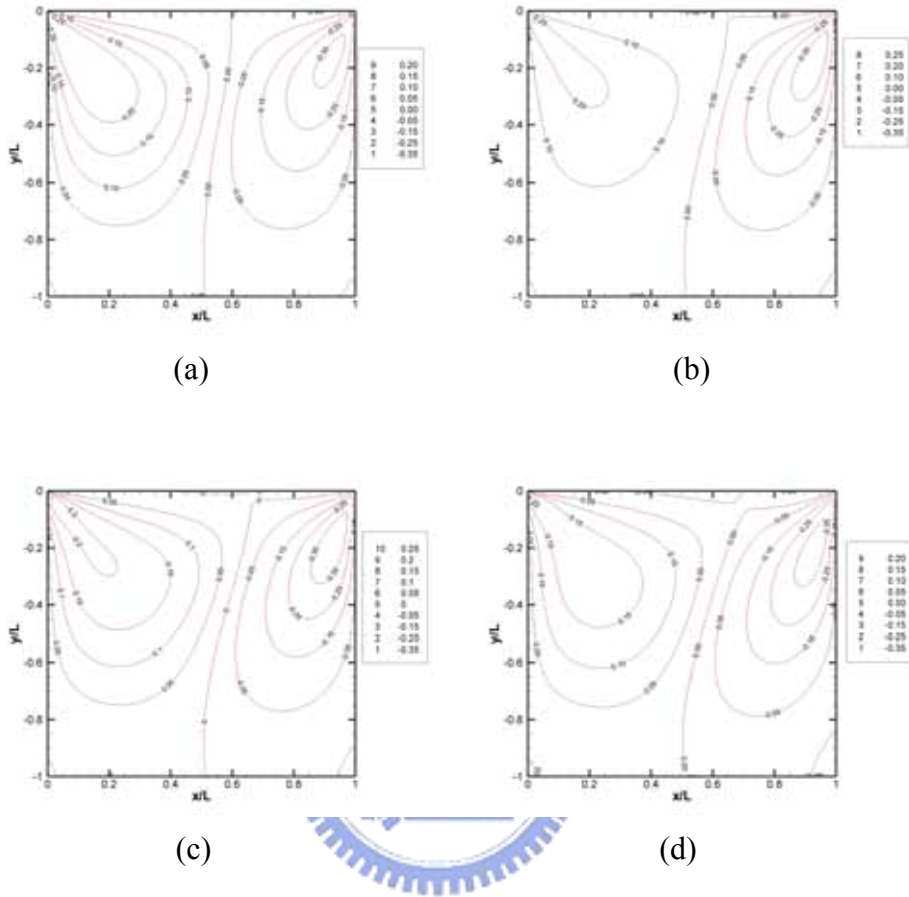


Fig. 3.76 Contours of V-velocity for $Kn=0.01$, (a) $M=0.5$; (b) $M=0.9$; (c) $M=1.1$; (d) $M=2.0$

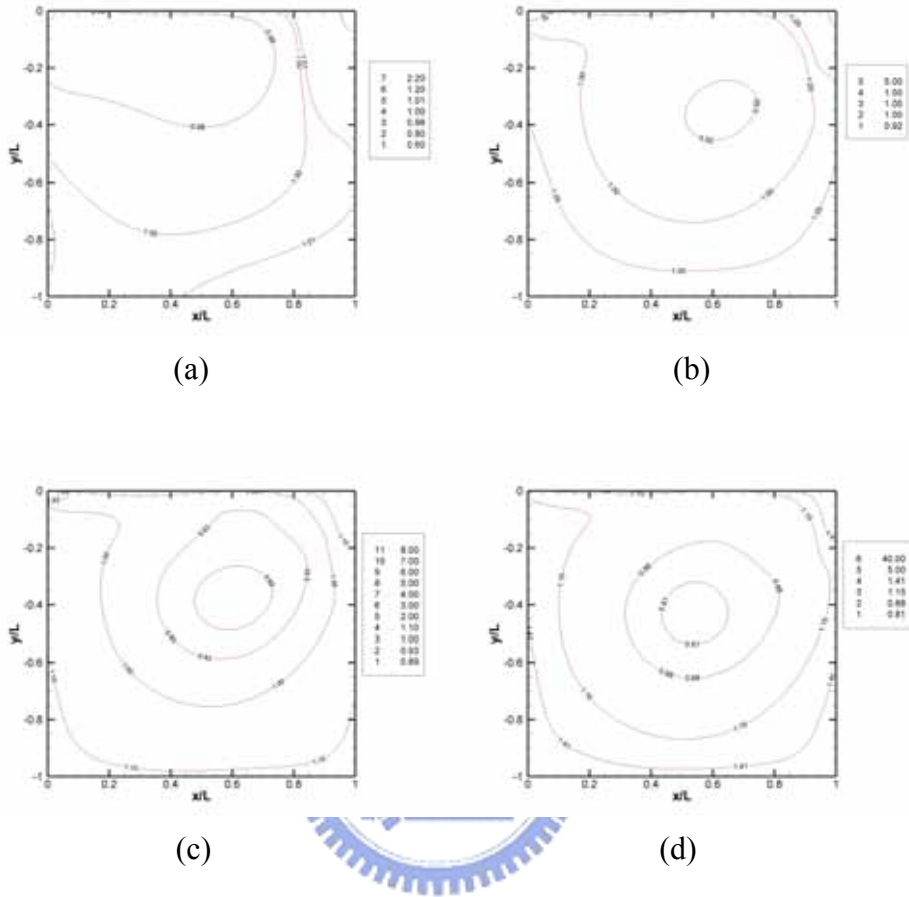


Fig. 3.77 Contours of number Density for $Kn=0.0033$, (a) $M=0.5$; (b) $M=0.9$; (c) $M=1.1$; (d) $M=2.0$

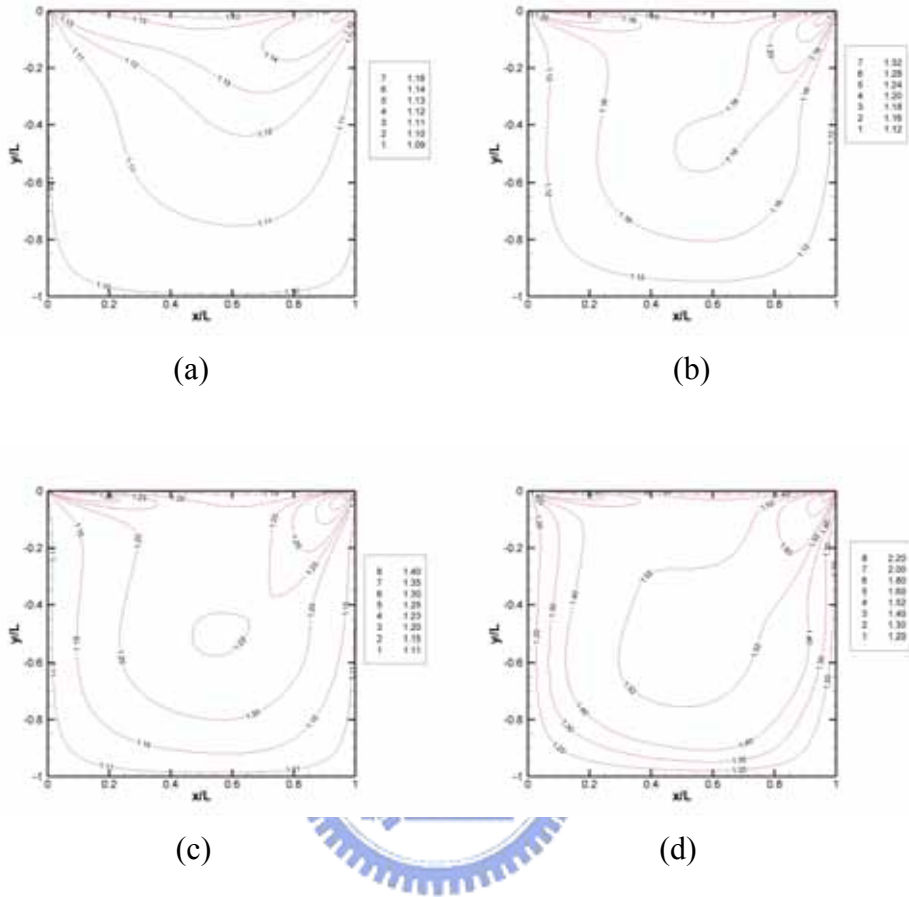


Fig. 3.78 Contours of Temperature for $Kn=0.0033$, (a) $M=0.5$; (b) $M=0.9$; (c) $M=1.1$; (d) $M=2.0$

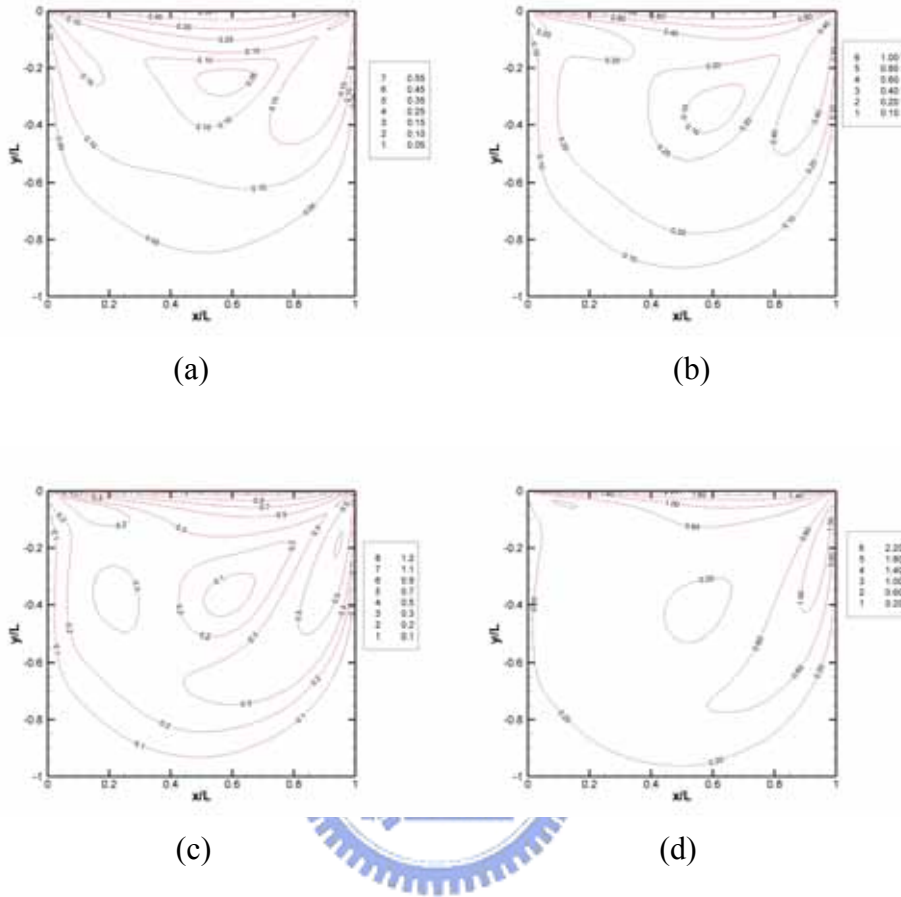


Fig. 3.79 Contours of Mach number for $Kn=0.0033$, (a) $M=0.5$; (b) $M=0.9$; (c) $M=1.1$; (d) $M=2.0$

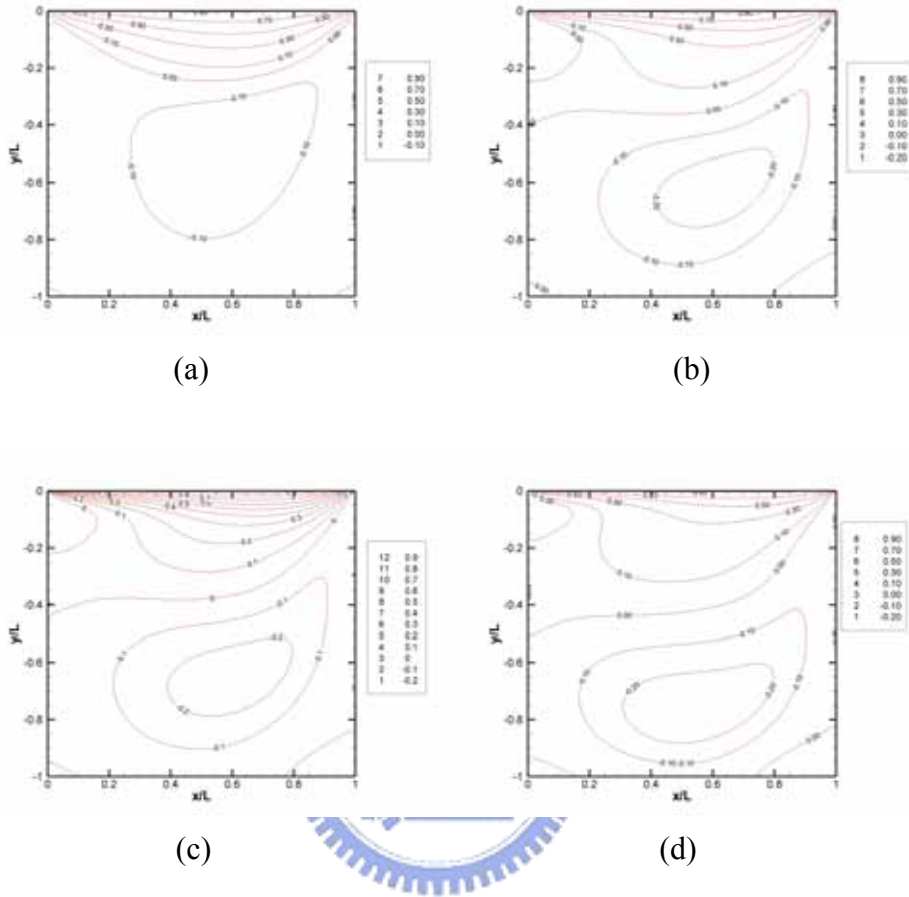


Fig. 3.80 Contours of U-velocity for $Kn=0.0033$, (a) $M=0.5$; (b) $M=0.9$; (c) $M=1.1$; (d) $M=2.0$

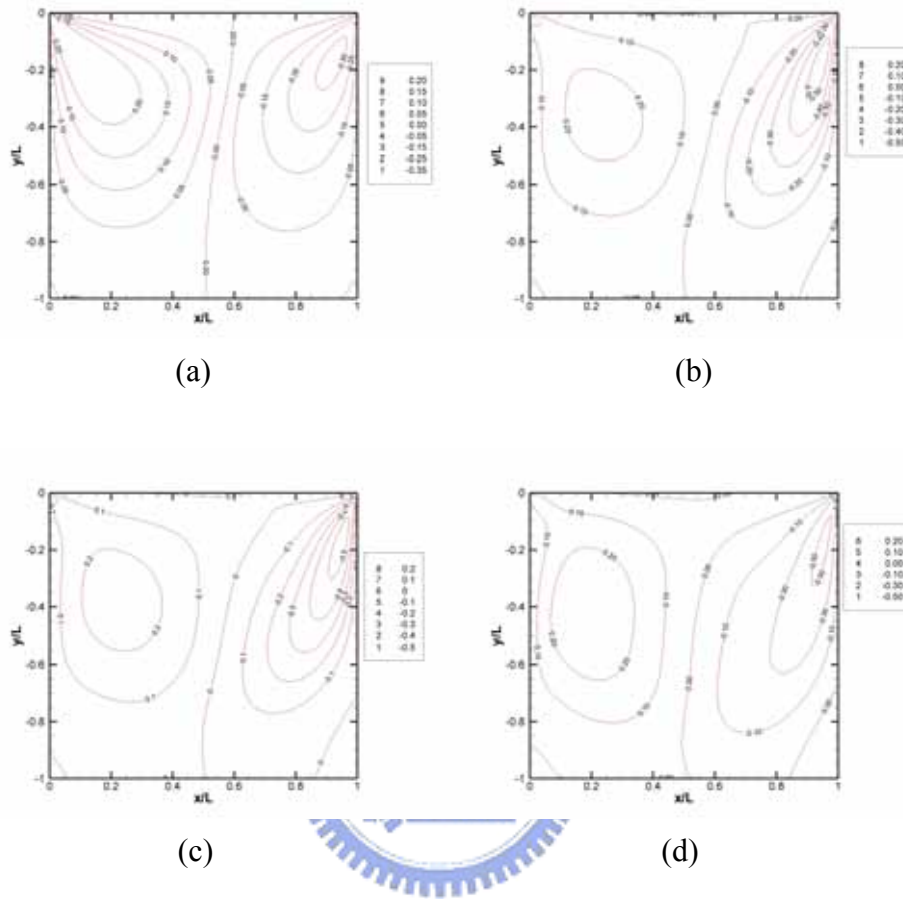


Fig. 3.81 Contours of V-velocity for $Kn=0.0033$, (a) $M=0.5$; (b) $M=0.9$; (c) $M=1.1$; (d) $M=2.0$

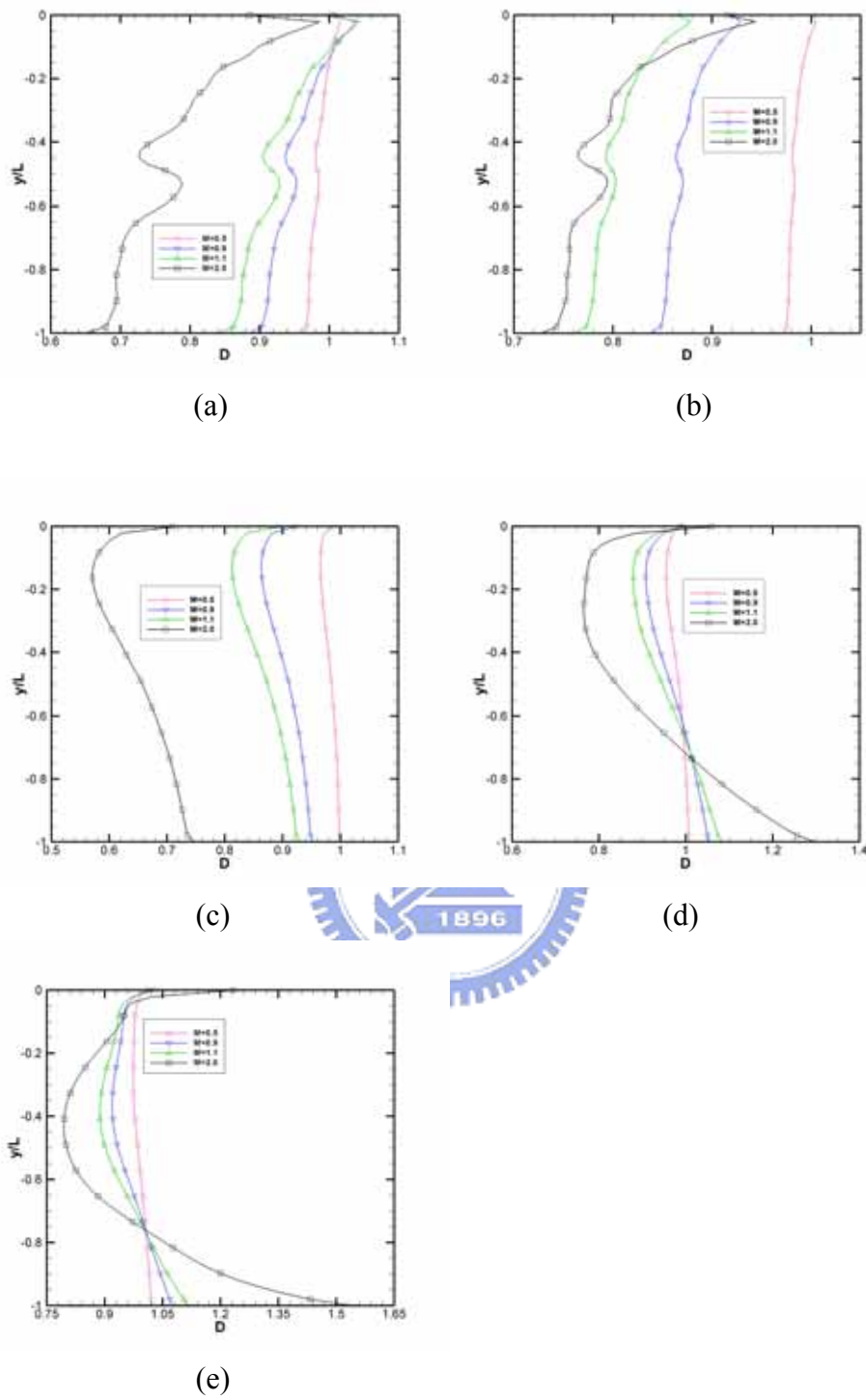


Fig. 3.82 Profile of the number Density on a vertical plane $x=0.5$ for (a) $Kn=10$; (b) $Kn=1$; (c) $Kn=0.1$; (d) $Kn=0.01$; (e) $Kn=0.0033$

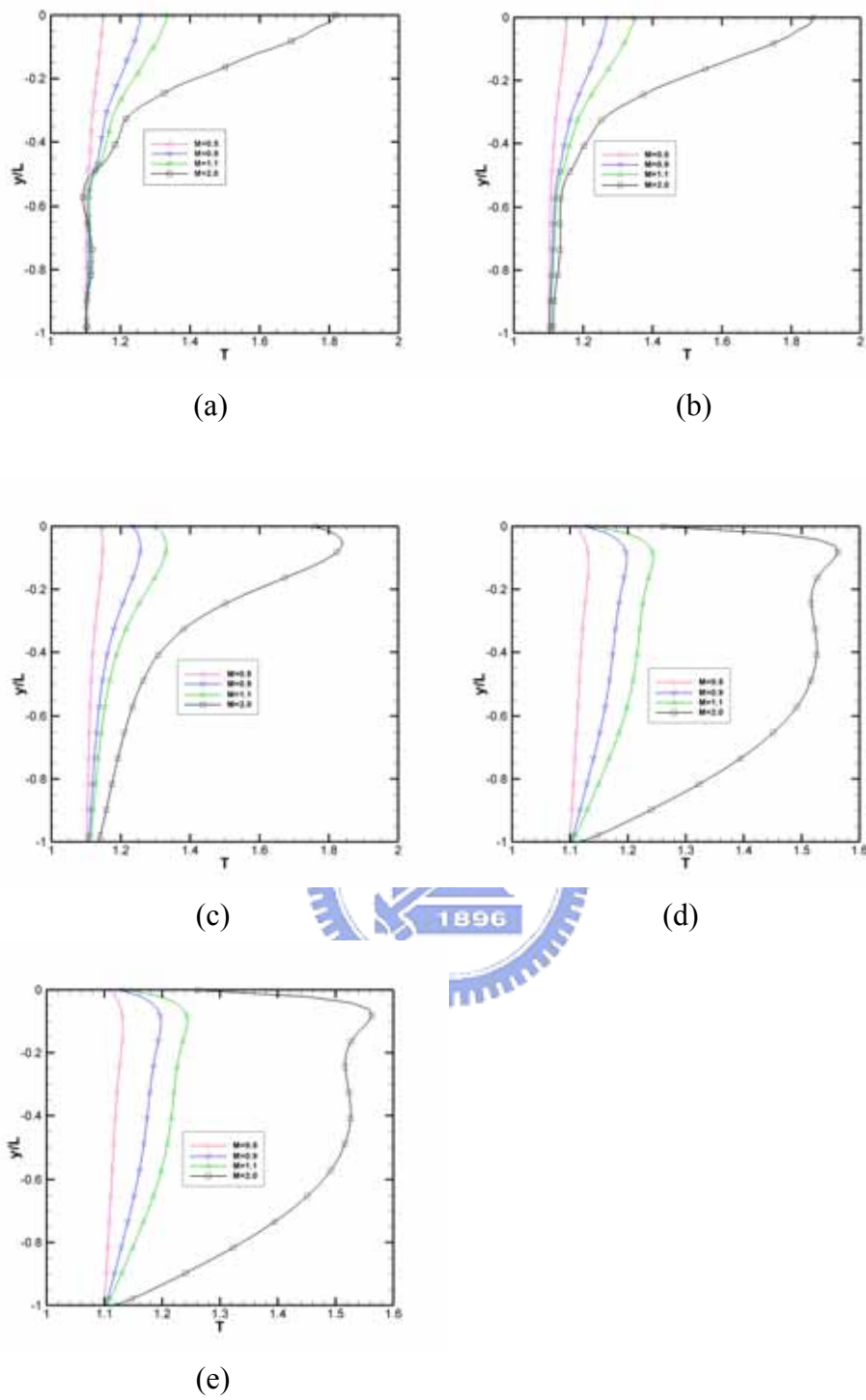


Fig. 3.83 Profile of the Temperature on a vertical plane $x=0.5$ for (a) $Kn=10$; (b) $Kn=1$; (c) $Kn=0.1$; (d) $Kn=0.01$; (e) $Kn=0.0033$

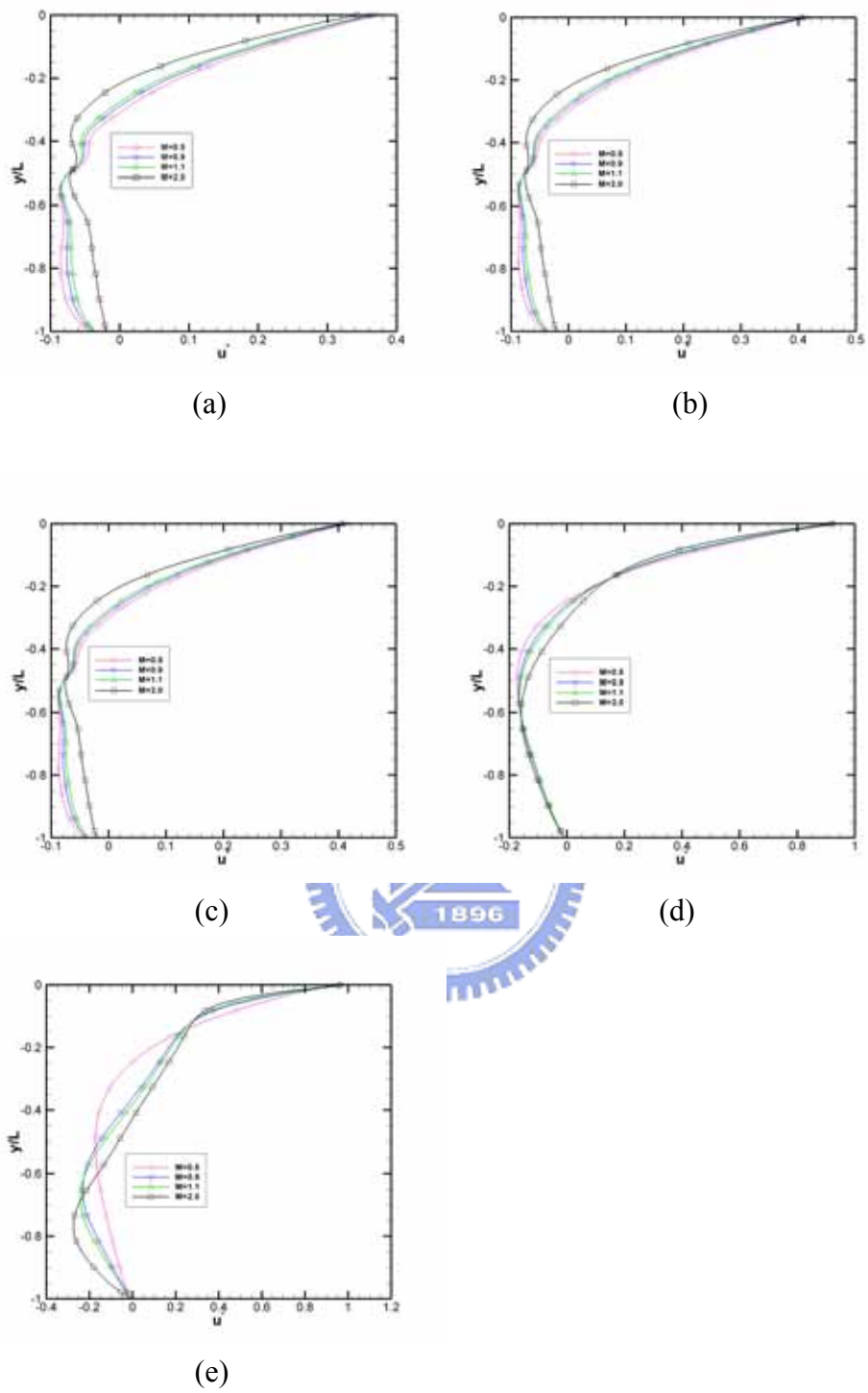


Fig. 3.84 Profile of the U-velocity on a vertical plane $x=0.5$ for (a) $Kn=10$; (b) $Kn=1$; (c) $Kn=0.1$; (d) $Kn=0.01$; (e) $Kn=0.0033$

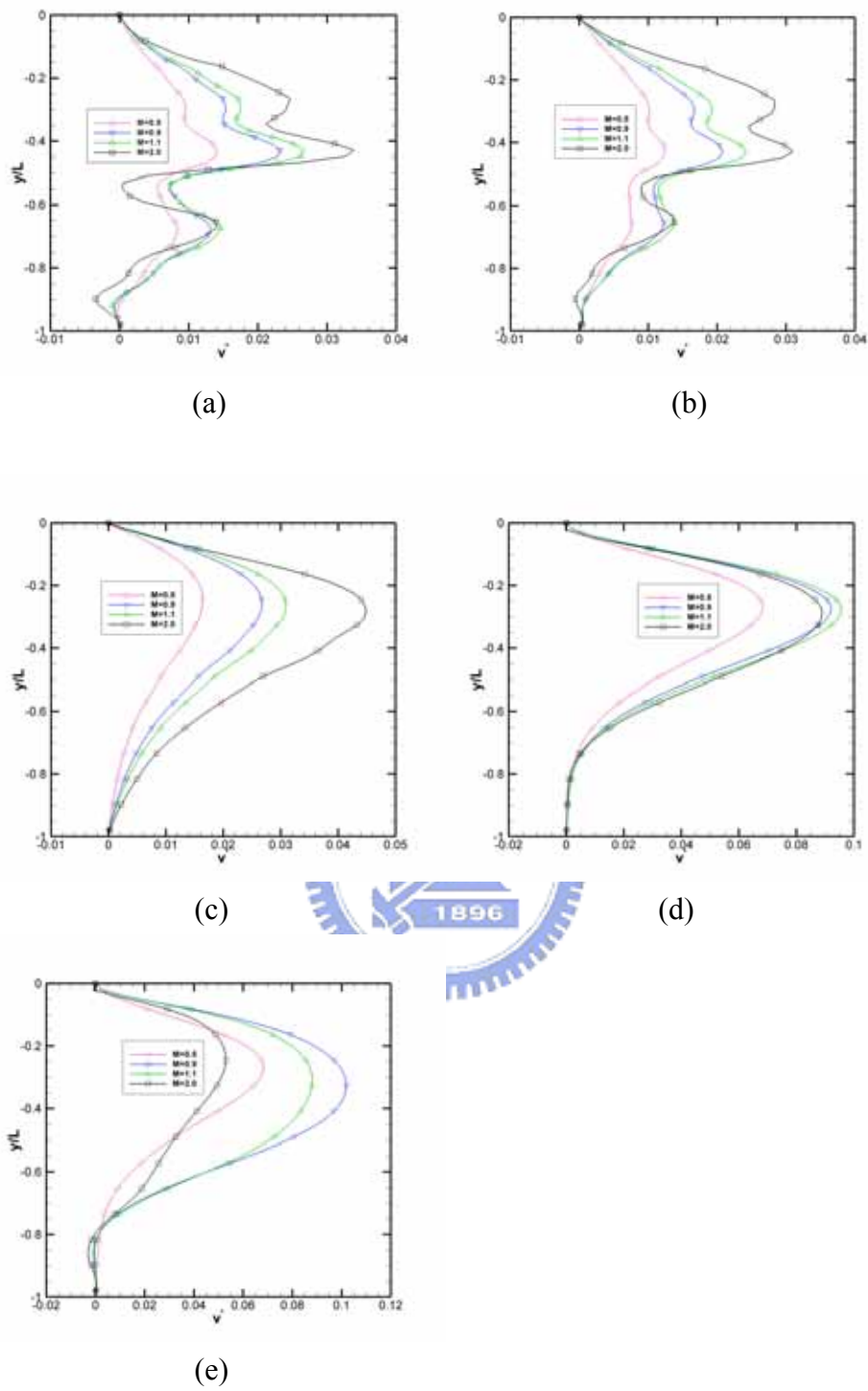


Fig. 3.85 Profile of the V-velocity on a vertical plane $x=0.5$ for (a) $Kn=10$; (b) $Kn=1$; (c) $Kn=0.1$; (d) $Kn=0.01$; (e) $Kn=0.0033$

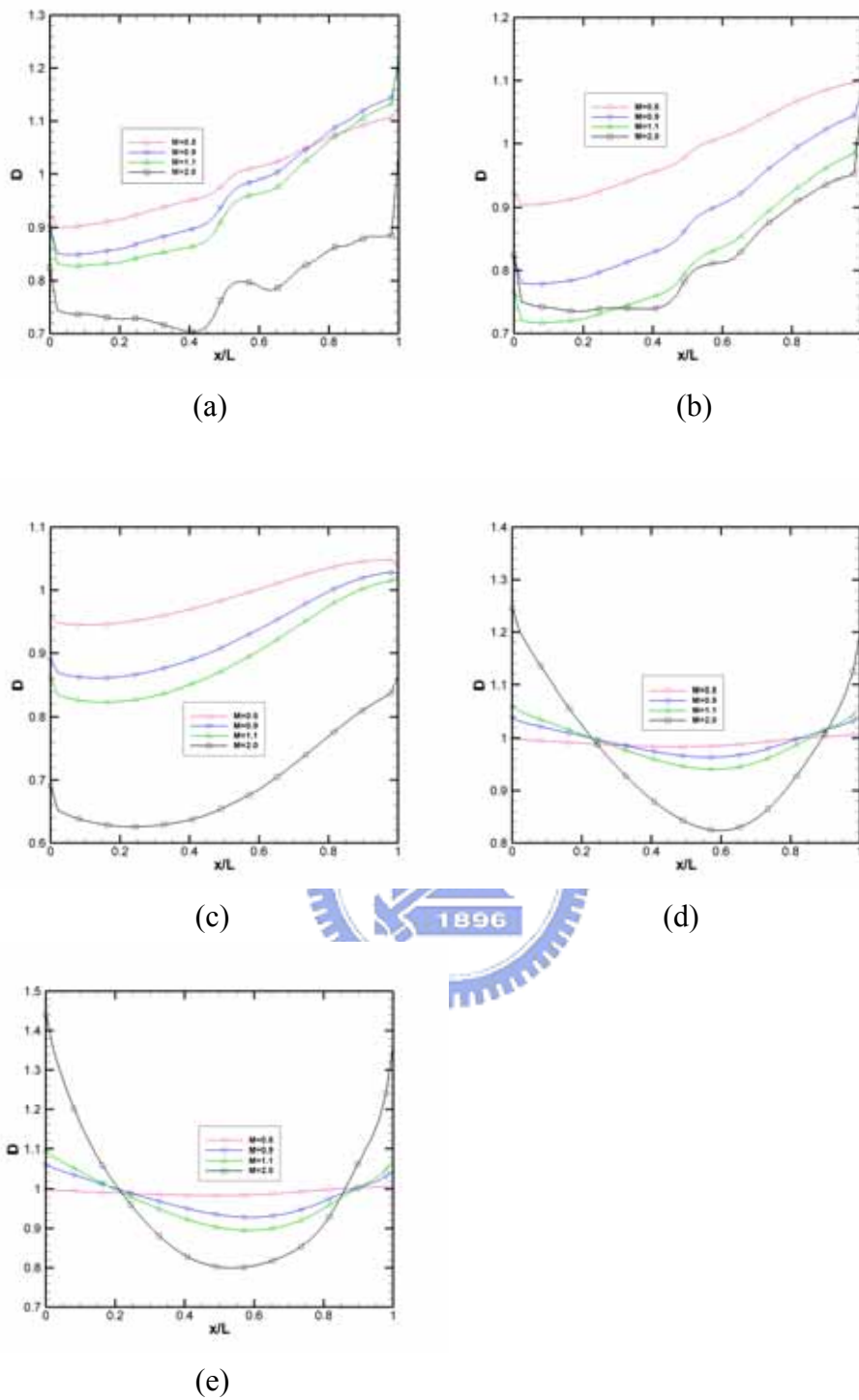


Fig. 3.86 Profile of the number Density on a horizontal plane $y=-0.5$ for (a) $Kn=10$; (b) $Kn=1$; (c) $Kn=0.1$; (d) $Kn=0.01$; (e) $Kn=0.0033$

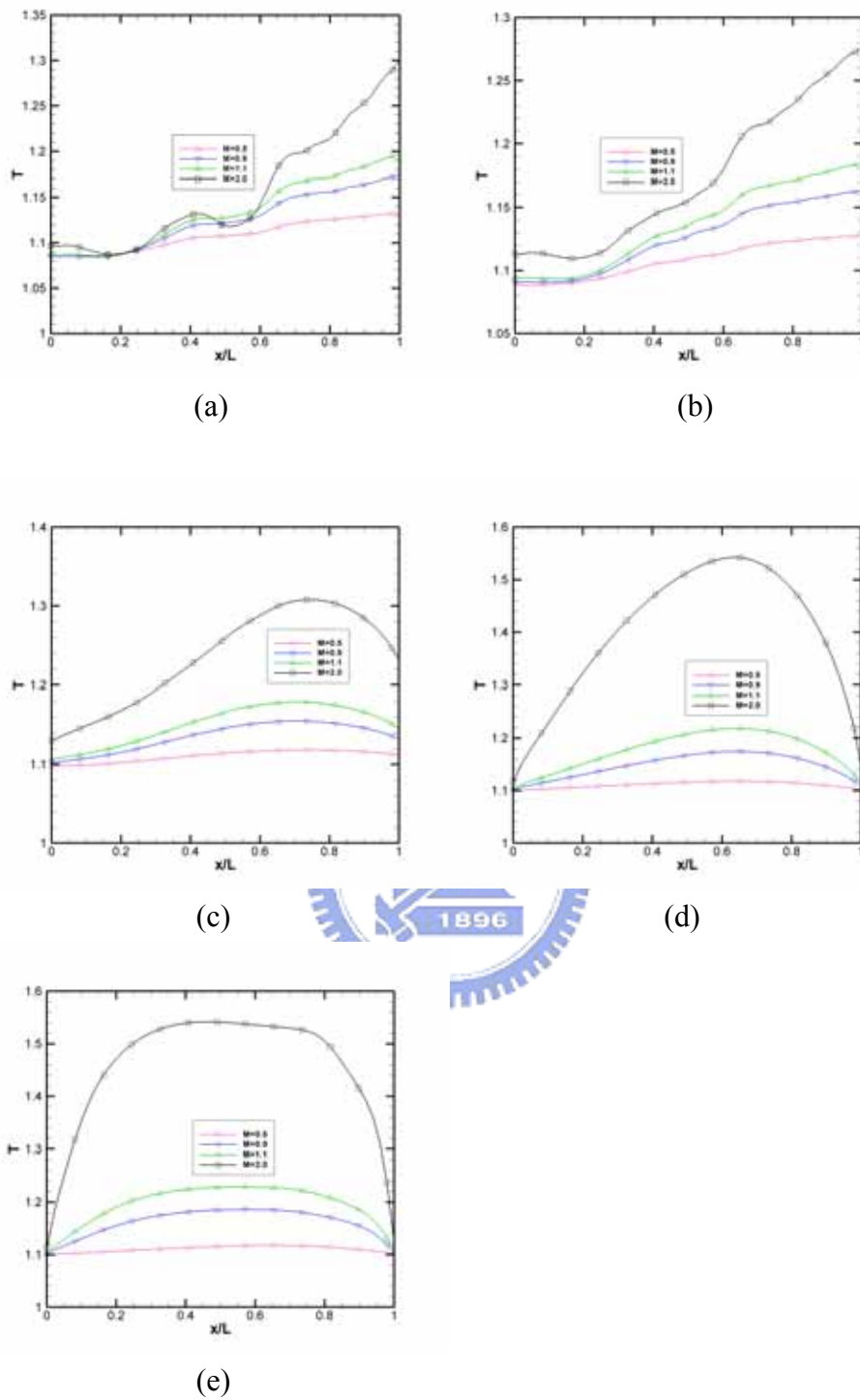


Fig. 3.87 Profile of the Temperature on a horizontal plane $y=-0.5$ for (a) $Kn=10$; (b) $Kn=1$; (c) $Kn=0.1$; (d) $Kn=0.01$; (e) $Kn=0.0033$

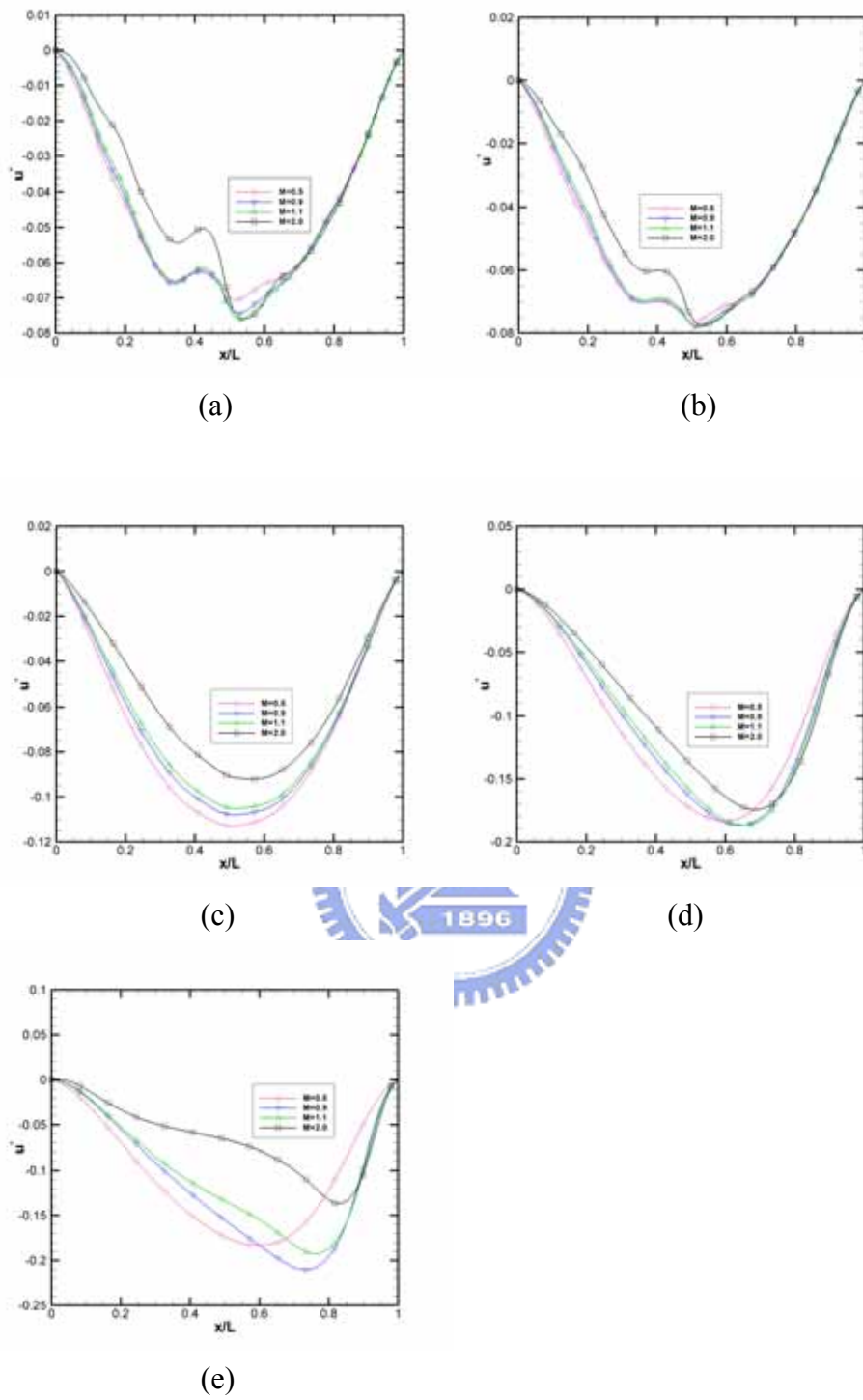


Fig. 3.88 Profile of the U-velocity on a horizontal plane $y=-0.5$ for (a) $Kn=10$; (b) $Kn=1$; (c) $Kn=0.1$; (d) $Kn=0.01$; (e) $Kn=0.0033$

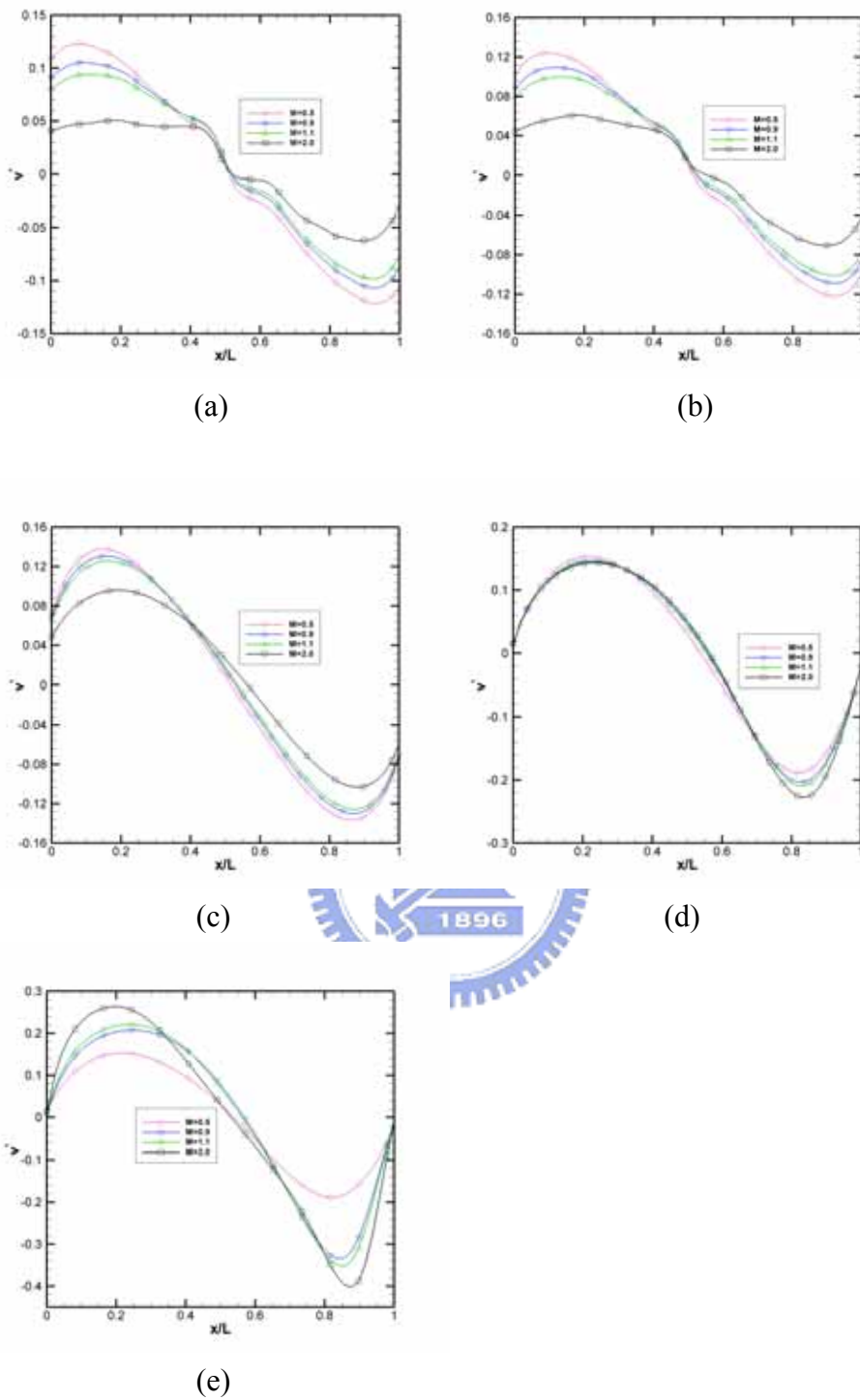


Fig. 3.89 Profile of the V-velocity on a horizontal plane $y=-0.5$ for (a) $Kn=10$; (b) $Kn=1$; (c) $Kn=0.1$; (d) $Kn=0.01$; (e) $Kn=0.0033$

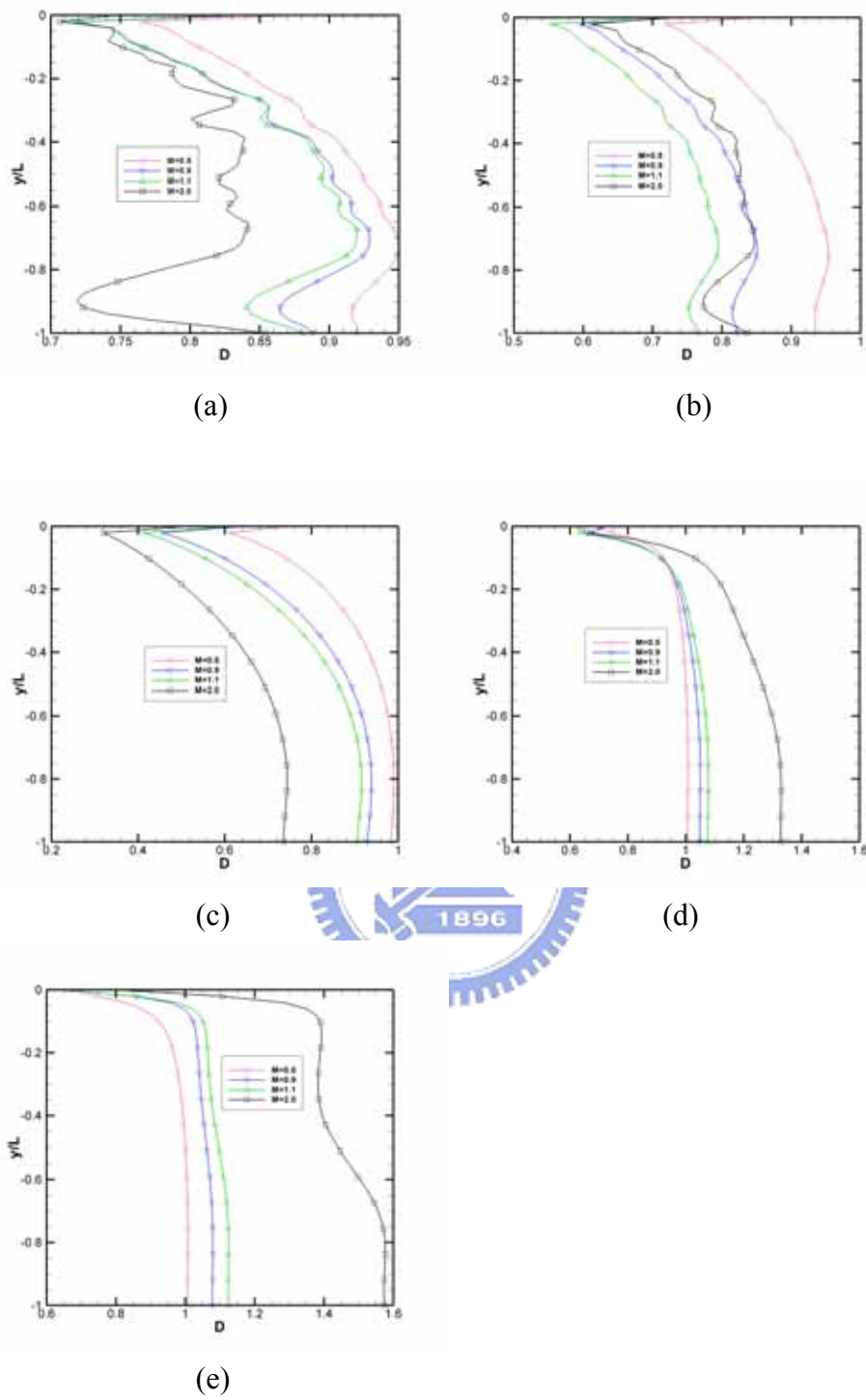


Fig. 3.90 Profile of the number Density on a vertical plane $x=0$ for (a) $Kn=10$; (b) $Kn=1$; (c) $Kn=0.1$; (d) $Kn=0.01$; (e) $Kn=0.0033$

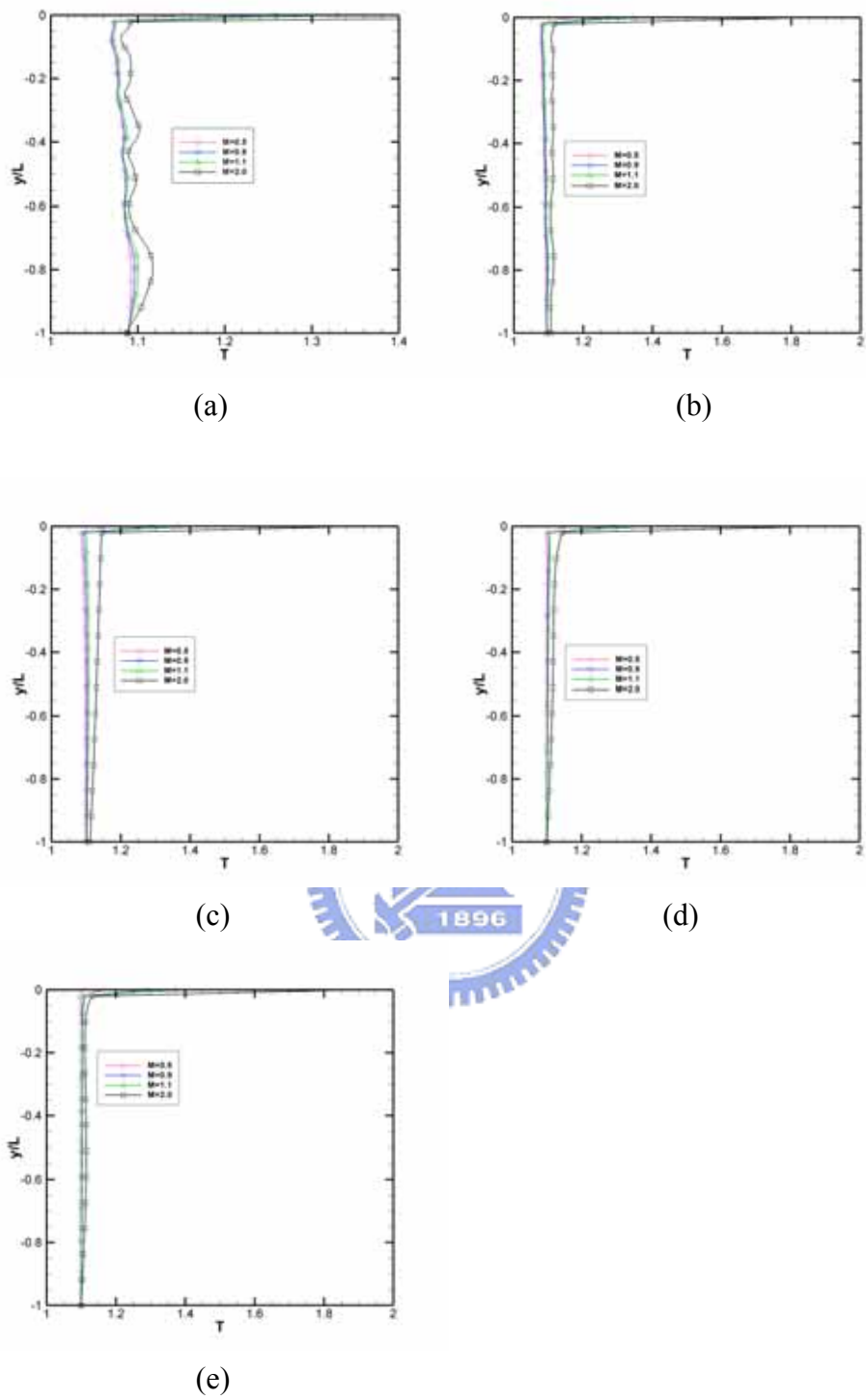
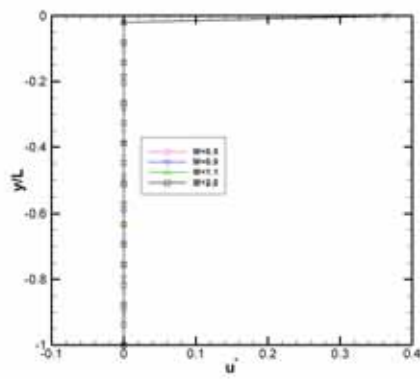
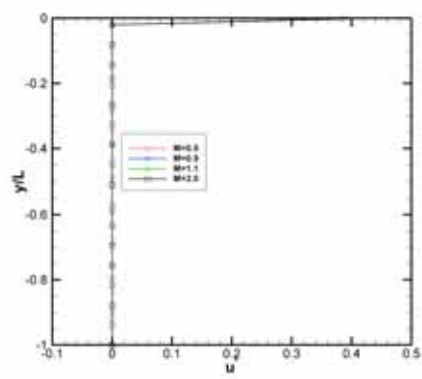


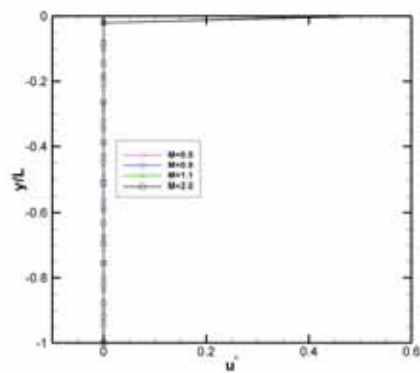
Fig. 3.91 Profile of the Temperature on a vertical plane $x=0$ for (a) $Kn=10$; (b) $Kn=1$; (c) $Kn=0.1$; (d) $Kn=0.01$; (e) $Kn=0.0033$



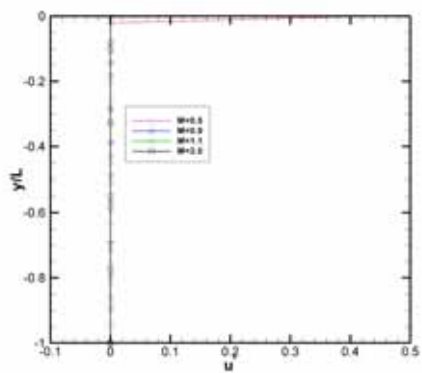
(a)



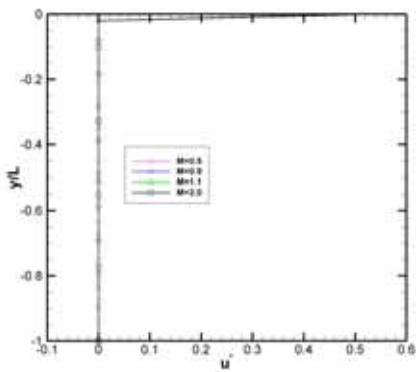
(b)



(c)



(d)



(e)

Fig. 3.92 Profile of the U-velocity on a vertical plane $x=0$ for (a) $Kn=10$; (b) $Kn=1$; (c) $Kn=0.1$; (d) $Kn=0.01$; (e) $Kn=0.0033$

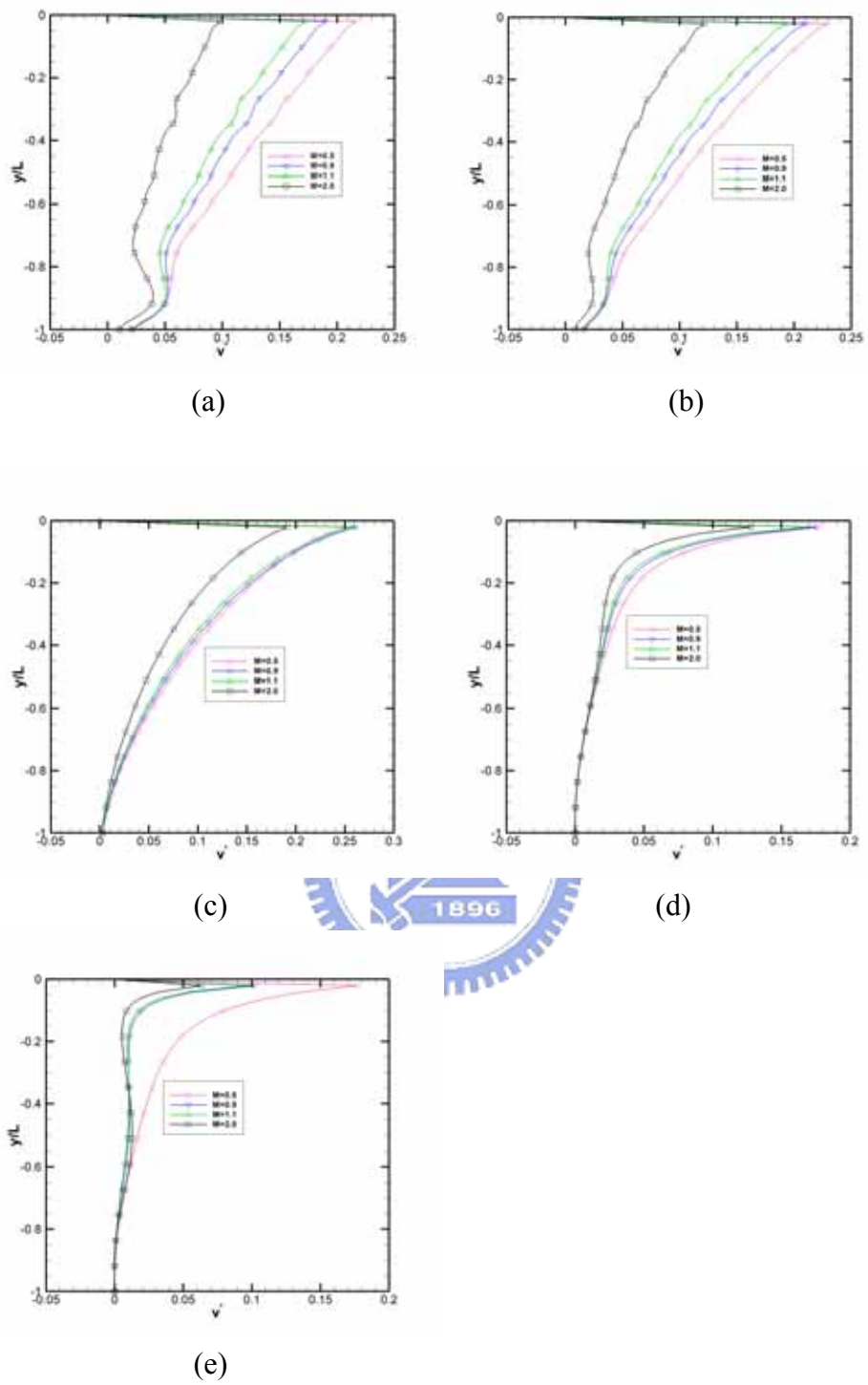


Fig. 3.93 Profile of the V-velocity on a vertical plane $x=0$ for (a) $Kn=10$; (b) $Kn=1$; (c) $Kn=0.1$; (d) $Kn=0.01$; (e) $Kn=0.0033$

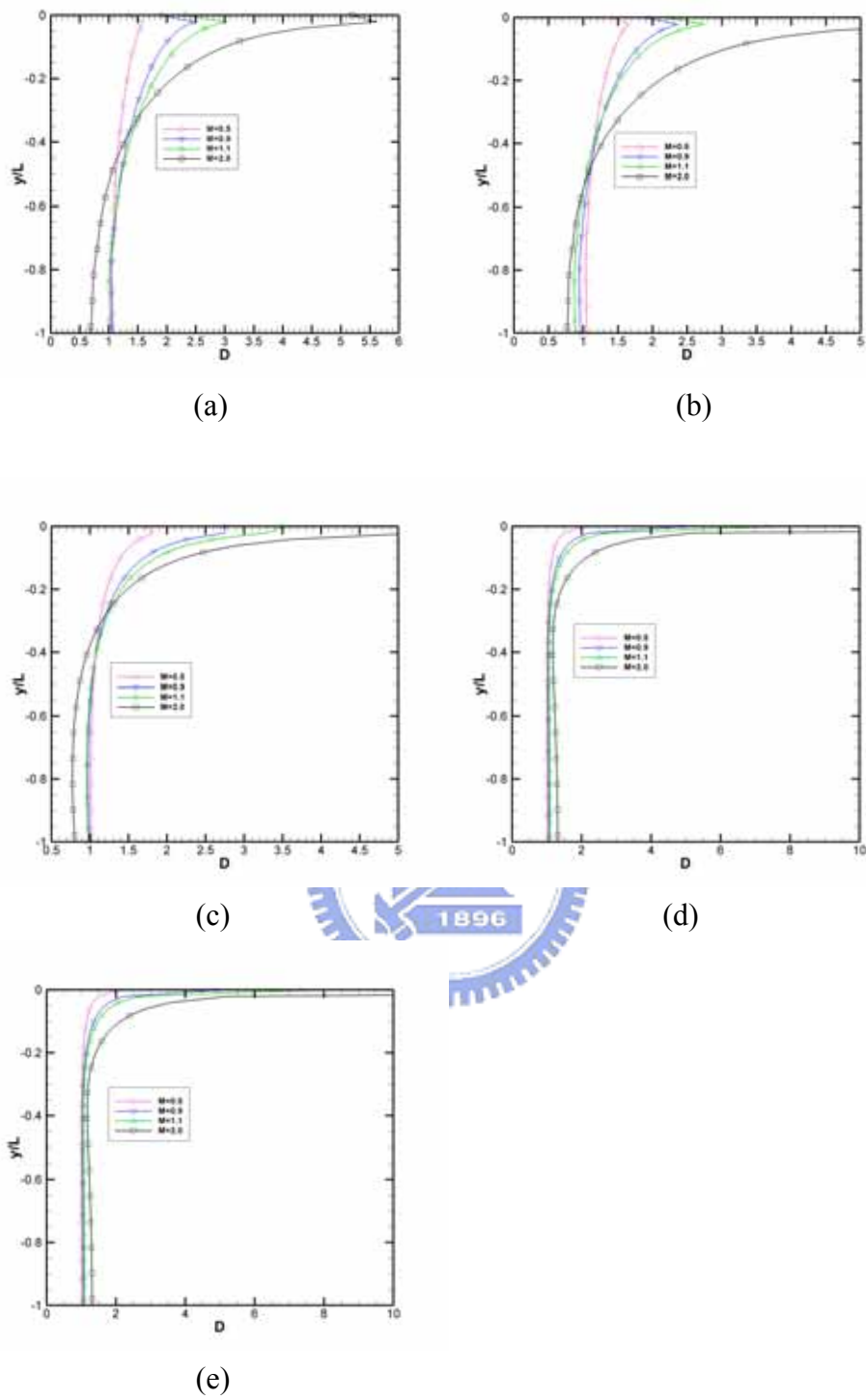
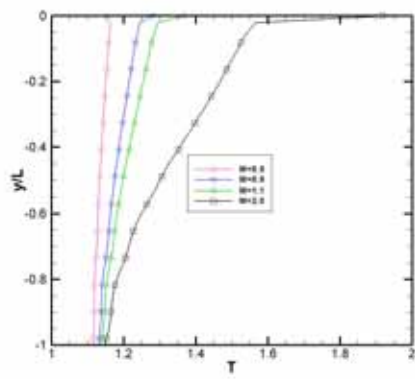
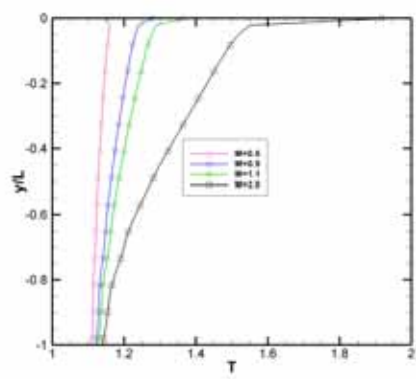


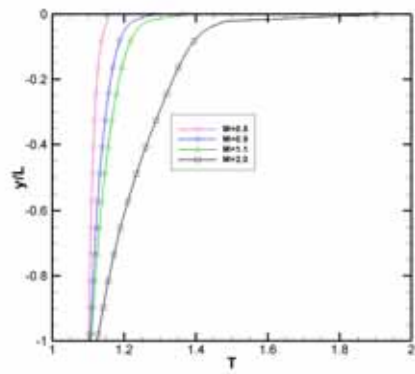
Fig. 3.94 Profile of the number Density on a vertical plane $x=1$ for (a) $Kn=10$; (b) $Kn=1$; (c) $Kn=0.1$; (d) $Kn=0.01$; (e) $Kn=0.0033$



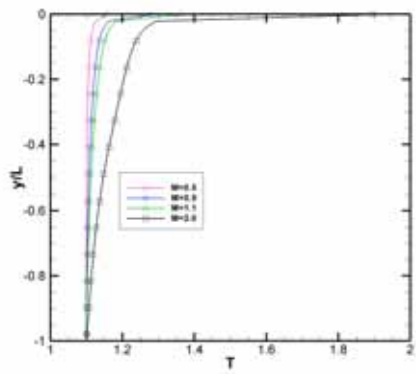
(a)



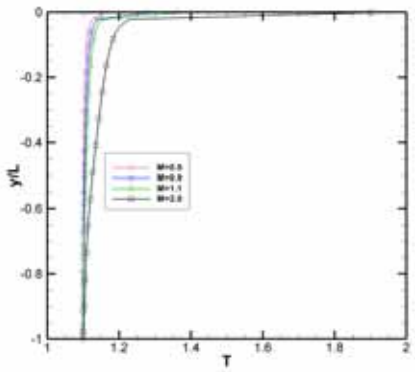
(b)



(c)



(d)



(e)

Fig. 3.95 Profile of the Temperature on a vertical plane $x=1$ for (a) $Kn=10$; (b) $Kn=1$; (c) $Kn=0.1$; (d) $Kn=0.01$; (e) $Kn=0.0033$

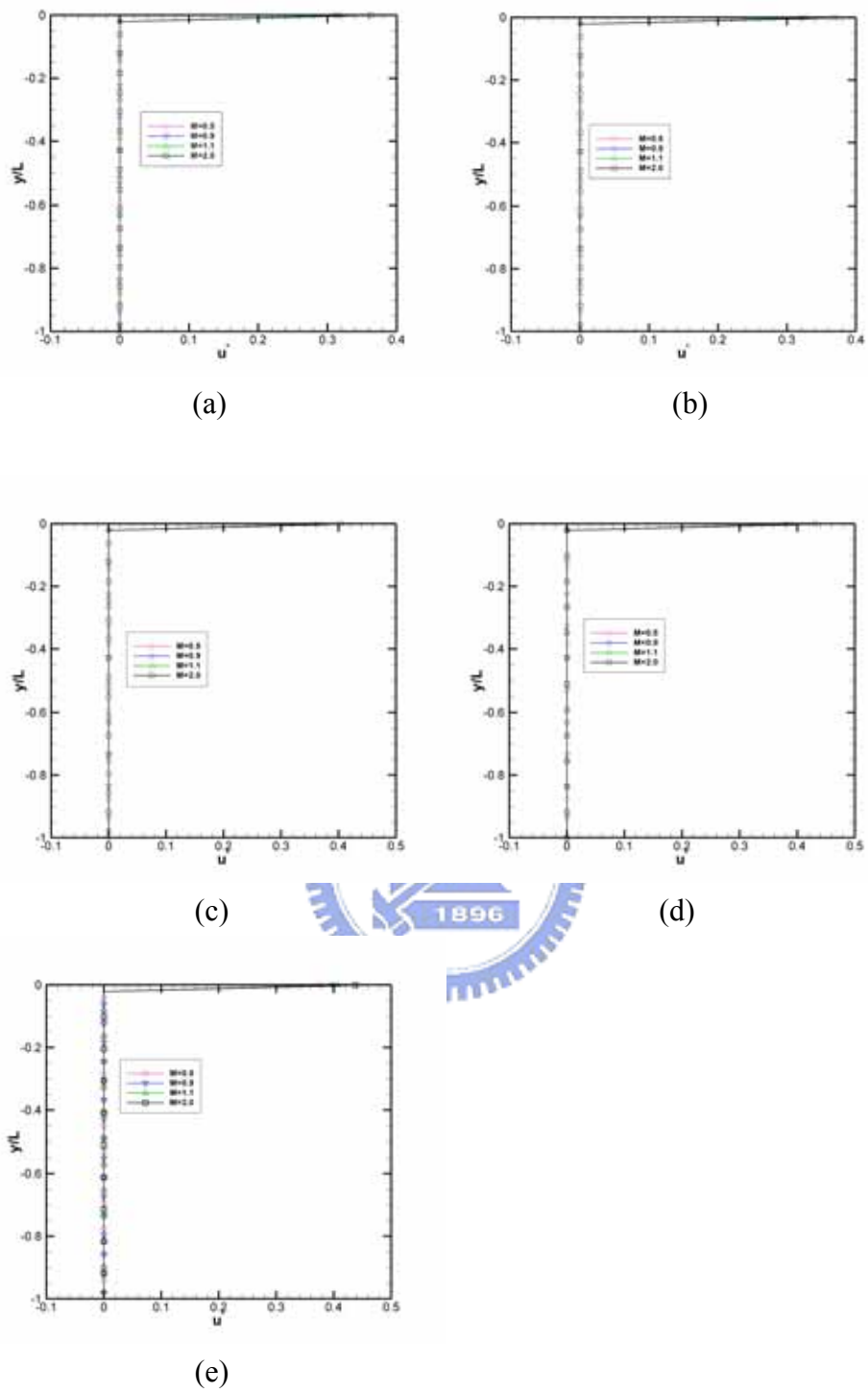


Fig. 3.96 Profile of the U-velocity on a vertical plane $x=1$ for (a) $Kn=10$; (b) $Kn=1$; (c) $Kn=0.1$; (d) $Kn=0.01$; (e) $Kn=0.0033$

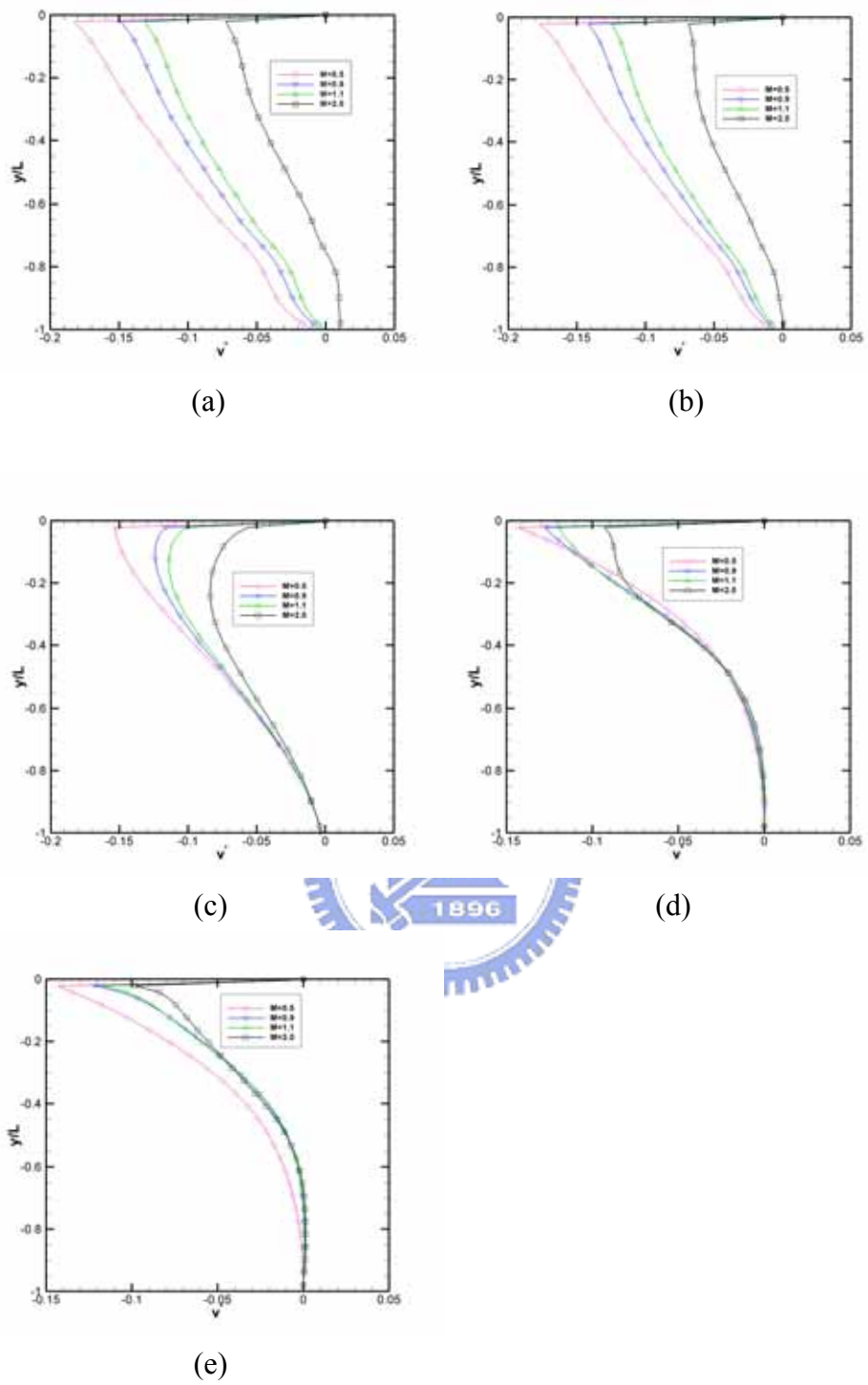


Fig. 3.97 Profile of the V-velocity on a vertical plane $x=1$ for (a) $Kn=10$; (b) $Kn=1$; (c) $Kn=0.1$; (d) $Kn=0.01$; (e) $Kn=0.0033$

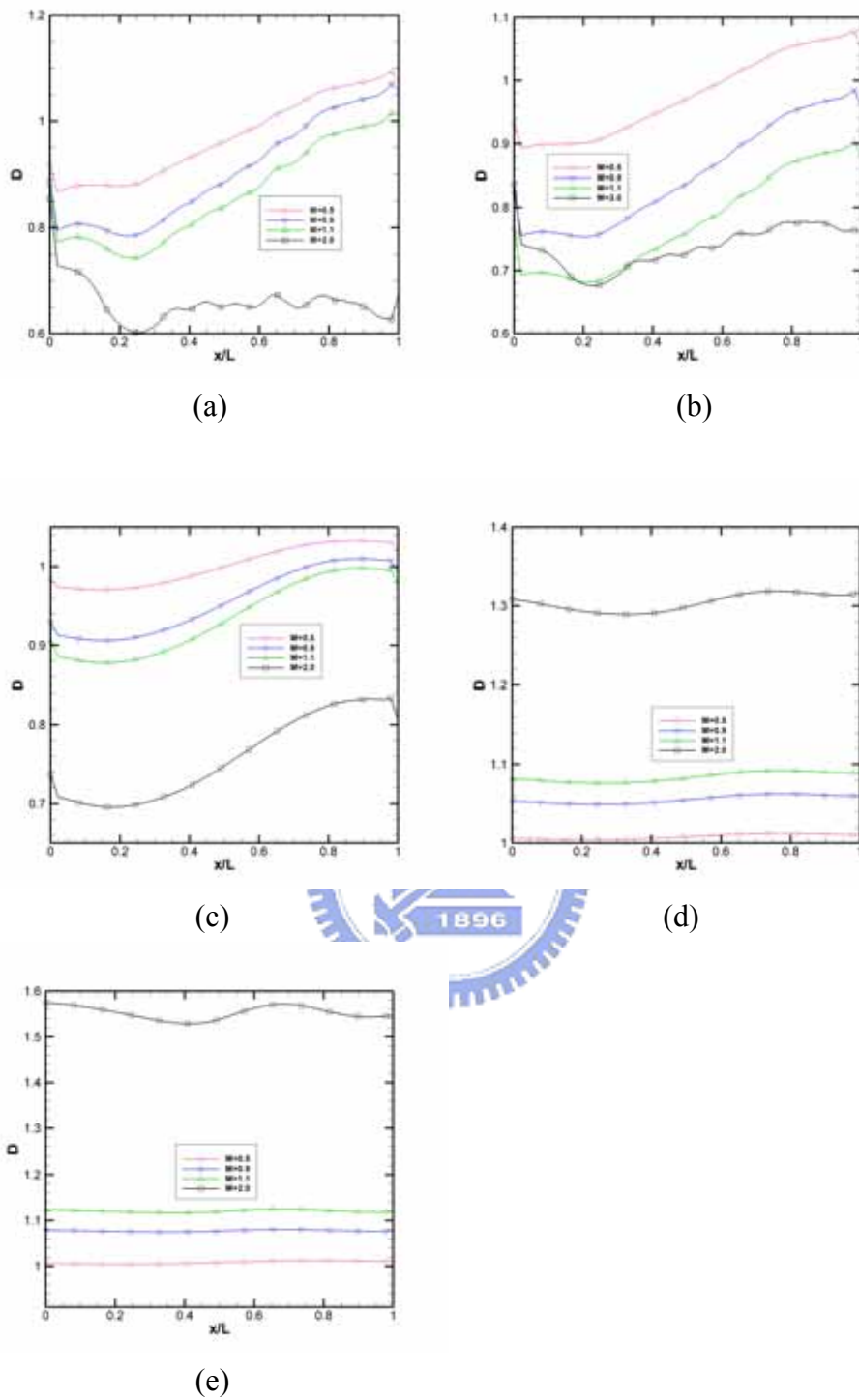


Fig. 3.98 Profile of the number Density on a horizontal plane $y=-1$ for (a) $Kn=10$; (b) $Kn=1$; (c) $Kn=0.1$; (d) $Kn=0.01$; (e) $Kn=0.0033$

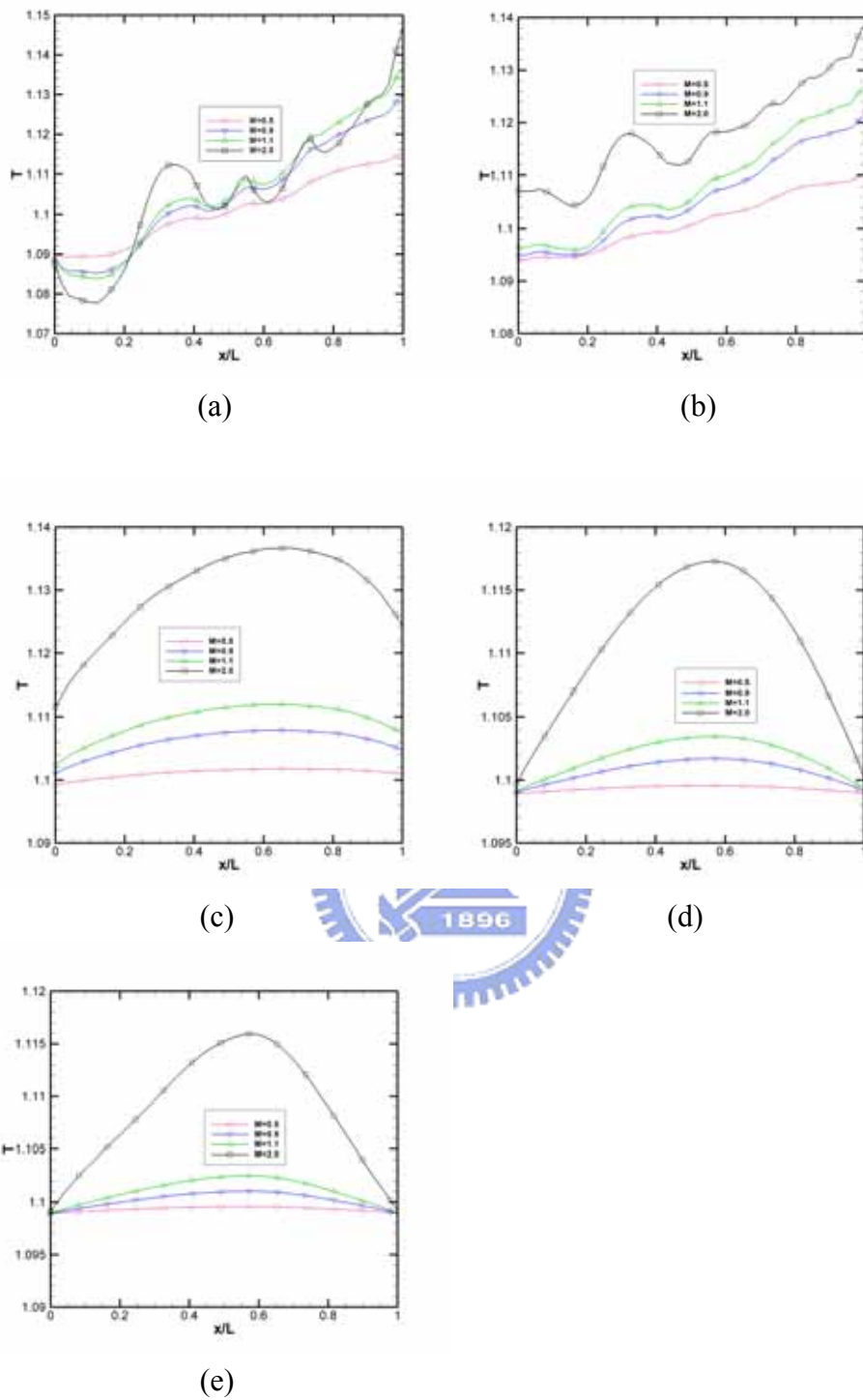


Fig. 3.99 Profile of the Temperature on a horizontal plane $y=-1$ for (a) $Kn=10$; (b) $Kn=1$; (c) $Kn=0.1$; (d) $Kn=0.01$; (e) $Kn=0.0033$

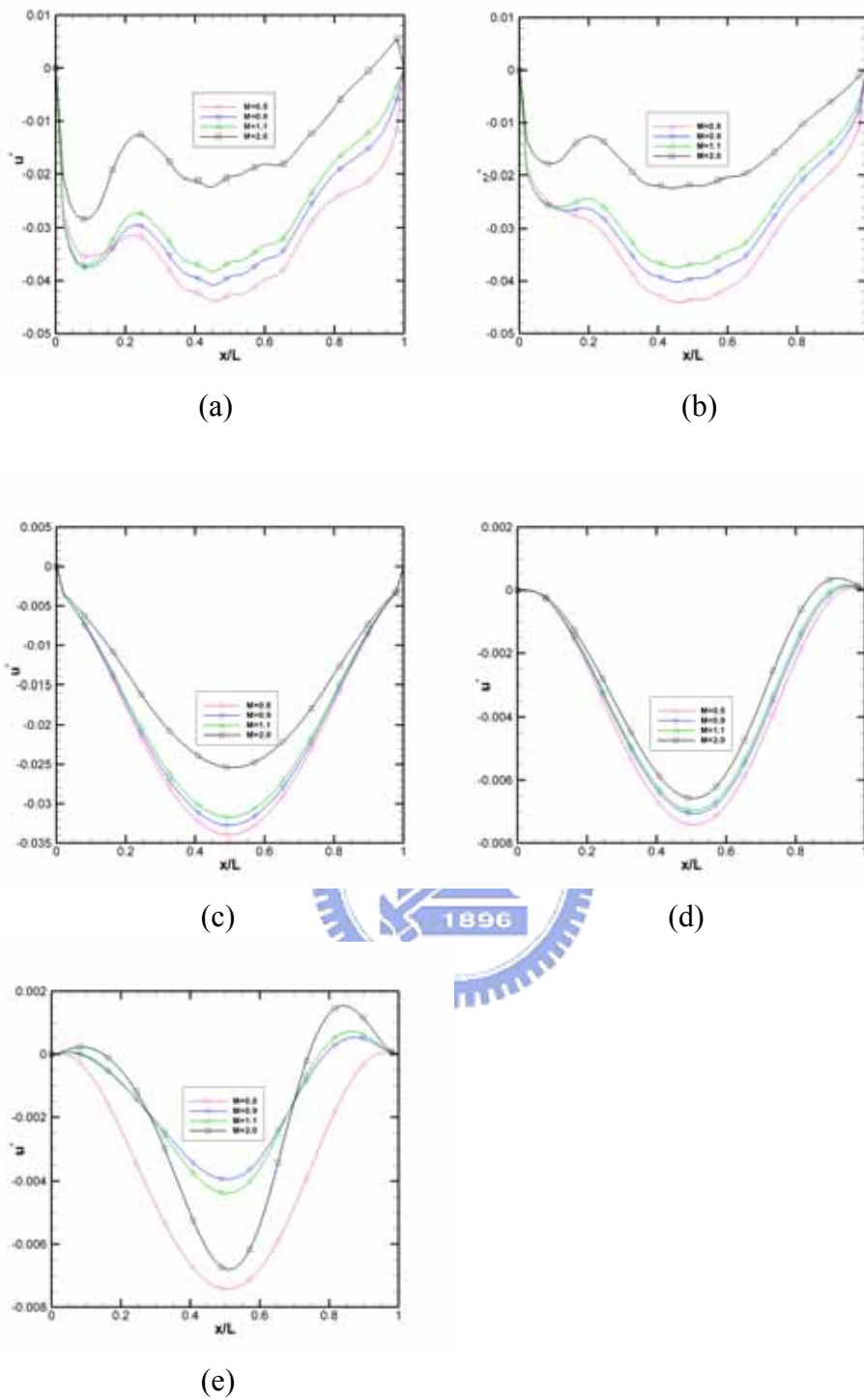


Fig. 3.100 Profile of the U-velocity on a horizontal plane $y=-1$ for (a) $Kn=10$; (b) $Kn=1$; (c) $Kn=0.1$; (d) $Kn=0.01$; (e) $Kn=0.0033$

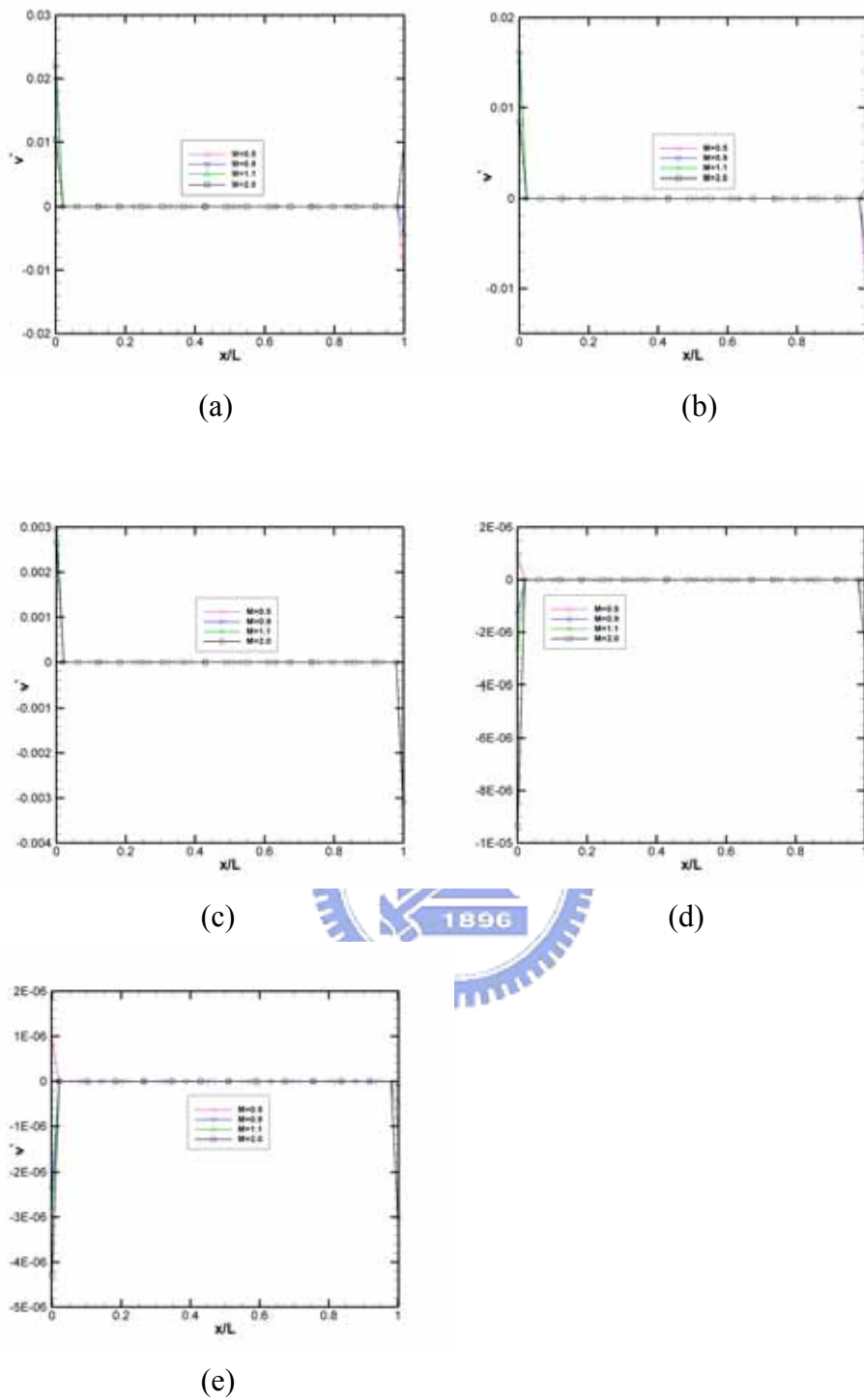


Fig. 3.101 Profile of the V-velocity on a horizontal plane $y=-1$ for (a) $Kn=10$; (b) $Kn=1$; (c) $Kn=0.1$; (d) $Kn=0.01$; (e) $Kn=0.0033$

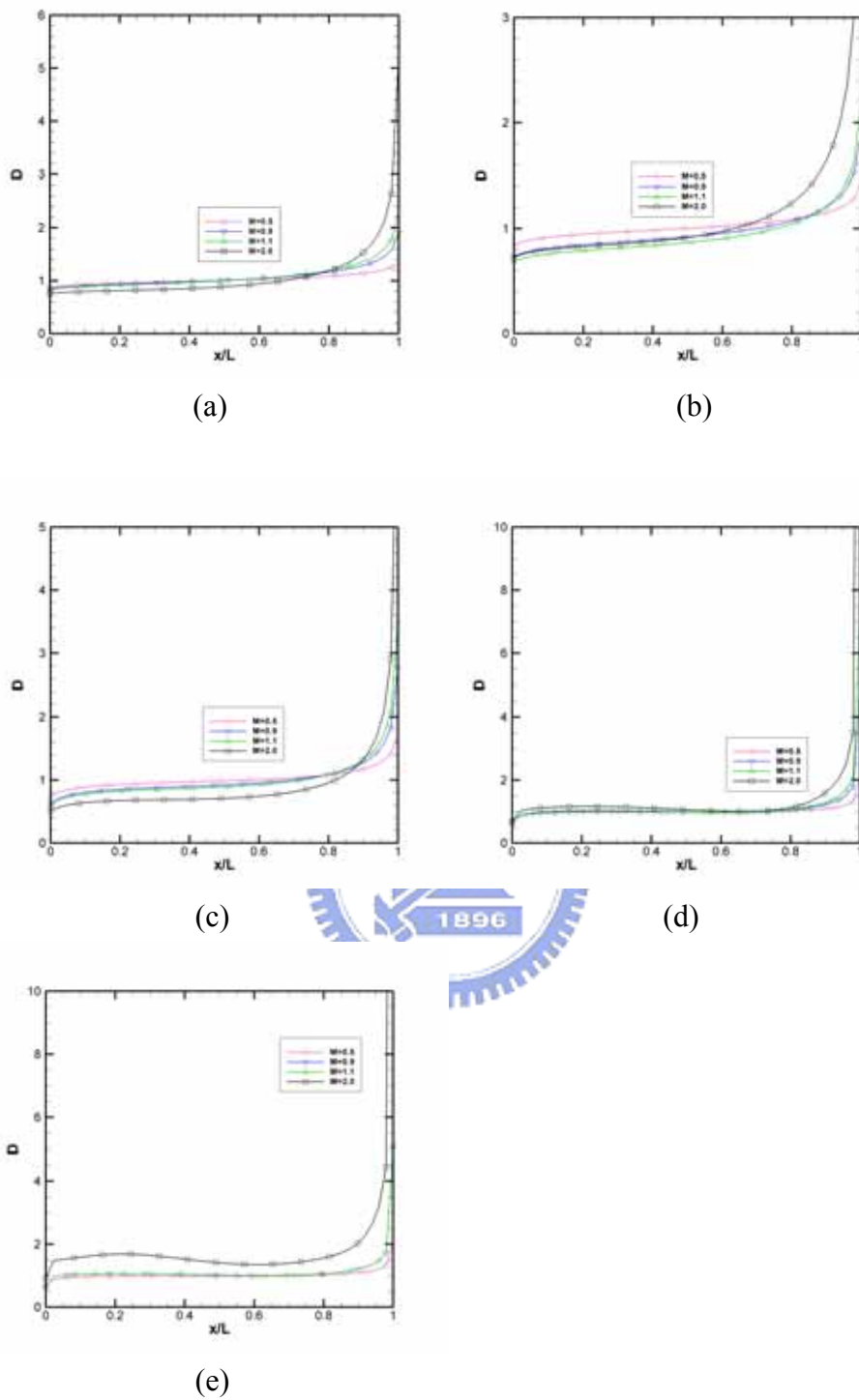


Fig. 3.102 Profile of the number Density on a horizontal plane $y=0$ for (a) $Kn=10$; (b) $Kn=1$; (c) $Kn=0.1$; (d) $Kn=0.01$; (e) $Kn=0.0033$

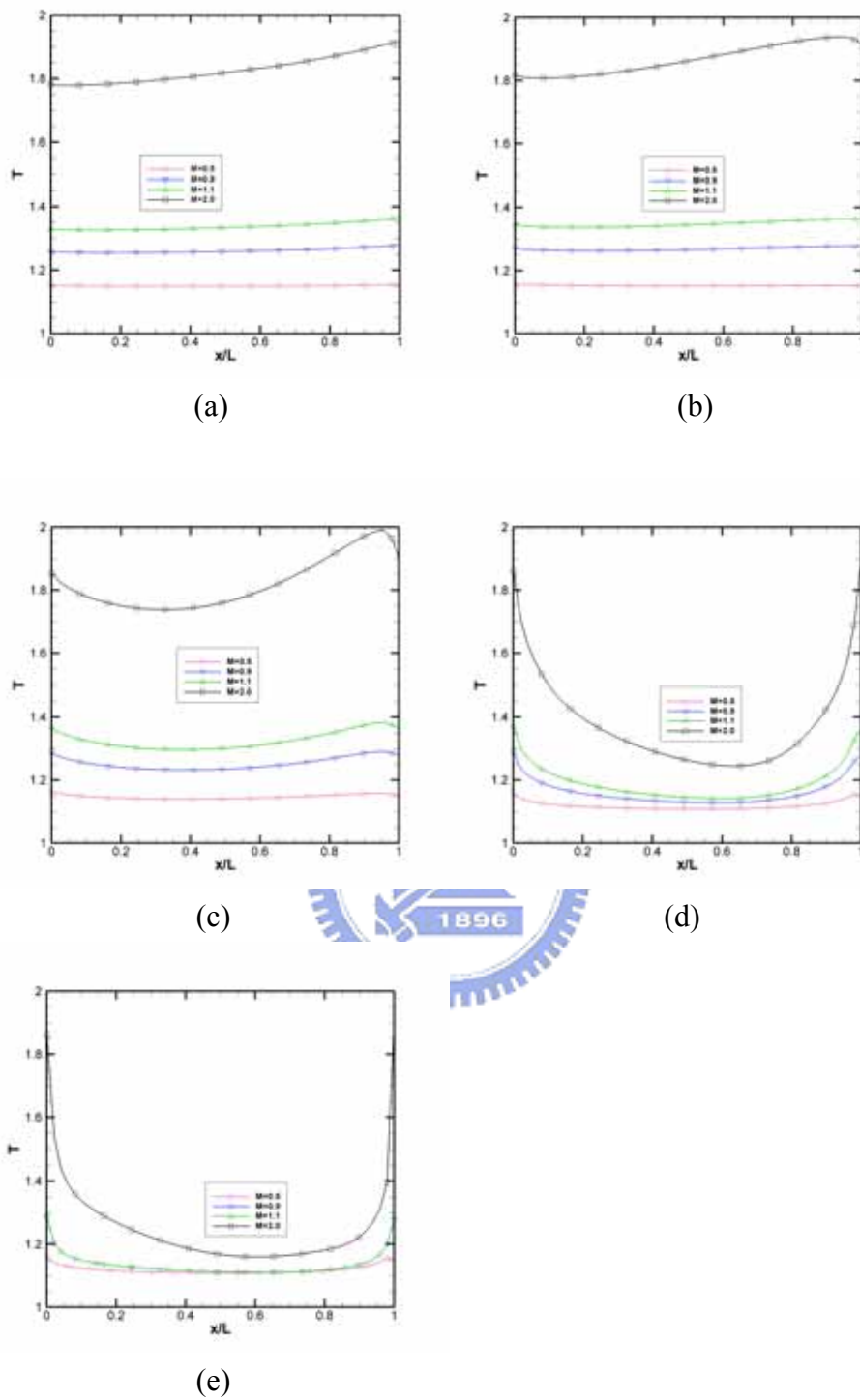


Fig. 3.103 Profile of the Temperature on a horizontal plane $y=0$ for (a) $Kn=10$; (b) $Kn=1$; (c) $Kn=0.1$; (d) $Kn=0.01$; (e) $Kn=0.0033$

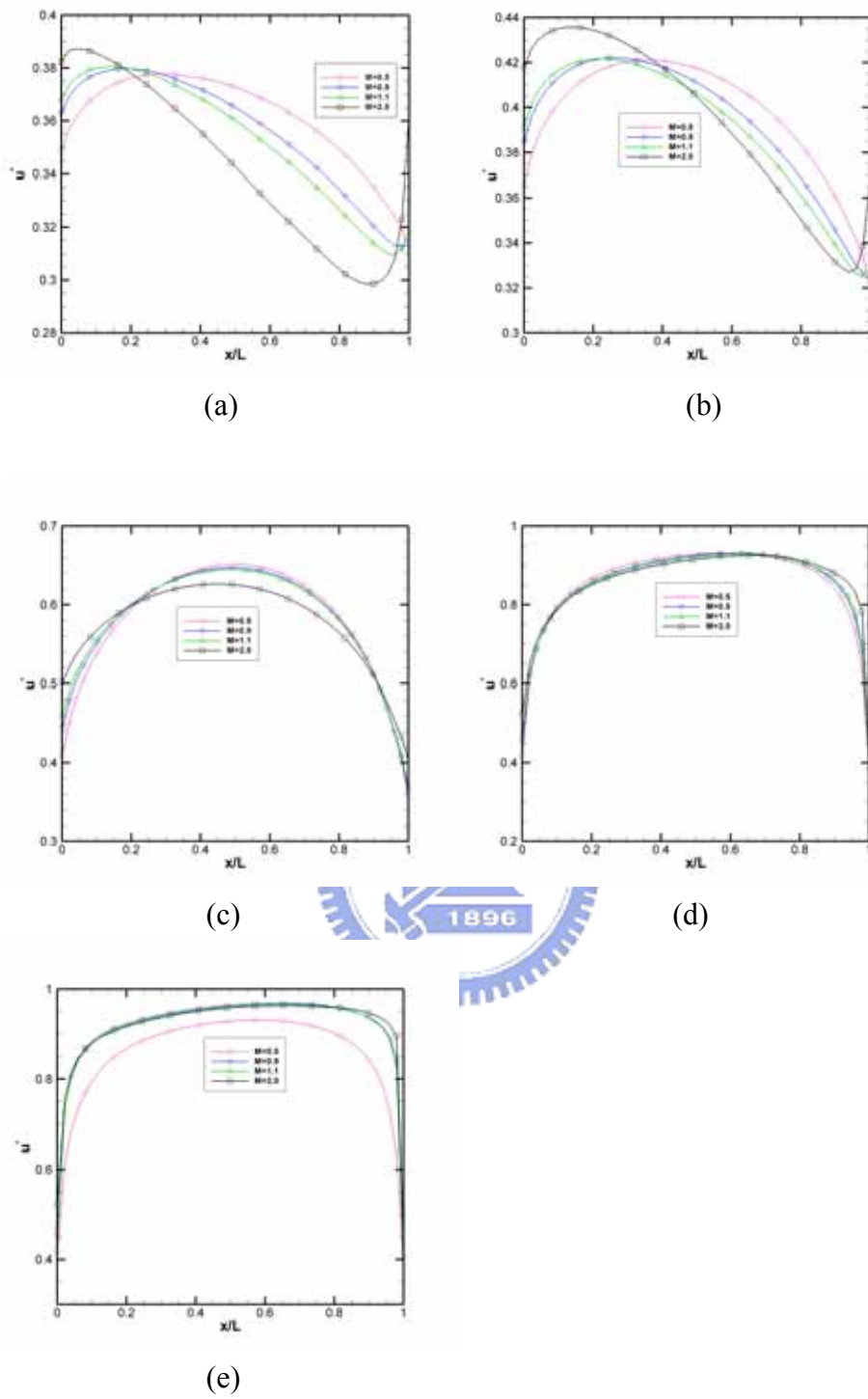


Fig. 3.104 Profile of the U-velocity on a horizontal plane $y=0$ for (a) $Kn=10$; (b) $Kn=1$; (c) $Kn=0.1$; (d) $Kn=0.01$; (e) $Kn=0.0033$

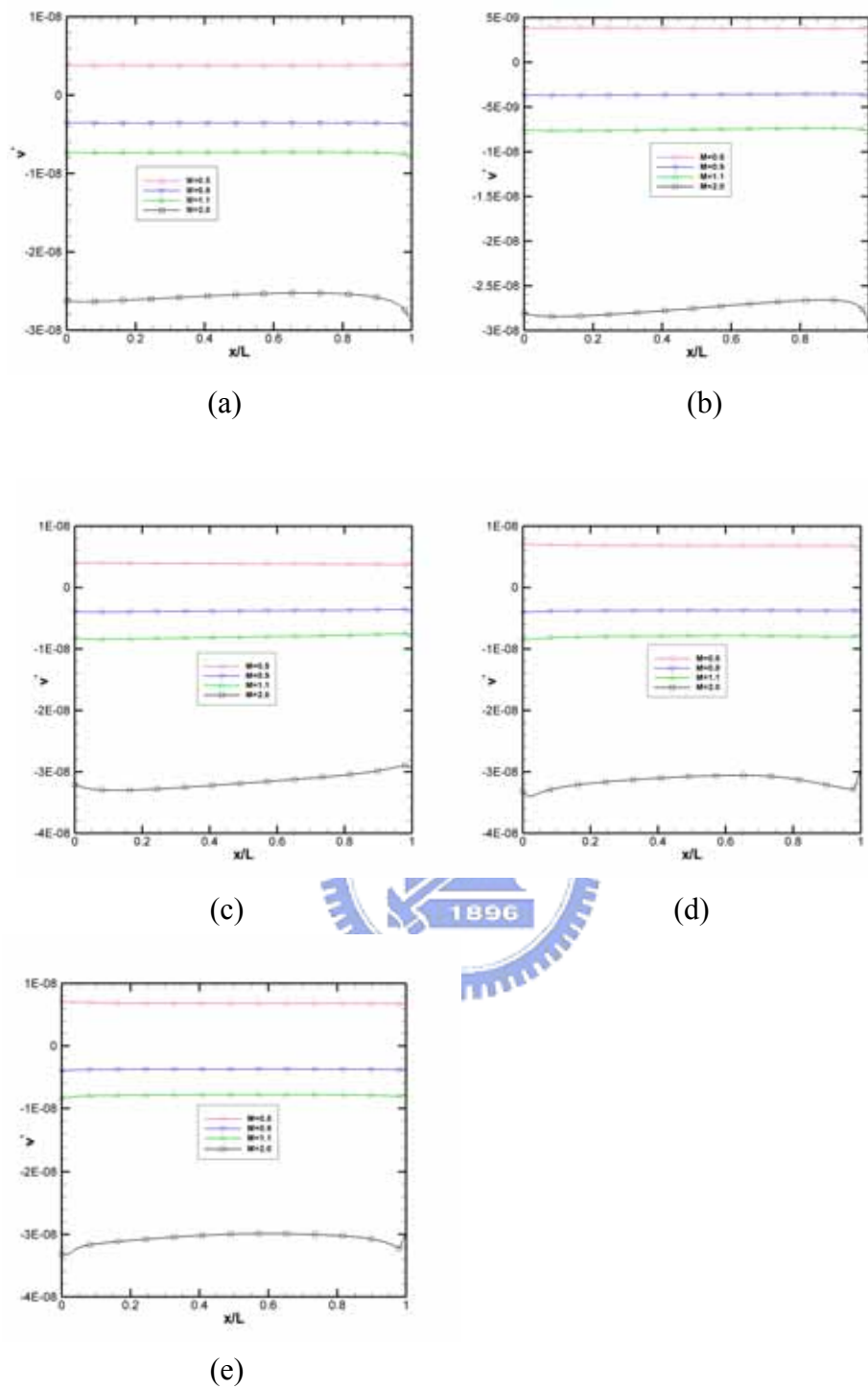
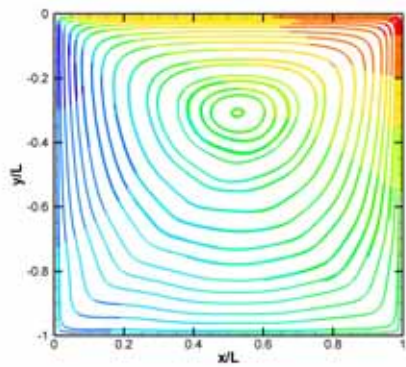
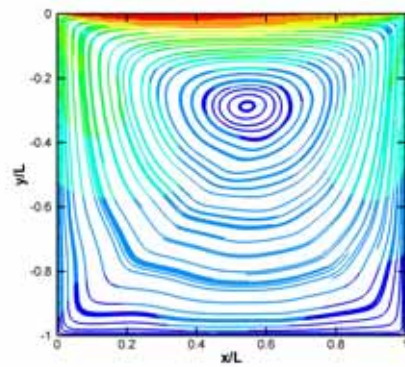


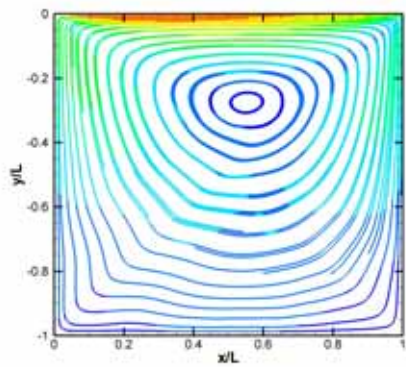
Fig. 3.105 Profile of the V-velocity on a horizontal plane $y=0$ for (a) $Kn=10$; (b) $Kn=1$; (c) $Kn=0.1$; (d) $Kn=0.01$; (e) $Kn=0.0033$



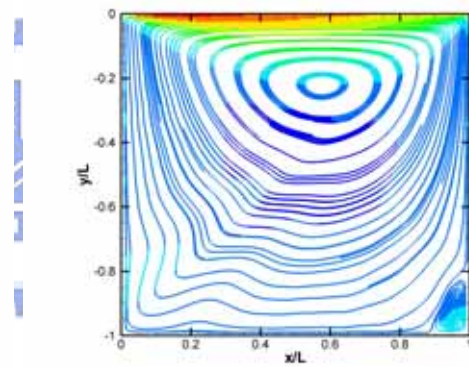
(a)



(b)

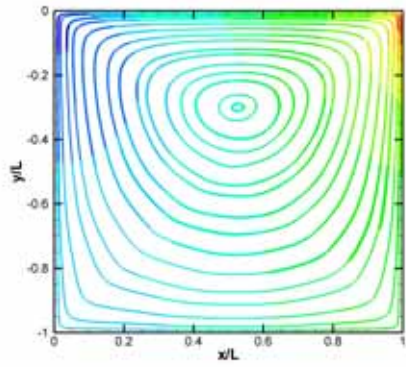


(c)

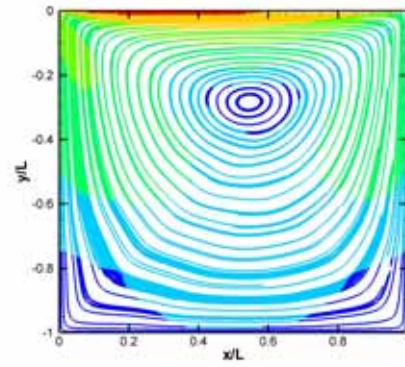


(d)

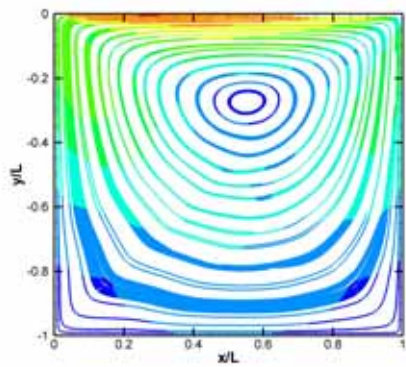
Fig. 3.106 Velocity streamlines for $Kn=10$, and (a) $M=0.5$; (b) $M=0.9$; (c) $M=1.1$; (d) $M=2.0$



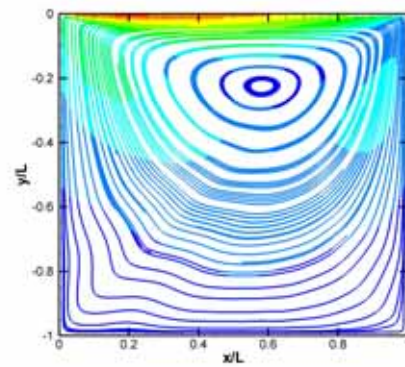
(a)



(b)

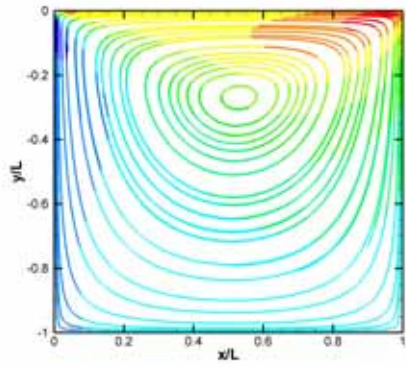


(c)

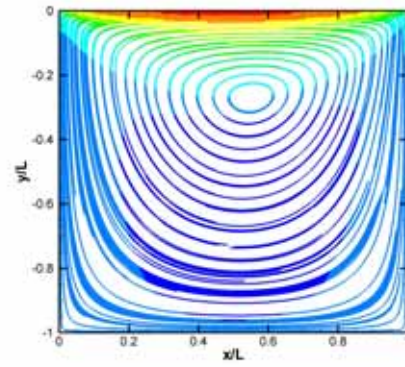


(d)

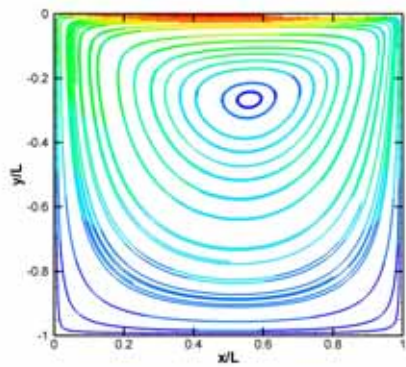
Fig. 3.107 Velocity streamlines for $Kn=1$, and (a) $M=0.5$; (b) $M=0.9$; (c) $M=1.1$; (d) $M=2.0$



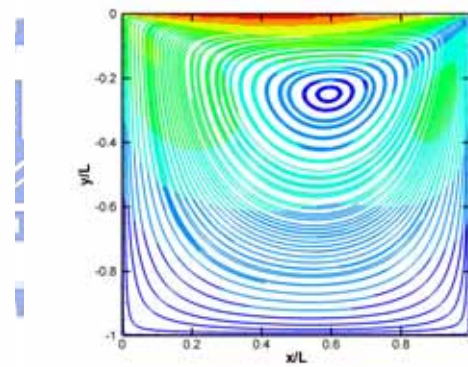
(a)



(b)

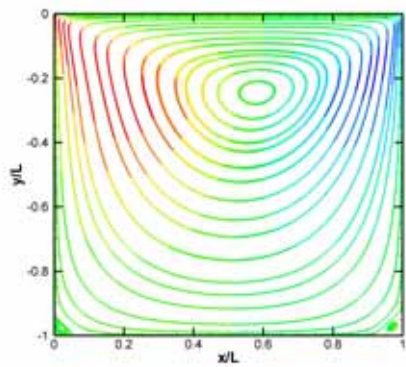


(c)

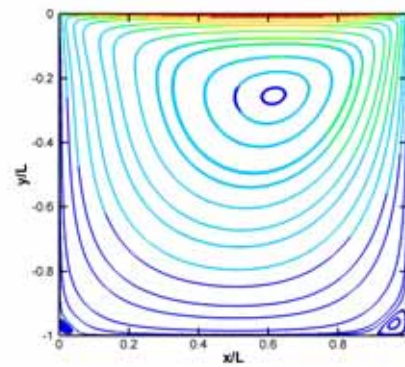


(d)

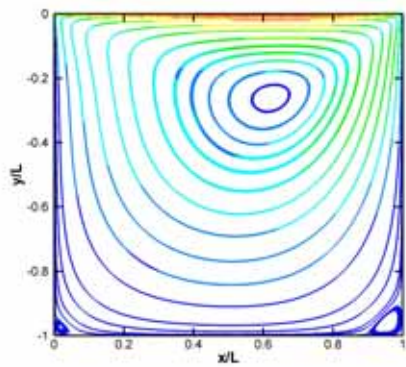
Fig. 3.108 Velocity streamlines for $Kn=0.1$, and (a) $M=0.5$; (b) $M=0.9$; (c) $M=1.1$; (d) $M=2.0$



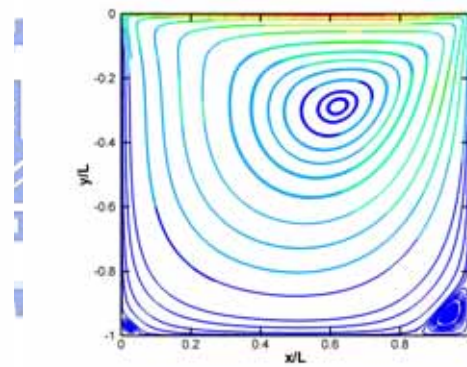
(a)



(b)

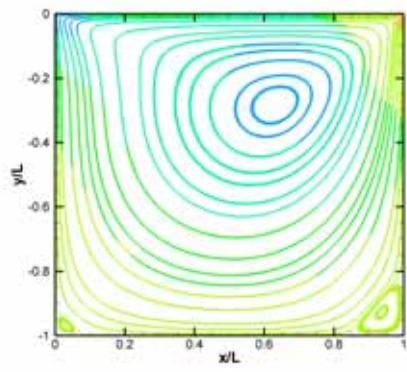


(c)

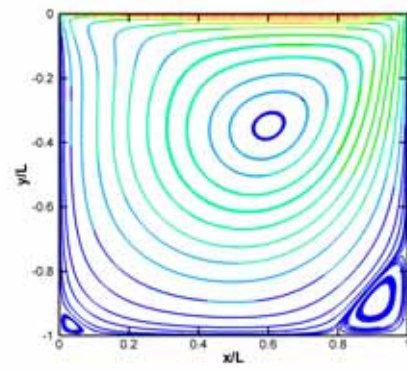


(d)

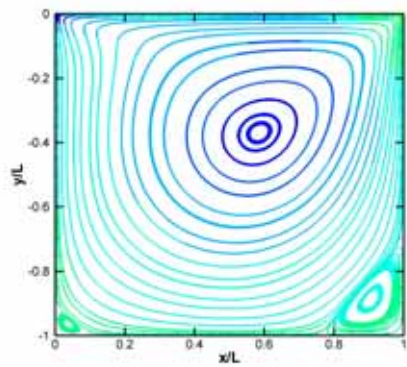
Fig. 3.109 Velocity streamlines for $Kn=0.01$, and (a) $M=0.5$; (b) $M=0.9$; (c) $M=1.1$; (d) $M=2.0$



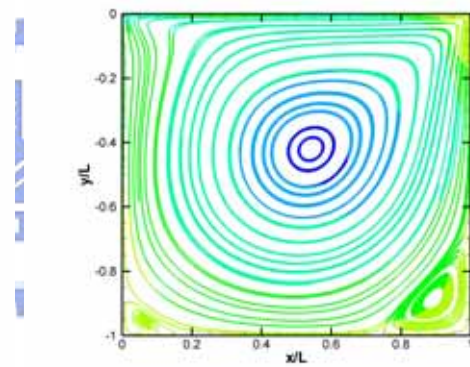
(a)



(b)



(c)



(d)

Fig. 3.110 Velocity streamlines for $Kn=0.0033$, and (a) $M=0.5$; (b) $M=0.9$; (c) $M=1.1$; (d) $M=2.0$

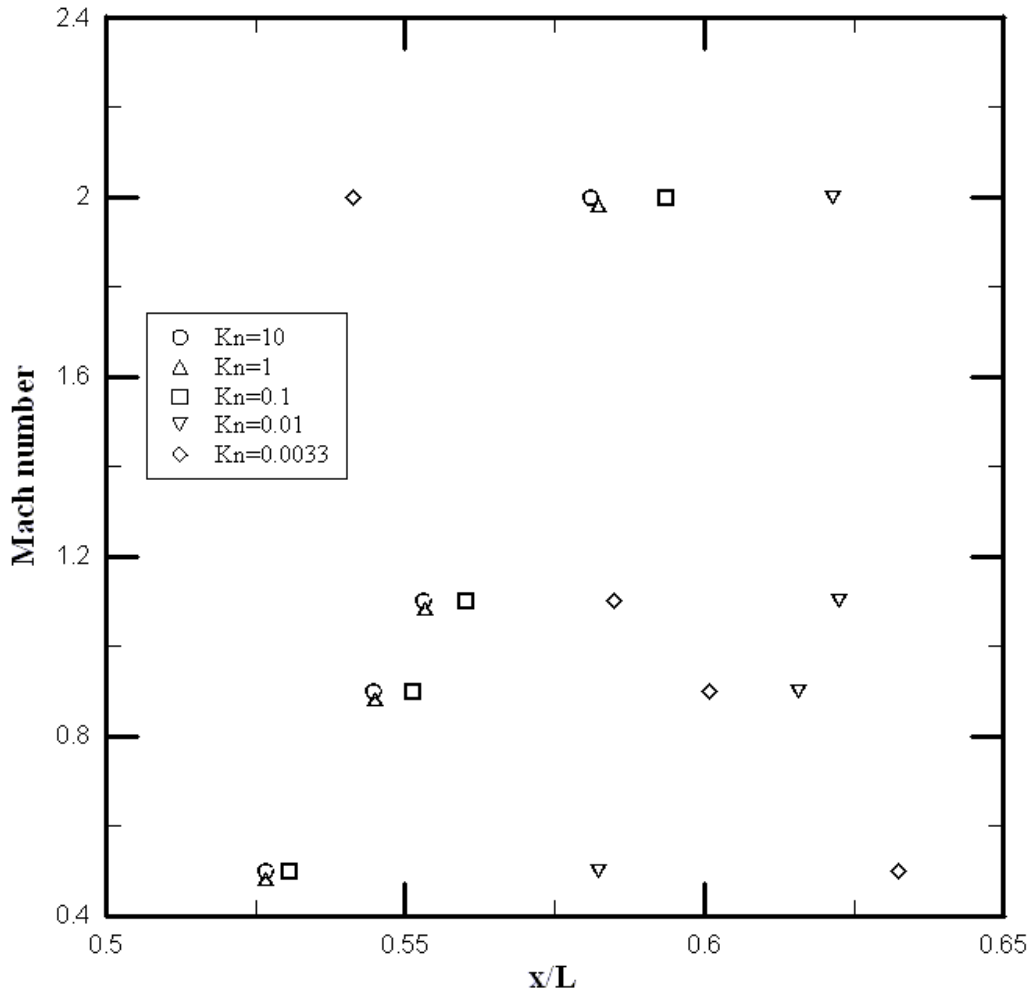


Fig. 3.111 Location of the center for x/L of the top vortex for various values of Mach number and Knudsen number.

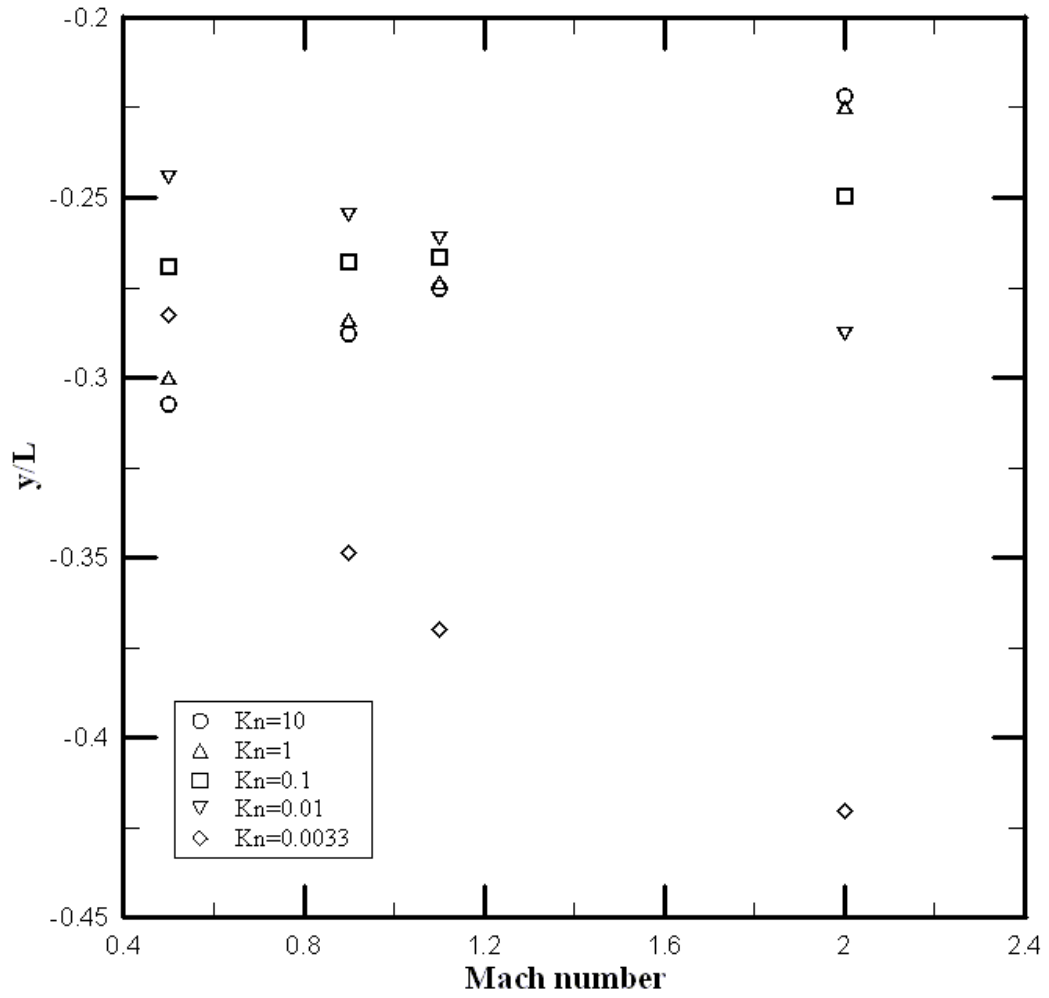


Fig. 3.112 Location of the center for y/L of the top vortex for various values of Mach number and Knudsen number.

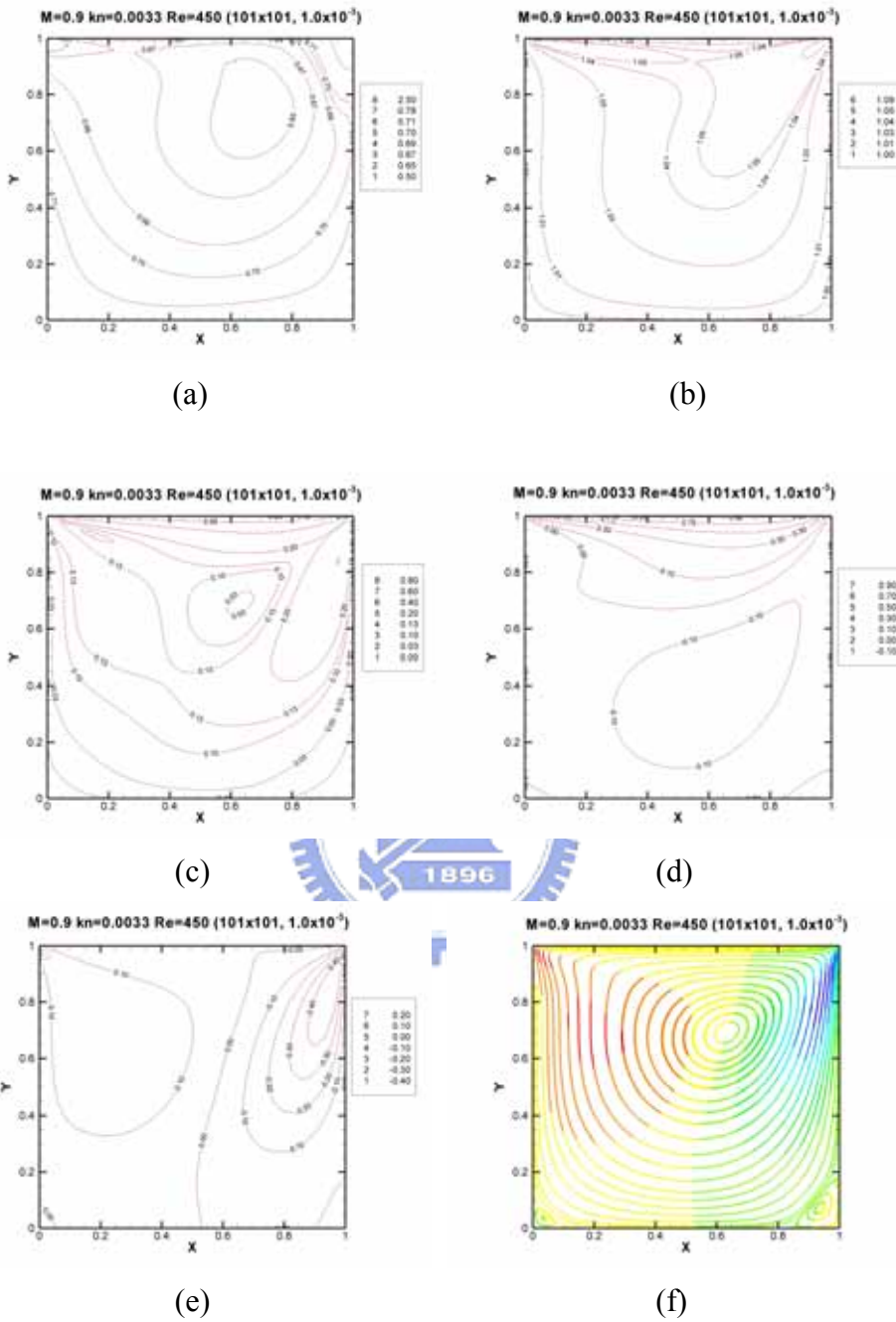
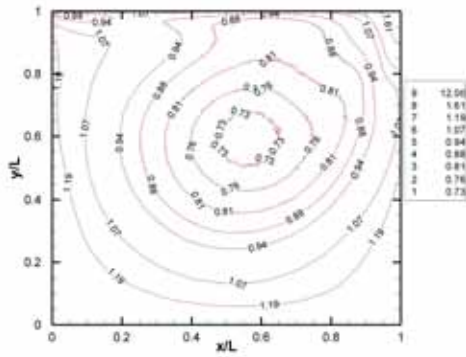
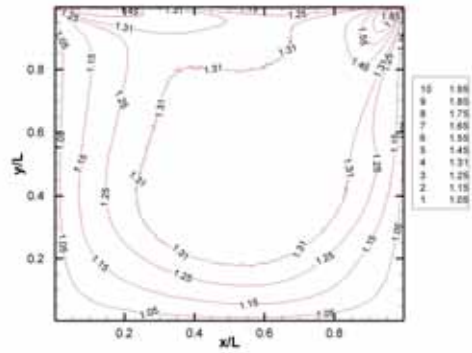


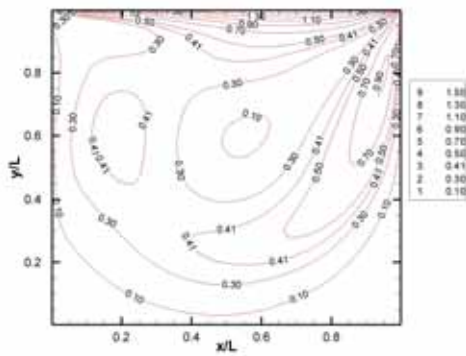
Fig. 3.113 Properties of $M=0.9$, $Kn=0.0033$ using UNIC for (a) number density, (b) temperature, (c) Mach number, (d) u-velocity, (e) v-velocity, (f) velocity streamlines.



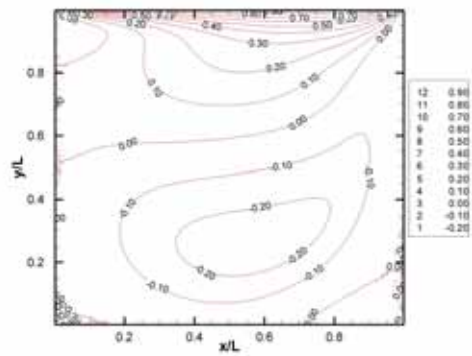
(a)



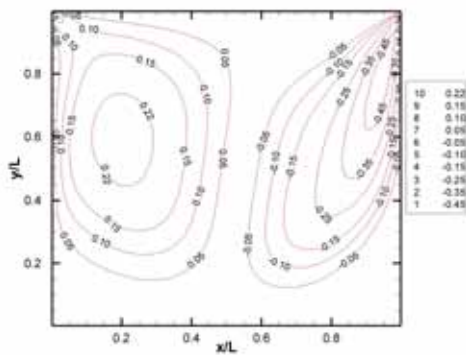
(b)



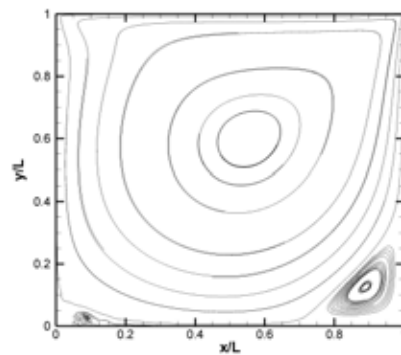
(c)



(d)



(e)



(f)

Fig. 3.114 Properties of $M=2$, $Kn=0.0033$ using DSMC for (a) number density, (b) temperature, (c) Mach number, (d) u-velocity, (e) v-velocity, (f) velocity streamlines.